Granite Petrogenesis in the Cordillera Real, Bolivia and Crustal Evolution in the Central Andes

Thesis

Granite Petrogenesis in the Cordillera Real, Bolivia and Crustal Evolution in the Central Andes

A Thesis submitted for the Degree of Doctor of Philosophy

by

James Fisher Miller B.Sc. A.R.S.M.

Dept. of Earth Sciences
The Open University

March, 1988

Date of submission: 9th March 1988
Date of award: 14th October 1988

ProQuest LLC
789 East Eisenhower Parkway
P.O. Box 1346
Ann Arbor, MI 48106 - 1346

Abstract

Isotopic, trace and major element studies of intrusives from the Cordillera Real, Bolivia have identified two distinct granitoid types. Crustally derived granitoids are characterized by high Rb/Sr and Rb/Ba ratios, high degrees of peraluminosity, high εSr and Nd model ages of approximately 1 Ga. Granitoids containing a mantle component are characterized by low Rb/Sr and Rb/Ba ratios, peraluminous or metaluminous character, low εSr and younger Nd model ages between 0.5 to 1 Ga.

Sr isotope geochronology has identified two periods of intrusion; late Carboniferous to early Permian and mid Miocene, both times of crustal thickening.

Within plate and subduction related mantle components have been identified in specific granitoids on trace element grounds. Both AFC and simple mixing have been identified and quantitatively modelled as processes of combining mantle and crustal components to produce the least evolved samples studied.

The observed evolution of the granitoids was an isotopically closed system process and is modelled as fractional crystallization. The dominant role of accessory phases in controlling the REEs has been quantitatively modelled.

Intra-pluton variations in εSr and εNd can be modelled as either mixing between mantle and crust or episodic crustal remobilization. Individual plutons display homogeneous εSr and heterogeneous εNd values, reflecting the role of xenocrystic accessory phases in preserving the Nd isotope heterogeneity of the source.

The boundary between Hercynian and Andean Orogenies (250 Ma), is marked by: a sharp fall in Nd model ages of magmatic samples, (1 to 0.5 Ga); a fall in the calculated average source Rb/Sr ratio (0.6 to 0.2); and decrease in the inferred crustal reworking rate from between 1.75x Ga^{-1} and 1.2x Ga^{-1} to below 1.2x Ga^{-1}. All these features reflect an increase in mantle involvement in the Andean orogeny relative to the Hercynian. A second shift in Nd model ages occurs at 25 Ma, the Nd model ages increase back to values comparable to the Hercynian data. Crustal thickening occurred at both these times, the first event probably involved magmatic underplating, the second was a purely intra-crustal event.

Acknowledgements

I would like to thank the following for their help during this project:

Dr. Nigel Harris and Prof. Geoff Brown for initiating this project and for their supervision and guidance both at the O.U. and in the field.

Lindsey O'Callaghan for his great help in the field, introducing me to life in S.America and more than a few interesting topics of conversation.

Ings. Herberto Perez, Raol Carrasco, Waldo Quisbert, Juan Pacheco, and Fernando Leyton from GEOBOL for their invaluable field assistance.

Kay Coombs and Debby Everard from the British Embassy for; helping to organize rock shipment, handling personal mail, and organising some good evenings out in La Paz.

John Watson for XRF analyses; Nick Rogers for INAA analyses; Andy Tindle and Ben van Wyk der Vries for 'probe analyses; and Ian Chaplin *et al.* for thin sections.

Peter Van Calsteren, Andy Gledhill, Mabs Kunka, and everyone else in the isotope lab. for the smooth running of the chemical separation facilities and the mass spectrometers and a few laughs.

Dave Wright, Andy Tindle, and David Ormerod for computing help and advice

John Taylor and Andy Lloyd for cartographic advice.

Nigel Harris, Geoff Brown, Chris Hawkesworth, Frank McDermott, Shan Da Silva, and Rob Ellam for useful discussions and reviewing parts of this work and one or two good jokes.

Helen for her help, support through three heavy years.

Franky (AKA Ian), for operating a unofficial taxi service and providing large quantities of chocolate biscuits for late night Mac sessions.

Stewart 'Boidy' Boyd, for drawing the same diagram hundreds of times and not seeming to care.

Sarah; for always buying a newspaper, officiating at an all in wrestling contest and winding me up all the time.

'Big' Shan for general enthusiasm and for almost getting me back to S.America.

Chris 'Lofty' Mac Leod, for making coffee at some odd times of the morning.

Little Matthew, for mixing the worst boomerang cocktail I've ever drunk.

Gavin, for helping to prove that ice screws don't work.

Brumley Marton, for apparently not knowing how to spell his own name; at least the NERD didn't hear of it.

Finally, my parents, sister, and the rest of my family for their encouragement and support throughout this work.

List of Contents

List of Figures

CHAPTER 4
Contact metamorphism and crustal melting

CHAPTER 5
Major and trace element geochemistry and modelling

CHAPTER 6
Isotope Geochemistry

CHAPTER 7
Summary

List of Tables

CHAPTER 6
Isotope Geochemistry

CHAPTER 7
SUMMARY

List of Plates

Preceding Page

CHAPTER 3
Field Studies and Petrography

CHAPTER 1
Introduction

The principle that orogenesis is important in the evolution of the continental crust is well recognised. Several distinct, important, geochemical processes can be identified in an orogenic event and include: the flux of new material from the mantle to the crust, the flux of the material from the lower to the upper crust, the magmatic recycling of upper crust, and the sedimentary recycling of the upper crust. The quantification of these interrelated processes is important if the growth and evolution of the continental crust is to be constrained. Granitoids are the products of the magmatic processes affecting the crust; therefore an understanding of their genesis forms an important part of this quantification. In this thesis an attempt is made to develop models of granitoid magmagenesis, evolution and crustal growth in an area although poorly studied, of considerable geotectonic significance: the Cordillera Real, Bolivia.

1.1 The location of the field area

The Andes form the longest mountain chain in the world (7000 km) and stretch the entire length of the western seaboard of the S.American continent (Figure 1.1). The central portion of the mountain chain is significantly broader than the northern and southern portions and forms two distinct cordilleras. The outer, Western Cordillera is Mesozoic in age and appears to be genetically related to the ongoing subduction of the Nazca plate. The inner, Eastern Cordillera is Palaeozoic in age and probably related to the, pre-Andean, Hercynian orogenic cycle. The area between the two cordilleras is occupied by the Altiplano (Figure 1.1), an intermontane basin of 10

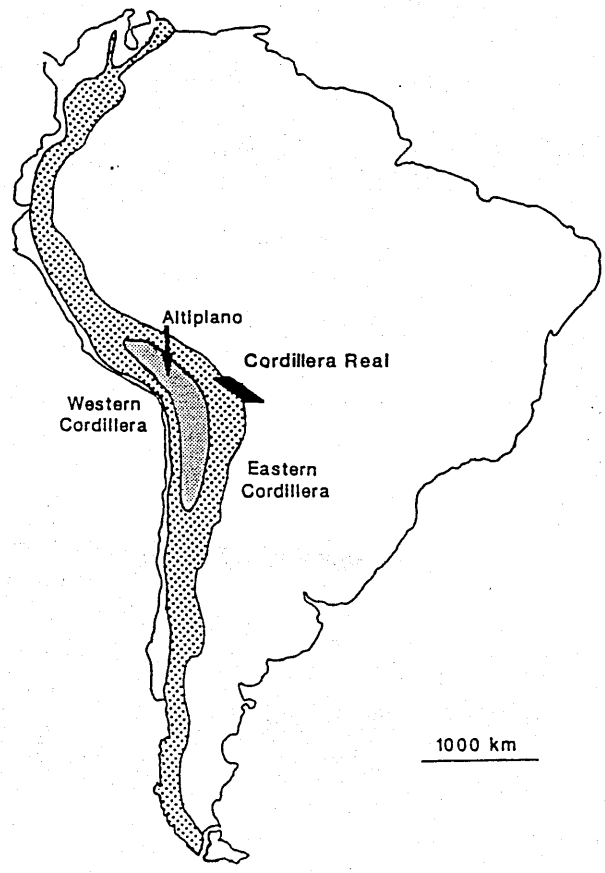

Figure 1.1

General geography of the Andes showing the location of the Cordillera Real, the Eastern and Western Cordilleras, Altiplano.

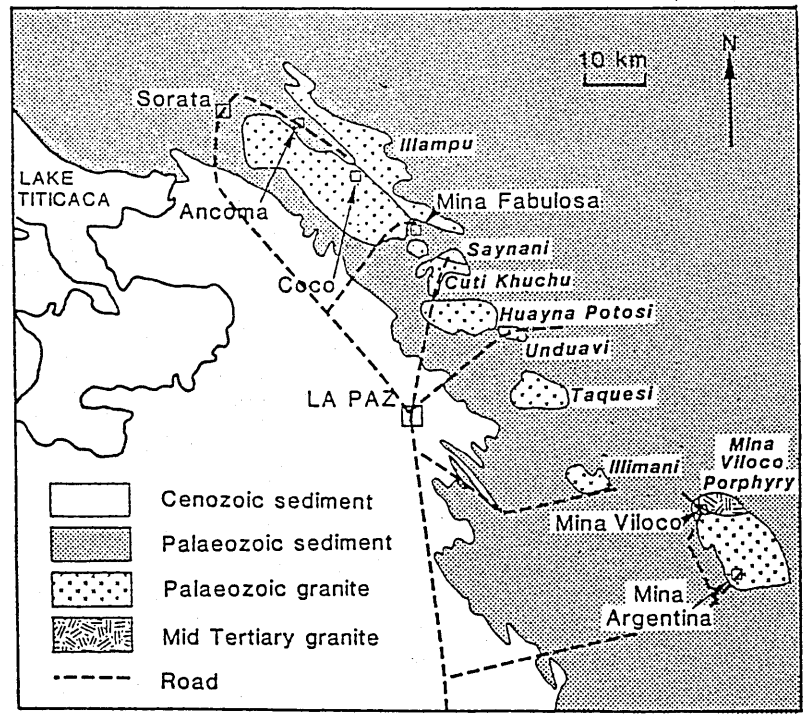

Figure 1.2

Location map of the plutons studied in this work, main towns and mines in the area, and main access routes.

to 15 km depth filled with Cretaceous and Tertiary sediments (Lehmann, 1978).

The Western Cordillera is bounded to the east by the Altiplano and to the west by the Atacama desert one of the driest places on earth. The Western Cordillera is formed by a chain of active or recently active north-south chains of stratovolcanoes rising to heights of up to about 6000 m separated by salar lakes. The rain fall in the Cordillera is extremely low and the vegetation sparse.

The Eastern Cordillera rises to a hight of up to 6500 m from the Amazon basin and Chaco plain to the east and the high level plateau (3800 m) of the Altiplano to the west. The eastern side of the cordillera therefore, has high rain fall and is highly vegetated below 2500 m. The western side of the cordillera is significantly drier and less vegetated.

The Cordillera Real forms the northern part of the Eastern Cordillera of Bolivia. The location of the granitoids of this study, the main towns, and the access routes are shown in Figure 1.2.

One of the major features of the Andes is the abnormal thickness of the crust beneath the central segment of the mountains which reaches values of greater than 70 km beneath the Western Cordillera (James, 1971) (Figure 1.3).

1.2 Previous work

The Cordillera Real has been mapped on a scale of 1:50 000 by the Geological Survey of Bolivia (GEOBOL). The maps are based largely on areal photo' interpretation with limited ground control and served as base maps for the field work.

From the GEOBOL maps and the author's own observations the granitoids of the Cordillera Real were emplaced into a thick sequence of lower Palaeozoic metapelites, which show clear evidence for large scale thrusting and faulting but no folding. Considering the elevation of the area, the observed deformation is relatively mild.

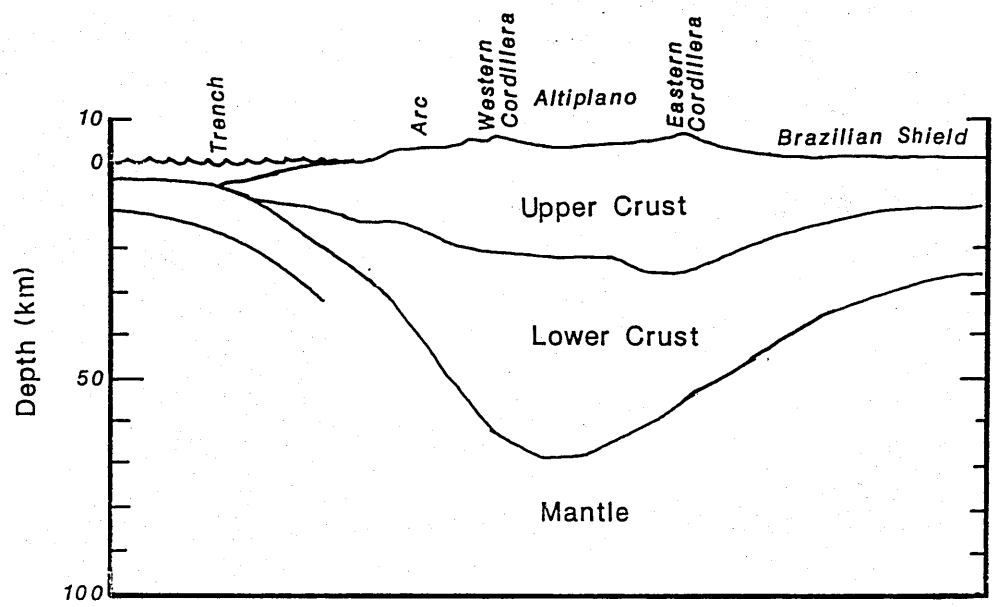

Figure 1.3

Cross section of crustal thickness beneath the Central Andes at the present day (after James, 1971). The crust thickens from 13 km in the Pacific to 70 km below the Western Cordillera and Western Altiplano, and 55 km below the Eastern Cordillera. The crust then rapidly thins to 30 km below the Subandes

Previous geochemical and isotopic work in the Cordillera Real can be divided into two fields; geochronology and economic geology.

K-Ar and ^{40}Ar-^{39}Ar work carried out on the granitoids of the Cordillera Real (Figure 1.2) dated the northern granitoids as Triassic and the southern members as Miocene (McBride, 1977; McBride *et al.*, 1983; McBride *et al.*, 1987; Grant *et al.*, 1979). This work is discussed further in section 6.1.1 together with new Rb-Sr isotopic data.

The Bolivian Eastern Cordillera is the location of the largest exploited Sn-W, vein style deposits in the world. The metallogenetic province is characterized by Sn, W, Mo, As, Bi, Cu, Zn, Pb, Sb, B; common Ag; rare Au, Ni, Co, Hg and is similar to the hypothermal zones of the Malayan tin belt (Ahlfeld, 1935; Grant *et al.*, 1974). The main mineralization occurs associated with sub-volcanic plugs to the south of the Cordillera Real, however the granitoids of this study are also mineralized and economically exploited. The deposits have a well zoned character; hypothermal veins rich in Sn and W are limited to the metasediments of the inner contact zone of the granitoid plutons; further out, Sn-poor, vein-like, mesothermal deposits of Cu, Zn, Pb occur (Ahlfeld, *op.cit.*). Kelly and Turneaure (1970) estimated the depth of emplacement of the granitoids at 2 to 4 km based on stratigraphic arguments. Fluid inclusion studies of the mineral veins support emplacement pressures of less than 12 kbar. Geothermometry on the veins has shown that the maximum temperature achieved was 500 °C (Kelly and Turneaure (*op. cit.*).

1.3 Objectives

The aims of this thesis are to date accurately the granitoids of the Cordillera Real and to assess the conditions of their emplacement, their internal evolution and their

growth of the crust in the Eastern Cordillera.

Two main theories of the cause of crustal thickening beneath the Central Andes have been suggested; magmatic underplating (James, 1971) and crustal underthrusting (Lyon-Caen *et al.*, 1985). These two models have implications for crustal growth rates in the region. It is the objective of this thesis to present Nd model ages of granitoids and sediments in order to constrain the growth of the Central Andes and to interpret their significance in light of the crustal thickening models for the area.

CHAPTER 2
Geological History of the Central Andes

2.1 Introduction: orogenesis in the Central Andes

The Andes are often cited as the classic example of an ocean-continent convergent margin, which indeed is their present day tectonic setting. However, detailed studies of the area have shown it to be the site of repeated orogenic cycles throughout the Proterozoic and Phanerozoic, and that the present mountain range is not the simple product of subduction it was once thought to be.

Along the west coast of S.America there is evidence for five parallel mobile belts, younging progressively to the west, and bounded on both sides by lower Proterozoic cratonic material, to the east by the Amazonic Craton and to the west the Arequipa Massif thought to be a remnant of a larger continental block, the South Pacific Continent of Dalmayrac *et al.*(1980) (Figure 2.1). The nature of the Arequipa Massif is of great importance in interpreting the evolution of the area. Palaeomagnetic data (Shackelton *et al.*, 1979) suggest that the massif is autochthonous and perhaps a fragment of the Brazilian Shield. This implies that the four pre-Andean mobile belts must be ensialic, and that Pacific subduction in the area only began in the Mesozoic. If, however, the massif is allochthonous then all the mobile belts may be related to subduction.

There is relatively little information on the evolution of the Proterozoic orogenies and their importance in this work is limited to the timing of basement formation.

Two Phanerozoic orogenies are recognised: the Palaeozoic Hercynian: dominated by sub-aqueous and glacial deposits; and the Mesozoic Andean; dominated by terrestrial sediments and volcanics. The Andean is more extensively studied and is better understood (Figure 2.2 for summary). The Hercynian cycle appears to have been unusual since it involved the development of an intra-cratonic basin in the north

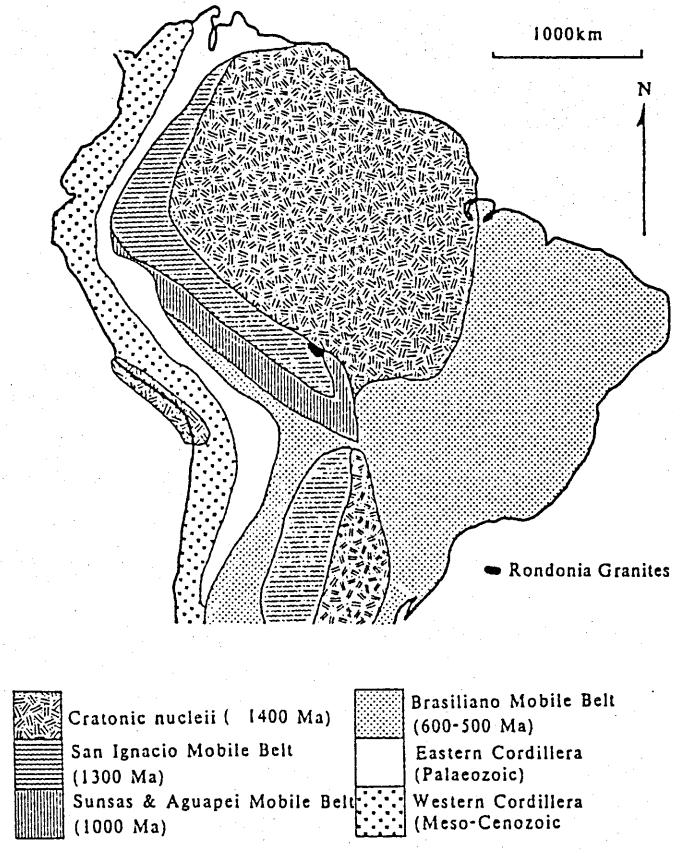

Figure 2.1

Main Precambrian basement units of S.America. Cratonic nucleus with successive mobile belts along its western margin younging towards the west and Rhondonia Massif (after Litherland *et. al.*, 1985).

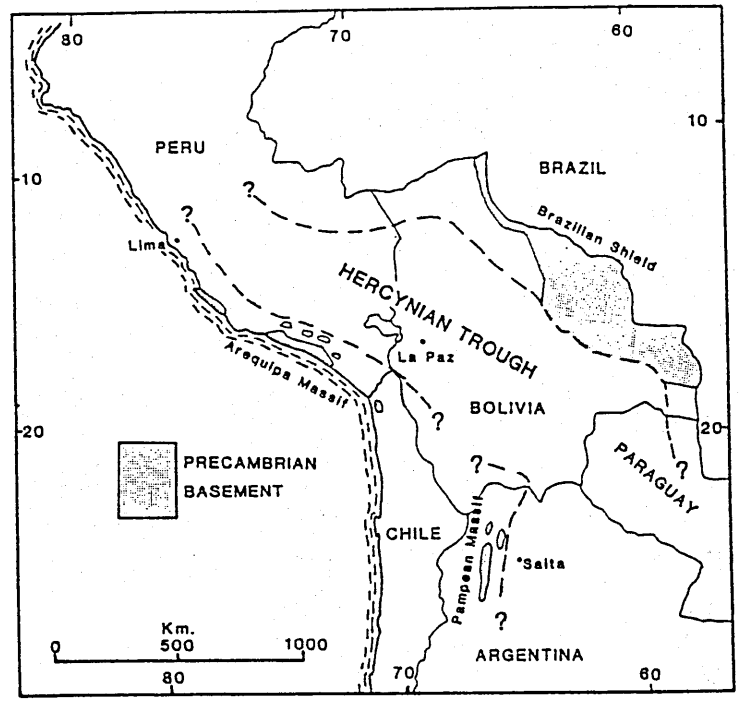

Figure 2.3

Map of Central Andean outcrops of Precambrian basement and outline of the Hercynian Trough (Pecked line) (after Dalmayrac *et al.*, 1980).

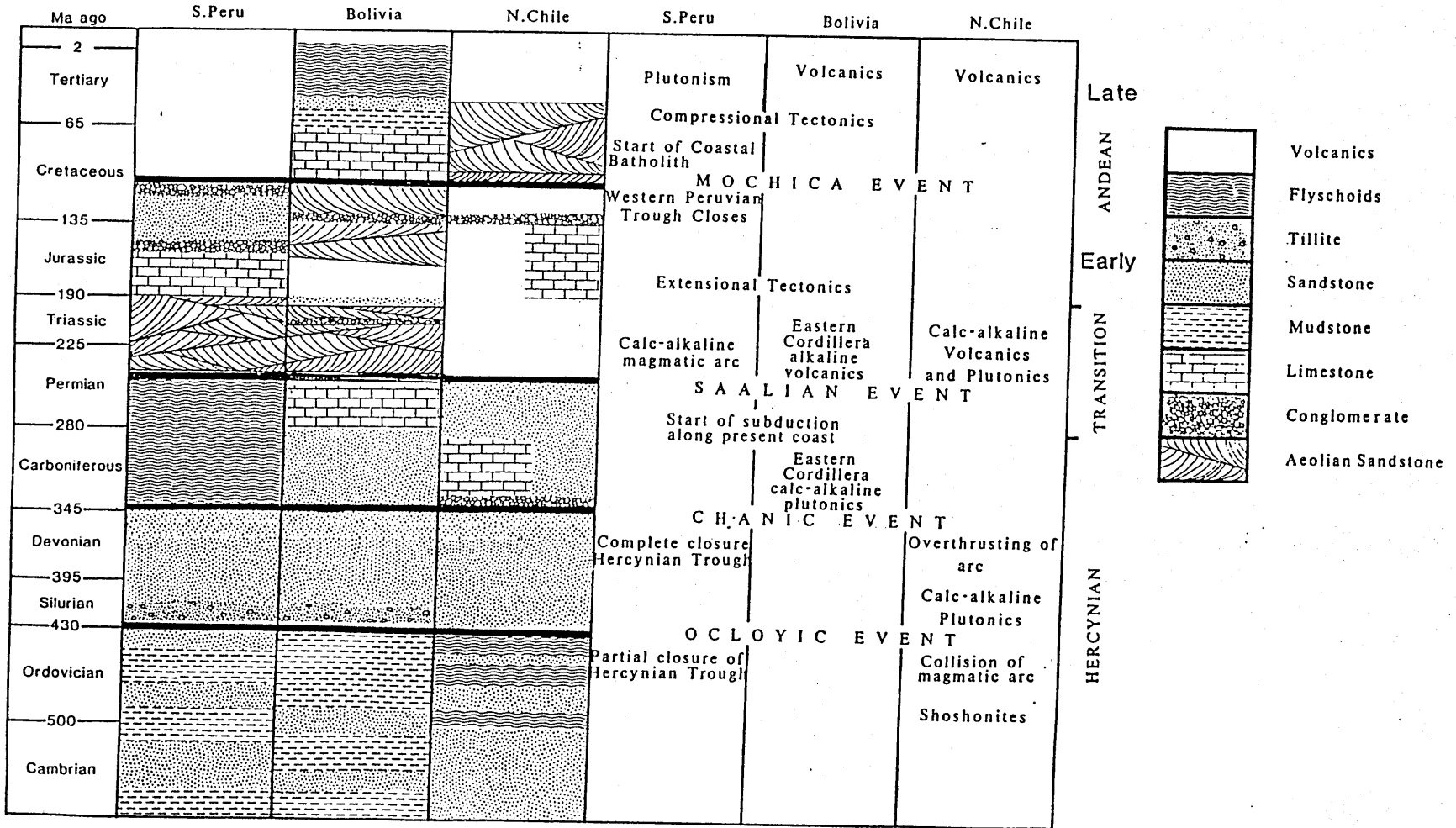

Figure 2.2

Summary of the Phanerozoic evolution of the Central Andes (For references see text).

(Peru and Bolivia) while to the south (in Chile and Argentina) a back-arc ocean basin developed. Figure 2.3 shows a cartoon of the probable environment. The intra-cratonic basin in Peru and Bolivia (the Hercynian Trough, Figure 2.3) was bounded to the east by the Brazilian shield and to the west by the large but now totally absent South Pacific Continent (Dalmayrac *et al.*,1980). To the south, in Chile, the back-arc basin was bounded to the east by the Pampean Massif (Figure 2.3). The nature of the basement under N.Paraguay and N.E.Argentina is not know, the outline in this area is therefore conjectural. The evidence for the existence and fate of the South Pacific Continent is discussed in section 2.2.2 iii

The style of the Andean orogeny clearly relates to the subduction of the Pacific plate. Early development produced a volcanic arc with an associated partially ensilalic back-arc basin along the line now marked by the Peruvian Coastal Batholith (section 2.3.2) in a dominantly extensional regime. Later (post mid Cretaceous) development saw the closure of the basin to leave only an eastward migrating arc, compressional tectonics and crustal thickening.

2.2 Geological history of the Central Andes

2.2.1 Proterozoic development

Pre-Hercynian (Precambrian) basement outcrop is not extensive in the central Andes (Figure 2.3); indeed no basement crops out in the Eastern Cordillera. However the large quantities of terrigenous Palaeozoic sediments in the stratigraphic record clearly indicate the importance of basement massifs in the evolution of the Central Andes. Therefore some knowledge of the pre-Hercynian evolution of the area is of use in determining source regions for both igneous and sedimentary rocks.

Reconnaissance mapping of the Brazilian shield in eastern Bolivia (Litherland *et al.*, 1985) identified three Precambrian mobile belts developed along the margin of

an older protolith; the San Ignacio (1300 Ma), the Sunsas and Aguapei (1000 Ma), the Braziliano (600 - 500 Ma) belts (Figure 2.1). The protolith is composed of granulites considered to have been a thick sedimentary sequence and a calc-alkali plutonic suite. Rb-Sr studies indicate ages of at least 2,000 Ma.

The San Ignacio Belt is composed of granulites, gneisses and metasedimentary schists as well as extensive syn- and post-tectonic granites. The metasedimentary schists include a metamorphosed sequence of pelites and psammites, with minor volcanics, mafic sills, ironstones, graphitic and calcareous sediments. The San Ignacio Orogeny was followed by the deposition of clastic, dominantly shallow water material. These sediments were deformed, metamorphosed and intruded by syn- and post-tectonic granites and mafic to ultramafic plutons in the Sunsas and Aguapei Orogeny, dated by Rb-Sr and K-Ar at 1000 Ma (Litherland *et al., op.cit.*). The Rondonia anorogenic alkali granites were also emplaced at this time to the north (Figure 2.1) (Preim *et al.*,1971). Evidence for the Braziliano Orogeny (600-500 Ma) in Bolivia is limited to the western margin of a large deformed sequence of eugeosynclinal sediments which extends to the east, and a north-west trending belt of miogeosynclinal rocks, the strike of which can be projected beneath the Phanerozoic cover, to link up with Andean trending Braziliano sequences recognized in the sub-Andean basement of N.Argentina (Litherland *et al., op.cit.*).

2.2.2 The Hercynian cycle

The Hercynian cycle of S.America spans the period Cambrian to Permian and can be split into two distinct stages separated by the Chanic tectonic event of Late Devonian to Early Carboniferous age (Figure 2.2) (Coira *et al.*,1982).

i) Early Hercynian stage

The Hercynian cycle began with the deposition of 5-7 km. of marine deep water silts and sandstones (Lohmann,1970). Isopach studies (Dalmayrac *et al.*, 1980)

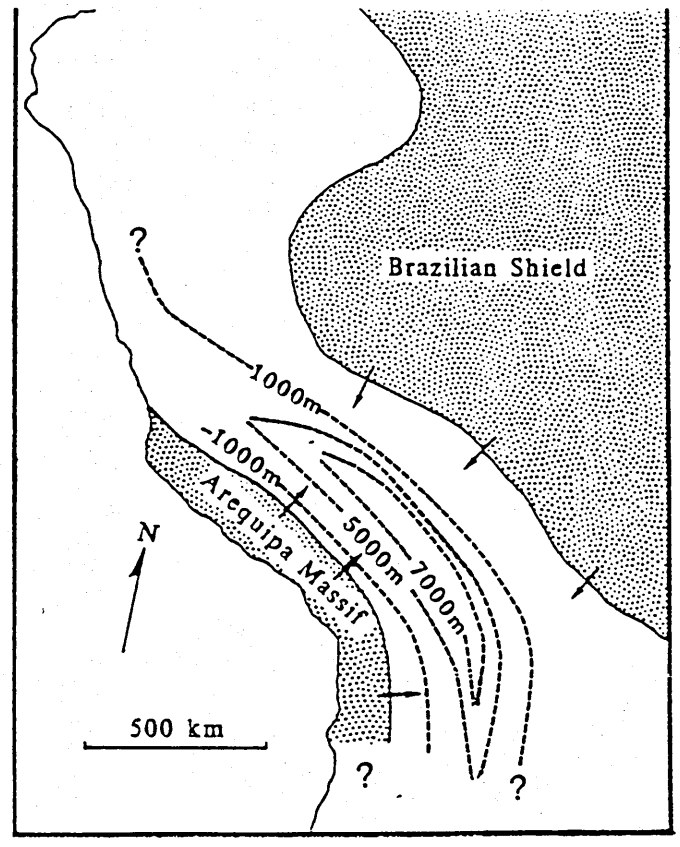

Figure 2.4

Palaeogeographic map of the Cambro-Ordovician in the Central Andes (after Dalmayrac *et al.*,1980). Large thicknesses of marine sediments accumulate in the Hercynian Trough fed from the northeast by the Brazilian shield and southwest by the South Pacific Continent.

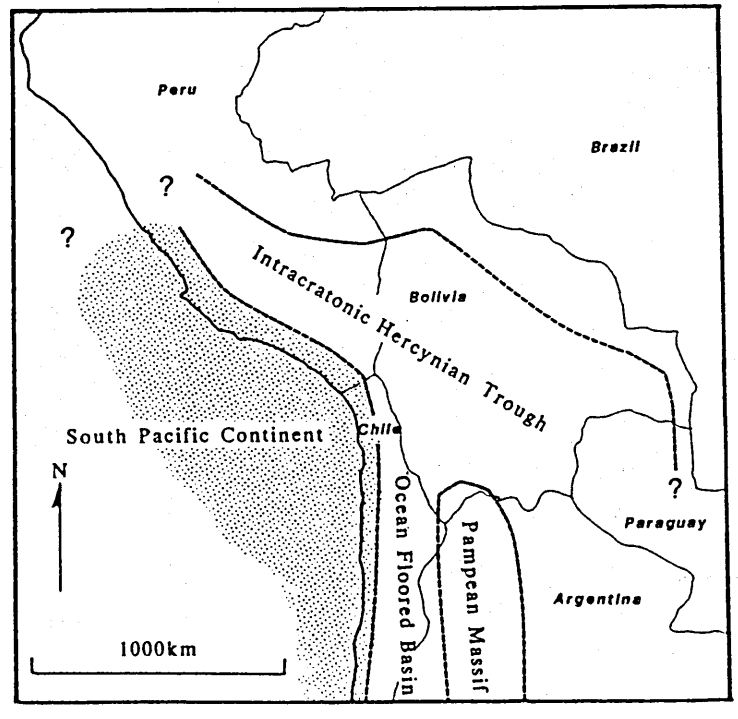

Figure 2.5

Palaeogeographic map of the Central Andes during the Devonian (after Issacson,1975). The outline of the South Pacific Continent was calculated using the volume of Devonian sediments in the Hercynian Trough.

show the deposition was controlled by the Hercynian Trough (Figure 2.4). Palaeocurrent indicators within these sediments indicate derivation from both the east and west (Figure 2.4). The lack of ophiolitic or subduction related volcanics in the sequence led Dalmayrac *et al.* (1980) to conclude that the basin was intra-cratonic, supporting an autochthonous origin for the Arequipa Massif.

In N.Chile, Coira *et al.*(1982) report the occurrence of Cambrian shallow marine sandstones overlain, probably unconformably, by Ordovician sediments which grade eastward from neritic platform facies to distal platform facies and flyschoids. Coira *et al.* (*op.cit.*) interpreted the sediments to have been deposited in a deep marine basin whose western boundary is not well defined but is postulated to be the South Pacific Continent.

Synchronous with the Ordovician sediments, large volumes of spilitic lavas occur, identified as low K arc tholeiites overlain by more extensive shoshonitic calc-alkali volcanics. The distribution of these lavas suggests a 1300 km long volcanic arc stretching from northern to southern Chile. Little geochronological data are available on these volcanics, some K-Ar whole rock mica ages of 420±5 and 416±20 Ma provide minimum emplacement ages (Linares, 1977, 1979). This indicates a profound change in the character of the arc along its length from intra-cratonic in the north to subduction related in the south.

ii) Ocloyic event

The Lower Palaeozoic lava sequence in N. Chile was terminated by the Ocloyic tectonic event (Turner and Mendez, 1979). Coira *et al.*(*op.cit.*) believe this event to mark the closure of the ocean basin and the thrusting of the magmatic arc onto the eastern margin.

To the north in S.Peru and Bolivia, the Ocloyic event is marked by a widespread unconformity in the Upper Ordovician (Lohmann, 1970; Laubaucher and Megard, 1985) and is believed to have also caused the closure but only minor uplift of the intra-cratonic basin.

iii) Silurian and Devonian evolution

The lowest Silurian unit in the Eastern Cordillera is the Cancaniri Tillite. The greatest thickness of the tillite occurs in the Central Altiplano suggesting deposition in the reactivated Hercynian Trough (Lohmann,1970). Within the tillite, erratics of basement gneiss occur. These have been identified as Arequipa Massif gneisses by Lohmann (1970) indicating a westerly sediment source. The tillite is overlain by shallow marine sediments; dominantly fossiliferous sandstones, shales and thick flyschoids of Silurian and Devonian age. All the units thicken towards the northwest and palaeocurrent indicators show currents to be flowing from the west (Lohmann,1970). Deposition again was controlled by the Hercynian Trough as shown by isopach maps. Issacson (1975), in an attempt to assess the size of the South Pacific Continent, calculated the minimum total volume of Devonian sediments in Bolivia to be 8.4×10^5 km^3. Based on the coarseness of the sediments, Issacson presumed a rapid rate of erosion implying high rate of uplift taken to be 1 km during the Devonian. Since sediments produced from the uplift of the landmass would have flowed to both the east and west, the source landmass must have been significantly larger than the 8.4×10^5 km^2 estimated. Figure 2.5 shows Issacson's estimate of the minimum areal extent of the South Pacific Continent. A similar marine sequence is seen in central Chile (Coira *et al.*, 1982) and strongly suggests that the South Pacific Continent extended southward of the area of study.

iv) The Chanic tectonic event

The Chanic tectonic event (Eohercynian event of Dalmayrac *et al.*,1980) affected the whole of the Central Andes at the end of the Devonian, causing widespread uplift. In the Eastern Cordillera of S. Peru strong deformation occurred, forming large folds of 1 to 2 km wavelength and large thrusts dipping to the northeast (Laubaucher and Megard, 1985).

In Central Chile and N.Argentina, Coira *et al.* (1982) have identified Chanic aged paired metamorphic belts. The high pressure, blueschist belt occurs to the east and a low pressure belt to the west which is related to the emplacement of large batholiths. In N.Chile only the low pressure belt can be identified. Coira *et al.* (*op. cit.*) argued that the high pressure belt may have occurred to the west of the present coast along the margin of the South Pacific Continent.

v) Late Hercynian

The Carboniferous of Andean Bolivia consists entirely of continental sediments with good evidence of glaciations in the area uplifted in the Chanic Event. Helwig (1972) noted a facies change from plant bearing deltaic facies (sandstones, shales, coals) in the northwest, to fluvioglacial lacustrine deposits in the southeast. From measured section thicknesses and Palaeocurrent studies, Helwig (1972) considered the palaeogeography to be as shown in Figure 2.6. Glaciers in the Western Proto-cordillera drained into the Hercynian Trough which connected with an open sea in the extreme north of the country. To the north in Peru, Laubaucher and Megard (1985) report Lower Carboniferous marine molasse deposits, formed from the Chanic highlands to the east. The Upper Carboniferous is represented by shallow water terrigenous marine deposits suggesting the effective erosion of the highlands by this time.

The lower Permian of Bolivia is composed of a wedge of fossiliferous marine carbonates and subordinate clastics thinning to the southeast. The contact between the Carboniferous and the lower Permian is conformable in the northwest but becomes disconformable towards the southeast. The outcrop of the lower Permian is limited to the axis of the Hercynian Trough and represents a marine transgression of the basin from the northwest (Figure 2.7). Acidic volcaniclastics occur throughout the carbonate sequence. Helwig (1972) notes a northwesterly increase in the number of tuffaceous beds. Similar tuffs and associated rhyolites have been reported in the

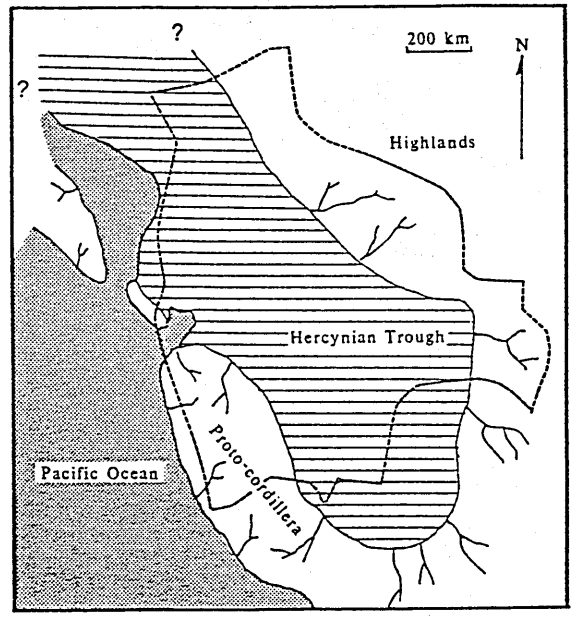

Figure 2.6

Palaeogeographic map of the Bolivia and adjoining areas during the mid Carboniferous (after Helwig, 1972). The Hercynian Trough in Bolivia was a well defined fluvioglacial nonmarine sedimentary basin bounded to the north-east by the Brazilian shield and to the southwest by a Protocordillera. To the north in Peru marine incursions occurred through gaps in the protocordillera and northern sea-lanes.

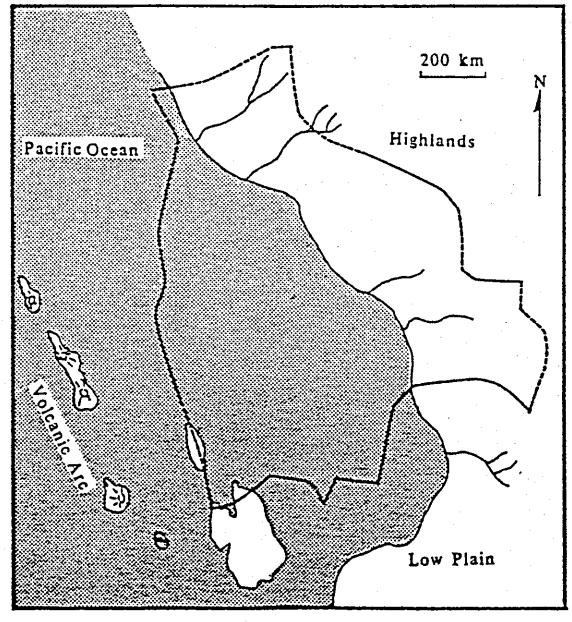

Figure 2.7

Palaeogeographic map of the Bolivia and adjoining areas during the early Permian (after Helwig, 1972). The entire Andean region was occupied by a shallow carbonate sea, with minor clastic input. The major source of detritus was the Brazilian shield to the northeast. The volcanic arc to the southwest supplied only minor detritus.

uppermost Carboniferous of S. Peru (Braun, 1967). These volcanics are almost certainly early members of the Late Hercynian / Early Andean tectonomagmatic event, which began in earnest during the Mid Permian.

vi) Hercynian - Andean Transition

The exact timing of the end of the Hercynian and the beginning of the Andean orogeny is not clear. The mid Permian Saalian Event (Coira *et al.* 1982), (Tardihercynian of Dalmayrac *et al.*, 1980) marks the beginning of the transition which continued through the Permo-Triassic and contained elements of both cycles. The nature of the change between the two cycles is also variable, since subduction had already started during the Hercynian in Chile but apparently not to the north, in Peru, Bolivia, while the whole of the Andean cycle was subduction related.

The Saalian Tectonic Event is recognised throughout the central Andes as a major uplift event, causing the reactivation of older Hercynian structures and forming highlands which were subsequently eroded to form continental Permian red beds and molasse deposits. Late Permian to Triassic magmatism occurred along the lines of both the Eastern and Western Cordilleras. The tectonic setting and chemistry of these two zones is believed to be distinct and is discussed below.

Eastern Cordillera

In S. Peru and N. Bolivia post-Saalian deformation was extensional. Continental molasse deposits (Mitu Group) were deposited in graben structures. Associated with this sedimentation, large quantities of magma were emplaced in the Cordillera. Volcanics, dominantly andesites, peralkali rhyolites and subalkali basalts occur. Nobel *et al.* (1978) on the basis of high HFSE/LILE and HREE/LILE ratios, identified the basalts and rhyolites as indicative of a back-arc rifting environment.

Western Cordillera

Coira *et al.* (1982) report the majority of the western magmatic belt to comprise rhyolites and dacites of calc-alkali affinities.

In summary the tectonic pattern during the Late Permian to Early Triassic in the Central Andes combines a westerly calc-alkali magmatic arc and an easterly, backarc, extensional zone. This general configuration strongly suggests that subduction was occurring at this time (Figure 2.8).

2.2.3 Andean orogenic cycle

In contrast to the earlier cycle the Andean is more clearly related to Pacific plate subduction. The Eastern Cordillera ceased to be a major site of magmatic activity which became centred on the Western Cordillera. Two periods of magmatism can be recognised in the Andean cycle throughout the Central Andes (Figure 2.2); an early period (Jurassic to early Cretaceous) characterized by an arc / backarc basin, and a late period (late Cretaceous to present) characterized by a lone, easterly migrating, magmatic arc.

i) Early development

The lower Jurassic of S. Peru is represented by marine carbonates suggesting a quiescent continental margin (Cobbing, 1985). The first major Andean structure to develop in the area was the Western Peruvian Trough. This back-arc basin developed in the mid Jurassic along the margin, but within the continental block and was composed of a complex structure of horsts and grabens which followed independent sedimentary and tectonic histories (Cobbing, *op cit.*). In general the upper Jurassic to mid Cretaceous sequence is of clastics interbedded with shale and quartzites grading westwards into volcaniclastic flyschoids. The upper Cretaceous,

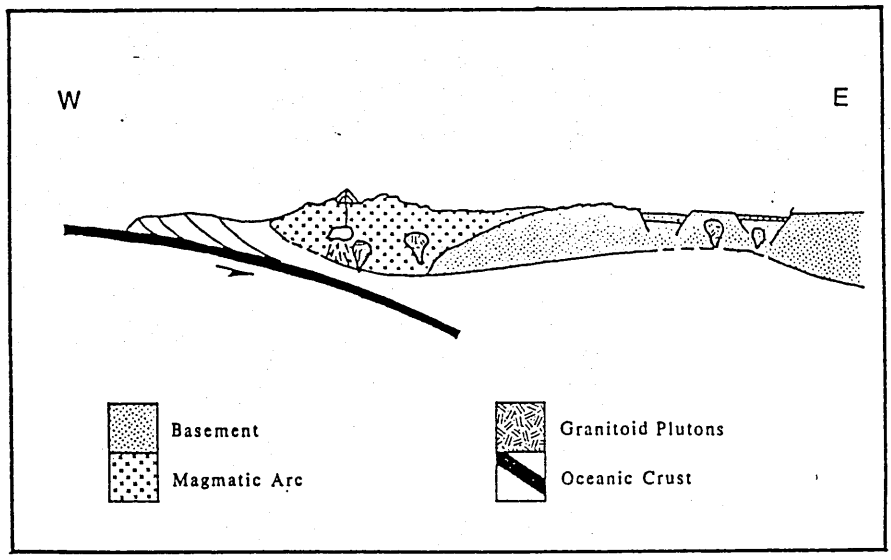

Figure 2.8

Cartoon section of the Central Andes at the end of the Hercynian (after Coira *et al.*, 1982)

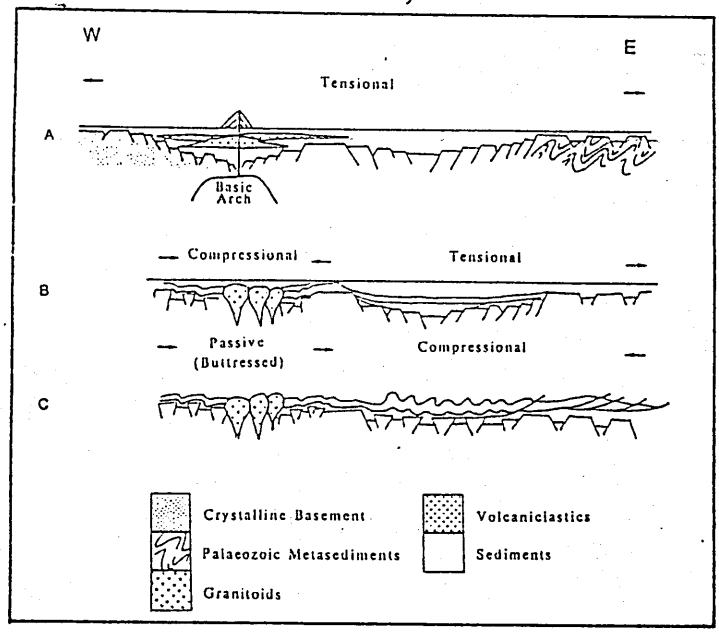

Figure 2.9

Structural evolution of the Huarmey and Chavin basins of the West Peruvian Trough (after Cobbing,1985).

A) Late Jurassic and Early Cretaceous formation of basins by development of horst and graben structures in an extensional tectonic regime.

B) Late Cretaceous. Inversion of horst and graben structure due to compressional tectonics in western basin followed by plutonic intrusion. Continued extension in eastern basin.

C) Early Tertiary. Closure of eastern basin, due to compression transferred through the buttressed western basin.

where present, is composed of carbonates.

Geophysical studies, both seismic and gravitational (Wilson, 1985), show the Western Peruvian Trough to be underlain at present by thinned continental crust; the attenuation is believed to date from the formation of the trough. The horst and graben structures and the thinned crust both indicate an extensional tectonic regime during the early Andean development of S.Peru.

The Jurassic lithologies of Bolivia are of sporadic and limited outcrop and are composed of the same red bed units as the Triassic. Likewise the lower Cretaceous units of the widespread Puca Group are composed of continental sandstones and conglomerates (Lohmann, 1970). These continental molasse deposits indicate a continuation of the Triassic continental regime, although the location of the extensional tectonics in Peru had moved from the Eastern Cordillera westwards.

In N.Chile, a volcanic arc / back arc basin pair similar to that of Peru developed. Along the present day coastal region, during the Jurassic to early Cretaceous a thick sequence of volcaniclastics was deposited. The formation is composed dominantly of andesites and olivine basalts, which show increasing potassium contents towards the east (Lohsert, 1973). Initial $^{87}Sr/^{86}Sr$ ranges from 0.7043 to 0.7059 and the formation is believed by McNutt *et al.* (1975) to be the product of early subduction, with magmas progressively contaminated by continental material. Dioritic, granodioritic, monzogranitic, and tonalitic calc-alkali intrusions occur within the volcaniclastics in north-south belts which young to the east and are believed to be related to the same subduction zone as the volcanics (Coira *et al.*, 1982 and McNutt *et al.*, 1975).

To the east of this volcanic sequence, a thick lower Jurassic marine calcareous succession occurs marking a broad marine backarc basin. Further to the east the carbonates wedge out onto basement rocks. The carbonates are overlain by upper Jurassic to Cretaceous red beds and sporadic shallow marine deposits (Van Hillebrandt, 1973). No evidence for oceanic floor in the Western Peruvian Trough has been reported for the Central Andes.

ii) Mochica tectonic event

The effects of the Mochica Tectonic Event are observed throughout the Western Cordillera. It marks the end of the Early Andean period and a major change in the tectonic style of the cycle from dominantly extensional to dominantly compressive.

In Peru, the closure of the Western Peruvian Trough commenced in the mid Cretaceous. Closure of individual basins was serial from west to east. Each basin was intruded by plutons of the Coastal Batholith after closure, thus initiating the closure of the next basin (Figure 2.9) (Cobbing, 1985). The most westerly basin finally closed in the Palaeocene.

In the Bolivian Eastern Cordillera, the event was not of major importance. A marine transgression occurred from the northwest in the Mid Cretaceous and deposited a carbonate sequence. There is evidence for only small scale syn-sedimentary tectonism during this period (Lohmann, 1970)

In Chile, as in Peru, no back-arc basin sediments occur after the Mid Cretaceous, indicating the closure of the basin.

Closure of the back-arc basins along the Central Andes is contemporaneous with increased spreading between S.America and Africa (Larson and Pitman, 1972) and probably marks the beginning of the westward movement of S. America over its own trench. Uyeda and Kanamori (1979) have suggested that this westward movement is the cause of the present day basic asymmetry of the destructive margin morphology around the Pacific. Along the west coast, the Asiatic plate either remains stationary or retreats from its trench resulting in back-arc basins. However, along the S. American coast the continental plate advances over the trench causing compressive tectonics in the back-arc area (Figure 2.10).

iii) Late Andean development

With the exception of the Late Cretaceous limestones of the Eastern Cordillera

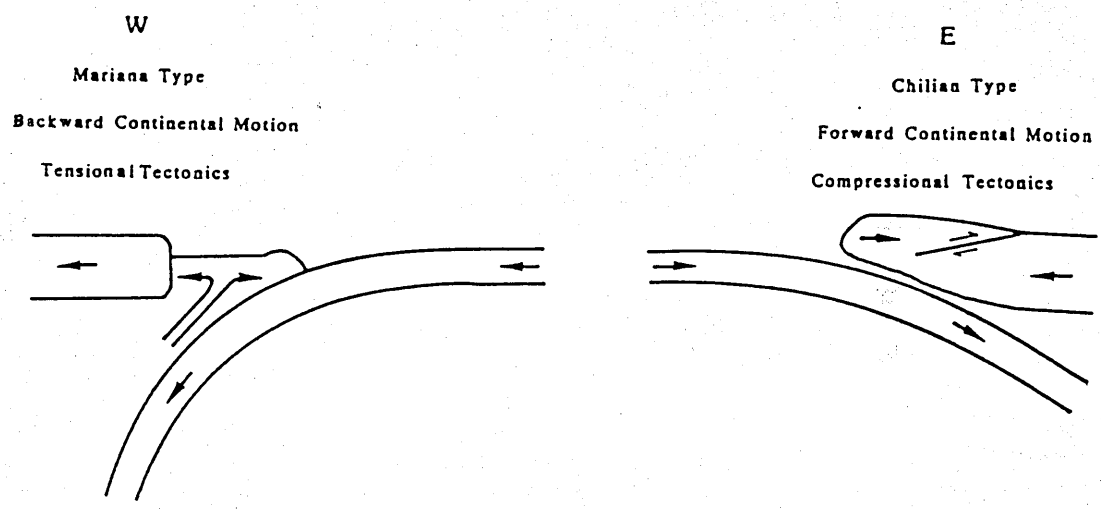

Figure 2.10

Cartoon of the varying stresses at destructive plate margins depending on the relative motion of the adjacent continental plate (after Uyeda and Kanamori, 1979).

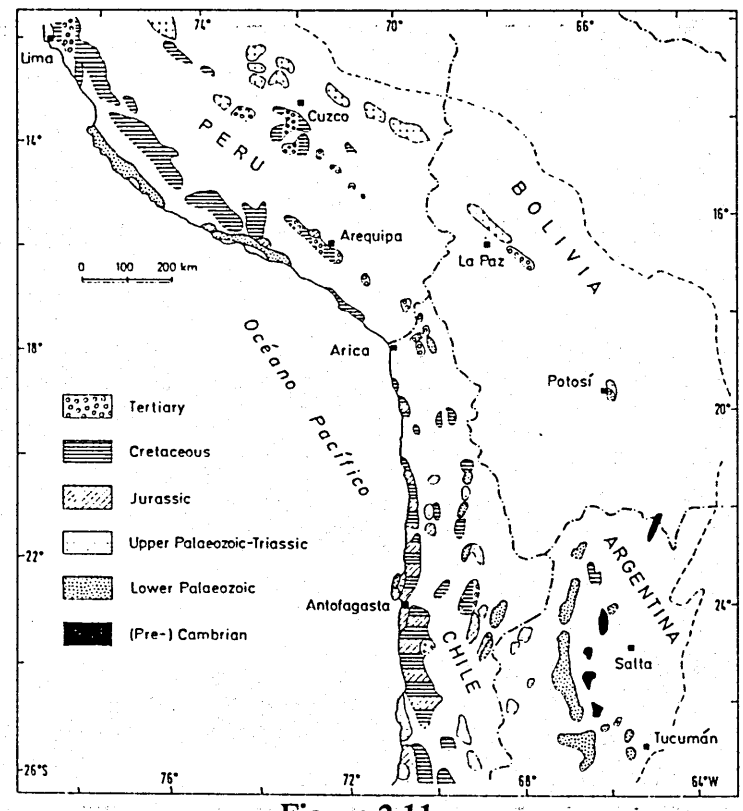

Figure 2.11

Location map for central Andean plutonics (after Breitkreuz, 1986)

and Altiplano, the sediments of this period are entirely continental and largely volcanic. Magmatism occurred throughout this period. The major volcanic event began in the Miocene, reached its zenith in the Pliocene-Pleistocene and continued with waning intensity till historic times. Coupled with the change in the intensity of the magmatism its location migrated quickly eastwards to the Eastern Cordillera in the Miocene before retreating to the Western Cordillera (James, 1971).

In S.Peru, rare outcrops of Cenozoic marine sediments occur (Bellido and Guevara, 1963). The Late Andean sequence is dominated by a thick succession of terrestrial volcanics, the lowest units of which are Eocene (Atherton *et al.*,1985). The volcanics are calc-alkali basalt-andesite-dacite-rhyolite sequences. The basic members dominate volumetrically indicating a large mantle input (Atherton *et al.*, *op.cit.*). Plutonic rocks also occur in the Late Andean period. Chemically they are of calc-alkali affinities similar to those of the Early period, but acidic members now predominate with an almost total lack of basic material. This shift towards more evolved units probably reflects the change in the general stress pattern causing slower upwelling of magma allowing increased crustal assimilation, crystal fractionation and whole-sale crustal melting.

The upper Cretaceous of Bolivia differs little from the mid Cretaceous. Major shallow marine limestone units were lain down over a wide area. The Tertiary sequence conformably overlies the Cretaceous but contains significantly different lithologies. The lowest Tertiary unit, the Chaco Inferior, is extremely widespread and composed of fine arkoses and siltstones. The immature nature of the sediments led Lohmann (1970) to identify the Western Cordillera as the sediment source. Minor evaporite units and diagnostic trace fossils indicate deposition in a lagoonal environment. The Chaco Inferior is overlain by Miocene continental molasse deposits of the Chaco Superior (Lohmann, *op. cit.*). This unit is typically composed of rhythms of conglomerates overlain by fining-upwards sequences of arkoses, sandstones, and silts. It crops out over the entire Eastern Cordillera. The coarser

nature of the sediments suggests a more proximal source than that of the Chaco Inferior strongly suggesting that the Eastern Cordillera had been uplifted during the Miocene (see section 2.5)

In N.Chile, upper Cretaceous magmatic activity shifted eastwards after the closure of the back-arc basin, to the western foothills of the Eastern Cordillera. Also at this time, small intra-cratonic basins developed in the N. Argentinian Eastern Cordillera. The red bed molasse deposits of these basins mark them as the southerly extension of the Bolivian Eastern Cordillera. Associated with the sediments, Coira *et al.* (1982) note the occurrence of trachy-andesites and alkali-basalts but no plutonics.

On the basis of the primitive nature of the magmatic arc rocks of the Upper Cretaceous in N. Chile and their low initial $^{87}Sr/^{86}Sr$ (0.7022 to 0.7035) McNutt *et al.* (1975) concluded that the rocks were uncontaminated mantle melts emplaced into thinned continental crust.

Calc-alkali volcanism continued in N. Chile gradually migrating towards the east until the early Tertiary, by which time a large calc-alkali volcanic pile had built up. The initial $^{87}Sr/^{86}Sr$ values increase with time. Eocene volcanics have initial $^{87}Sr/^{86}Sr$ of 0.7043 but change with time to 0.7057. This change is interpreted by McNutt *et al.*(*op.cit.*) to be due to increasing crustal contamination due to progressively thickening continental crust.

An uplift and minor folding event occurred in the mid Eocene of N. Chile, synchronous with the final closure of the Peruvian back-arc basin and the end of the upper Cretaceous to lower Tertiary volcanism. The Late Eocene and Oligocene sequence of N. Chile does not contain any major magmatic units. However, great thicknesses (10km) of red bed molasse accumulated in inter-mountain basins formed by the Eocene uplift (Coira *et al.*,1982).

During the late Oligocene to early Miocene, magmatic activity resumed further east of previous locations along the whole of the N.Chilean Andes (Coira *et al.*, *op.*

cit.). These volcanics represent the start of an extensive Mio-Pliocene magmatic event. Chemically, the volcanics are calc-alkali andesites and dacites with volumetrically important ignimbritic members, generated by subduction related melts contaminated by crustal material.

A major reorganization of the spreading activity in the East Pacific occurred in the Miocene. Active spreading ceased along the old Galapagos Rise (Anderson and Sclater, 1972) and started to the west along the present East Pacific Rise (Mammerickx *et al.*,1980). Associated with this alteration in spreading activity, deformation occurred along the continental margin and magmatism ceased.

Intermittent ignimbrites and lavas began to be erupted after the deformation in both Chile and N. Argentina. During the Pliocene many earlier active centres were reactivated but eruptions were volumetrically restricted and commonly show a basification trend from dacites to less evolved andesites and basalts. Holocene volcanic activity was still more restricted and is represented by dacitic to rhyolitic ignimbrites and andesitic to basaltic lavas.

2.3 Phanerozoic plutonism in the Central Andes

Granitoids form an important constituent of each of the tectonic regimes which developed in the Central Andes during the Phanerozoic. The main periods of Palaeozoic plutonism are related to major tectonic events (Figure 2.2) (Coira *et al.*, 1982) and are grouped accordingly. Unfortunately the little work which has been done on these rocks is mainly limited to geochronology and some major element analyses. Mesozoic plutonism in the area was dominated by the Peruvian Coastal Batholith, although magmatism did occur elsewhere. Figure 2.11 shows the locations of the main plutonic bodies of the Central Andes.

2.3.1 Palaeozoic plutonism

i) Ocloyic Plutonism

Related to the late Ordovician, Ocloyic tectonic event (see section 2.2.2 ii) several plutons were emplaced in the north of Chile. Halpern (1978) reported a quartz diorite pluton from the Chilean Precordillera with low initial $^{87}Sr / ^{86}Sr = 0.7045$ (εSr +5.18), suggesting a non mature crustal source. Caminos *et al.* (1982) also noted large granitic batholiths of Ocloyic age to the south in Central Chile, but provide no geochemical data. To the north, in the Arequipa Massif Shackelton *et al.* (1979) noted the biotite, hornblende granodioritic batholith of San Nicholas. This body is composed of plutonics ranging from diorites to adamellites with low initial $^{87}Sr/^{86}Sr$ (0.7087) and low Rb/Sr (0.3 to 0.2) indicative of a mantle component. The occurrence of the batholith is remarkable when compared with the lack of equivalent plutons in the Hercynian Trough itself. No plutons of Ocloyic age have been reported from the Eastern Cordillera of Peru or Bolivia.

ii) Chanic Plutonism

Comparatively little plutonism occurred associated with the widespread Chanic tectonic event (see section 2.2.2 iv). Calc-alkali plutons from northern Argentina have been reported with ages ranging from 360 ± 1 to 323 ± 5 Ma (K-Ar $\pm 2\sigma$ error, Turner and Mendez, 1979), also calc-alkali plutons of Chanic age have been recognised in northern Chile (Huete *et al.*, 1977). In the Peruvian Eastern Cordillera, only small scale magmatism occurred during the Chanic. Carlier *et al.*(1982) reported isolated calc-alkali peraluminous syntectonic granites of Chanic age in Peru. It has been suggested, on structural grounds that the Sorata Complex in the Cordillera Real of Bolivia is of Chanic age. Rb-Sr whole rock geochronology detailed in Chapter 6 supports this age for the Sorata and Tres Cruses Complexes of the Cordillera Real.

iii) Saalian Plutonism

In the north of Chile, following the Saalian uplift, a magmatic belt developed along the line of the present Western Cordillera and was the major early Mesozoic magmatic event in N. Chile (Coira *et al.*,1982) (see section 2.2.2 vi). Damm *et al.* (1981) have studied one Super-unit of the batholith, the Albayay Super-unit, located between 26° and 26.5°S, in the Coastal Cordillera of Chile. The Super-unit ranges in age from 300 to 200 Ma and shows a trend from early granites to later gabbros; the whole Super-unit is reported to have initial $^{87}Sr/^{86}Sr > 0.71$ and the acidic members are metaluminous. Cross cutting calc-alkali high-Al basaltic dykes and basic and ultrabasic enclaves indicate the involvement of subduction related mantle derived melts in the generation of the volumetrically dominant granites of probable crustal origin. Berg and Baumann (1985) report U-Pb zircon and whole rock Rb-Sr ages for this Super-unit; the Rb-Sr ages show resetting due to later intrusions but the U-Pb ages indicate emplacement during the Permo-Triassic. A slight discord in the U-Pb age is interpreted as indicating a contribution from old (>1 Ga.) crust. Also, Damm *et al.*(1981) reported the occurrence of xenocrystic zircons in the granites with U-Pb ages of 1730 Ma, supporting their crustal origin. The close relation of the basic material to the granites suggests that subduction related basic melts supplied the heat for the crustal melting.

To the south Rogers (1985) reports a Saalian Rb-Sr whole rock age for the calc-alkali Limon Verde Pluton. The initial of $^{87}Sr / ^{86}Sr$ 0.7062 (εSr +26.5) suggests derivation from : either a mantle melt, which had incorporated an old crustal component, at low crustal levels to allow later closed system evolution; a young crustal source; or an uncontaminated melt of old enriched lithospheric mantle. The broad spectrum of SiO_2 values militates against a purely crustal origin. Also crustal melts will have high Rb/Zr values due to the residual nature of zircon and the easy breakdown of amphiboles and biotite during crustal anatexis (Rogers, 1985). The

Limon Verde Pluton has moderate values of Rb/Zr (<0.8) compared to crustal melts such as collision granites Rb/Zr >1 (Harris *et al.*, 1986). High values of LILE/HFSE ratios (e.g. Rb/Zr =0.7-0.8), as for mantle derived melts, suggest the presence of a significant subduction related component .

In the Eastern Cordillera during the Permo-Triassic extensive magmatism was associated with the deposition of continental red beds in large scale grabens. Related to them high K-rhyolitic and dacitic ash flows and lavas of peralkali character exist, with low LILE/HFSE ratios (e.g. Rb/Zr =0.2), indicating a within plate character (Noble *et al.*,1978) along with peralkali plutonics (e.g. the Macusani syenite, Francis,1956). The association of rift related sediments and within plate, peralkali magmatism fits well with a model of crustal extension (Pitcher, 1984). Associated with the deposits, four groups of granitoids have been identified: Central Peru, northwest and east of Cuzco, north of lake Titicaca, and in the Cordillera Real, Bolivia (Figure 2.11). Within these plutons biotite granites predominate, often coarse grained, alkali feldspar megacrystic and generally lacking in xenoliths except marginally (Pitcher,1984). In general these granites are calc-alkali to sub-alkali and mildly peraluminous typical of subduction related plutons (Pitcher, 1984). Kontac *et al.* (1985), working to the north of Lake Titicaca, have identified two groups of Permo-Triassic plutons. The first, characterized by sub-alkali peraluminous granites of restricted high silica contents, is believed to be crustal in origin. The second, characterized by alkali to sub-alkali metaluminous to peraluminous granodiorites to granites, is believed to contain a mantle component.

2.3.2 Mesozoic plutonism

Although one of the major features of the Andean orogeny was the development of the Peruvian Coastal Batholith, other plutonics were also emplaced during this period.

In Chile during the early Andean development (see section 2.2.3 i) Coira *et al.*(1982) report north-south trending belts of diorites, granodiorites, monzodiorites

and tonalites, with ages decreasing towards the east and emplaced into an active volcanic arc. Also, on the continental foreland to the east, alkali and calc-alkali plutonics of Upper Jurassic to Late Cretaceous age occur. These syenites and alkali granites exhibit very high initial $^{87}Sr/^{86}Sr$ (0.7437 to 0.7501) indicating a mature crustal component (Halpern and Latorre,1973); their alkali chemistry indicates a within plate mantle component.

Predating the granitic plutons of the Peruvian Coastal Batholith, a string of basic plutons and associated basaltic dykes was emplaced along the centre of the Mesozoic marginal basin (see section 2.2.3 i) (Pitcher, 1984). These units were emplaced between the termination of sedimentation and the earliest members of the batholith, and so span the mid Cretaceous Tectonic Event. Gabbros chemically equivalent to high-Al olivine tholeiite (Regan, *op.cit.*), volumetrically dominate the units, which range from ultrabasics to meladiorites. The basic plutons have undergone a complex multistage emplacement and many are polygenetic. Also there is clear textural evidence for differentiation, syncrystallizational deformation and recrystallization, amphibolitization and hybridization (Regan, 1985). These plutons appear to have been shallow crustal, subvolcanic, magma chambers emplaced in thinned continental crust above upwelling mantle during a period of crustal extension.

There is no major element continuum between the basic rocks and the granitoids; also their trace element characteristics are profoundly different. For these reasons, the basic plutonics of the Peruvian Coastal Batholith are believed not to be genetically linked to the later granitoids (Pitcher, 1979).

The Western Cordillera of Peru is dominated by the coastal batholith. This composite body is comprised of over one thousand plutons forming a 60 km wide belt some 1600 km in length. It was emplaced between 97 and 35 Ma ago mainly along the axis of the Mesozoic Trough, although in the north and south the batholith intrudes Precambrian basement (Pitcher, 1984). The location of the batholith was probably controlled by a major fault system cutting the whole of the crust and tapping

the mantle over a period of about 60 Ma. Compositionally the batholith is dominated by tonalites and granodiorites forming large zoned lenticular complexes, whilst true granites are restricted to late stage homogeneous plutons and ring dykes (Pitcher, 1984). Within the batholith, groups of plutons (Super-units) showing distinct textural and mineralogical as well as geochemical and isotopic characteristics, indicating evolution from specific magma sources have been identified (Pitcher, 1984).

Geochemically the batholith is calc-alkali. With time the Super-units show a tendency to have evolved towards more acidic compositions both internally and as units in the batholith. Atherton *et al.*(1979) identified two groups within the super-units. The first, composed of older Super-units, includes granitoids ranging from diorites to monzogranite with a weighted average near a granodioritic composition and forms the majority of the batholith. The second group consists of major ring complexes of similar age displaying more evolved chemistry ranging from tonalite to monzogranite with a weighted average near a monzogranitic composition. The ultimate stage of the development of the batholith was the emplacement of several isolated, homogeneous monzogranite plutons.

The high level evolution of each Super-unit is in detail distinctive; however, general evolutionary patterns can be recognised. Petrographically, Atherton (1984) recognised a crystallization sequence of euhedral plagioclase, clinopyroxene and rare orthopyroxene, amphibole often replacing earlier clinopyroxene, biotite, quartz and alkali feldspar. Figure 2.12 shows a typical trace elemental trend for the Santa Rosa Super-unit. Atherton and Sanderson (1985) believe the trends to be the product of initial fractional crystallization of plagioclase and clinopyroxene; with evolution the clinopyroxene was replaced by amphibole and later by biotite. Detailed major element modelling of the Santa Rosa Super-unit supports this model (Atherton and Sanderson, 1985).

Figure 2.13 shows the REE patterns of the Santa Rosa Super-unit. The patterns

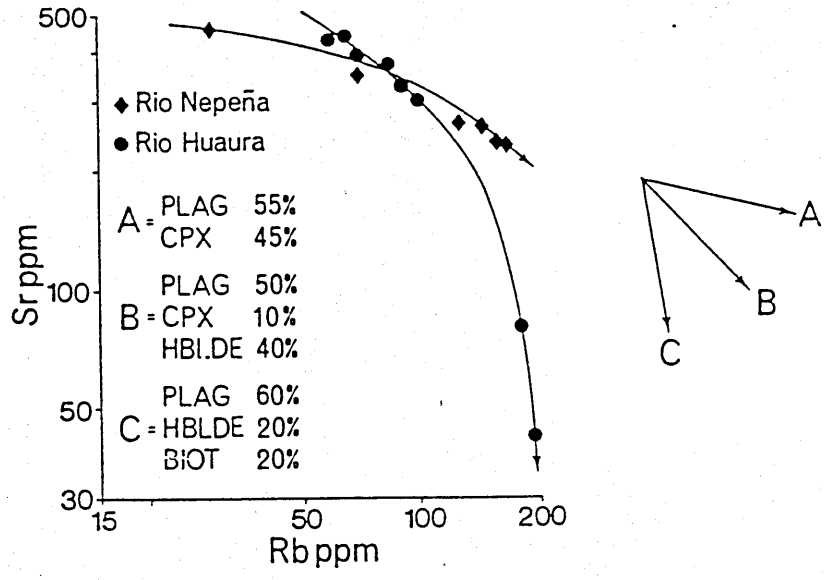

Figure 2.12

Sr vs. Rb diagram for the Santa Rosa Super-unit with postulated fractionation assemblages (after Atherton, 1984)

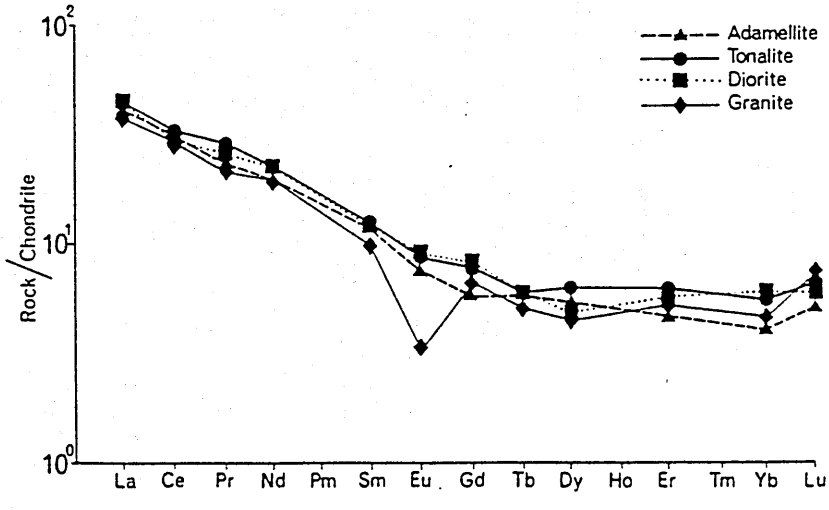

Figure 2.13

REE trends for typical members of the Santa Rosa Super-unit. Strong coherence indicates cogenetic nature. The high HREE concentrations indicate lack of garnet in residue.

are characterized by LREE enrichment (Ce_N /Yb_N= 4-5). With fractionation, the LREE behave compatibly and the HREE are slightly incompatible or maintain constant concentrations. The relatively high HREE concentrations (≈9-10x chondrite), indicate a garnet free source. The absence of a negative Eu anomaly until the late stage monzonite is probably due to the earlier coprecipitation of hornblende and plagioclase (Hanson, 1978).

Figure 2.14 shows the εSr characteristics of the batholith. A major feature of the εSr values is their uniformly low value. However, some relationship exists between the εSr and the nature of the surrounding crust (Beckinsale *et al.*,1985). The Arequipa and Toquepata segments were emplaced partly into old basement material (Precambrian gneisses, Palaeozoic intrusives and sediments) and display slightly higher εSr than the Lima segment which was intruded only into the axis of the Western Peruvian Trough (see section 2.2.3 i), composed of new crust (i.e. basic lavas, dykes, and plutons). This suggests some crustal contamination of all the granitoids, but only significant changes in the Sr isotopes of those emplaced into old crust. The Chaparra section of the Tiabaya Super-unit is an exception to this and is believed by Beckinsale *et al.*(1985) to have undergone large scale contamination by the upper crust.

Few Nd isotopic values are available for the Coastal Batholith. Le Bel *et al.* (1985) studied the Linga-Arequipa Super-unit of Southern Peru. The Linga Super-unit ranges in composition from gabbro to granite, both the major and trace element variations are consistent with low pressure fractional crystallization of a plagioclase dominated assemblage within the continental crust. Isotopically the Linga Super-unit lies in the enriched quadrant of an εNd vs εSr diagram (Figure 2.15) implying either derivation from old enriched mantle or contamination of a mantle melt by old crustal material. The local basement is 2 Ga old and isotopically distinctive, characterized by high initial $^{87}Sr/^{86}Sr$ (0.74), low initial $^{143}Nd/^{144}Nd_I$ (0.5115) and high $\partial^{18}O$ (10‰), any interaction by a basic melt with it should be isotopically identifiable. The

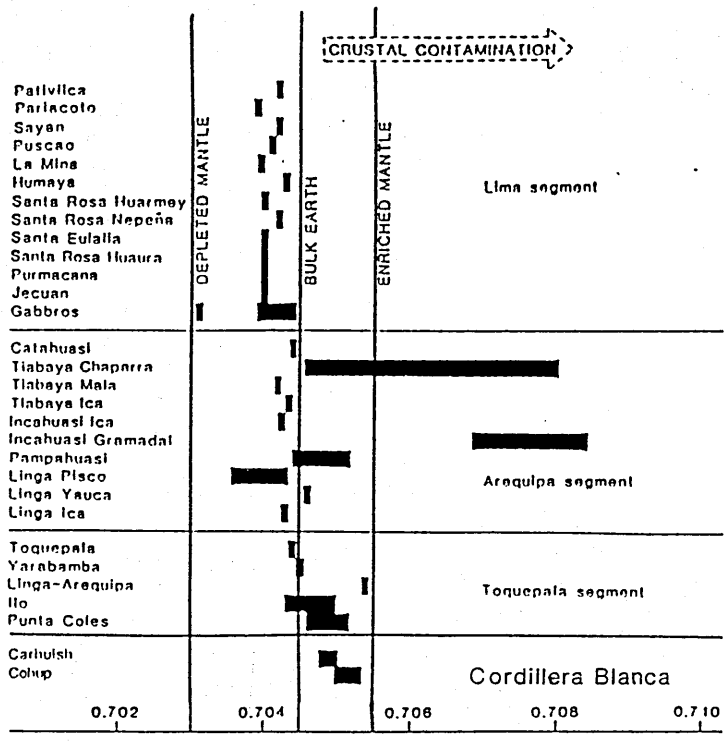

Figure 2.14

Sr isotope character of the Coastal Batholith and Cordillera Blanca Batholith, only plutons of the Arequipa segment were emplaced into Precambrian crust reflected by their elevated isotopic values.

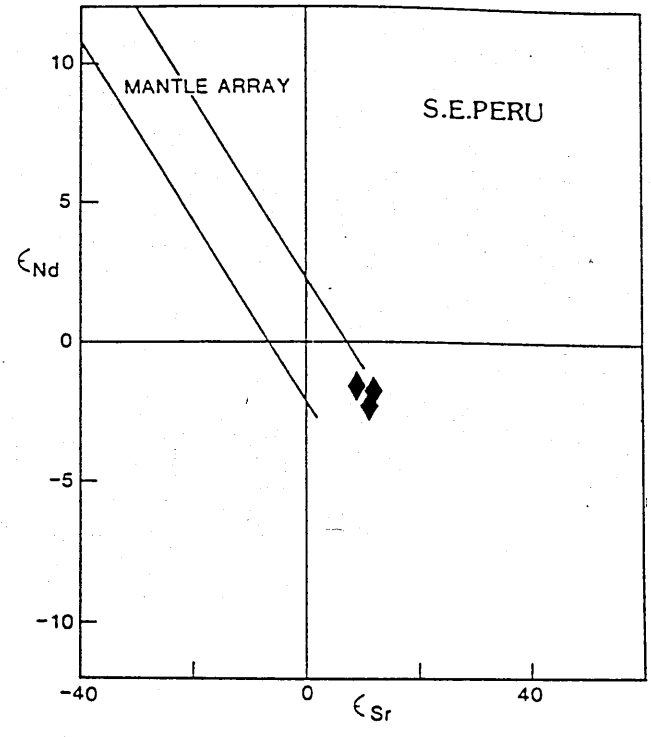

Figure 2.15

εSr vs. εNd diagram for the Linga-Arequipa Super-unit (after Le Bel *et al.*, 1985)

closed system evolution of the Linga Super-unit is indicated by the lack of correlation of $^{87}Sr/^{86}Sr$ with any fractionation index, also the isotopic character of the least evolved sample of the suite is significantly different from the local crust and within the composition of primary mantle melts as postulated by James (1982) for the Andes. Le Bel *et al.* (1985) believe the calc-alkali Super-unit to have been derived directly from an old enriched mantle source. The characteristic LREE enrichment of all the complexes could support derivation from such a source.

Atherton and Sanderson (1985) suggest a similar enriched mantle source for the Coastal Batholith and have successfully modelled the genesis of a typical Coastal Batholith tonalite by a 5% melt of an enriched spinel peridotite followed by the precipitation of a mix of clinopyroxene and olivine. It is however questionable if the volumes of acidic material observed can be generated in this way. Isotopically there is evidence for interaction with the upper crust in areas where it is isotopically distinct, this interaction is probably more widespread than at present recognised.

In conclusion Atherton and Sanderson (1985) believe the Coastal Batholith to be the product of partial melting of a spinel peridotite enriched (probably in several events) by fluids derived from the subducted Pacific slab, followed by extensive fractional crystallization. It is probable that the local crust also played a role in the formation of the batholith.

Minor granitic plutonics associated with a migrating continental magmatic arc occur in the north of Chile. Farrar *et al.* (1970) note five belts of Mesozoic plutonics in the north of Chile, younging towards the east, two of which post-date the mid Cretaceous tectonic event. However no geochemical studies have been made of these rocks.

To the east of the Coastal Batholith, the Cordillera Blanca Batholith is the final phase of acidic plutonism in the Central Andes. The batholith was emplaced into a belt of argillaceous and arenaceous sediments along the axis of an early Mesozoic sedimentary basin (part of the Western Peruvian Trough) and, like the Coastal Batholith, its location is related to a major crustal lineament (the Cordillera Blanca

Fault) (Atherton and Sanderson, 1987). Two distinct Super-units have been recognised in the batholith. The Cohup Super-unit consists largely of leuco-granodiorite and leucogranite with rare secondary muscovite and makes up the bulk of the batholith. The Carhuish Super-unit consists of biotite hornblende granodiorites and tonalites; it is limited in outcrop to the southern end of the batholith and to separate plutons to the east. Field studies of Egler and De Booy (1956) identified ample field evidence that members of the Carhuish Super-unit are intruded by members of the Cohup Super-unit. A K-Ar geochronological study of the batholith (Cobbing *et al.*, 1981) identified two groups of ages: an older group, 9-11 Ma and a younger group, 3-6 Ma. No correlation exists between these two groups and the Super-units; however, a U-Pb zircon age of 9-12 Ma for the Cohup granodiorite (Mukasa and Tilton, 1984) suggests that the younger group of K-Ar ages may be reset.

Geochemically the Cordillera Blanca Batholith shows clear calc-alkali trends, although all the batholith is mildly peraluminous. However, Atherton and Sanderson (1987) believe this to be the product of late stage interaction with the sedimentary envelope. Although two Super-units have been identified in the batholith, Atherton and Sanderson (1987) have treated the batholith as one unit due to a lack of mapping and field control. On log vs. log trace element plots linear or curved trends are not present, indicating a lack of a simple fractionation link between the samples. REE patterns for the batholith are all similar, suggesting a common source; all are LREE enriched (Ce_N/Yb_N= 13.5-27). Only the most evolved samples display negative Eu anomalies, suggesting a lack of residual plagioclase and plagioclase fractionation only in the late stage melts, a feature supported by the high concentrations of Sr in the batholith. Hornblende fractionation is not responsible for the HREE depletion as there is no clear decrease in the HREE concentration with increasing SiO_2. Atherton and Sanderson (1987) can identify no simple fractional crystallization or mixing model to explain the observed trace elemental variations or REE patterns.

The Sr isotopic character of the Cordillera Blanca Batholith is shown in Figure 2.14. The two Super-units show a broad separation with the more evolved Cohup exhibiting higher εSr values, although both Super-units lie within the range of the Coastal Batholith. Mukasa and Tilton (1984) used Pb isotopes to constrain the source of the Cordillera Blanca Batholith. They found no evidence for an old crustal component, although the evolved units do contain a Pb component likely to have come from the sedimentary envelope. It is not clear if this component entered via bulk assimilation or a fluid phase. The dominant Pb component of the batholith was derived from an isotopically homogeneous reservoir believed to have been enriched lithospheric mantle (Mukasa and Tilton, 1984).

In conclusion then the Cordillera Blanca Batholith is believed to have been derived from a plagioclase free enriched mantle source and to show only minor late stage evidence for interactions with the upper crust. Atherton and Sanderson (1987) cannot model the observed variations in the trace elements by fractional crystallization or mixing, this may be due to late stage fluid interactions with surrounding sediments having disturbed the magmatic patterns. This batholith marks the end of large scale plutonism in the Central Andes.

2.4 Summary

The evolution of the western margin of S.America is characterized by the build up of successive mobile belts along the margin of the Brazilian shield. At least three Proterozoic belts have been identified and all are believed to be related to eastward dipping subduction zones. The Phanerozoic Hercynian and Andean events are better understood. The Hercynian was an intra-crustal event in the north but subduction related to the south. There is good evidence for a large continental block (the South Pacific Continent) to the west of the present coast line. Two major tectonic events

occurred in the Hercynian; the Ordovician Ocloyic event and the Devonian Chanic event. The Ocloyic was related to the partial closure of the northern Hercynian Basin and the collision of a magmatic arc with the mainland to the south. Several granitic plutons have been reported of Ocloyic age from northern Chile and southern Peru. They are characterized by significant mantle components. The Chanic event marked a further closure of the Hercynian trough and the trusting of the magmatic arc onto the continental foreland. Little plutonism appears to be related to the Chanic event, a few calc-alkali plutons of Chanic age have been identified in the Eastern Cordillera of Peru, Bolivia and Argentina.

The Hercynian and Andean orogenies are separated by the Permian Saalian tectonic event which marks the initiation of subduction along the entire length of the Central Andes and widespread uplift. Following the Saalian major calc-alkali plutonic arcs developed on the foreland of Peru and Chile, the limited geochemical data indicate a significant subduction related mantle component. In the Eastern cordillera peralkali syenites and granitoids were emplaced with trace elementally within plate character. Calc-alkali subduction related granitoids also occur.

The Early Andean was dominated by extensional tectonics with a complex back arc basin forming along the Peruvian coast and probably extending southwards. The Basin started to close in the mid Cretaceous Mochica tectonic event which marked a change to compressional tectonics, related to the initiation of forward motion of S.America over its trench driven by the opening of the southern Atlantic. Deposition during the late Andean was almost entirely continental and dominated by volcanism. Throughout the initial part of the Late Andean the Coastal batholith of Peru was built up. The first stages of its development were the emplacement of gabbroic bodies followed by large quantities of calc-alkali tonalitic and granodioritic magma believed at least in part to be derived from subduction enriched mantle. Small quantities of true granite were emplaced in the later evolution of the batholith. The Cordillera Blanca was the last major exposed plutonic event in Peru; this calc-alkali batholith like the Coastal Batholith is believed to have been derived from enriched mantle.

2.5 Crustal thickening in the Central Andes

One of the most striking features of the Andes is the great thickness of the crust in the area (James,1971). Along a cross section at right angles to the mountain chain crustal thickness varies from 11 km in the Pacific basin to 30 km along the coast but reaches more than 70 km beneath the Western Cordillera and Western Altiplano. Further to the east the crust thins rapidly to 55 km beneath the Eastern Cordillera and 30 km beneath the Subandes (Figure 1.3). The timing and cause of the crustal thickening event or events is of major importance in understanding the evolution of the Andes.

Two main methods by which the Andean crust may have been thickened have been proposed; magmatic underplating and crustal underthrusting. Within the two major Cordilleras of the Central Andes it is possible that both have contributed at different times to the uplift. The lack of marine deposits from the beginning of the Tertiary in the Western Cordillera and from the Miocene in the Eastern Cordillera, indicate limits for the initiation of uplift in the areas.

Within the Western Cordillera geomorphological work has identified three major stages of post Oligocene uplift (Tosdal *et al.*,1984). Initial uplift occurred in the early Miocene and major topographic relief was achieved in the mid to late Miocene by a series of closely spaced uplift events. The main period of uplift in the mid Miocene was accompanied by granitic melt formation and emplacement, and tectonic activity in the Eastern Cordillera suggesting magmatic underplating. However, there are other possibilities as to the cause of uplift; the South Pacific Continent (described in section 2.2.2 iii) could have been subcreted beneath the Western Cordillera (Rogers, 1982).

There is broad agreement amongst workers in the Central Andes as to the time of uplift in the Eastern Cordillera. Lohmann (1970) noted a marked change in lithology

of the Bolivian Andes at the beginning of the Miocene from fine arkoses derived from the Western Cordillera to coarse molasse deposits derived from the east (section 2.2.3 iii). Benjamin *et al.*(1987) using fission track dating techniques on granites from the Cordillera Real and presuming a geotherm calculated the granites to have been emplaced at about 7 km. 40-45 Ma ago uplift began at a rate of 0.1-0.2 mm/year, the rate increased rapidly at 15 Ma reaching rates of 0.7 mm/year. Magmatism occurred within the Cordillera during the Miocene and recent structural and sedimentological work in the Sub-Andes (Sheffels, *Pers. Comm.* and Allmendinger, 1986) have shown that all deformation and underthrusting in the area started in the Tertiary. McBride *et al.*(1987) have dated an Upper Eocene, major thrusting event, along the north-eastern margin of the Cordillera Real. Lyon-Caen *et al.* (1985) estimated the minimum amount of crustal shortening in Bolivia caused by underthrusting to be 25% to 36%. However, Allmendinger (1986) considered underthrusting to be an order of magnitude too small to explain the total crustal thickening and suggested that there was a magmatic underplating component. Granitic magma was emplaced into part of the Cordillera Real in Bolivia at this time (Chapter 6), but the source of the magma is believed to be purely mature sedimentary crust (Chapter 5). Allmendinger (1986) also supported the view that major underthrusting occurred in the Eastern Cordillera during the Miocene.

The general conclusion therefore is that uplift in the Central Andes occurred in the Miocene. The cause of the uplift is not clear; crustal underthrusting appears to have been the dominant, if not the only cause of uplift in the Eastern Cordillera, while in the Western Cordillera, an element of crustal subcretion is probable as is magmatic underplating.

CHAPTER 3
Field Studies and Petrography

3.1 Introduction

The aims of this chapter are as follows:

i) To describe the field relationships and petrography of the groups of genetically related rocks (facies) and enclaves identified below

ii) To establish crystallization sequences for each facies and comment on the controls of this sequence

iii) To identify the styles of alteration and indicate their possible effects on the chemistry of the facies

This chapter contains information on the field relationships and petrography of Tres Cruses and Sorata Complexes, which are the main interest of this thesis and have been investigated geochemically (chapter 5) and isotopically (chapter 6), and five other plutons, the Huayna Potosi Granite (HPG), the Cuti Khuchu Granite (CKG), the Saynani Granite (SG), the Unduavi Granite (UG) and the Illimani Granite (IG) for which limited geochemical data are available.

In order to model the chemical variations of any suite of samples it is necessary to identify the possible fractionating phases. The terms cumulus and intercumulus are used divide phases into those which crystallized during the ascent of the magma (cumulates) and those which crystallized after the magma ceased to behave in a fluid manner (intercumulates). No implications for separation from the melt are implied by the terms in this work. In granitoids, the identification of cumulus phases is not a simple matter, since acidic magmas usually have high viscosities and are probably crystal rich mushes throughout their existence (Wickham, 1987). However the textural separation of the mineralogy into cumulus and intercumulus grains is of

Sorata Complex		Tres Cruses Complex	
Coco Granite	60	**Mina Argentina Granite**	47
Associated aplites	5	Associated aplites	4
Associated autoliths	1	Associated autoliths	9
Ancoma Granodiorite	13	Associated xenoliths	4
Associated autoliths	1	**Mina Viloco Granite Porphyry**	9
		Associated autoliths	6
		Associated xenoliths	2
		Mina Maraion Microgranite	4

Other Plutons

Huayna Potosi Granite	11	**Illimani Granite**	14
Associated aplites	4	Associated aplites	3
Unduavi Granite	4		
Cuti Khuchu Granite	8	**Saynani Granite**	5

Table 3.1

Numbers of thin sections studied for each facies

Facies name	Comp. range	Texture Grain size	Mafic phases	Accessory phases	Enclaves
Tres Cruses Complex					
MAG	Monzogranite rare granodiorites	Equigranular Medium grained	Biotite	Zircon Apatite FeTi oxides	Autoliths and xenoliths
MV GP	Monzogranite	Porphyry Coarse grained	Biotite	Zircon Apatite Cordierite	Autoliths and xenoliths
MMM	Monzogranite	Equigranular Medium grained	Biotite	Zircon Apatite	None
Sorata Complex					
CG	Monzogranite rare granodiorites	Equigranular Medium grained	Biotite	Zircon Apatite Magnetite	Autoliths
AG	Granodiorite rare monzogranites	Equigranular Medium grained	sec. Amph. Biotite	Zircon Apatite Opaques	Autoliths
Others					
HPG	Monzogranite	Equigranular Medium grained	Biotite	Zircon Apatite	Autoliths
UG	Monzogranite	Equigranular Medium grained	Biotite	Zircon Apatite	None
CKG	Monzogranite	Foliated Medium grained	Biotite	Zircon	None
SG	Monzogranite	Equigranular Fine Grained	Biotite	Zircon	None
IG	Monzogranite	Equigranular Medium Grained	Biotite	Zircon Sphene Magnetite	None

Table 3.2

Petrographic summary table of the Cordillera Real granitoids. Fine grained- <1 mm diameter crystals, medium grained- 1-7.5 mm diameter crystals, coarse grained- >7.5 mm.

importance in the geochemical modelling of the facies (section 5.2.3).

More than two hundred thin sections have been examined to determine the mineralogy and textural relationships of the granitoids (Tables 3.1 and 3.2). Modal mineralogies estimated from studies of the thin sections agree well with those calculated using major element data and the GRANITE NORM Fortran program of N.B.W. Harris (*pers. comm.*). These calculated mineralogies have been used to classify the rocks in the manner of Streckeisen (1976) Figures 3.3 and 3.4.

In some of the facies described, enclaves (used in a non-genetic sense, as by Didier (1973)) were observed. The terms autolith and xenolith are used to describe enclaves of igneous (not necessarily cogenetic with their host) and metasedimentary origin respectively. The term megacryst is used in a non-genetic sense to describe crystals significantly larger than the surrounding grains.

3.2 Field locations and access

The Sorata and Tres Cruses Complexes form the northern and southern limits of the Cordillera Real respectively (Figure 1.2). Access within the Cordillera was hampered both by the high altitude (4500 to 5200 m) and by the lack of roads in the granitoid terrain.

The Sorata Complex, approximately 70 km north of La Paz, consists of a 60 km long chain of snow-capped peaks including Iliampu (6485 m) the highest peak in the Eastern Cordillera. The complex is the largest in the Cordillera Real (950 km^2). Access to the complex is from the north via roads to the villages of Ancoma and Coco and from the south via roads to Mina Fabulosa (Figure 1.2). From these bases multi-day treks, supported by pack animals and porters, were undertaken on which the majority of samples were collected.

The Tres Cruses Complex lies 150 km to the south-west of La Paz. It covers

some 110 km^2; glaciated peaks form the western edge of the complex and relief falls rapidly to the east with an associated increase in vegetation. Road access is limited to the western margin, where several large tin mines exist. The mines acted as bases for day-trips both on foot and by jeep.

3.3 The Tres Cruses Complex

3.3.1 Field relationships

Three distinct granitic facies have been identified in the Tres Cruses Complex; the dominant Mina Argentina Granite (MAG), the Mina Viloco Granite Porphyry (MVGP) and the Mina Maraion Microgranite (MMM) (Figure 3.1). The MAG was observed at both the southern and northern ends of the complex, while the MVGP was only observed *in situ* around Mina Viloco at the northern end, and as boulders in the Rio Carabuco to the south-east of the complex. The outcrop of the MMM is limited to a small area at Mina Maraion at the northern end of the complex and is the least extensive of the facies identified.

The contacts between the facies are not well known; the MVGP was observed to intrude the MAG in a large block but not *in situ.* The MMM was not observed in contact with either of the other facies.

In the field the MAG was identified as a homogeneous, unzoned, equigranular, biotite granite. Along the margin of the pluton two types of enclave were observed. For petrographic reasons, discussed below these are thought to be metasedimentary xenoliths and igneous autoliths. The autoliths occur as well rounded, fine grained, equigranular mafic rich masses of up to 50 cm diameter sometimes rimmed by felsic material (Plate 3.1). The xenoliths are more variable in form, ranging in size from 1 cm to 1m diameter. Their outlines vary with size from subrounded small bodies to angular large bodies (Plate 3.2); no reaction rims or chilled margins are observed in

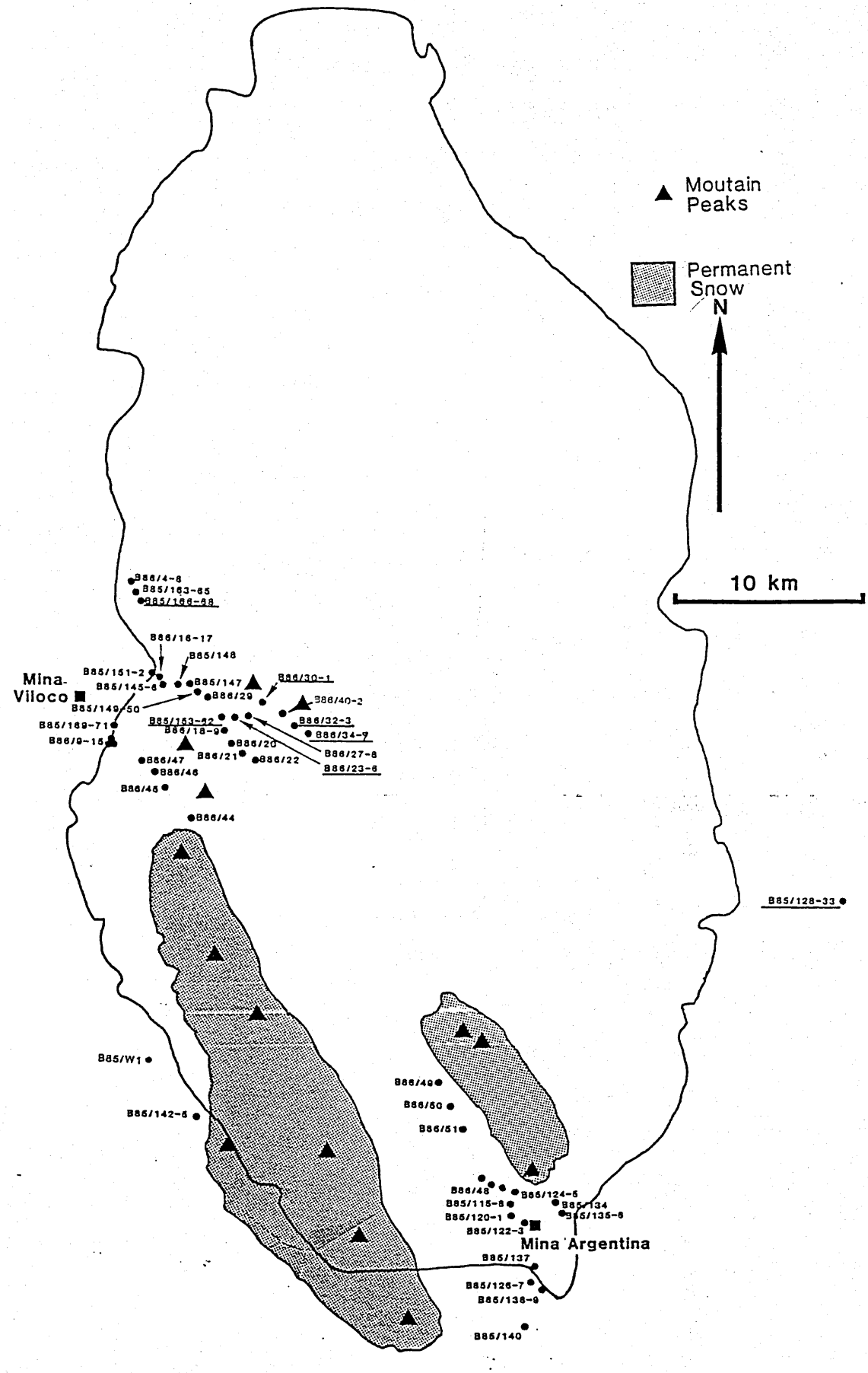

Figure 3.1

Location map for samples of the Tres Cruses complex. Samples of the MVGP are underlined.

Plate 3.1

Typical autolith from the MAG. Note the well rounded outline, fine grain size, high mafic mineral content, and felsic rim.

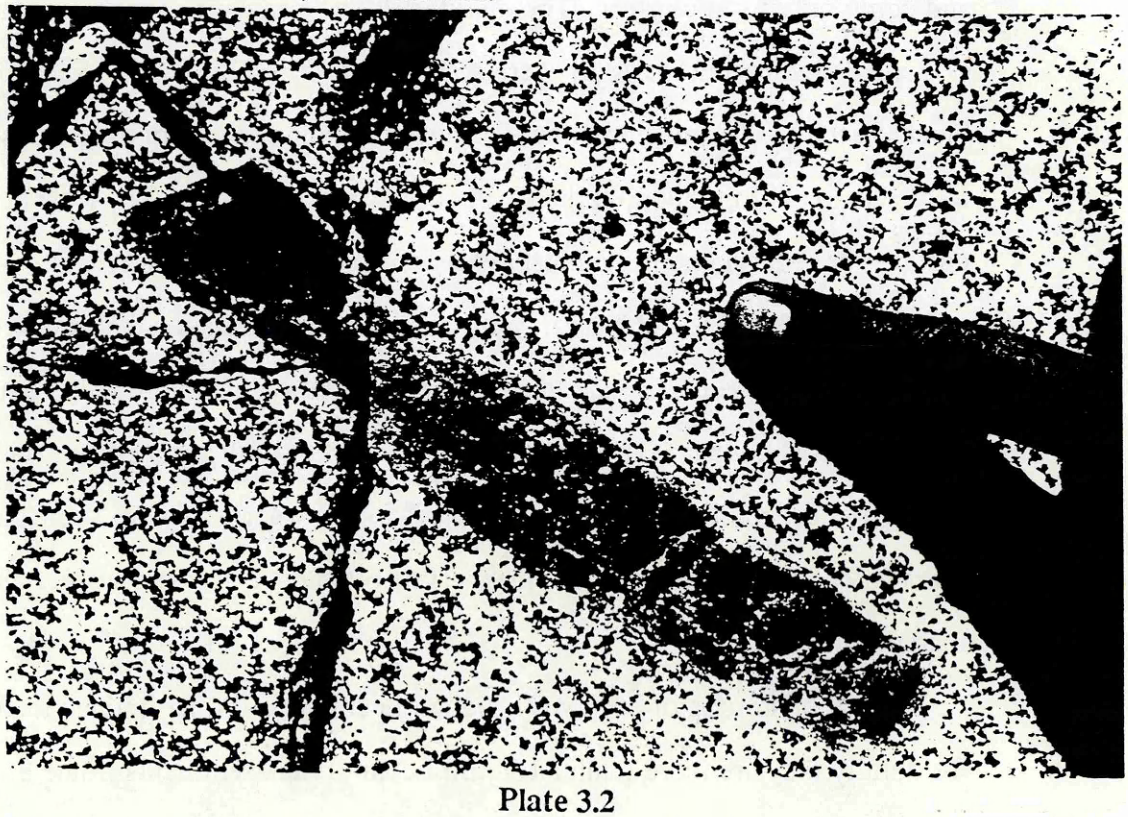

Plate 3.2

Small xenolith from the MAG. Note the angular outline, dark colour, and granular texture, all indicative of a meta-sedimentary origin.

the granite in direct contact with the xenoliths. Commonly large xenoliths display original sedimentary bedding. Also in the MAG rare, large (up to 5 cm) rounded masses of quartz thought to be of hydrothermal origin are observed; identical bodies were also noted in the MVGP.

The characteristic feature of the MVGP is the presence of abundant, large (up to 7 cm) megacrysts of white alkali feldspar, the origin of which is discussed in section 3.3.2. The MVGP is internally highly heterogeneous. The main variations are: i) the density of megacrysts, which changes dramatically over short distances, in places the megacrysts showing a weak alignment; and ii) the habit of quartz grains, which varies from small intergranular masses to larger (up to 2 cm) rounded blebs believed to be of late stage hydrothermal origin.

Two distinct groups of rounded enclaves occur in the porphyry. The dominant group are fine grained, equigranular, microgranitoids, slightly more mafic than the porphyry and often containing alkali feldspar megacrysts similar to those of their host. These bodies are up to 2 m in diameter, are occasionally rimmed by muscovite and commonly form clusters. The margins of these enclaves are commonly diffuse (Plate 3.3) indicating that they were soft, easily deformed bodies rather than rigid blocks in the MVGP magma. These enclaves exhibit a spectrum of features believed to be due to assimilation into the porphyry (Plates 3.4 and 5). The least assimilated enclaves are coarse grained, almost as felsic as the host granite and rich in megacrysts of both alkali feldspar and quartz. With progressive assimilation the enclaves become finer grained, more mafic, and the megacrysts start to develop rounded outlines and become less abundant . The most extreme examples of the process are fine grained, mafic bodies, totally devoid of megacrysts. Megacrysts were seen cutting the boundary of the enclaves. These megacrysts often have a rim of leucocratic granitic material (Plate 3.6).

The second group of enclaves is lighter in colour and finer grained than the first. Texturally they are more granular, reminiscent of metasediments (Plate 3.7). These enclaves do not contain alkali feldspar megacrysts. See section 3.3.2 for discussion .

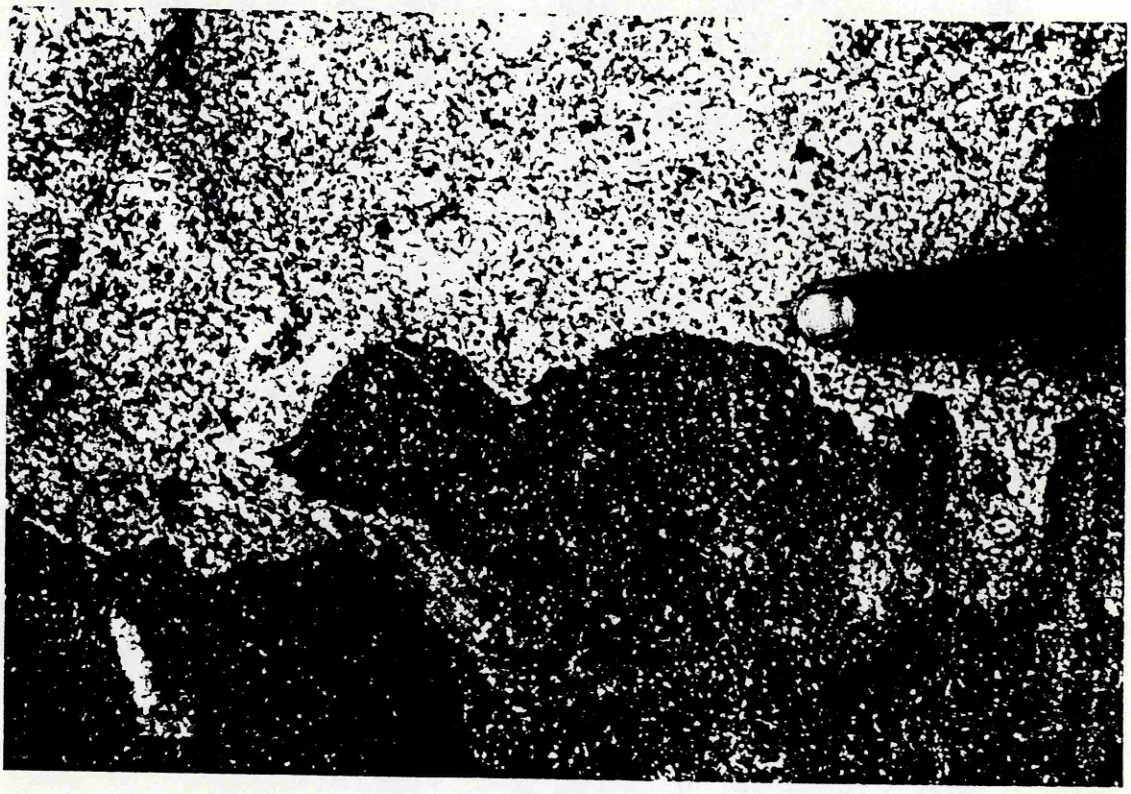

Plate 3.3

Undulose margin of an autolith from the MVGP. This style of contact indicates that the autolith was a soft body when incorporated into the magma.

Plates 3.4 and 3.5

Autoliths in the MVGP displaying varying degrees of assimilation from felsic, megacryst rich bodies to more assimilated mafic, megacryst poor examples.

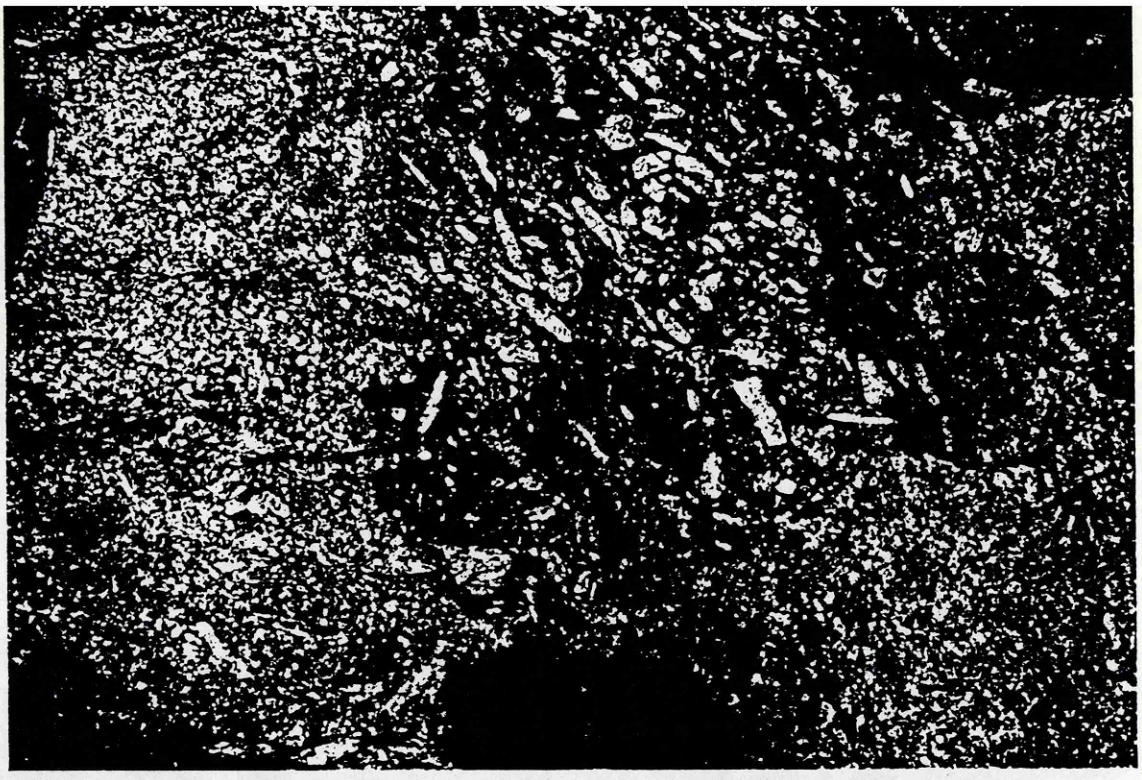

Plate 3.5

See Figure 3.4 caption.

Plate 3.6

Field photograph of a single megacryst cutting the margin of an autolith in the MVGP.

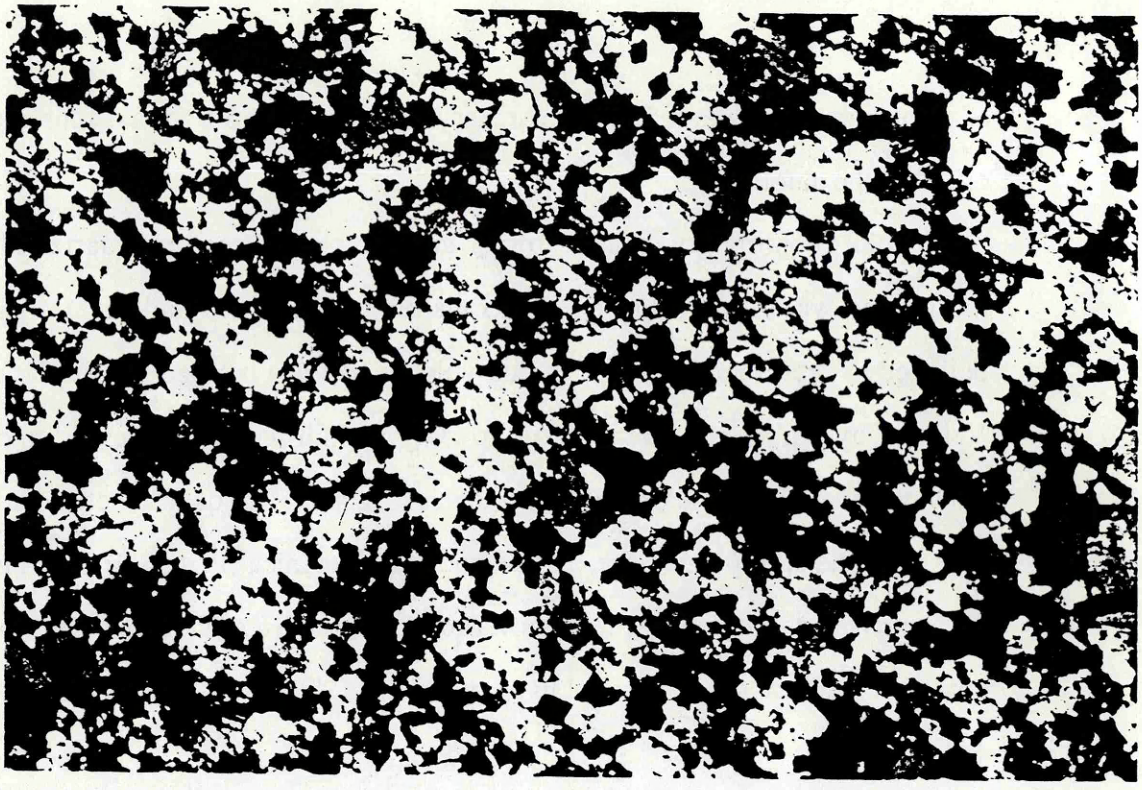

Plate 3.7

Photomicrograph of a xenolith from the MAG. The granular texture of the quartz, plagioclase, alkali feldspar and biotite assemblage is typical of a meta-sediment (crossed polars, 8 mm field of view, sample B85/126).

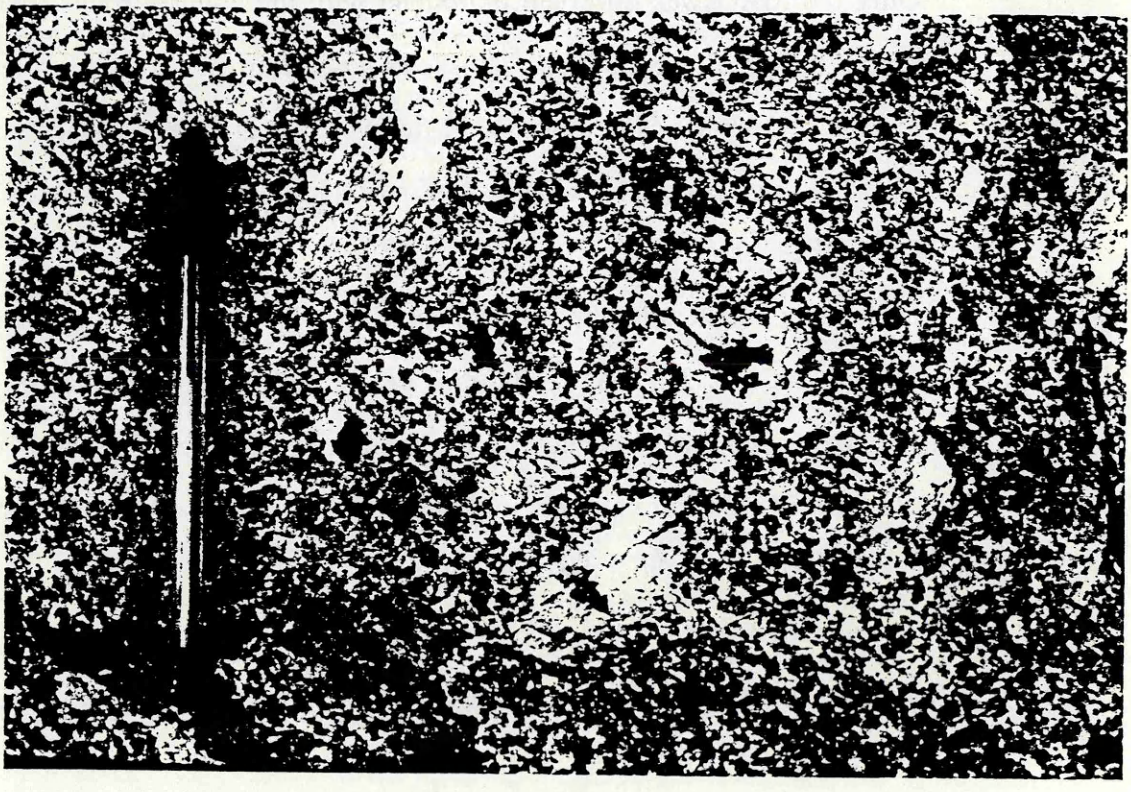

Plate 3.8

Tourmaline-biotite clots in the MVGP. These indicate the presence of B-rich aqueous 'bubbles' within the magma.

of the origin of the alkali feldspar megacrysts and section 3.5 for a discussion of the origin of the autoliths.

Within the porphyry, small (up to 1 cm) clots of muscovite, quartz, and black tourmaline were seen (Plate 3.8; also visible in plates 3.3 and 3.5). These are believed to represent late stage B-rich volatile bubbles trapped within the magma. Veins of hydrothermal alteration (up to 20 cm width) containing pseudomorphs of black tourmaline after alkali feldspar megacrysts, abundant quartz blebs, epidote and clay minerals after plagioclase, and secondary white mica (Plate 3.9) were also seen. The veins are controlled by the same vertical joint pattern as the mineralization of the complex but were only observed in the porphyry (Plate 3.10), see below and section 1.2.

The MMM was observed in a limited area at Mina Maraion, and is a homogeneous, fine grained, equigranular, leucogranite. No contacts between it and the other facies were seen.

Only the MAG was observed in contact with the country rocks. Near Mina Argentina the granite is faulted against the host sediments by a high level, near vertical fault which has caused intense fracturing of the granite; elsewhere the granite intrudes the country rocks forming up to 1 m of hornfels, and there is some marginal chilling of the granite.

Hydrothermal alteration in the complex is associated with tin-tungsten mineralization (see section 1.2). Veins containing kaolinized feldspar bounded by silicified zones two or three times the width of the kaolinized vein, transgress both the MAG and the MVGP. The alteration is joint controlled and follows a uniform north-east south-west trend throughout the complex.

The occurrence of large quartz 'blebs' in both the MAG and MVGP indicate that silica has been mobilized in the granites. No fracturing was observed associated with the quartz blebs which are therefore, believed to be formed by localized diffusion on a cm scale.

Plate 3.9

Pseudomorphs of tourmaline after alkali feldspar megacrysts in the MVGP. Plagioclase is totally altered to clay minerals and large rounded 'blebs' of quartz and white mica have been introduced. See Plate 3.10 for larger scale view.

Plate 3.10

The alteration associated with the tourmaline pseudomorphs is controlled by the same fracture set as the mineralization in the MAG but was only observed in the MVGP.

3.3.2 Origin of the megacrysts

The alkali feldspar megacrysts in both the MVGP and the associated autoliths are strikingly similar to those of the granites of SW England (Stone and Austin, 1961). Two modes of origin for alkali feldspar megacrysts have been suggested in the literature; metasomatic growth or primary magmatic growth. Stone and Austin (1961) believed the megacrysts in the granites of SW England to be of metasomatic origin based largely on field evidence of megacrysts cutting the margins of xenoliths and aplite-pegmatite veins and occurring in autoliths. The following features suggest that they are of igneous origin: common euhedral shape, although resorbed crystals do occur in the autoliths; crystal alignment; growth zones; oriented inclusions; inclusions of igneous plagioclase and biotite. However the occurrence of megacrysts in the autoliths and their relationship to the degree of assimilation of the autoliths (see section 3.5) must be explained. Vernon (1986) addressed this problem and made several salient observations, discussed below.

The large size of the alkali feldspar megacrysts is their most distinctive feature. Experimental data (Clements and Wall, 1981) have shown that a peraluminous granitic melt becomes saturated in alkali feldspar only a few degrees above the solidus. Even at these low temperatures, however, a granitic magma will only contain a small fraction of crystals, leaving sufficient room for large megacrysts to grow. Only when cotectic crystallization of plagioclase, quartz and alkali feldspar begins are large volumes of crystals produced; this occurs rapidly through a small drop in temperature. Therefore the alkali feldspar megacrysts can only grow unimpeded for a short period of time, implying a rapid growth rate. The large size and relatively low abundance of the megacrysts compared to other phases, also suggests a low nucleation rate and a rapid growth rate. Experimental results (Swanson, 1977) have shown that in a granodioritic magma the growth rate of alkali feldspar is at a maximum when the nucleation rate is a minimum, a feature which

would promote the development of few large crystals. Also Swanson (*op. cit.*) showed that, at the degree of under cooling at which alkali feldspar reaches its maximum growth rate, the growth rate of plagioclase is much lower than that of alkali feldspar. It follows that an alkali feldspar crystal would tend to be larger than an accompanying plagioclase crystal. Therefore the alkali feldspar megacrysts of the MVGP and associated autoliths are believed to be of igneous origin.

The inverse relationship between the density and euhedral nature of alkali feldspar megacrysts in the porphyry and the degree of assimilation reflects the extraction of felsic minimum melt from the autoliths by the host magma to leave a refractory, mafic residue (discussed further in section 3.5).

The occurrence of megacrysts cutting the margins of the autoliths (Plate 3.6) is believed to be further evidence for the extraction of a minimum melt. The extraction of a minimum melt is thought to have caused a reduction in volume of the autoliths, and the resistance of the megacrysts to melt, due to their large size, has left them partially extracted from the host autolith.

3.3.3 Petrography

3.3.3 i) The Mina Argentina Granite

The MAG is a homogeneous, medium grained, equigranular, biotite monzo-granite (Figure 3.3, Plate 3.2), composed of plagioclase, quartz, alkali feldspar, biotite and accessories. Plagioclase forms large individual euhedral to anhedral grains usually displaying complex oscillatory zoning, polysynthetic twinning and growth zones; glomerocrysts of smaller crystals often occur with continuous outer growth rims, indicating continued growth of the clot after formation. Quartz forms rounded, usually anhedral crystals of interstitial habit with undulose extinction. Inclusions of plagioclase and biotite are commonly observed within quartz grains.

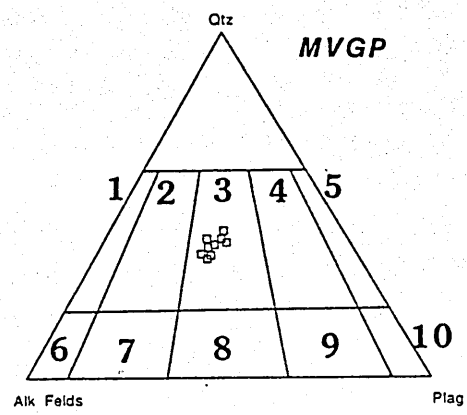

Key

1 Alkali feldspar granite
2 Syno-granite
3 Monzo-granite
4 Granodiorite
5 Tonalite
6 Alkali feldspar syenite
7 Syenite
8 Monzonite
9 Monzo-diorite
10 Diorite

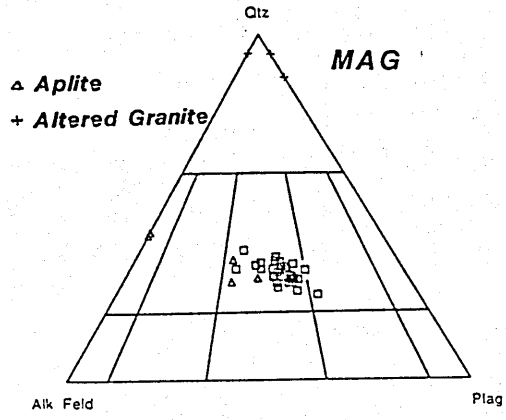

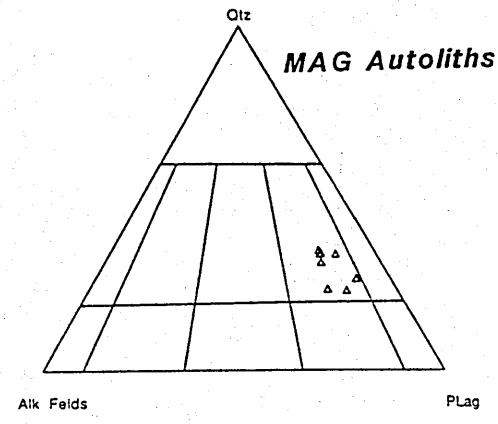

Figure 3.3

Streckeisen diagram of the Tres Cruses facies.

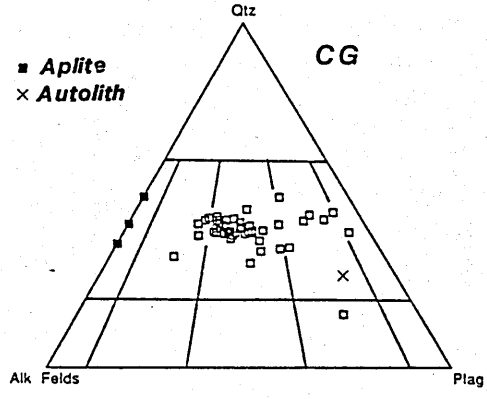

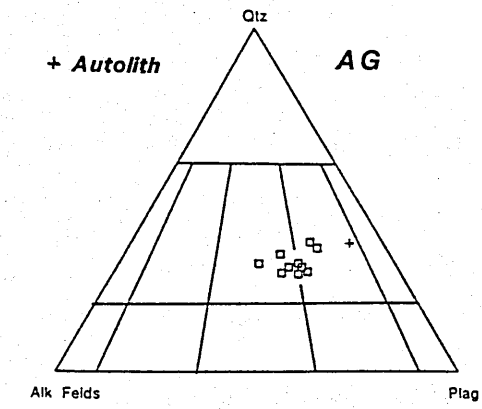

Figure 3.4

Streckeisen diagram for the Sorata Complex facies

Large (up to 5 cm) rounded bodies of quartz also occur (Plate 3.11) and are believed to be of secondary origin, as noted in section 3.3.1 the scale of this mobility is thought to be of cm scale. This indicates that SiO_2 may be a questionable fractionation index for this suite. Microperthitic alkali feldspar forms small anhedral intergranular grains. Biotite, the only mafic phase, displays euhedral to subhedral, brown, pleochroic, crystals, often containing inclusions of apatite, zircon, and rare FeTi oxides. The two main accessory phases are apatite and zircon. Large euhedral apatites occur dominantly as inclusions in biotite. Zircon occur mainly as small, euhedral, elongate crystals, often as inclusions in biotite.

The sequence of initiation of crystallization of the phases present, based on grain morphology and inclusions was as follows:

1) Zircon and apatite

2) Plagioclase

3) Biotite

4) Alkali feldspar

5) Quartz ?

See section 3.6 for discussion of control on sequence. On textural grounds only alkali feldspar, is believed to be totally intercumulus and as such probably did not occur in the fractionating assemblage. The conclusion is of relevance in major element fractionation modelling (section 5.2.3).

Alteration of two distinct styles affected the specimens collected. The more pervasive appears to have affected mainly the texture of the granite, causing a reduction in the grain size of the quartz and alkali feldspar to produce a fine grained equilibrium texture surrounding unaffected crystals of biotite and plagioclase. Associated with this textural change in places biotite has been altered to brown tourmaline. A second style of alteration, associated with mineralization, was observed. Alkali feldspar and plagioclase have been replaced by clay minerals and sericite; and biotite by chlorite, opaques, and sphene. Commonly associated

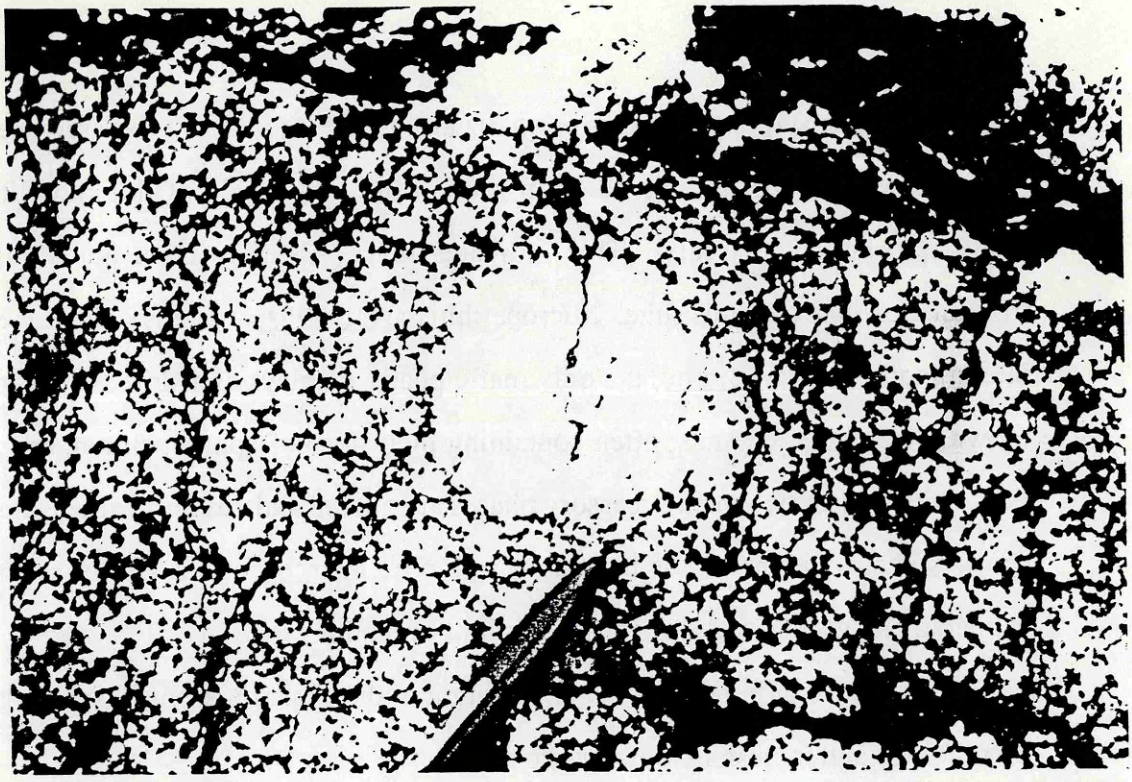

Plate 3.11

Large, secondary quartz 'bleb' from the MAG.

Plate 3.12

Photomicrograph of an autolith from the MAG. The interlocking plagioclase laths, micro-perthitic alkali feldspar and acicular apatite crystals indicate an igneous origin (crossed polars, 8 mm field of view, sample B85/141).

anhedral, interstitial quartz blebs are believed to be of hydrothermal origin. This second style of alteration will have caused major changes to the original chemistry of the samples affected. The total alteration of the feldspar will have remobilized some of the CaO, Na_2O and K_2O; alteration of the biotite will have remobilized FeO, MgO, K_2O; the mobility of silica, as noted in section 3.3.1 is believed to be small, likewise the mobility of the other major/minor elements may be only local. Silica is a questionable fractionation index due to its mobility; Zr and Ti, contained in unaltered phases or in new phases precipitated close to the site of alteration, will probably serve as the best indices of fractionation.

3.3.3 ii) Mina Argentina Granite Enclaves

Two distinct types of enclave have been described from the MAG (section 3.3.1); igneous autoliths and metasedimentary xenoliths.

The autoliths display igneous textures (Plate 3.12) and are fine grained, mainly equigranular granodiorites (Figure 3.3). Plagioclase occurs as euhedral, elongate, simply twinned,laths; biotite as subhedral crystals, totally devoid of amphibole or pyroxene cores, but often surrounded by interstitial alkali feldspar and quartz, and there are small needle-like crystals of apatite. Rare large subhedral phenocrysts of plagioclase and biotite also occur. See section 3.5 for a discussion of the origin of the autoliths.

The xenoliths are formed of quartz, plagioclase, alkali feldspar, biotite, and opaques. There is textural evidence for metamorphic recrystallization of originally sedimentary rocks; quartz overgrowths on original quartz grains have produced a near equilibrium texture in some samples, while in others quartz has a subpoikilitic form, partially enclosing crystals of biotite and plagioclase (Plate 3.7). Alkali feldspar and plagioclase grains also show signs of metamorphic growth and occasionally have a subpoikiloblastic texture.

3.3.3 iii) The Mina Viloco Granite Porphyry

The MVGP is a coarse grained, alkali feldspar megacrystic, monzogranite (Figure 3.3) composed of alkali feldspar, quartz, plagioclase, biotite, muscovite, and accessory zircon, apatite, cordierite, and tourmaline. Alkali feldspar occurs in two distinct forms: as large (3-7 cm) euhedral to rounded subhedral megacrysts (Plate 3.13), occasionally rimmed by biotite; and as small anhedral interstitial crystals in the groundmass. Internally the megacrysts display microperthitic textures and contain oriented inclusions of plagioclase, quartz, biotite and muscovite outlining growth patterns. Texturally there is no evidence for the late stage subsolidus growth of the megacrysts, as they do not disrupt the texture of the surrounding porphyry. Quartz also occurs in two distinct forms: as large (up to 5 cm) rounded 'blebs', composed of several individual crystal domains similar to those of the MAG (Plate 3.11), containing inclusions of biotite and plagioclase; and as smaller, subhedral to anhedral grains in the groundmass. Plagioclase only occurs as subhedral crystals often displaying complex oscillatory zoning, polysynthetic twinning and normal gradational zoning in the groundmass, and as inclusions in alkali feldspar megacrysts. Individual euhedral grains of biotite in the groundmass contain inclusions of zircon and apatite; clots of biotite, quartz and brown pleochroic tourmaline are common. The accessory phases are dominated by apatite and zircon, but primary magmatic cordierite and opaques also occur. Euhedral apatites occur as inclusions in biotite and throughout the groundmass. Zircon occurs in two habits; as small, elongate, primary magmatic crystals and as larger grains with rounded outlines and metamict interiors, thought to be xenocrysts. Small grains of cordierite displaying distinctive sector twinning and alteration to pinite are present in the groundmass.

The MVGP has a highly peraluminous mineralogy, indicated by the occurrence of cordierite, which confines crystallization pressure to less than 5 kbar (Clements and

Plate 3.13

Margin of a megacryst in the MVGP. Note the lack of disruption of the surrounding material (crossed polars, 8 mm field of view, sample B85/155A).

Plate 3.14

Photomicrograph of an autolith from the MVGP. Note the interlocking igneous texture of the plagioclase laths and biotite crystals and the interstitial quartz and alkali feldspar (crossed polars, 8 mm field of view, sample B85/167A).

Wall, 1981).

The sequence of crystallization of the major phases is believed to be as follows;

1) Zircon

2) Plagioclase

3) Biotite

4) Quartz

5) Alkali feldspar (including the megacrysts)

see section 3.6 for discussion of the significance of this sequence. None of the phases are of purely intergranular character and all may have formed part of the fractionating assemblage.

Alteration has slightly affected all the samples of the porphyry collected. Plagioclase has partially altered to clay minerals, alkali feldspar crystals are commonly turbid with patches of kaolin and biotite has often partially altered to chlorite and opaques. Quartz displays a dominantly secondary habit related to local mobility as noted in sections 3.3.1 and 3.3.3 i. This alteration will probably produce minor scatter in the geochemical evolution trends of the porphyry. Zr and Ti are contained in resistant phases and will all serve as fractionation indices.

3.3.3 iv) Mina Viloco Granite Porphyry enclaves

Two types of enclave were collected from the porphyry. The more abundant group (Plates 3.3 and .14) are fine grained, inequigranular rocks. These enclaves contain megacrysts (up to 5 mm) of subhedral, polysynthetically twinned, plagioclase with growth zones defined by inclusion trails. Subhedral biotite megacrysts (up to 4 mm) with inclusions of zircons and associated disruption haloes and partially resorbed large quartz grains (up to 5 mm) also occur. These large crystals are contained in a granular matrix of anhedral and subhedral quartz, alkali feldspar and plagioclase grains. Small subhedral to anhedral biotites are scattered throughout the groundmass. The interlocking texture of this group of enclaves is thought to indicate

an igneous origin. Large (up to 5 cm) alkali feldspar megacrysts in the autoliths, have rounded outlines and have not grown displacively in the enclave. The megacrysts are thought to be magmatic and their rounded outlines are due to partial resorption related to the extraction of an minimum melt from the autolith.

The second group of enclaves, believed to be xenoliths, is richer in felsic phases and contains quartz , alkali feldspar, biotite, and a little plagioclase (Plate 3.15). The alkali feldspar grains display no twinning or exsolution features and the plagioclase grains rarely exhibit simple twinning. All the phases except biotite are anhedral giving the samples granular textures reminiscent of metapsammites, common in the surrounding metasediments.

3.3.3 v) Aplites

Typical aplites composed almost exclusively of felsic minerals are common around the margins of the complex and are probably related to the MAG. Mineralogically the aplites are monzogranites and alkali feldspar granites (Figure 3.3) composed of quartz, alkali feldspar, plagioclase, muscovite and minor biotite. The aplites have fine grained saccharoidal textures. Plagioclase occurs both as subhedral laths and anhedral crystals displaying normal zoning. Muscovite and rare biotite form subhedral grains, whereas quartz and alkali feldspar occur as anhedral grains. The crystal morphology of the rock appears to have been controlled primarily by surface free energies rather than order of crystallization and the equigranular texture suggests simultaneous crystallization.

3.3.3 vi) Mina Maraion Microgranite

The Mina Maraion Microgranite has been petrographically identified as a fine grained, equigranular, biotite monzogranite. Small plagioclase laths displaying simple twinning and gradational zoning are partially enclosed by anhedral quartz and microperthitic alkali feldspar grains; subhedral muscovite, rare biotite and zircon also

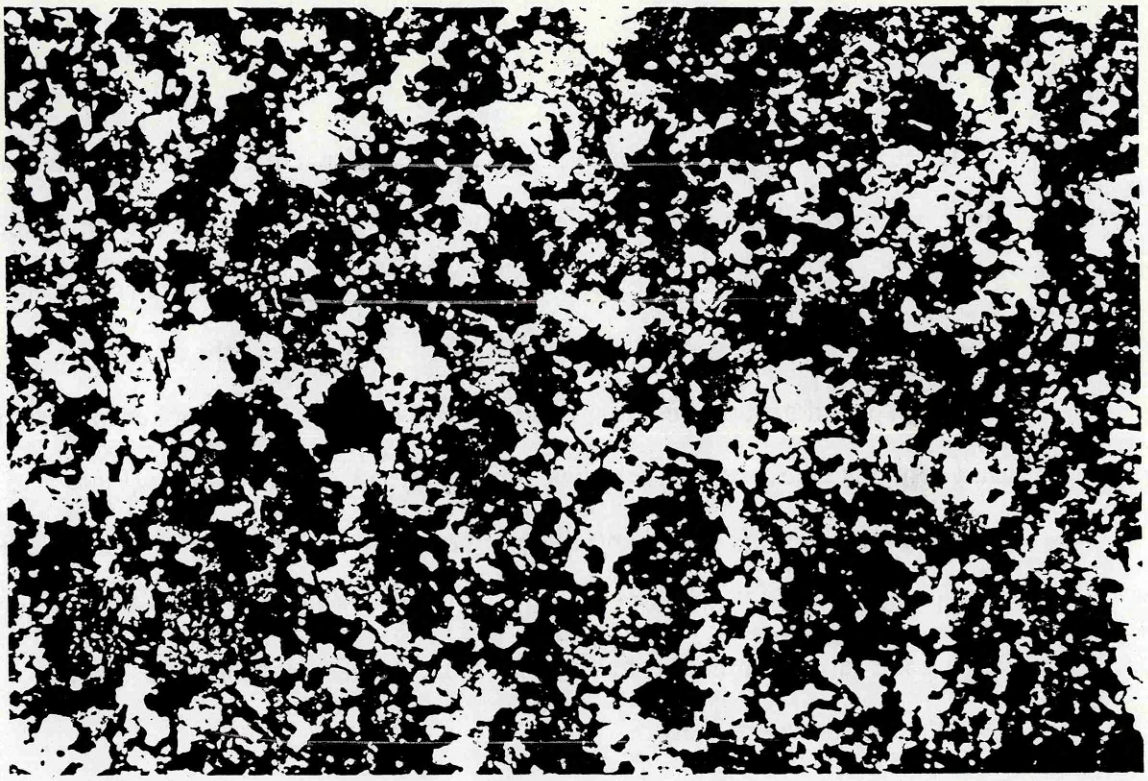

Plate 3.15

Photomicrograph of the granular metasedimentary texture of a xenolith from the MVGP. The sample consists of plagioclase, quartz, alkali feldspar, biotite and opaques (crossed polars, 8 mm field of view, sample B85/161).

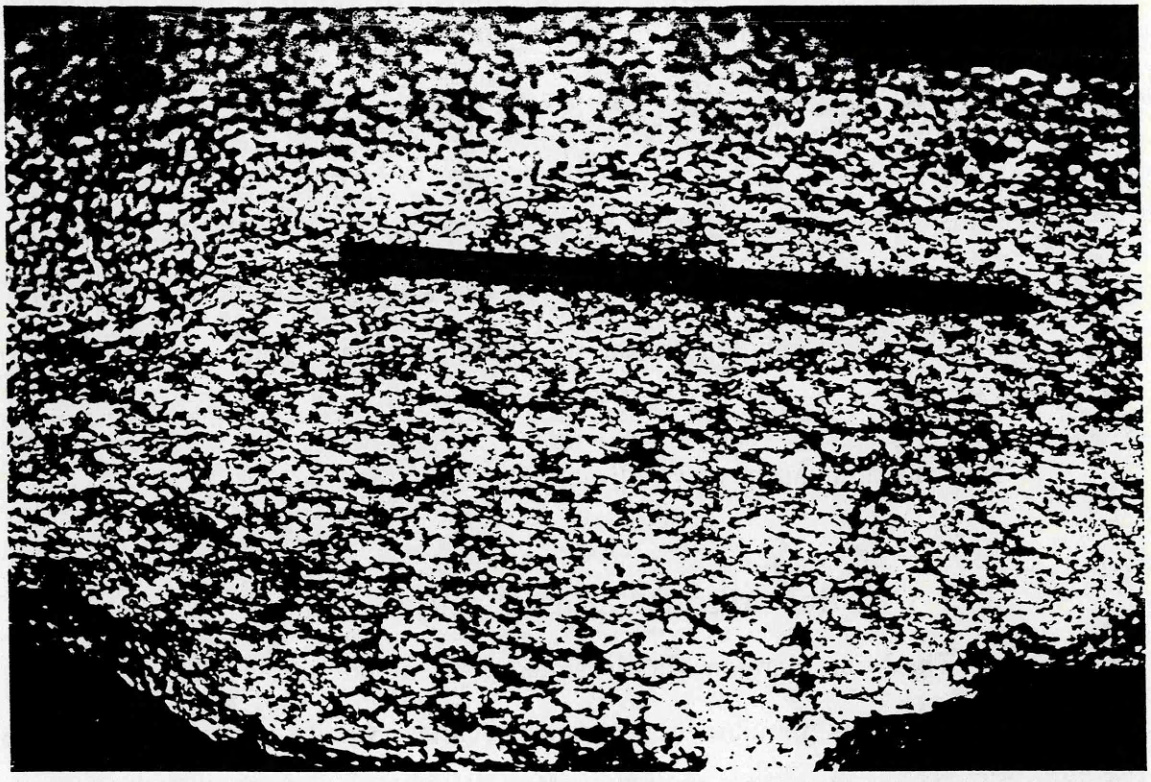

Plate 3.16

Specimen of the Coco Granite displaying a penetrative foliation defined by mica laths.

occur. The overall texture is granular.

3.4 The Sorata Complex

3.4.1 Field relationships

Two distinct, homogeneous facies; the Ancoma Granodiorite (AG), a medium grained, hornblende, biotite granodiorite and the Coco Granite (CG), a medium-fine grained, two mica granite, were identified in the Sorata Complex with associated aplites and pegmatites. The CG was observed to be more common than the AG, which was only observed in the north-western corner of the pluton. No zoning was detected within either facies. The AG was only observed *in situ* at one location and no contact between the two facies was observed in the field. However, all the non *in situ* samples of the AG collected came from recent moraines and their close grouping is believed to indicate short transport distances (Figure 3.2). The CG alone was observed in contact with the country rocks. The contact is sharp and intrusive, with common garnet-bearing pegmatites cutting both the granite and the country rock. Along the southern contact, up to 1m of hornfels and minor chilling of the granite was observed.

The CG occasionally displays a weak penetrative tectonic foliation (Plate 3.16), defined by mica laths and quartz shear bands. The foliation occurs in widely spaced samples and is not believed to form single, mappable feature. The presence of a tectonic foliation in the dominant facies of the pluton, its elongation parallel to the strike of the major faults of the area (see Figure 3.2) and the large metamorphic aureole along the northern contact (see section 4.2) all suggest a syntectonic emplacement.

Rare enclaves occur in both the CG and the AG. Two types were observed in the CG; angular blocks of layered, fine grained, dark, granular, material believed to be blocks of the country rock (i.e. xenoliths) and small, well rounded, mafic rich

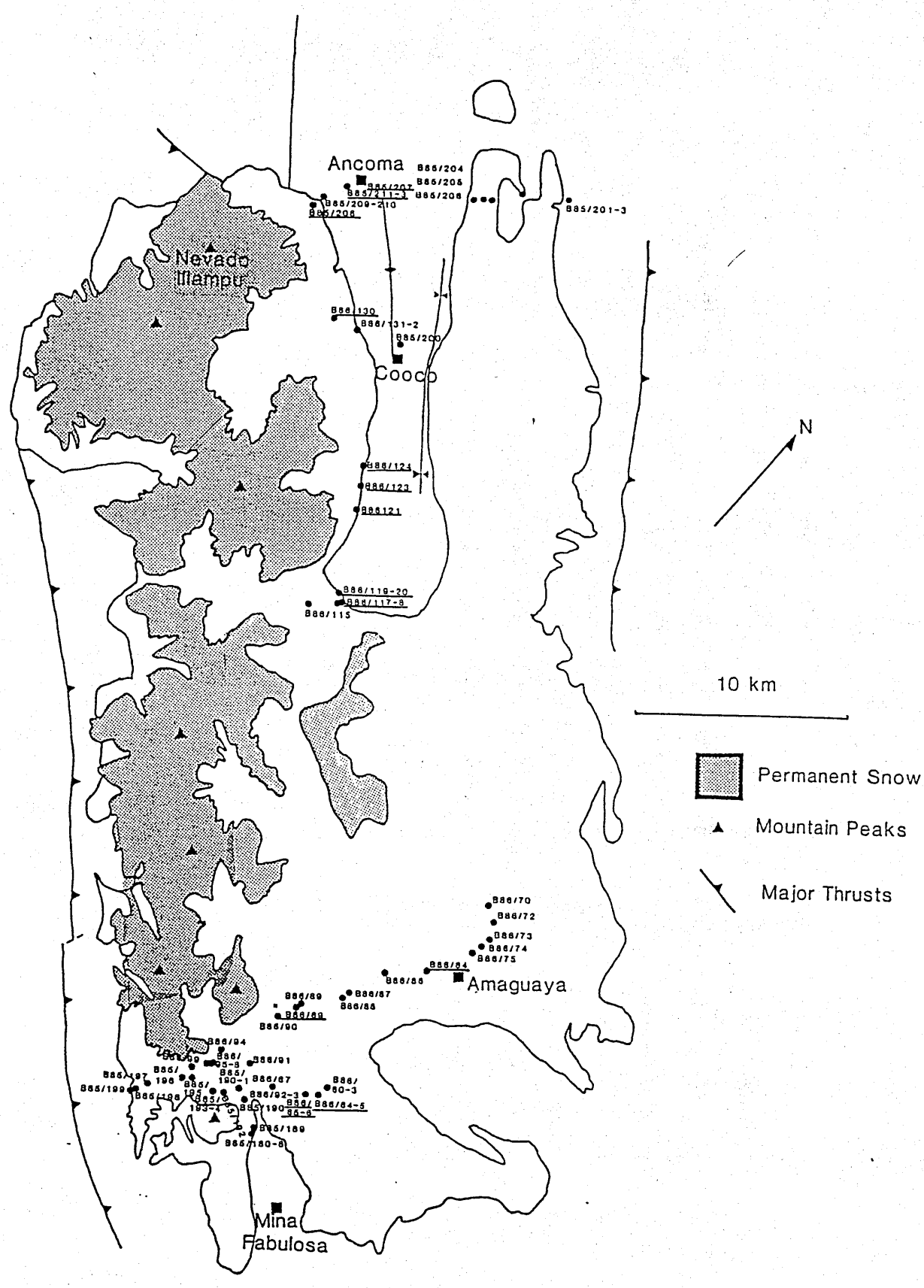

Figure 3.2

Location map for samples of the Sorata complex. Samples of the AG are underlined.

bodies, with interlocking textures thought to be of igneous origin (i.e.autoliths). In the AG only enclaves of this second type were observed. The textures and origins of these bodies are discussed in sections 3.3.3 ii, 3.3.3 iv and 3.5.

3.4.2 Petrography

3.4.2 i) The Coco Granite

The CG is a medium-fine grained, two mica monzogranite (Figure 3.4) with clear microtextural evidence of widespread deformation (Plate 3.17). Undeformed samples are typically composed of plagioclase, alkali feldspar, quartz, biotite, muscovite and accessories, mainly apatite and zircon. Plagioclase occurs as 3-5 mm subhedral laths exhibiting polysynthetic twinning and both normal and complex oscillatory zoning. Also, along the margins of many crystals, myrmekitic overgrowths occur. Microcline crystals, displaying cross-hatch twinning, have anhedral outlines and interstitial habit; inclusions of plagioclase and biotite are common. Quartz is generally anhedral and intergranular but a few well developed crystal faces have been developed. Even in the grossly undeformed samples, quartz grains exhibit strained extinction and some marginal recrystallization. Euhedral crystals of biotite, commonly containing inclusions of zircon and apatite, are the only mafic phase present and are often partially included by plagioclase crystals. Muscovite occurs in two habits; large clots of interstitial crystals, and smaller clots associated with biotite or within plagioclase. The former is believed to be of primary magmatic origin while the latter is probably an alteration product. Three accessory phases have been identified; apatite, zircon and an opaque phase. Apatite occurs as large and small, euhedral, equant or elongate crystals often included in biotite and occasionally in plagioclase. Zircon is a common inclusion in biotite, often with associated pleochroic haloes. Crystals are usually elongate and euhedral but rare larger crystals with rounded outlines and turbid metamict interiors are believed to be

Plate 3.17

Photomicrograph (crossed polars) of deformed texture of the Coco granite. Note the ridged behaviour of the feldspar crystals the plastic deformation of the quartz and the brittle behaviour of the mica (crossed polars, 8 mm field of view, sample B85/194).

Plate 3.18

Photomicrograph of a large, metamict, probably inherited zircon in the Coco Granite. See text for discussion (plane polarized, 3.47 mm field of view, sample B85/205).

xenocrysts possibly inherited from the source of the granite (Plate 3.18). Rare magnetite octahedra, usually associated with biotite are also present.

The sequence of initiation of crystallization of the phases based on crystal outlines and inclusions, was as follows;

1) Zircon

1) Plagioclase

2) Quartz

3) Biotite

4) Alkali feldspar

5) Muscovite

see section 3.6 for discussion of the significance of this sequence.

Deformation of varying degrees is a ubiquitous feature of the granite. With increasing deformation, quartz grains, the least competent phase present, exhibit marginal recrystallization, total recrystallization and elongation of original grain outlines and at the highest degrees of deformation 'smearing out' of original grains into shear bands (Plate 3.19). At low degrees of strain, biotite and muscovite develop kinks in the cleavage traces of crystals. With increasing deformation crystals breakup into small internally unstrained fragments which were carried passively by the plastically deforming quartz. Alkali feldspar and plagioclase are least affected by the deformation; crystals behave competently, with only minor mechanical attrition of the margins, producing rounded outlines: internally there is no evidence for deformation in these phases. The deformation of the granite appears to have been a purely mechanical effect and not to have affected the chemistry of the granite.

The amount of alteration in the specimens collected is variable; the majority of samples show little or no evidence of it. Plagioclase is the most commonly altered phase; initially the Ca-rich cores of crystals break down to clay minerals, outer zones only become affected by increasing alteration. Biotite has been observed in some specimens to be partially altered to chlorite and opaques.

Plate 3.19

Photomicrograph of a highly deformed sample of the Coco Granite with well developed quartz shear bands (crossed polars, 8 mm field of view, sample B85/181).

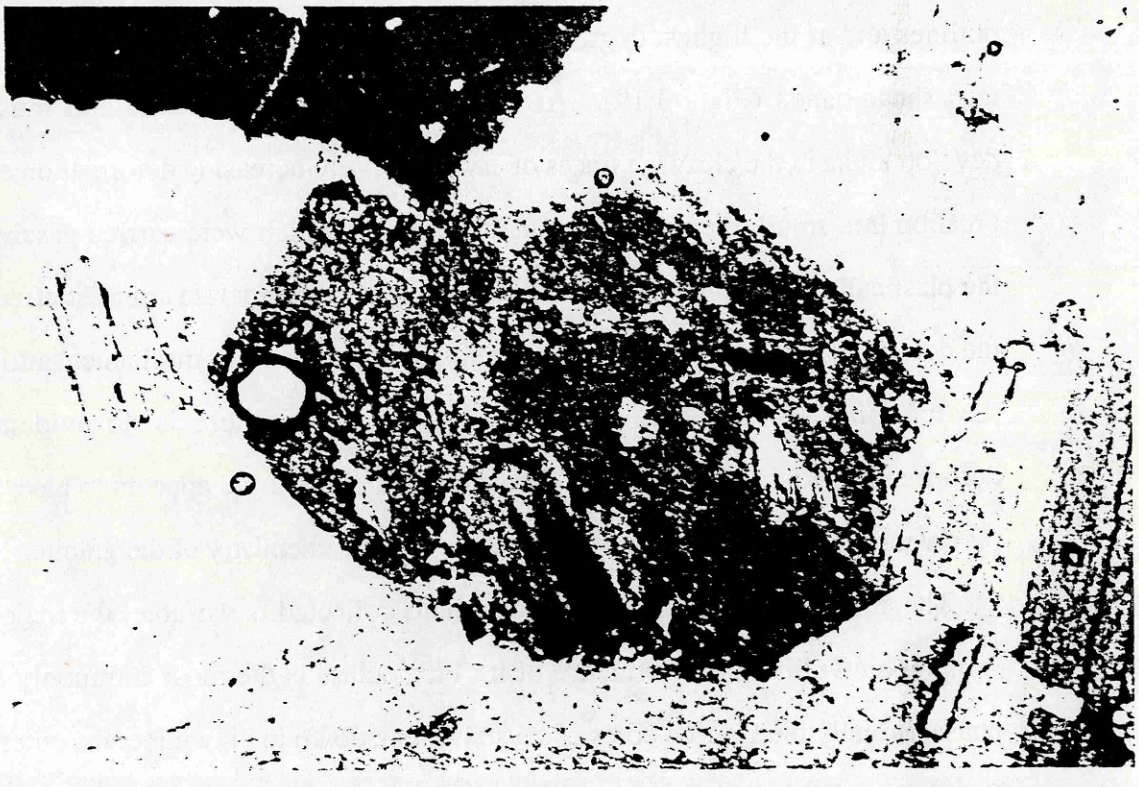

Plate 3.20

Photomicrograph of an amphibole crystal from the Ancoma Granodiorite. Note the ragged outline, uneven colour, and included biotite believed to indicate secondary replacement of pyroxene (plane polarized, 3.47 mm field of view, sample B85/245).

One sample (B85/210) is distinct from all the others. The texture of the rock is that of a plagioclase orthocumulate. It consists of large (3-5 mm), euhedral, plagioclase laths, displaying heavy oscillatory and normal gradational zoning; these laths comprise about 80% of the rock (see Figure 3.4). The interstices of the laths are filled with quartz and microperthitic alkali feldspar; grains of both minerals have totally anhedral forms. Rare, singular crystals of muscovite also occur in the interstices. Plagioclase laths in the sample are partially altered to clay minerals, a process which has in places totally obscured the zoning. Alkali feldspar is similarly altered to clay minerals. Quartz and muscovite are unaffected by alteration.

The main effects on the chemistry of the samples due to alteration will be a scattering in the concentrations of CaO, K_2O and Na_2O, Rb and Sr on variation diagrams. The minor alteration of biotite may have caused the depletion of MgO in the samples affected. SiO_2, Ti and Zr should all serve as good fractionation indices.

3.4.2 ii) Coco Granite enclave

A single sample of a mafic rich, fine grained, well rounded enclave was collected from the CG. The enclave is mineralogically a granodiorite but richer in mafic phases than its host, (Figure 3.4). The texture of the body is similar to that of the autoliths described from the MAG. Plagioclase occurs as subhedral laths and quartz and alkali feldspar as interstitial grains. Biotite forms elongate subhedral crystals with heavily included margins, distinctive acicular apatite crystals are also common. The texture of this enclave suggests it is an autolith and is similar to that of the MAG autoliths.

3.4.2 iii) The Ancoma Granodiorite

The AG is a medium grained, equigranular, hornblende, biotite granodiorite/ monzogranite (Figure 3.4). Unlike the CG there is no microtextural evidence for deformation. Typically, the granodiorite is composed of plagioclase, quartz, alkali feldspar, biotite, hornblende and accessories. Plagioclase, the dominant felsic mineral, occurs as large, subhedral crystals up to 1cm long. These often have

euhedral homogeneous cores with normally zoned margins and subhedral outlines displaying lamellar twinning, oscillatory and gradational zoning as well as myrmekitic overgrowths. Glomerocrysts of plagioclase are common and their small grain size and euhedral form indicate early crystallization. Quartz occurs as anhedral, unstrained grains often with sutured margins. Microperthitic, alkali feldspar grains have a well developed interstitial habit and partially enclose all the major phases except hornblende. Biotite is the dominant mafic phase and occurs as subhedral to euhedral, elongate to equant crystals. Several phases occur as inclusions in biotite; small crystals of plagioclase oriented parallel to the cleavage, large apatite crystals and equant zircons. Amphibole occurs as 'ragged' green pleochroic crystals of uneven colour often containing inclusions of biotite, apatite, and plagioclase (Plate 3.20). Chemically the amphiboles are ferro-actinolitic hornblende and ferro-hornblendes (Table 3.3) (Leake, 1978) and are compositionally similar to secondary hornblendes and actinolitic hornblendes identified by Tindle (1982) Figure 3.5. The textural and chemical data suggest the amphiboles are subsolidus replacements probably after pyroxene although no pyroxene cores were observed. The amphiboles do not form accurate pseudomorphs after the pyroxenes and the timing of pyroxene crystallization therefore cannot be assessed by textural means.

The probable sequence of initiation of crystallization in the granodiorite was as follows:

1) Zircon and apatite

2) Plagioclase — Pyroxene?

3) Quartz

4) Alkali feldspar

5) Biotite

see section 3.6 for discussion of the possible significance of this sequence. Alkali feldspar and a large portion of the quartz has a clearly interstitial habit and therefore may not have been part of the fractionating assemblage, an important point

Sample	B85/213	B85/213	B85/213	B86/85	B86/85	B86/85	B86/125	B86/125
SiO_2	46.47	49.08	44.18	47.67	47.63	48.34	47.05	50.38
TiO_2	1.07	0.58	1.49	1.00	0.87	0.76	1.00	0.38
Al_2O_3	5.62	3.6	7.26	5.35	5.14	4.31	6.19	3.61
FeO	17.81	16.70	17.17	18.02	18.18	16.67	18.09	17.00
MnO	0.73	0.68	0.49	0.76	0.73	0.68	0.6	0.51
MgO	11.6	12.85	11.17	11.32	11.26	12.34	10.9	12.05
CaO	11.07	11.75	10.92	11.23	11.31	11.25	11.7	12.32
Na_2O	1.22	0.75	1.61	0.84	1.05	0.94	1.19	0.03
K_2O	0.62	0.32	0.86	0.55	0.52	0.4	0.58	0.25
Total	96.21	96.31	94.97	97.03	96.69	95.69	97.3	96.8
Si	6.783	7.075	6.542	6.882	6.906	7.016	6.787	7.197
Ti	0.117	0.063	0.166	0.108	0.095	0.083	0.108	0.041
Al	0.967	0.611	1.268	0.911	0.879	0.737	1.052	0.608
Fe	2.174	2.013	2.126	2.177	2.204	2.023	2.183	2.032
Mn	0.090	0.083	0.062	0.0925	0.0891	0.084	0.074	0.062
Mg	2.524	2.762	2.466	2.436	2.434	2.669	2.344	2.566
Ca	1.732	1.815	1.732	1.737	1.758	1.750	1.809	1.887
Na	0.346	0.208	0.462	0.317	0.294	0.265	0.332	0.084
K	0.115	0.059	0.129	0.101	0.097	0.074	0.107	0.046
Total	14.502	14.689	14.953	14.762	14.756	14.701	14.841	14.624

Table 3.3

Probe analyses of amphiboles from the AG. Formula units based on 23 oxygens

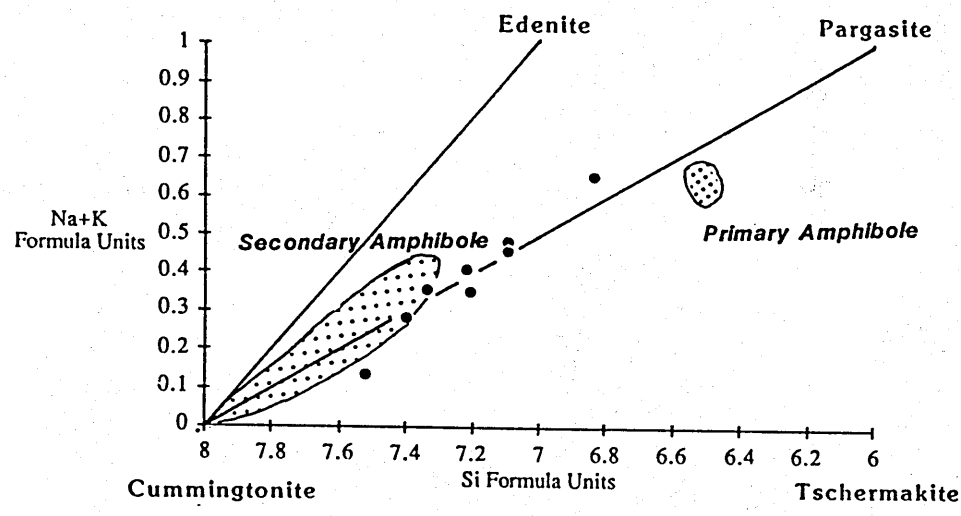

Figure 3.5

Compositional variation in amphiboles from the AG (based on 23 oxygens). The fields of secondary and primary amphibole from Tindle (1982) are shown for comparison.

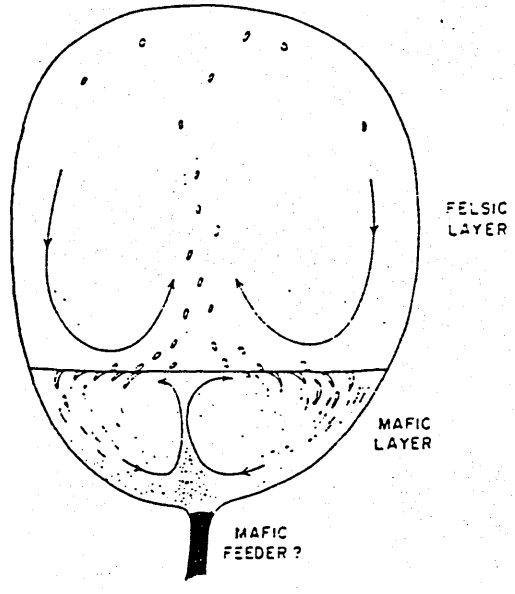

Figure 3.6

Diagram illustrating one possible origin for autoliths (after Vernon, 1983).

in the assessment of the major element modelling of the granodiorite (section 5.2.3).

Alteration has affected some of the samples studied although not extensively. Plagioclase has decomposed to clay minerals and sericite; likewise alkali feldspar crystals often display turbid interiors due to slight alteration to clay minerals. Biotite occasionally shows alteration to chlorite and associated opaques. Hornblende does not appear to have been affected by any low grade alteration. The alteration of the feldspars will have caused the partial mobilization of CaO, BaO, K_2O and Na_2O, Rb, Sr from the samples affected.

3.4.2 iv) Ancoma Granodiorite enclave

One homogeneous enclave was collected from the granodiorite. Mineralogically the enclave is a granodiorite but is richer in biotite and hornblende than its host (Figure 3.4). Texturally the enclave is distinct from its host (Plate 3.21). The overall grain size is finer and the grains equigranular, with an interlocking texture. Individual minerals show differing morphologies. Plagioclase occurs as euhedral laths displaying only gradational zoning; biotite as subhedral crystals with a slightly interstitial form and inclusions of zircon. Hornblende as in the granodiorite forms anhedral crystals of uneven colour and generally 'ragged' outline believed to be due to resorption. Both quartz and alkali feldspar have totally interstitial habits and in places poikilitic forms, enclosing plagioclase and biotite crystals. The interlocking texture of the enclaves indicates an igneous origin. See section 3.5 for a further discussion.

3.4.2 v) Aplites

Only aplites related to the CG were observed in the field. Mineralogically, the aplites collected are composed predominantly of quartz, microperthitic alkali feldspar, muscovite and minor garnet, plagioclase, and biotite. Like the granite, the aplites show clear microtextural evidence for deformation. Texturally undeformed samples

Plate 3.21

Photomicrograph of autolith from the Ancoma Granodiorite. Lath shaped plagioclase crystals, zircon inclusions in biotite, and micro-perthitic alkali feldspar and interlocking texture are though to indicate an igneous origin (crossed polars, 8 mm field of view, sample B85/227).

Plate 3.22

Stoped blocks of country rock at the margin of the IG.

are saccharoidal with all phases displaying interlocking, anhedral outlines except garnet which occurs as rounded grains. Nonperthitic alkali feldspar displays tartan twinning and plagioclase occurs both as unzoned, polysynthetically twinned grains and interstitial, microgranophyric masses. Deformation of the aplites produced similar effects as in the granite. Quartz absorbed the majority of the strain by plastic deformation, muscovite disaggregated and alkali feldspar, plagioclase and garnet behaved competently.

3.5 Origin of the autoliths

Autoliths occur in; the CG (section 3.4.2 ii) the AG (section 3.4.2 iv), the MAG (section 3.3.3 ii) and the MVGP (section 3.3.3 iv). The presence of abundant, euhedral, plagioclase laths; euhedral biotites, often containing zircons with associated disruption haloes; and anhedral, subpoikilitic, quartz all indicate an igneous origin for the autoliths (Plates 3.12, 3.21) and are clearly distinct from the metamorphic textures of the xenoliths (Plate 3.7).The origin of the autoliths is not as clear as that of the xenoliths, but several features of their occurrence, internal textures and composition, are thought to be significant:

1) No country rocks similar to the autoliths were observed
2) The autoliths have rounded, sometimes diffuse outlines
3) They are generally small bodies (up to 30 cm diameter), although significantly bigger samples were observed
4) The contacts between the autoliths and the granitoid are always sharp although they may be cut by megacrysts
5) Internally the autoliths have uniform igneous textures
6) The autoliths are usually finer grained than the host granitoid
7) The autoliths are composed of the same modal phases as their host

8) Mineralogically the autoliths are always slightly richer in mafic minerals than their host and commonly much richer in mafics
9) Megacrysts identical to those in the host occur within the autoliths
10) They always contain abundant apatite displaying a distinctive acicular form

The rounded outlines of the autoliths suggests their incorporation into the granitoid as soft bodies. The acicular nature of the apatite crystals is characteristic of granitoid autoliths (Vernon, 1973; Tindle and Pearce, 1983) and experimentally the habit has been shown to be the result of rapid cooling (Wyllie *et al.*, 1962), which would also account for the fine grain size. Two possible models, which can explain the incorporation of autoliths as soft bodies with rapid cooling textures have been proposed by Vernon (1973):

i) That autoliths are the result of mingling of hot, mafic and cool, felsic magmas across a boundary layer in a stratified magma chamber (Figure 3.6).

ii) The autoliths may be fragments of the granitoid magma chilled at the margins of the magma chamber and then reincorporated into the magma, after a period of time during which the magma had evolved to more felsic compositions.

The second argument given the lack of any mafic material other than the autoliths is believed to be correct for the autoliths under study. The range of compositions observed in the autoliths is believed to relate to their assimilation by the host magma; this process is believed to involve the extraction of a minimum melt from the autolith to leave a residue of refractory mafic material.

3.6 Magma water content and crystallization sequences

Experimental results (e.g.Maaloe and Wyllie, 1975) have shown that the order of precipitation of phases in a granitic system at constant pressure is controlled by the water content of the system. The study, carried out at 2 kbar on a biotite

	MG-1	B85/118 MAG	B85/158 MVGP	B86/120 AG	B85/204 CG
SiO_2	71.30	68.64	71.13	69.49	71.56
TiO_2	0.40	0.50	0.23	0.51	0.18
Al_2O_3	14.44	16.01	16.20	15.21	14.87
Fe_2O_3	2.20	2.88	1.61	3.27	1.44
MnO	0.03	0.05	0.05	0.06	0.03
MgO	0.40	1.27	0.26	1.20	0.22
CaO	1.69	2.4	0.69	2.68	0.70
Na_2O	3.44	3.22	3.65	3.32	3.00
K_2O	5.45	4.40	6.57	3.80	5.51
LOI	0.51	0.74	0.69	.71	0.74
TOTAL	99.86	100.11	101.08	100.25	98.25

Table 3.4

Compositions of granite (MG-1) used by Maaloe and Wyllie (1975) and comparative granitoids from this study.

monzogranite of similar composition to the granitoids of this study (Table 3.4) shows that the timing of biotite precipitation is controlled by the water content of the magma (Table 3.5). Table 3.6 shows the order of precipitation, determined from inclusion studies and grain morphologies, of the granitoid facies studied in this work. By comparison with the results of Maaloe and Wyllie (op. cit.), it can be concluded that the Tres Cruses Complex is composed of wetter melts than the Sorata Complex and that the AG was the driest melt. The level of emplacement of a granitoid pluton may be controlled by it's water content (Hyndman, 1981); if this is so, then the wetter nature of the Tres Cruses Complex melts may indicate a deeper level of emplacement.

3.7 Other plutons studied

This section contains brief field and petrographic descriptions of the five other plutons visited in the Cordillera Real. Three of these, the Huayna Potosi Granite (HPG), the Cuti Khuchu Granite (CKG) and the Saynani Granite (SG) form a large composite body cut by the Zongo river to the south of the Sorata Complex (Figure 1.2). The Unduavi Granite (UG) forms an apophysis of the HPG. The fifth, the Illimani Granite (IG) forms a single mountain of the same name to the west of the Tres Cruses Complex.

3.7.1 The Huayna Potosi Granite

The HPG forms a distinct pluton of 160 km^2, with a apophysis the UG. Major faults of several orientations, and throws of several hundred meters cut the granite, including a thrust placing the south-western margin of the granite over the surrounding Palaeozoic metasediments. Sharp intrusive contacts between the granite and the country rocks were also observed with chilling of the granite and several meters of hornfels developed.

0 % water	0.2-1.2 % water	1.2-2.5 % water	2.5-20 % water
Plagioclase	Plagioclase	Plagioclase	Plagioclase
Alkali feldspar	Alkali feldspar	Alkali feldspar	Biotite
Quartz	Quartz	Biotite	Alkali feldspar
Biotite	Biotite	Quartz	Quartz

Table 3.5

Varying sequence of crystallization of granite at 2 kbar with varying water content (from Maaloe and Wyllie, 1975)

CG	AG	MAG	MVGP
Zircon	Zircon	Zircon and apatite	Zircon
Plagioclase	Plagioclase	Plagioclase	Plagioclase
Quartz	Quartz	Biotite	Biotite
Biotite	Alkali feldspar	Alkali feldspar	Quartz
Alkali feldspar	Biotite	Quartz	Alkali feldspar
Muscovite			

Table 3.6

Crystallization sequences for the facies studied

Internally the granite is homogeneous and unfoliated. Rare, mafic enclaves occur, but were not collected due to their small size (2-3 cm).

Petrographically the HPG is a two mica, medium grained granite , with clear microtextural evidence for deformation, as seen in the CG. Plagioclase forms euhedral polysynthetically twinned, normal gradationally zoned, crystals with overgrowths producing overall subhedral forms. Tartan twinned microcline forms anhedral crystals commonly containing inclusions of biotite, muscovite, and plagioclase. Quartz occurs as totally recrystallized masses or in shear bands. Muscovite and biotite form euhedral laths.

3.7.2 The Cuti Khuchu Granite

The Cuti Khuchu Granite (CKG) covers approximately 25 km^2, occurs to the north of the HPG and is separated from it by a 0.5 km screen of metasediment, which is was observed to intrude with the development of minor hornfels. The CKG is a two mica, medium grained, granite slightly coarser and more leucocratic than the HPG. The characteristic feature of the granite is a penetrative foliation, the intensity of which varied, apparently at random, throughout the body. The foliation like that of the CG is defined mica laths and quartz rich shear bands. The contact between the granite and the country rocks was sharp and intrusive with minor hornfels and chilling of the granite. The contact between the CKG and the SG was not observed. Pegmatites associated with the CKG were observed and contain tourmaline, uranium minerals, garnet, beryl and petalite.

Petrographically the CKG is a deformed, medium grained, two mica granite. Both texturally and mineralogically, the CKG is like the CG; all the samples studied show evidence for deformation and the style of deformation of individual minerals is identical to that described for the CG (section 3.4.2 i).

3.7.3 The Saynani Granite

The Saynani Granite (SG) occurs to the north of the CKG and covers an area of 10 km^2. The southern contact with the CKG was not observed in the field; the northern contact with the country rocks is intrusive with common pegmatites.

Petrographically the SG is a fine grained, two mica granite. There is clear micro-textural evidence for deformation of the style observed in the CG, the HPG and the CKG although a much lower degree of strain has accumulated. The morphology of plagioclase in the granite is slightly different to that in the other facies described. In the SG plagioclase forms elongate, euhedral laths, with only simple twinning and no zoning, suggesting a faster cooling rate than the other plutons. Alkali feldspar occurs as subhedral, microperthitic grains and quartz as rounded, strained, anhedral grains. Muscovite and biotite form euhedral and subhedral crystals.

3.7.4 The Illimani Granite

The Illimani granite (IG) forms a distinct pluton of 50 km^2 with good evidence for stoping of the surrounding country rocks along it's margin (Plate 3.22).In the field the IG was described as a medium grained biotite granite. Internally the only observed heterogeneity is the rare occurrence of alkali feldspar megacrysts. No control on their distribution was observed and their density never reached that of the megacrysts in the MVGP.

Petrographically the IG is a dominantly medium grained, biotite granite. In places, alkali feldspar megacrysts, give the rock a porphyritic texture similar to that of the MVGP. Texturally and mineralogically the majority of the granite is very similar to the MAG. Plagioclase forms subhedral, polysynthetically twinned crystals, displaying both normal and reverse gradational zoning. Microperthitic, alkali feldspar occurs as anhedral crystals and quartz forms rounded, anhedral masses. Brown, pleochroic, subhedral, biotite crystals and rare magnetite octahedra are the only mafic phases. Zircon and sphene are the only accessory phases identified.

CHAPTER 4
Contact metamorphism and crustal melting

4.1 Introduction

The plutons of the Cordillera Real were emplaced into a thick sequence of Palaeozoic metapelites. The regional metamorphism of the metapelites is characterized by greenschist facies, chlorite-muscovite assemblages.

This section describes the contact metamorphism as observed in the field and attempts to define the pressure and temperature of the emplacement of the granitoids of the Cordillera. The most widely proposed origin for granites is crustal melting (Chappell and White, 1974; Miller, 1986); a possible method of achieving this is also discussed.

4.2 Field relationships

Contact metamorphism associated with the Sorata Complex has been studied by Bard *et al.* (1974); to the north-east of the complex they identified a wide (up to 15 km) zoned metamorphic aureole. To the south-west the aureole is much narrower (2-3 km), but some correlation with the zones of Bard *et al.* (*op cit.*) can be made. Within the aureole four isograds based on the first appearance of biotite, andalusite, staurolite or cordierite, and sillimanite (Figure 4.1) were identified. The probable temperature, pressure conditions of the metamorphism were estimated at 650 °C, 4 kbar. Samples of metamorphic rocks collected from the south-west margin of the complex exhibit two metamorphic assemblages; quartz + plagioclase + alkali feldspar +- biotite, with some alteration of plagioclase and biotite to white mica and

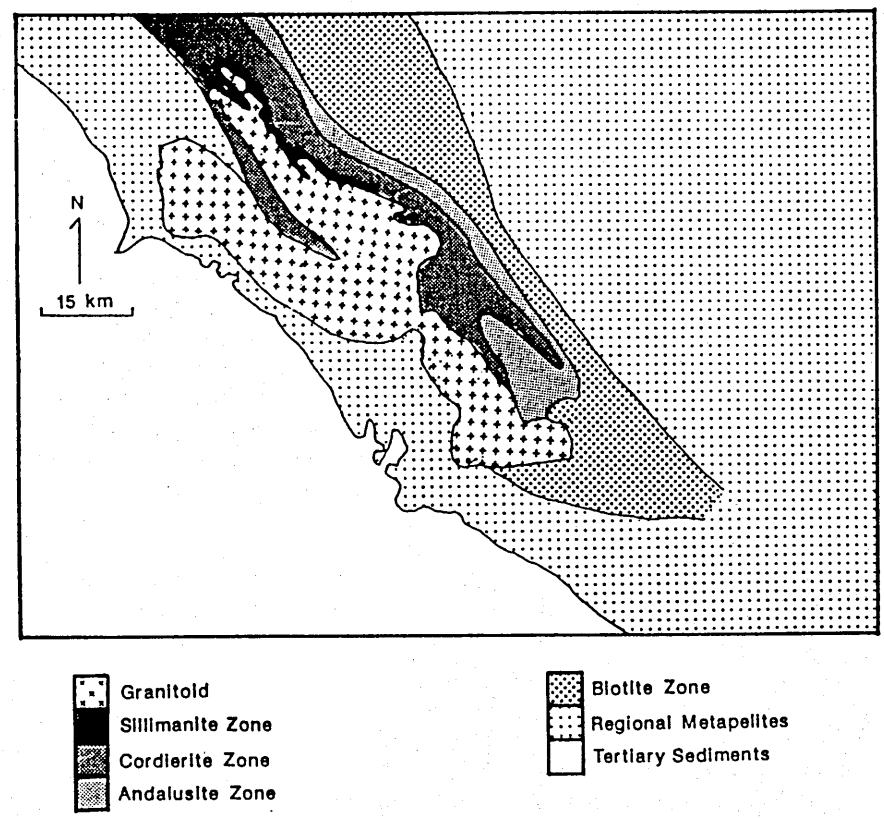

Figure 4.1

Metamorphic aureole associated with the Sorata Complex (after Bard *et al.* , 1974)

chlorite respectively, and closer to the contact, quartz + plagioclase + biotite + cordierite, with minor plagioclase alteration to white mica; these assemblages correspond to zones one and three of Bard *et al.*(*op cit.*) respectively. Sampling was not extensive enough to locate the cordierite-in or the andalusite-in isograds. The samples do however support the observation of Bard *et al.* (*op cit.*) that the SW metamorphic aureole is comparatively narrow (Figure 4.1).

The Zongo valley complex displays a very similar asymmetric metamorphic aureole to that described by Bard *et al.* (*op. cit.*) for the Sorata Complex. The southern margin of the Huayna Potosi Granite (HPG) is associated with a narrow contact metamorphic zone of the order of 10's m width, however, the northern contact of the Cuti Khuchu Granite (CKG) is associated with a wide aureole mapped by GEOBOL and shown to be 5 to 6 km wide (Figure 4.2).

The grade of contact metamorphism related to the Tres Cruses Complex is similar to that observed around the Sorata Complex, however the dimensions of the aureole along its northern margin are not known. The country rocks are mainly Palaeozoic argillites and metamorphic assemblages of quartz + alkali feldspar + plagioclase + biotite were found up to distances of 2 km from the granitoid. Closer to the contact, assemblages of quartz + feldspar + biotite + cordierite were found with some alteration of plagioclase and biotite to white mica and chlorite respectively. A single garnet hornfels sample was collected from a locality thought to be close to the granite contact (see Figure 4.3).

The occurrence of primary muscovite in the CG, MAG and MVGP (sections 3.4.2.i, 3.3.3 i, and 3.3.3 iii) places a lower limit on the pressure of crystallization of the phase of approximately 3 kbar (Clements and Wall, 1988). The possibility that the muscovite is primary, but out of equilibrium with the granitic melt cannot be ignored and the actual pressure of emplacement may have been below 3 kbar.

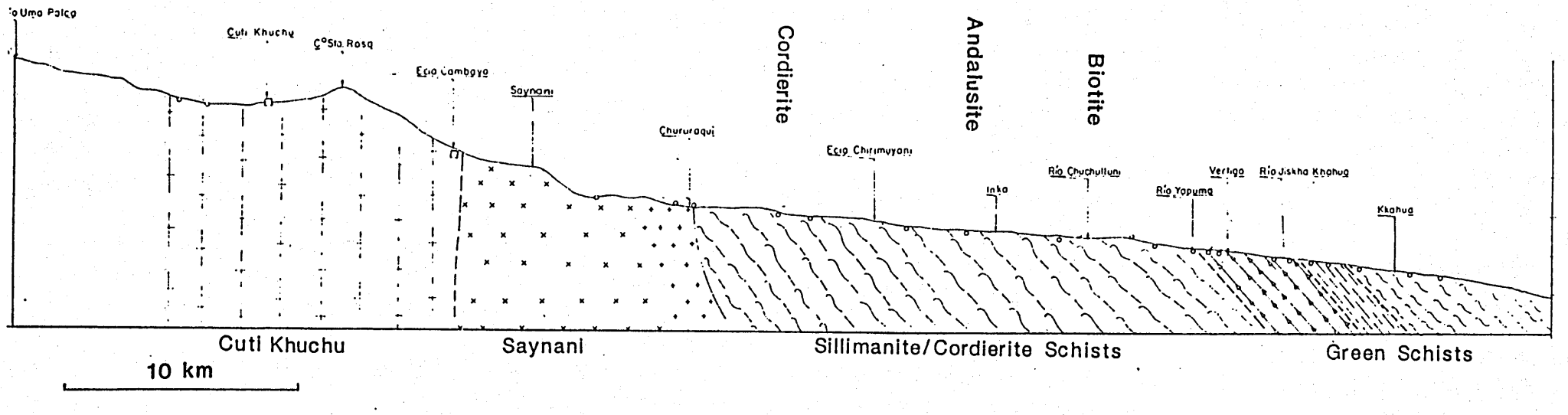

Figure 4.2

Section through the metamorphic aureole of the Rio Zongo Complex (after GEOBOL report)

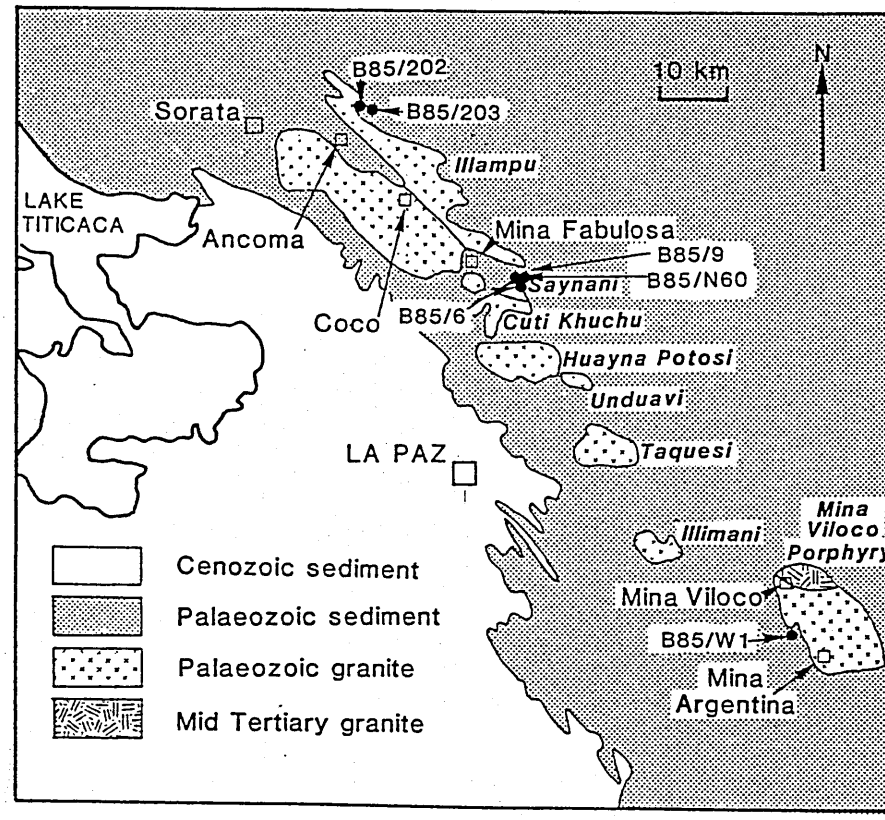

Figure 4.3

Location map of metasediment samples analysed to determine the pressure, temperature conditions of contact metamorphism.

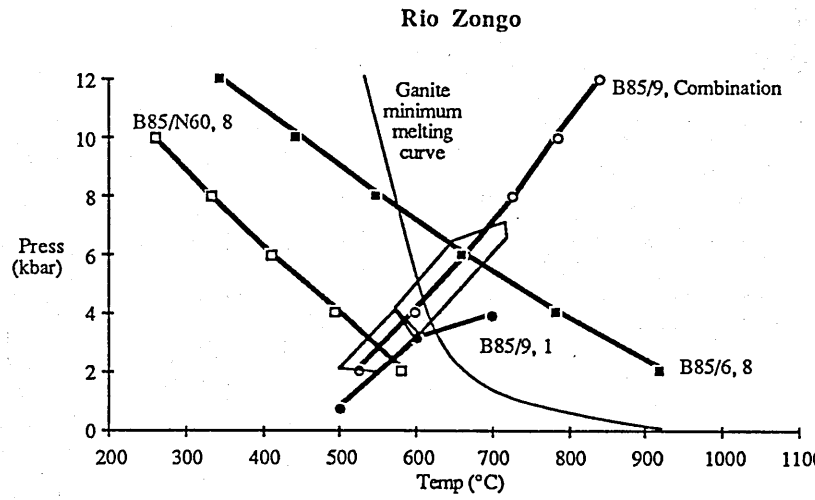

Figure 4.4

Pressure, temperature plot for the calculated equilibria of the Rio Zongo samples. Specific equilibrium in table 4.2 indicated by number after sample name.

4.3 Geothermometry and barometry

In an attempt to define the minimum pressure, temperature conditions of the emplacement of the plutons of the Cordillera Real, the metamorphic assemblages of metapelites from the contact aureoles of the Tres Cruses, Sorata, and Rio Zongo Complexes have been analysed (see Table 4.1 for assemblage and Figure 4.3 for location). The assemblages all probably equilibrated at different distances from the relative granite, therefore the temperature values are not comparable and the pressure estimates may be significantly different for samples from the same aureole. Mineral compositions were determined by standard microprobe techniques (see Appendix A for details and Appendix C for analyses).

The metamorphic assemblages have been interpreted using a computer package, written by Holland and Powell on the basis of Holland and Powell (1985) and Powell and Holland (1985). All possible balanced equations, involving relevant mineral end members, have been calculated (Table 4.2) and solved for temperature at a range of pressures. The errors in these calculations were also calculated, based on the uncertainties in the activities, and variances and covariances among the enthalpies of the mineral endmembers . For B85/9, a sufficiently large group of equilibria exist for the data analysis to be taken a stage further. At a given temperature the most likely pressure was calculated based on the entire suite of metamorphic reactions (Table 4.2). The results of this analysis are complicated by large errors and their interpretation is therefore only semiquantitative.

Figure 4.4 shows a pressure vs. temperature plot for the results from the Rio Zongo samples; two lines for B85/9 are shown, one based on the lowest error geothermometer and a second based on the most likely formation pressure of the assemblage for a range of temperatures. These two lines are within one sigma error

Sample	Locality	Assemblage						
		q	mu	bt	chl	and	crd	gnt
I) B85/9	RZ	X	X	X	X	X	X	
II) B85/6	RZ	X	X	X		X		
III) B85/N60	RZ	X	X	X		X		
IV) B85/202	S	X	X	X		X	X	
V) B85/203	S	X	X	X		X		
VI) B85/W1	TC	X	X	X	X			X

bt	biotite	gnt	garnet
chl	chlorite	mu	muscovite
crd	cordierite	q	quartz
and	andalusite		

Table 4.1

Metamorphic assemblages of the metapelite samples studied to determine the pressure and temperature of emplacement of the Rio Zongo (RZ), Tres Cruses (TC) and Sorata (S) Complexes.

	Relevant assemblage
1) crd + phl + 4 H_2O = 2 q + mu + clin	**I**
2) 5 crd + 2 an + 8 H_2O = 4 q + 3 fcd + 2 mu + 2 clin	**I**
3) 53 crd + 26 ann + 72 H_2O = 39 fcd + 10 mu + 16 cel + 18 clin	**I**
4) 7 crd + 13 phl + 36 H_2O = 5 mu + 8 cel + 9 clin	**I**
5) 3 fcd + 5 phl + 12 H_2O = 6 q + 3 fcd + 2 ann + 3 clin	**I**
6) 5 q + crd + 4 phl + 8 H_2O = 4 cel + 2 clin	**I**
7) 3 fcd + 5 phl + 12 H_2O = 6 q + 3 fcd + 2 ann + 3 clin	**I**
8) 5 q + 2 mu + phl = 2 and + phl	**II, III, V**
9) crd + 2 cel = 9 q + 2 mu + 2 phl	**IV**
10) 3 fcd + 4 cel = 9 q + 2 crd + 2 mu + 2 ann	**IV**
11) ann + py = phl + alm	**VI**
12) mu + 2 ann + 6 q + py = 3 cel + 2 alm	**VI**
13) mu + phl + ann + 6 q = 3 cel + alm	**VI**

ann	annite	fcd	iron cordierite
and	andalusite	mu	muscovite
alm	almandine	phl	phlogopite
cel	celadonite	py	pyrope
clin	clinoclore	q	quartz
crd	cordierite		

Table 4.2

Mineral equilibria used to determine the pressure, temperature conditions of contact metamorphism. Roman numerals indicate the relevant assemblage in Table 4.1

of each other in the pressure, temperature range 2 to 4 kbar, 500 to 600 °C. The assemblages for B85/N60 and B85/6 yield only one balanced equation of interest (Table 4.2); the pressure, temperature path of these equations are also shown as are the areas of overlap with the one standard deviation error for the B85/9 data. The B85/N60 equation defines a point of intersection with the B85/9 data at about 2 to 4 kbar, 500 to 600 °C. The B85/6 data define a point of intersection at significantly higher temperatures and pressures of 600 to 700 °C and 5 to 7 kbar.

In a fission track study of the Zongo Complex Benjamin *et al.* (1987) assuming a geothermal gradient of 30 °C/km and an annealing temperature for zircon of 200 °C calculated the HP granitoid to have been emplaced at a depth of at least 7 km (2 kbar), lending some support to the low pressure results above.

The two Sorata samples have been treated in a similar way in Figure 4.5. Two possible equations for the B85/202 assemblage were calculated (Table 4.2). However, one of these, equation 10, produces results with temperatures in the range 1000 °C (at 2 kbar) to 370 °C (at 12 kbar); these conditions are well above those for the dehydration temperature of muscovite (Winkler, 1967) and consequently these results are believed to be incorrect. Assuming one standard deviation errors, the two assemblages are in equilibrium from 500 °C (at 3 kbar) to 450 °C (at 11 kbar); these temperatures are well below a granite minimum and therefore represent conditions some distance from the contact. Due to the high errors of the determinations, as shown in Figure 4.5, the assemblages could have equilibrated at the same pressures and temperatures as those of the Rio Zongo aureole, the conditions for which are believed to be better defined and are less unusual.

The assessment of the metamorphic assemblage by Bard *et al.* (1974) estimated the Sorata complex to have been emplaced at 3 to 4 kbar, 650 to 700 °C consistent with the pressures and temperatures estimated above.

The assemblage of the garnet bearing hornfels from the aureole of the Tres Cruses Complex allowed three balanced equations to be written and solved. Figure

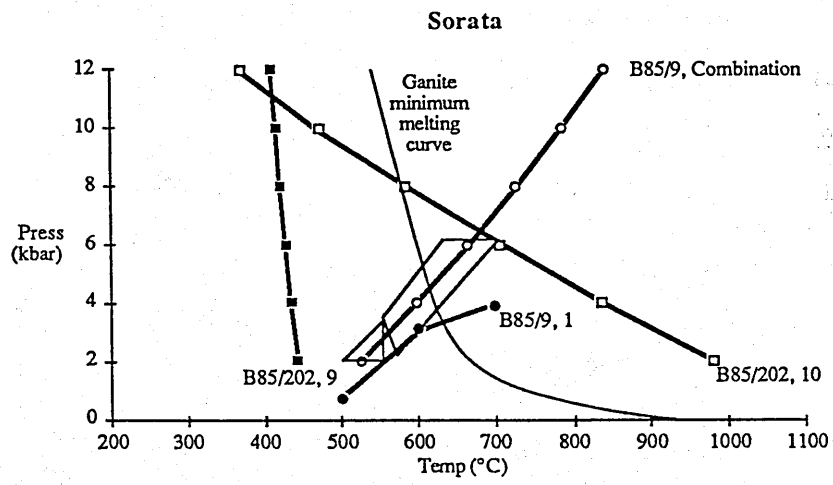

Figure 4.5

Pressure, temperature plot for the equilibria for the Sorata metasediments compared to those of the Rio Zongo. Specific equilibrium in table 4.2 indicated by number after sample name.

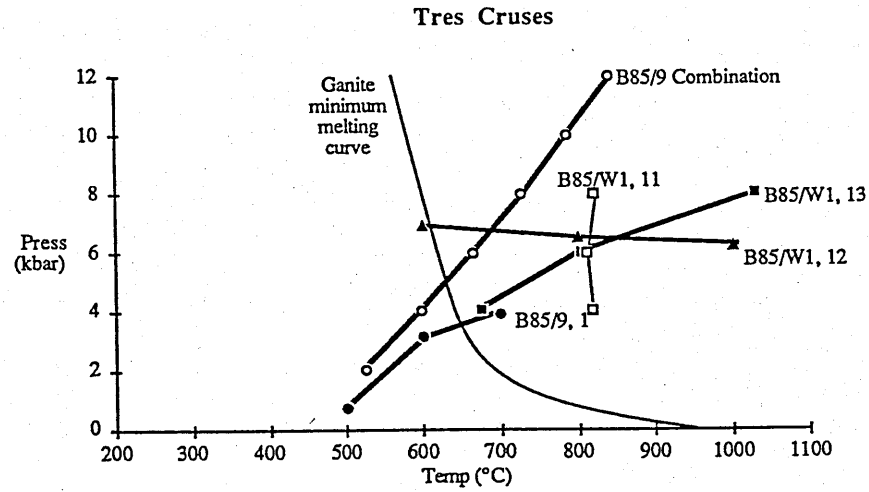

Figure 4.6

Pressure, temperature plot for the calculated equilibria for the garnet hornfels (B85/W1) from the Tres Cruses Complex aureole compared to those of the Rio Zongo samples. Specific equilibrium in table 4.2 indicated by number after sample name.

4.6 shows the traces of the equations in terms of pressure vs. temperature; the equations are satisfied by one unique point (800 ± 100 °C, 5 ± 4 kbar). This high temperature estimate suggests that the granite was not emplaced as a water saturated melt, the large error on the pressure estimate reflects the uncertainty in the calculations.

In summary; the metamorphic aureoles of the Sorata and Rio Zongo Complexes are markedly asymmetric, a feature believed to be related to the symmetry of the intrusive contacts of the plutons; the plan shape of the Tres Cruses Complex metamorphic aureole is not known. The Rio Zongo aureole appears to have equilibrated between 500 °C at 2 kbar and 600 °C at 4 kbar, indicating the granite was emplaced at pressures of about 4 kbar, consistent with fission track work (Benjamin *et al.*, 1987). The Sorata Complex data considered in isolation provide results with too large uncertainties to be useful but are within error of the estimates made by Bard *et al.* (1974) and similar to those in the Rio Zongo. The Tres Cruses complex data record higher temperatures (800 ± 100 °C) with pressures within range of those from the Rio Zongo.

These estimates of the pressures of emplacement of the granitoids are considerably higher than the emplacement depth of 2 to 4 km calculated made by Kelly and Turneaure (1970) based on stratigraphic arguments; this probably reflects the large errors of both methods.

4.4 Granitic melt generation and emplacement

The granitoids of the Cordillera Real occur as individual or clusters of two or three plutons. All the plutons display sharp intrusive contacts and many show well developed metamorphic aureoles. The depth of emplacement is estimated at about 15

km. Geochemically two distinct types of granitoid have been recognised; purely metapelitic melts and granitoids containing a significant mantle-derived component.

4.4.1 Pelitic anatexis

Since the work of Tuttle and Bowen (1958) the generation of crustal melts and the importance of water in crustal melting have been topics of research and debate. However, discrepancy exists between natural systems which are commonly water undersaturated (Brown and Fyfe, 1970) and the majority of experimental systems which are investigated under water-saturated conditions. Not only does the abundance of water control the temperature at which anatexis will begin at a given pressure but it also partially controls the viscosity of the melt and the initial and residual mineralogy of the source. The occurrence of a pervasive free fluid phase under conditions of high grade metamorphism is unlikely; any fluid phase present will be concentrated into zones of high permeability such as shear zones or faults (Clements and Vielzeuf, 1987). The role of hydrous minerals, particularly biotite and muscovite in metapelites, during anatexis is therefore of great importance. Figure 4.7 illustrates the pressure, temperature conditions for biotite and muscovite dehydration under dry conditions and the wet granite solidus; because the micas are complex mixtures of phases, dehydration occurs over a range of pressures and temperatures (Miller, 1986). Muscovite in the absence of free water will control the metapelite solidus by breakdown under upper amphibolite facies conditions (665 °C at 5 kbar, 710 °C at 10 kbar; Clements and Vielzeuf, *op.cit.*) to leave a residue of quartz, biotite, an Al_2SiO_5 phase, K-feldspar, and plagioclase ± garnet and cordierite (Miller, *op.cit.*). Increasing temperature will cause biotite to dehydrate under lower granulite facies conditions (850 °C at 5 kbar, 840 °C at 10 kbar; Clements and Vielzeuf, *op.cit.*) leaving a residue including quartz, an Al_2SiO_5 phase, K-feldspar, plagioclase and garnet or cordierite (Miller, *op.cit.*). The restite mineralogies are clearly dependent on the chemical composition of the source.

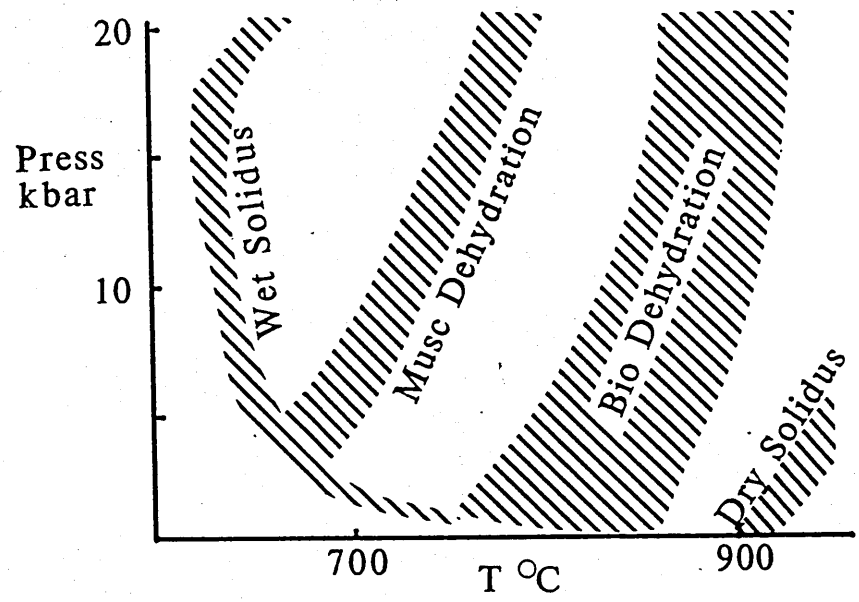

Figure 4.7

Pressure and temperature conditions for muscovite and biotite dehydration and wet and dry solidus for a typical granite (after Miller, 1986).

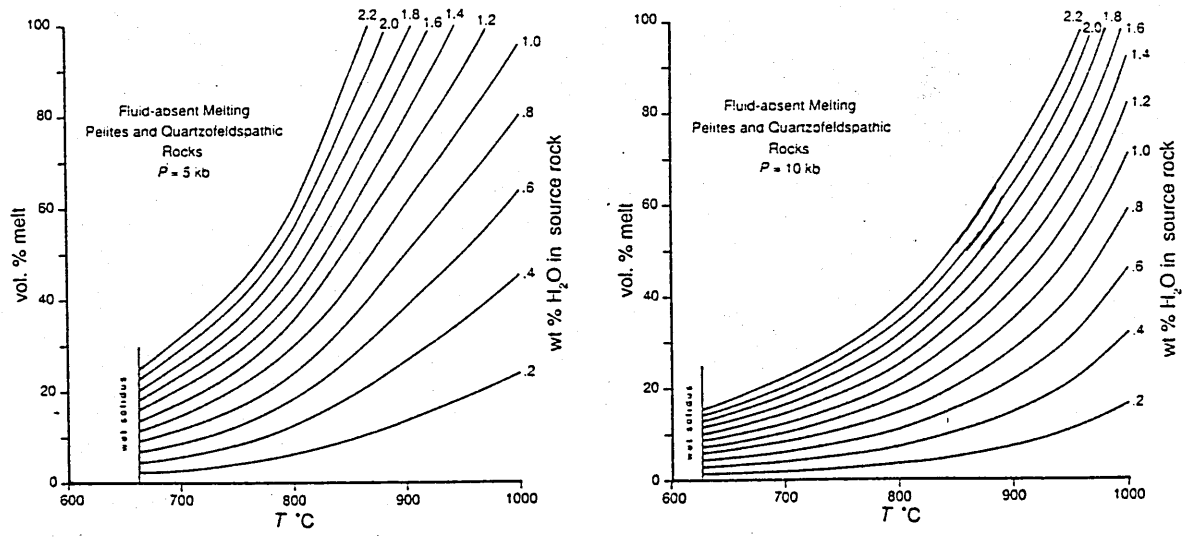

Figure 4.8

Melt fraction versus temperature for a metapelitic melt, contours indicate the water content of the melt (after Clements and Vielzeuf, 1987).

Clements and Vielzeuf (1987) have pointed out that if a melt is produced by a fluid absent reaction then its H_2O content is uniquely defined. Figure 4.8 shows the amount of melt formed from a metapelite by fluid absent reaction as a function of temperature and source rock water content. Results of this style of analysis for a metapelite are shown in Table 4.3.

The segregation of a crustal melt from its source is strongly dependent on the effective viscosity of the melt; which in turn is highly dependent on the quantity of entrained crystals (Wickham, 1987). A rapid fall in the relative viscosity will occur at a critical melt fraction, due to a change in the behaviour of the magma from that of a granular framework to that of a dense suspension as illustrated in Figure 4.9. The exact value of the critical melt fraction is not well defined for geological materials and depends on grain size and geometry; estimates range from 20 ± 10 % (Arzi, 1978) to 40 ± 10 % (Wickham, *op. cit.*).

The viscosity of a granitic melt is dependent on the water content of the magma; however, the melt fraction, which controls the effective viscosity, in a high viscosity range of granitic melts, is of greater importance, Figure 4.10.

Among the implications of this behaviour are that the separation of crustal melt from its source will only occur if the critical melt fraction is exceeded; this will lead to high melt proportion, mobile, water undersaturated, crustal melts.

From Table 4.3 it is clear that muscovite dehydration cannot produce melt proportions sufficiently high to segregate from their source but results in low volume, cool, water rich melts, which are unlikely to segregate from their source. Under fluid-absent conditions temperatures must be high enough for biotite dehydration to occur for a plutonic volume of melt to be generated. The high temperatures necessary for this to occur, 850-840 °C (5-10 kbar), place some constraints on the production of granitic melts and are in excess of those often proposed for granitic melts (Wickham, *op. cit.*). The association of granitoids containing mantle components with the pure crustal melts may indicate the importance of the mantle as a heat source for crustal melting.

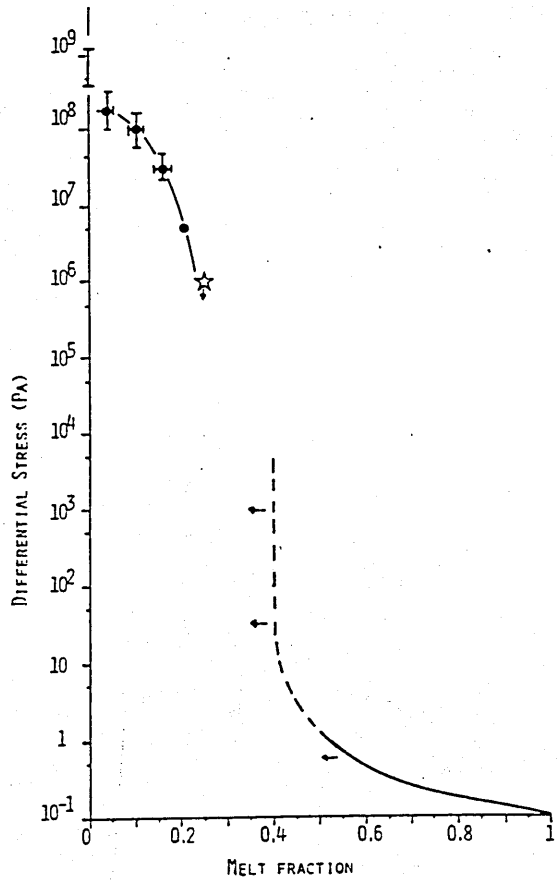

Figure 4.9

Relative viscosity versus percentage melt for a partially molten granite at 3 kbar and a strain rate of 10^{-5} s^{-1}. The rapid fall in the strength of the partially molten rock at between 30 and 50% melt is evident.

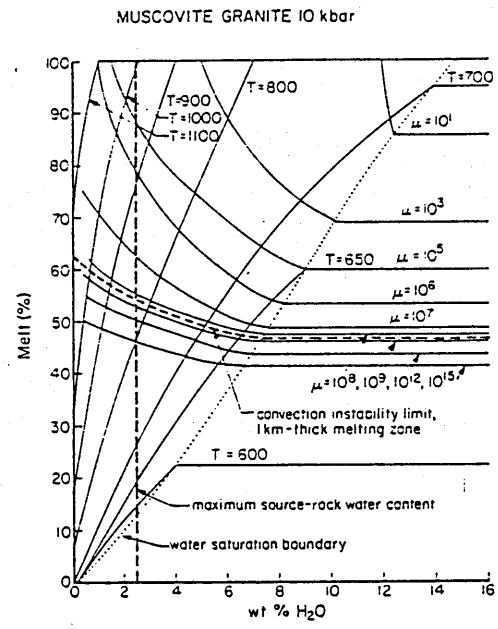

Figure 4.10

Melt percentage versus water content. Isopleths for constant temperature and relative viscosity are shown (after Wickham, 1987).

Hydrous phase	Press (kbar)	Melting Temp (°C)	Phase water content (wt%)	Melt percentage	Melt water content (wt%)
Mus	5	665	0.45	6	10.7
Mus + Bt	5	850	0.78	33	2.9
Mus	10	710	0.45	5	12.1
Mus + Bt	10	840	0.78	20	3.7

Table 4.3

Conditions of biotite and muscovite fluid free melting of a metapelite (after Clements and Vielzeuf, 1987)

CHAPTER 5
Major and trace element geochemistry and modelling

5.1 Introduction

Over 130 samples from the Tres Cruses, Sorata Complexes and the Illimani granite have been analysed for major and trace elements using X-ray energy dispersive techniques (see Appendix A). For comparative purposes 21 samples from the Huayna Potosi Granite (HPG), 13 from the Cuti Khuchu Granite (CKG), 12 from the Saynani Granite (SG), 10 for the Unduavi granite (UG) and 18 from the Illimani Granite (IG) have also been analysed for trace elements only. A subset of the Tres Cruses and Sorata samples has also been analysed for rare earth elements (REE) and Ta by induced neutron atomic activation (INAA) (see Appendix A for techniques).

The aims of this chapter are:

1) To describe the major and trace element compositions of the four facies under study and to outline the trace element characteristics of the other plutons of the Cordillera Real.
2) To model the major and trace element evolution of the facies in terms of fractional crystallization.
3) To characterize the major and trace element characteristics of the granitoid sources.

5.2 Major element variations

5.2.1 Harker diagrams

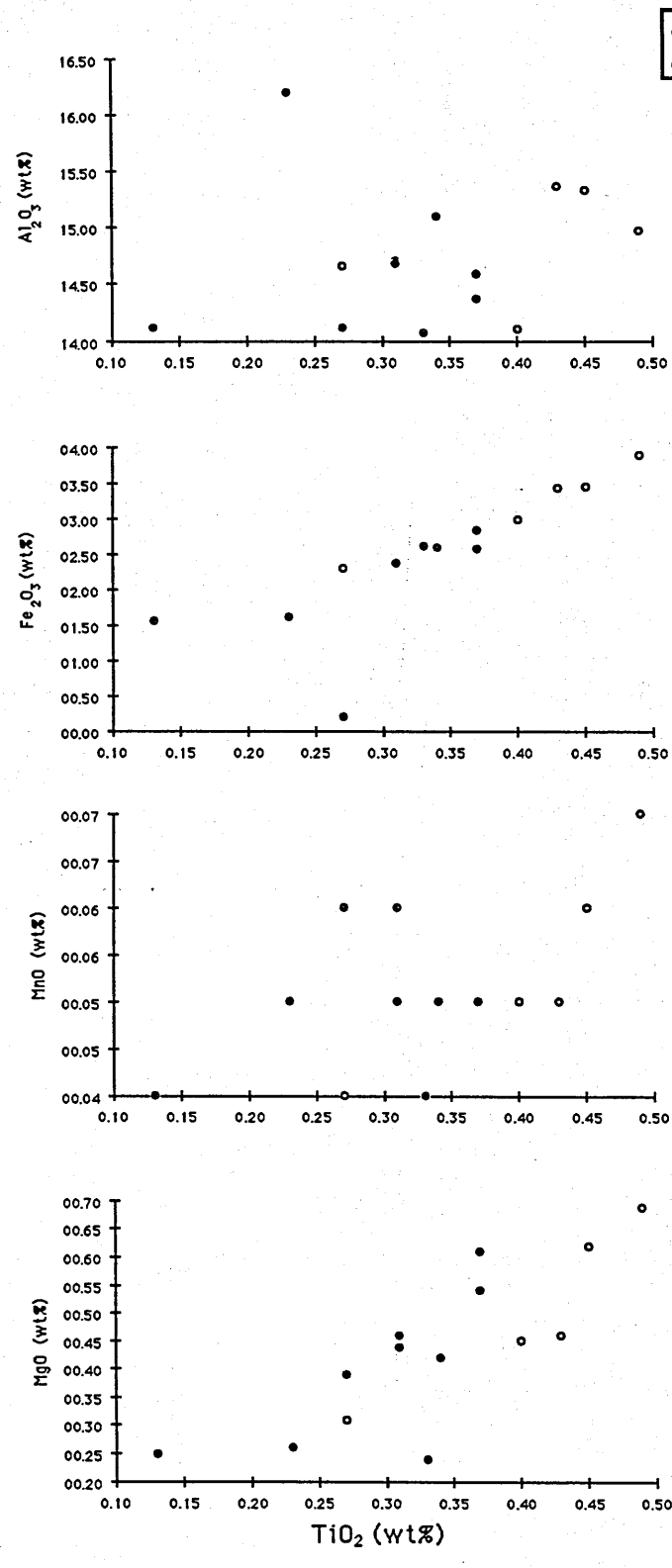

Figure 5.1

Major element variation diagrams for MVGP data

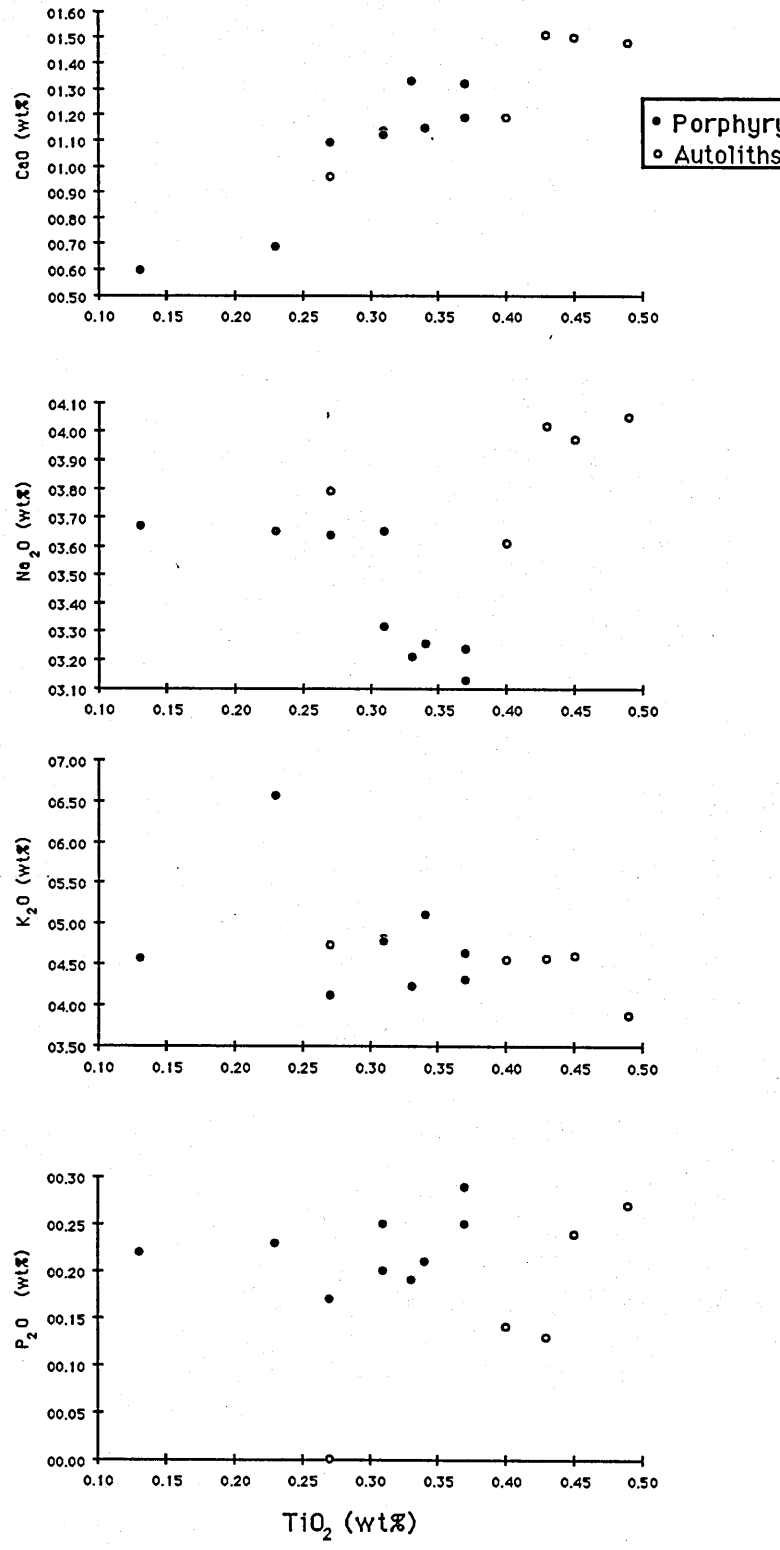

Figure 5.1 Cont.
Major element variation diagrams for MVGP data

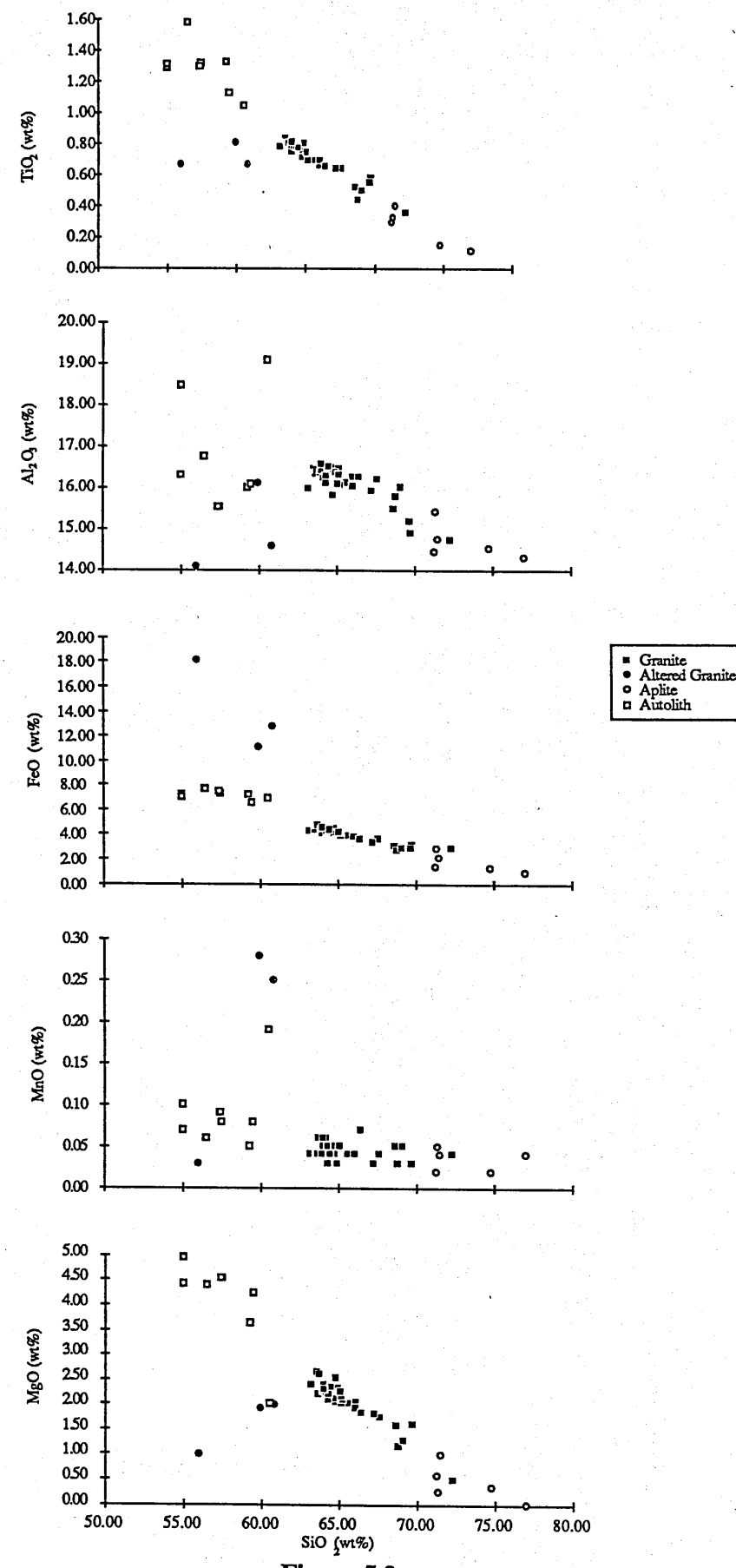

Figure 5.2

Major element Harker diagrams for MAG data

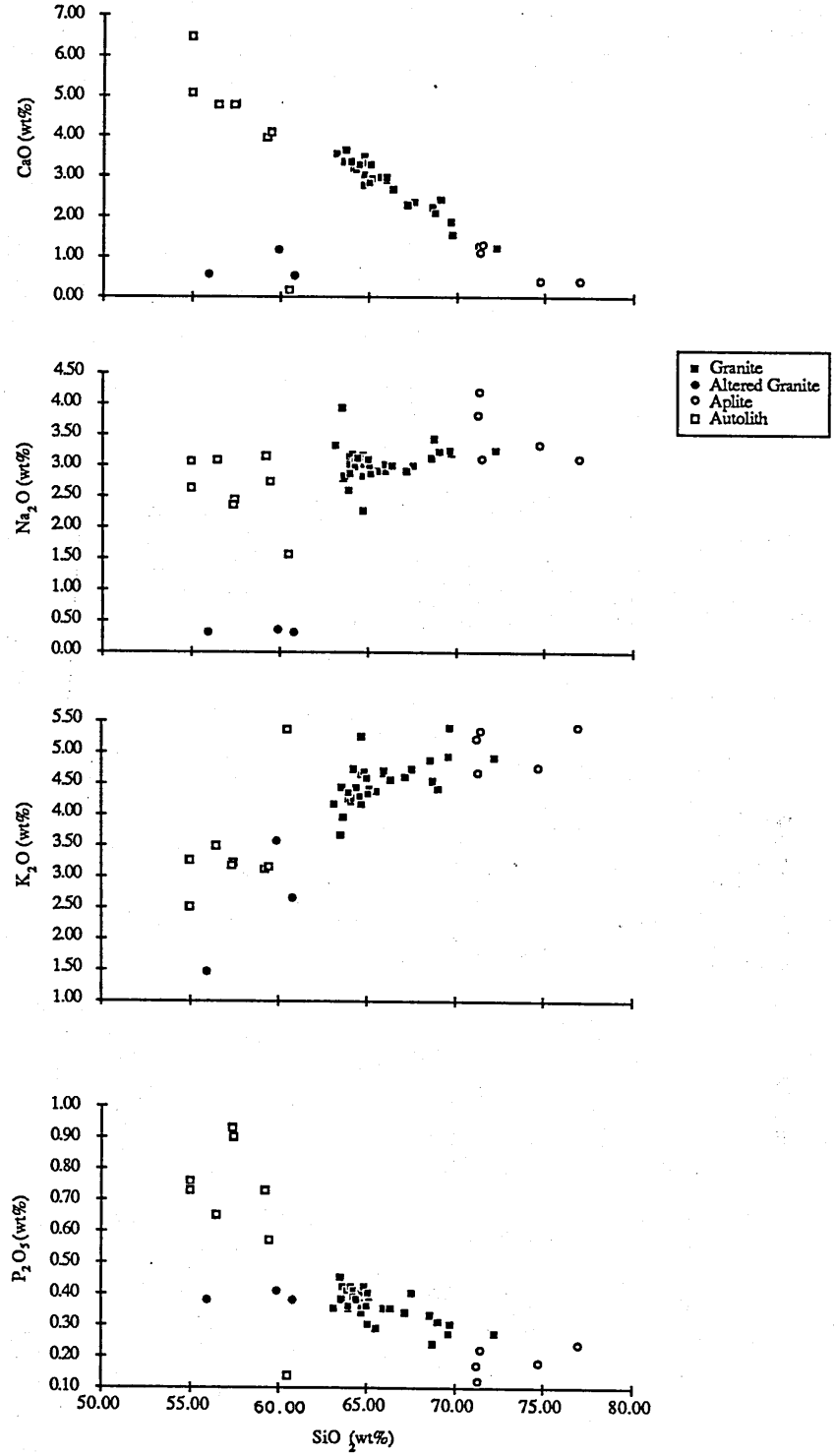

Figure 5.2 Cont.
Major element Harker diagrams for MAG data

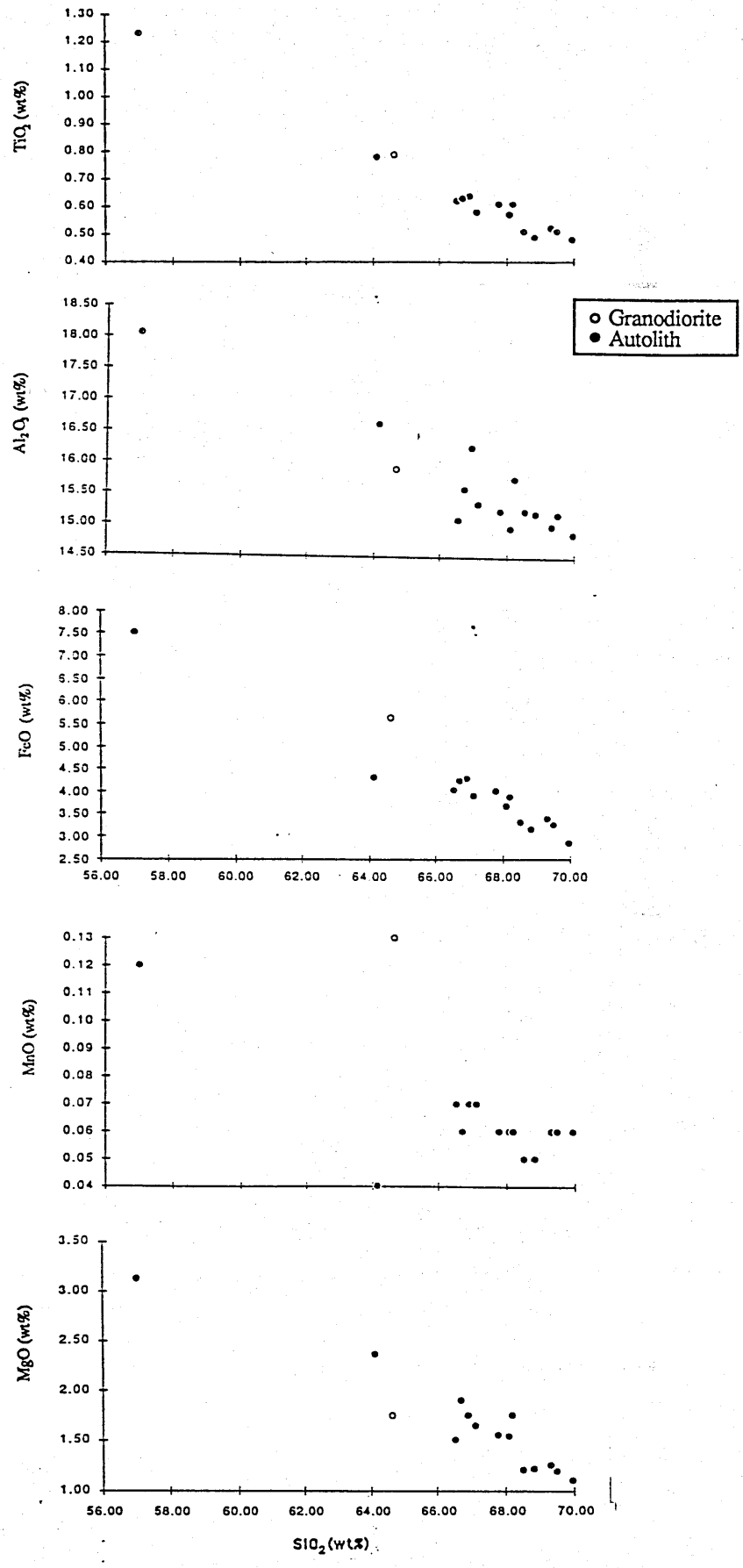

Figure 5.3

Major element Harker diagrams for AG data.

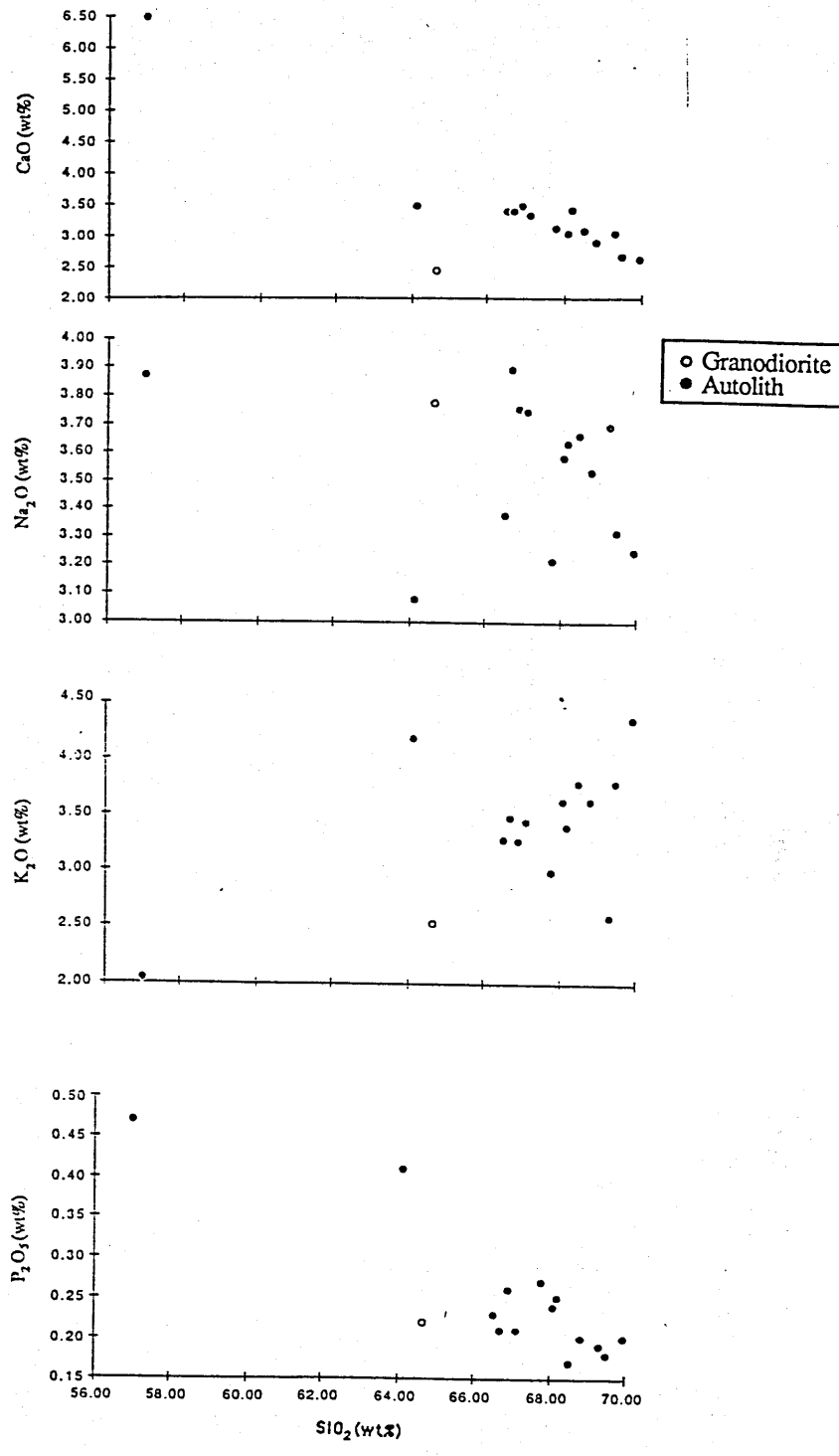

Figure 5.3 Cont.

Major element Harker diagrams for AG data.

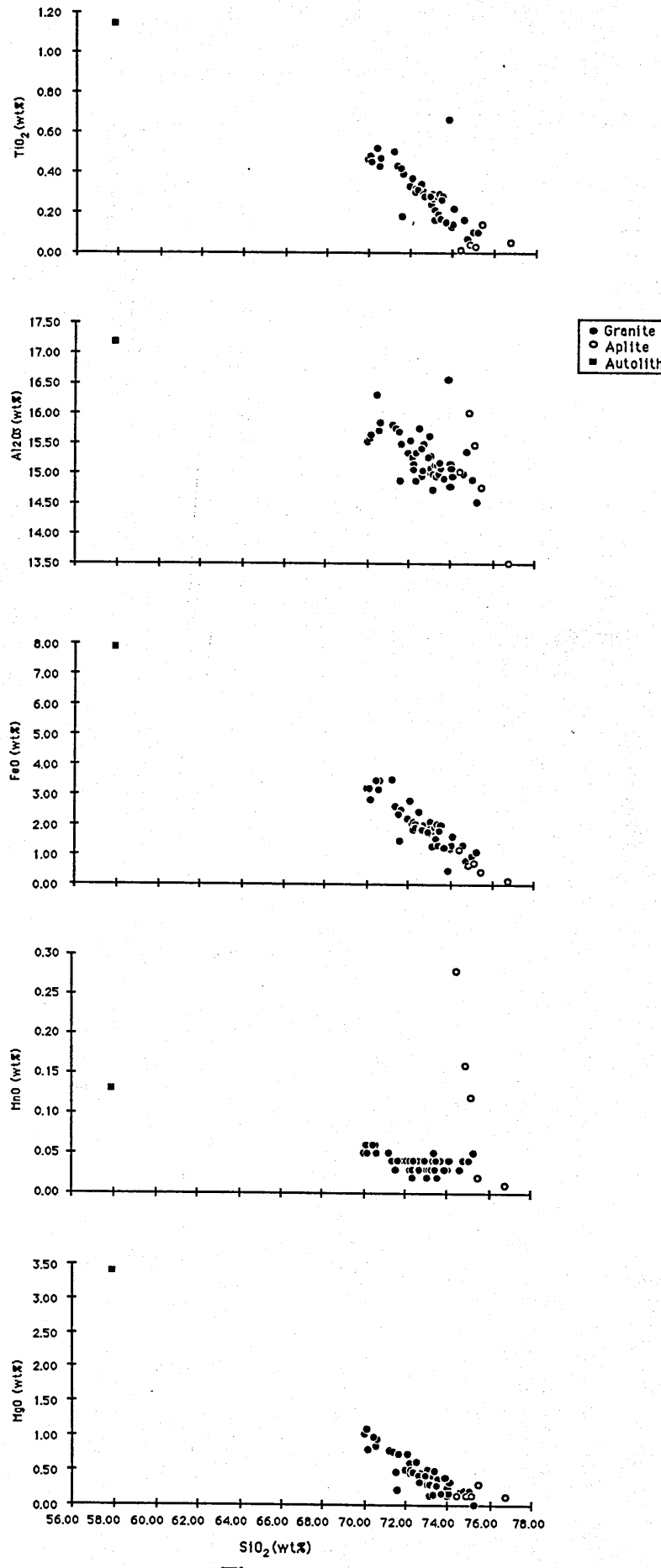

Figure 5.4
Major element Harker diagrams for CG data

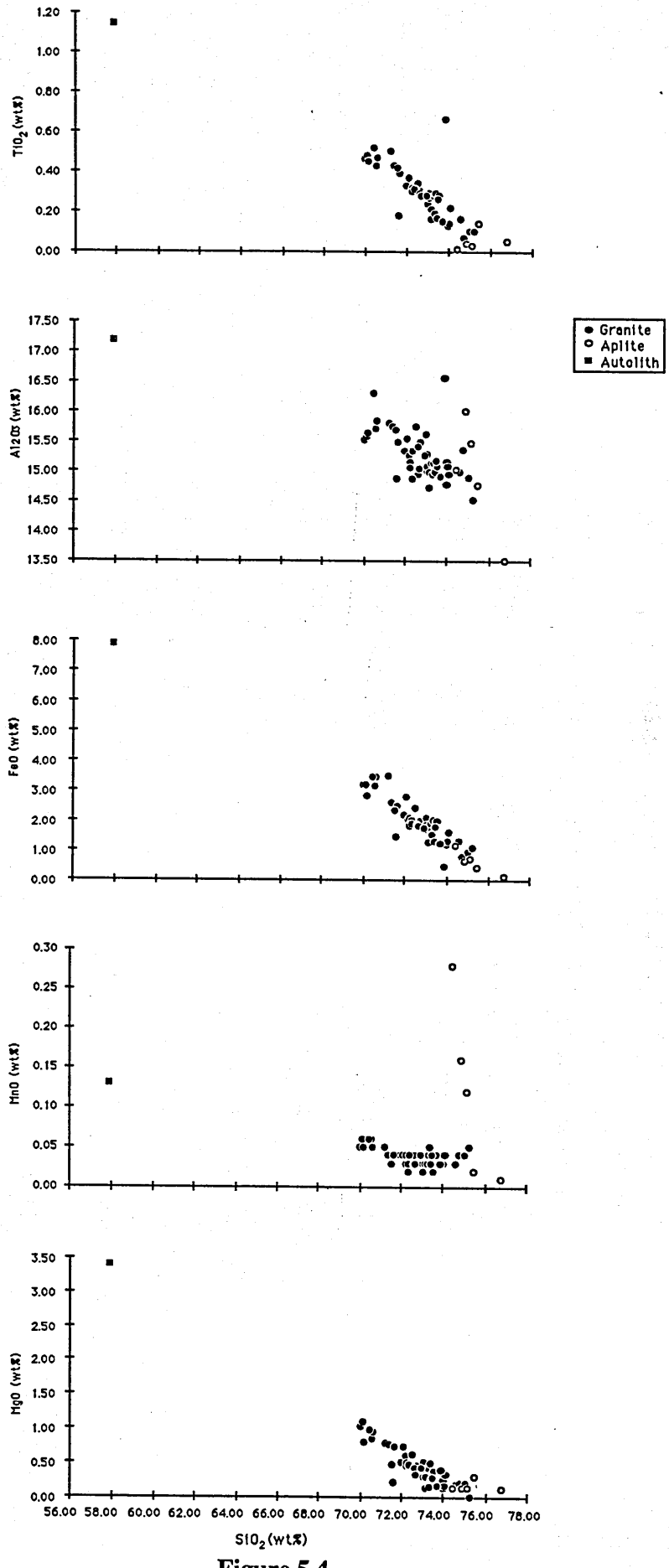

Figure 5.4
Major element Harker diagrams for CG data

Figures 5.1 to 5.4 show major element variation diagrams for the four facies under study. TiO_2 is used as a fractionation index for the MVGP due to the petrographic evidence (section 3.3.3 iii) for SiO_2 mobility. Linear trends, indicative of magmatic processes occur on the majority of the plots except for the MVGP. The lack of good trends on the MVGP variation diagrams, indicates that, element mobility in the MVGP was not limited to Si.

The MAG displays linear trends on all the variation diagrams. This suggests that the petrographically identified silica mobility (section 3.3.3 i) acted on a scale smaller than the sample size and therefore has not affected the trends. Three highly altered samples have low SiO_2 contents and lower abundances of all the major elements, except FeO and MnO, than the unaltered granites. The autoliths related to the MAG are significantly more primitive than the host granite and fall on extrapolations of all the major element trends except for FeO, CaO, and P_2O_5. The autoliths, therefore, cannot be simply related to the granite by accumulation or fractionation, further discussion is given in section 5.5.

One sample (B86/85) in the AG is significantly less evolved than the majority of the facies. However, for the elements which define clear magmatic trends B86/85 lies on an extrapolation of the trend and therefore is believed to be part of the same magmatic sequence. The lack of a clear trend for Na_2O and a poor trend for K_2O reflects the slight feldspar alteration and hence alkali mobility noted in section 3.4.2 iii on petrographic grounds. The single autolith sample in the AG is included within the compositional range of the AG. It lies on the magmatic trends of the host granite for all the major elements except MnO, CaO, and P_2O_5. This suggests that the autolith cannot be simply related to the host granite in some way , see sections 3.5 and 5.5 for a discussion of the origin of the autoliths based on petrographic and geochemical arguments.

The considerable scatter in the Na_2O and K_2O variation diagrams for the CG indicate the mobility of these elements within the facies. The single autolith sample

from the CG, only falls on an extrapolation of the granite trend for MgO indicating that, in this case, there is no simple fractional or accumulation link between the granite and the autolith.

5.2.2 Comparison with experimental systems

Tuttle and Bowen (1958) undertook an experimental study of the quaternary system $NaAlSi_3O_8$ - $KAlSi_3O_8$ - SiO_2 - H_2O (alkali feldspar - quartz - water) in order to gain insight into natural granite systems. They identified a thermal minimum in the quartz-feldspar cotectic and a thermal valley within the feldspar field at low pressures (<5 kbar), replaced by the two feldspar cotectic at higher pressures. They also showed that the quartz field expands with increasing pressure and mapped the location of the thermal minimum with changing pressure which is illustrated in Figure 5.5 in a water saturated system.

Von Platen (1965) and Winkler (1967) investigated the addition of $CaAl_2Si_2O_8$ (plagioclase) to the system. Figure 5.6 illustrates the shift in the thermal minimum caused by the changing anorthite/albite ratio in the system $CaAl_2Si_2O_8$ - $NaAlSi_3O_8$ - $KAlSi_3O_8$ - SiO_2 - H_2O at 2 kbar H_2O projected from the anorthite apex . The contraction of the quartz field and shift towards the quartz-orthoclase side of the diagram is significant for albite/anorthite ratios of less than about 7.8. Although this effect has only been investigated at one pressure it seems likely that similar trends occur at other pressures.

The effect of F on the system $NaAlSi_3O_8$ - $KAlSi_3O_8$ - SiO_2 - H_2O at 1 kbar H_2O was investigated by Manning (1980) and the results are shown in Figure 5.7. Small quantities of F cause large shifts in the position of the thermal minimum towards the albite apex and a significant decrease in the liquidus temperature from 730 °C (0% F) to 630 °C (4% F) at 1 kbar H_2O. The F content of the granitoids under study is not known, but values in the range 0.1 to 1 % have been suggested for similar granites

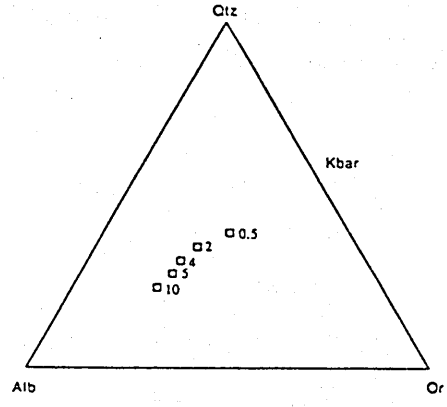

Figure 5.5
Location of thermal minimum and feldspar eutectic in the system $NaAlSi_3O_8$ - $KAlSi_3O_8$ - SiO_2 - H_2O for P_{total} = 0.5, 2, 4, 10 kbar $P_{total} = P_{H_2O}$ (after Tuttle and Bowen, 1958)

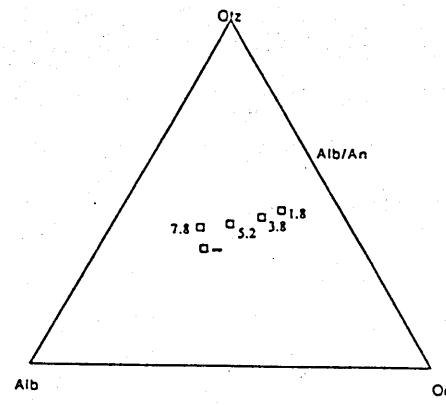

Figure 5.6
Shift in thermal minimum caused by the introduction of $CaAl_2Si_2O_8$ to the system $NaAlSi_3O_8$ - $KAlSi_3O_8$ - SiO_2 - H_2O for P_{total} = 2 kbar, $P_{total} = P_{H_2O}$ (after Von Platen, 1965 and Winkler, 1967).

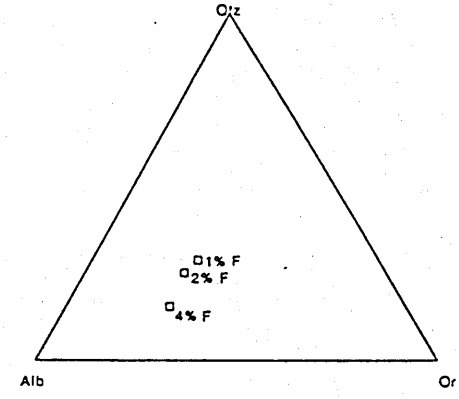

Figure 5.7
The effect of varying fluorine content on the thermal minimum at 1 kbar in the system $NaAlSi_3O_8$ - $KAlSi_3O_8$ - SiO_2 - H_2O $P_{total} = P_{H_2O}$ (after Manning, 1980)

(Bailey, 1977).

The comparison of true analysed rock data, with experimental data, is complicated by the fact that granite samples probably do not represent pure liquid compositions, rather they are a mixture of liquid and entrained cumulate crystals (McCarthy and Groves, 1979), and the whole rock composition will lie on a mixing line between the true liquid and the cumulate composition.

Figures 5.8 to 5.11 show the spread of data for the CG, AG, MAG, and MVGP in the system; CIPW normative $NaAlSi_3O_8$ - $KAlSi_3O_8$ - SiO_2 and H_2O. Comparing natural systems with the simple experimental system of Bowen and Tuttle (*op.cit.*), although common practice, is problematic since natural magmas are not restricted to three or four components. The use of CIPW norms to assess the orthoclase content of a rock is not accurate since the total K_2O content of the rock is assigned to orthoclase although a significant proportion may actually occur in micas. A second major problem occurs due to the presence of CaO in the natural system. The range of albite/anorthite ratios is also shown for each pluton. Due to the low values of the albite/anorthite ratios for the CG, AG, MAG and MVGP, as shown in Figures 5.8 - 5.11, by analogy with the results of Van Platen (*op. cit.*) and Winkler (*op.cit.*) the correct thermal minimum for the natural system lies nearer the quartz-albite side of the diagram at a given pressure (Figure 5.6).

The MAG, and to a lesser extent the MVGP data define clusters, with distinct tails, displaced towards the two feldspar side of the diagrams relative to the thermal minima. The variation within the data can be interpreted in two ways; crystal settling, or *in situ* fractional crystallization. The crystal settling model assumes, that, the observed variation is due to liquid evolution. A liquid could evolve down the thermal valley between the albite and orthoclase compositions towards the thermal minimum by the removal of unseen feldspar cumulates; the samples nearest the two feldspar join in this case being samples of the most primitive liquid. The autolith data for the MAG forms a cluster displaced away from the quartz apex, this may be interpreted in

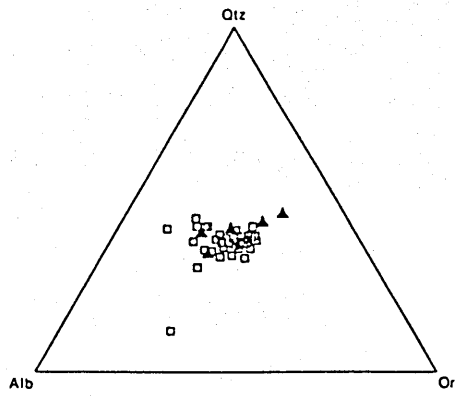

Figure 5.8
Location of CG CIPW norm data in system $NaAlSi_3O_8$ - $KAlSi_3O_8$ - SiO_2 - H_2O, thermal minima of Tuttle and Bowen (1958) superimposed. Alb/An = 3-4.

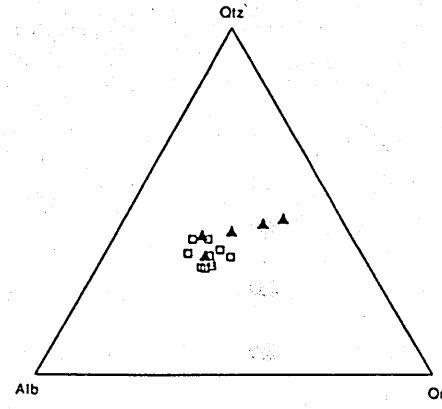

Figure 5.9
Location of AG CIPW norm data in system $NaAlSi_3O_8$ - $KAlSi_3O_8$ - SiO_2 - H_2O, thermal minima of Tuttle and Bowen (1958) superimposed. Alb/An = 1.8-2.3.

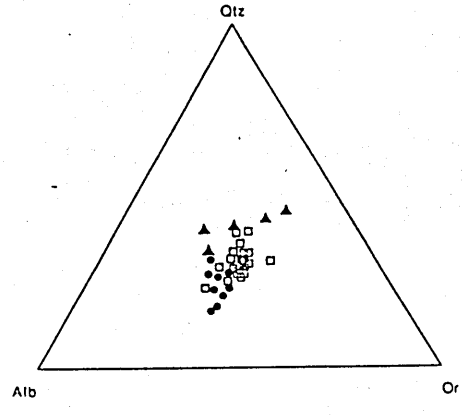

Figure 5.10
Location of MAG CIPW norm data (autoliths solid circles) in system $NaAlSi_3O_8$ - $KAlSi_3O_8$ - SiO_2 - H_2O, thermal minima of Tuttle and Bowen (1958) superimposed. Alb/An = 2.5-3.5.

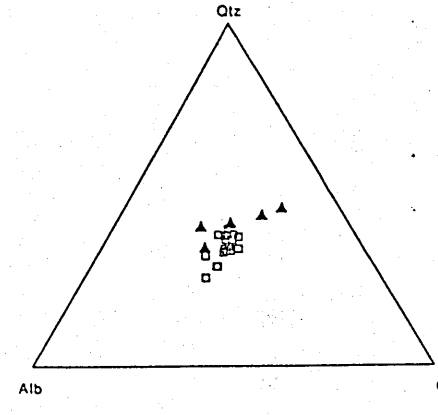

Figure 5.11
Location of MVGP CIPW norm data in system $NaAlSi_3O_8$ - $KAlSi_3O_8$ - SiO_2 - H_2O, thermal minima of Tuttle and Bowen (1958) superimposed. Alb/An = 5.5-7.5.

several ways; the samples may represent true liquid compositions in the two feldspar thermal valley, they may be samples enriched in cumulate feldspar or more likely they are mafic rich residues left after the extraction of a minimum melt, as suggested in section 3.6 and and discussed further in section 5.3.1.

The AG data cluster around the 2 kbar thermal minimum for the simple $NaAlSi_3O_8$ - $KAlSi_3O_8$ - SiO_2 - H_2O system, but the low albite/anorthite ratios indicate that the correct thermal minimum lies further towards the quartz-orthoclase join. As with the Tres Cruses results, the analysed samples are mixes of melt and entrained cumulate crystals and their position on the diagram is open to the same interpretations as discussed above.

The CG data like the other data sets cluster around the low pressure thermal minima of Tuttle and Bowen (*op. cit.*), the high anorthite/albite ratios of the samples however, negates their interpretation in terms of these minima.

In summary the data cannot be interpreted with any degree of certainty in terms of the experimentally investigated major mineral systems due to several factors including: the major moderating effects of components in the natural systems not extensively investigated in the experimental ones. The autolith compositions all plotted further from the thermal minima than the host data consistent with the autoliths being residue material after the extraction of a minimum melt as proposed in section 3.5 and further investigated in section 5.5.

5.2.3 Major element fractionation modelling

Mixing calculations allow the observed major element variations in a pluton to be modelled in terms of the removal (fractionation) of the petrographically observed phases. Inaccuracies are inevitable in this style of modelling, as noted above, since the compositions of the analysed samples probably do not represent the compositions of true liquids (as assumed in the modelling) but mixtures of liquids and cumulates (McCarthy and Groves, 1979).

The computer program used is based on the least squares method of Wright and Doherty (1970) and uses the simple relationship:

parental magma = cumulus crystals + residual liquid

The aim of the modelling is to precisely reproduce the composition of the initial magma by mixing the cumulate phases and the most evolved sample (taken to represent the residual liquid). The accuracy of the model is measured in terms of the sum of the square of the residuals ($\sum R^2$), a measure of the deviation of the data from the model. The lower the $\sum R^2$ value the better the fit of the model.

Modelling was carried out for the MAG, the CG and the AG. Mineral compositions used are given in Table 5.1. Pyroxene was used in the AG model on the basis of the secondary nature of the amphibole, augite compositions from Tindle (1982) were used in the models.

The two models discussed in section 5.2.2 and the results are shown for each pluton in table 5.2:

i) The crystal settling model: this assumes that the most primitive sample of each pluton is the parental magma and the most evolved the residual liquid. These assumptions imply a body of unseen cumulates lie below the granite.

ii) The *in situ* fractional crystallization model: this model assumes that a sample close to the middle of the observed range of compositions is representative of the parental magma and the most evolved sample is the residual liquid. In this model the calculated cumulus assemblage should approximate to the less evolved samples of the pluton.

A summary of the results is shown in Table 5.2. Several observations can be made. The *in situ* fractional crystallization model for the MAG has the lower $\sum R^2$

MAG

	Qtz	Pl	Kspar	Bt	Opq	Ap	B86/9	B86/26	B86/18
SiO_2	100	57.8	64.85	35.76	0	0	63.36	66.05	69.06
TiO_2	0	0	0	3.92	50	0	0.8	0.69	0.5
Al_2O_3	0	25.59	18.3	15.29	0	0	16.42	16.03	16.01
FeO	0	0	0	17.51	50	0	4.72	3.8	2.88
MgO	0	0	0	11.16	0	0	2.6	1.92	1.27
CaO	0	8.08	0.07	0.01	0	53	3.65	2.95	2.4
Na_2O	0	6.57	1.39	0.18	0	0	2.81	3	3.22
K_2O	0	0.38	14.18	9.02	0	0	3.94	4.7	4.4
P_2O_5	0	0	0	0	0	42	0.38	0.35	0.31

AG

	Qtz	Pl	Kspar	Bt	Opq	Ap	Cpx	B86/85	B86/125	B86/115
SiO_2	100	58.26	64.85	35.38	0.51	0	53.35	57.02	66.7	69.95
TiO_2	0	0	0	1.98	50	0	0.13	1.23	0.63	0.48
Al_2O_3	0	26.18	18.3	16.03	0	0	0.87	18.06	15.6	14.88
FeO	0	0.06	0	20.9	47	0	11.62	7.53	4.23	2.86
MgO	0	0	0	0.32	1.5	0	13.04	0.12	0.06	0.06
MnO		0	0	9.03	0.5	0	0.86	3.13	1.91	1.1
CaO	0	8.27	0.07	0	0.7	53	23	6.49	3.39	2.63
Na_2O	0	7	1.39	0.09	0	0	0.38	3.87	3.9	3.25
K_2O	0	0.08	14.8	9.14	0	0	0	2.04	3.48	4.37
P_2O_5	0	0	0	0	0	42	0	0.47	0.21	0.2

CG

	Qtz	Pl	Kspar	Bt	Mus	Opq	Ap	B86/65	B85/195	B85/182
SiO_2	100	60.2	64.27	34.85	45.76	0.86	0	70.58	72.58	75.2
TiO_2	0	0.02	0.02	2.63	0.45	52.73	0	0.47	0.3	0.1
Al_2O_3	0	24.82	18.34	18.64	35.17	0.35	0	15.84	14.99	14.52
FeO	0	0.01	0.01	22.71	1	42.33	0	3.45	1.98	1.08
MgO	0	0	0	0.32	0	4.44	0	0.05	0.04	0.05
MnO	0	0	0	6.03	0.57	0	0	0.95	0.4	0
CaO	0	6.62	0.01	0	0	0	56	2.26	1.11	0.61
Na_2O	0	7.8	0.7	0	0.35	0	0	3.62	3.24	3.91
K_2O	0	0.13	15.45	9.01	10.71	0	0	2.64	4.53	4.15
P_2O_5	0	0	0	0	0	0	44	0.16	0.22	0.24

Table 5.1

Mineral and whole rock compositions used in major element modelling

Model	Parent % of rock	ΣR^2 Qtz	Pl	Kspar	Cumulate mineralogy Bt	Mus	Opq	Ap	Sph	Cpx	Residual Liquid	Residual liquid	
MAG													
Crystal settling	B86/9	22.0	42.0	6.9	29.7	X	0	1.2	X	X	B86/18	26	0.12
In situ	B86/26	20.8	34.8	17	27.8	X	0.02	1.5	X	X	B86/18	60	0.04
AG													
Crystal settling	B86/85 0.004	10.4	54.5	0	18.5	X	2.42	1.2	0	16.17	B86/115		7.75
In situ	B86/125 0.35	21	49.5	0	22.1	X	0.84	0	0	7.6	B86/115		65.1
CG													
Crystal settling	B86/65 0.04	33.4	44.7	0	18.2	4.8	0.5	0	X	X	B85/182		25.3
In situ	B85/195 0.002	32	25.5	17.8	13.8	9.5	1.1	0.4	X	X	B85/182		61.6

Table 5.2
Results of major element mixing calculations for the MAG, AG and CG. An X denotes a mineral not considered in the model

and the calculated cumulus assemblage is in good agreement with the composition of the most primitive sample, suggesting that the model is broadly correct. If this is so, then, the assumed parental magma underwent 40% crystallization to produce the most evolved sample. This value is close to, but lower than, the theoretical maximum percentage (50% to 70%) of solids a magma can contain and continue to act as a fluid (Wickham, 1987; and section 4.4.1). The discrepancy is probably due to the assumption that the parental magma was totally liquid.

Major errors in the mixing model can occur due to several types of inaccuracies in the input data and the nature of the model. The compositions of the fractionating phases has been estimated from probe analyses but may be significantly different to those of crystals already fractionated from the melt. Phases not considered in the model may have exercised control over some of the elements considered. The nature of the modelling is such that it will identify the first minimum in the discrepancy between the observed data and the model; this process can cause errors due to other error minima, smaller than the first one being ignored; also geologically unreasonable assemblages may be proposed since no limits on mineral abundances can be set.

The results for the AG (Table 5.2) indicate a total lack of alkali feldspar fractionation. The highly interstitial nature of the alkali feldspar noted in section 3.4.2 iii supports this conclusion. The crystal settling model has a lower ΣR^2 than the *in situ* fractional crystallization model. However the composition of the theoretical cumulates is highly unusual containing over 18% biotite, 16% pyroxene and only 10% quartz. The composition of the cumulates in the *in situ* fractional crystallization model is close to that of the most primitive sample, again suggesting the correctness of the model.

The results for the CG show slightly different results; the *in situ* model has a significantly lower ΣR^2 than the crystal settling model but predicts a cumulate assemblage unlike that of the most primitive sample or autolith known. The crystal settling model predicts a plagioclase rich cumulate and appears a more feasible model.

5.3 Trace element geochemistry and modelling

Trace elements studies of granitic systems have played a major role in the understanding of their formation and evolution. However, the variations of the trace elements in granitic systems are complex and controlled by several factors, including the following:

1) In highly acidic systems (75 to 77% SiO_2) the partition coefficients of trace elements are not controlled by the ease with which they can enter the lattice of crystallizing phases, rather, the melt structure plays the dominant role (Mahood and Hildreth, 1983). The liquid structure of a silica rich melt is, at its simplest, a highly organized three dimensional network, of SiO_4^{4-} tetrahedra. Al can substitute for Si in the tetrahedra causing local charge inbalance (Si valency 4+, Al valency 3+) and the coupled substitution of low charge metal species such as the alkali and alkaline earth metals. Highly charged species, such as some trace metals, are excluded from the melt and can therefore have high distribution coefficients for the crystallizing phases.

2) Volatiles can play a major role in the evolution of high silica melts; they cause two separate effects, both of which lower the distribution coefficients of trace metals. Volatiles such as H_2O, Cl, F, etc. act as network modifiers; that is, they disrupt the alumino-silicate lattice allowing high charge density trace metals to be accommodated within the liquid. Also volatiles can complex with trace metals lowering their chemical potential in the melt and therefore lower their distribution coefficients.

3) Preliminary studies (Schreiber *et al.*, 1980 and Paul, 1976) suggest that metal-metal complexing can occur in silicate melts and cause a lowering of

the chemical potential and hence distribution coefficient of trace metals in high silica melts.

4) In less silica rich granitic liquids the REE, Ti, Zr, Nb, Ta, and P are controlled dominantly by accessory phases, although biotite and hornblende can also contain significant quantities of some of these trace elements. In allanite and monazite the LREE are stoichiometric constituents comprising about 20% and 50% respectively. The effective distribution coefficients are therefore in the range 10^3 to 10^4 (Miller and Mittlefeldt, 1982) and fractionation of tiny quantities of these and other accessory phases (xenotime, zircon etc.) will have a significant effect on the REE composition of the melt, see section 5.6.1 for examples of accessory phase importance to REE budgets.

5) The controls on the precipitation of the various accessory phases in granitic systems are not totally understood. Watson and Harrison (1983) have shown that the solubility of zircon in acidic melts is controlled by the silica content of the melt; zircon is more soluble in intermediate magmas than highly siliceous magmas at the same temperature. Also the solubility of zircon is related to the alkalinity of the melt; solubility rises from peraluminous to peralkaline melts; this may be related to the network modifying effect of the alkalis decreasing the distribution coefficient of Zr in the highly silicic magma.

6) Due to their high viscosities, the separation of cumulus crystals from acidic liquids is probably a very inefficient process and such magmas probably never exist as pure liquids. Miller and Mittlefeldt (1982) have suggested that small accessory phase grains may only separate from the melt as inclusions in larger crystals (e.g. biotite). Even large crystals of major silicate phases may well not separate efficiently (McCarthy and Groves,

1979). A granitic magma therefore is composed of three important components: the true liquid; the entrained cumulates, which have crystallized from the magma but not separated from it; and the inherited crystals, possibly the majority of the accessory phases, which did not crystallize from the melt or equilibrate with it.

5.3.1 Trace element variations

Figures 5.12 to 5.15 show Harker diagrams for the trace elements of the MAG, MVGP, CG, and AG. The high correlation of immobile elements such as Ti and Zr with SiO_2 is taken as proof of magmatic evolution, since it would be difficult to produce such trends by post-magmatic alteration, metasomatism or sampling bias as the elements considered are controlled by differing phases.

Hine *et al.* (1978) predicted that true linear trends on trace element diagrams will result from simple mixing but not from Rayleigh fractionation, which will produce curved trends. The curvature of Rayleigh fractionation trends will not be great for the range of distribution coefficients encountered in granitic systems. Wall *et al.* (1987) have shown that for a range of trace element distribution coefficients of 0.3 to 3 and a range of silica apparent distribution coefficients of 0.75 to 0.9 the model curvature will be slight (Figure 5.16) and probably well within the spread of any real data set. Therefore, near linear trends on trace element Harker diagrams are not a strong argument against fractional crystallization as the causative process.

The MAG trace element data displays strong negative correlations of Ti, Zr, Nb,Sr, and Ba with SiO_2. Only Rb and Pb are positively correlated with SiO_2 indicating incompatible behaviour. The five aplite samples display extreme depletions or enrichments of the fresh granite trend except for U which is significantly enriched in the aplites. The autolith samples lie off an extrapolation of the fresh granite trend except for Zr and Ti; Zr being controlled solely by zircon and Ti by ilmenite and biotite. This may reflect the extraction of a felsic minimum melt

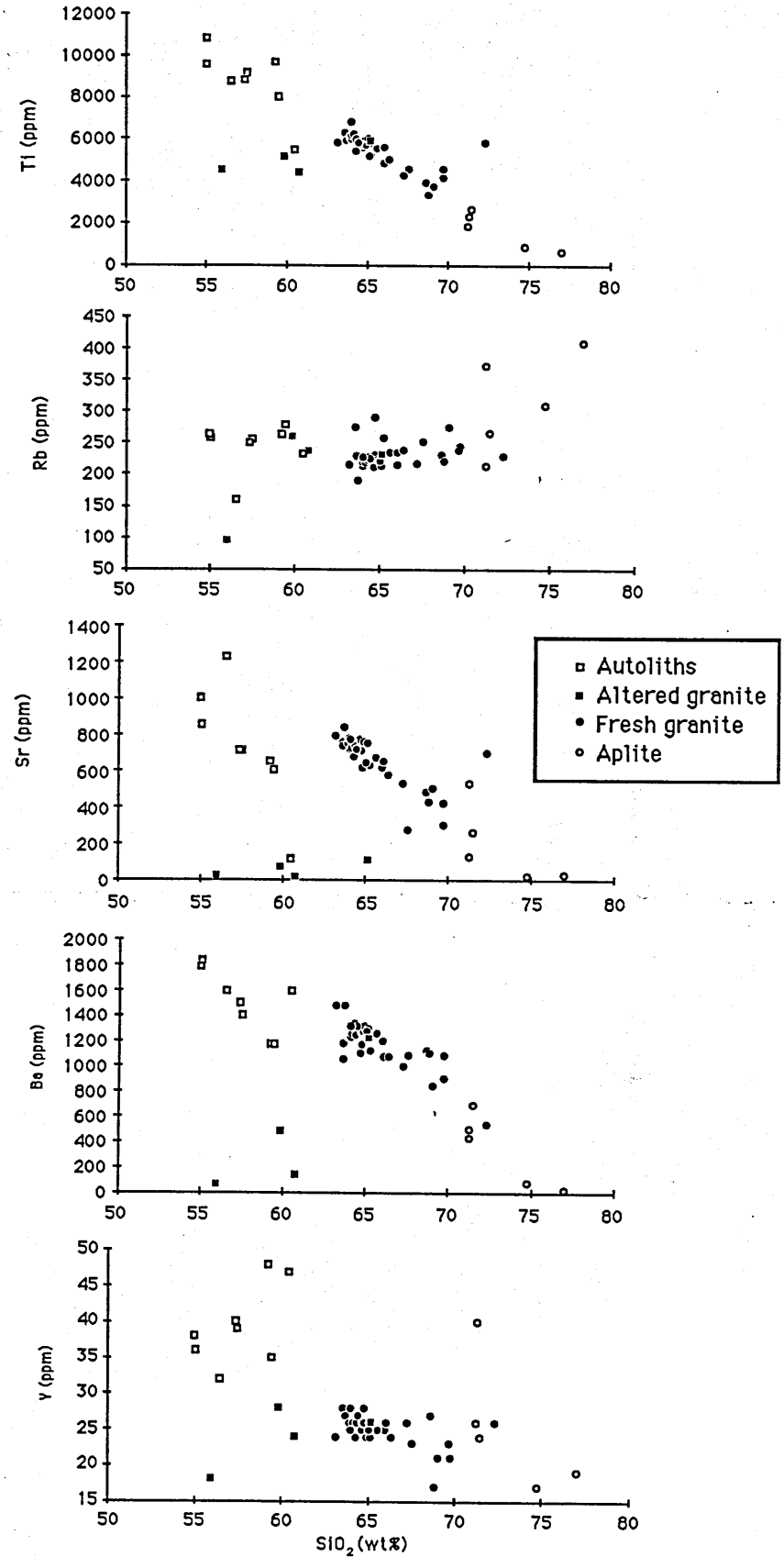

Figure 5.12

Harker diagrams for MAG trace element data

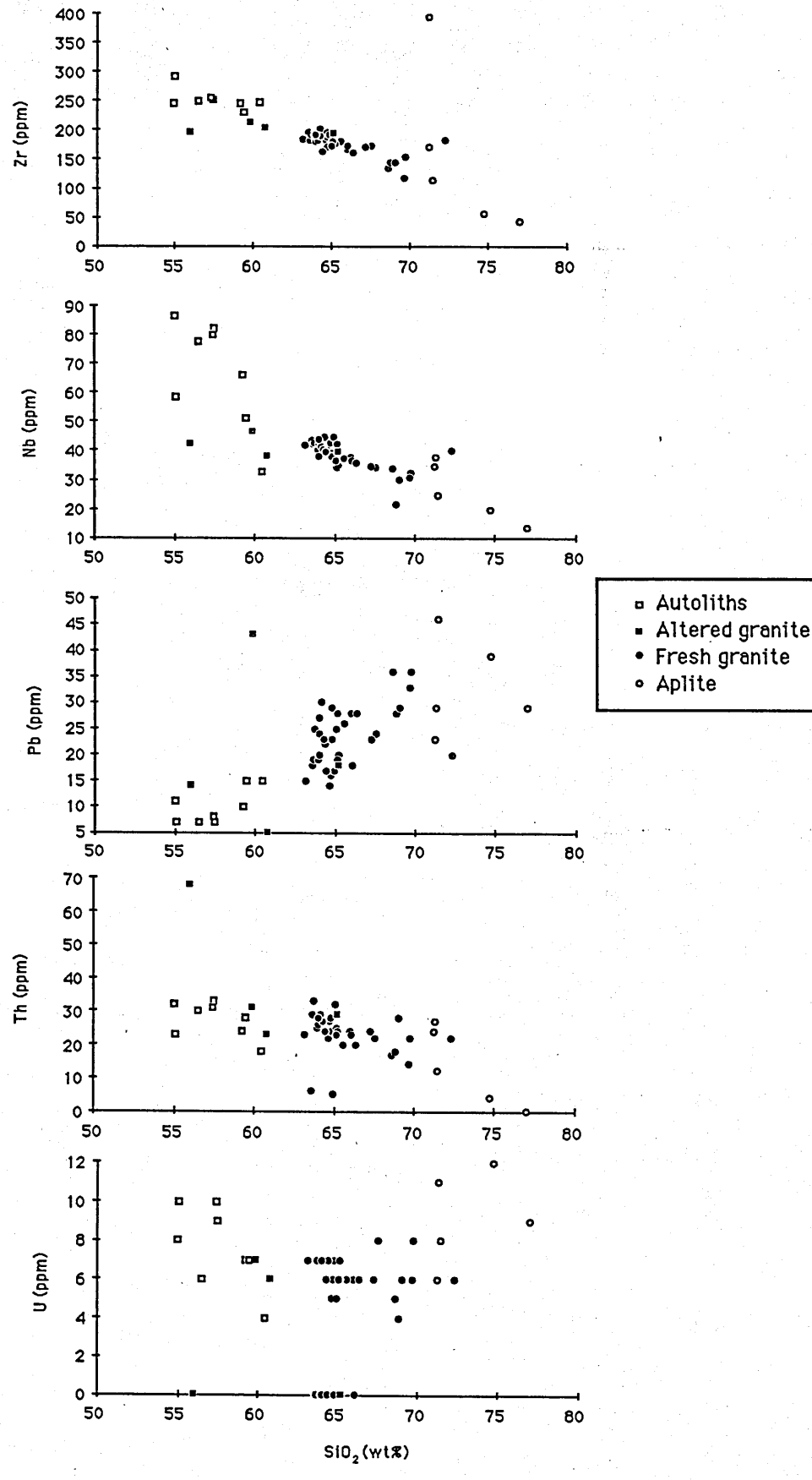

Figure 5.12 Cont.

Harker diagrams for MAG trace element data

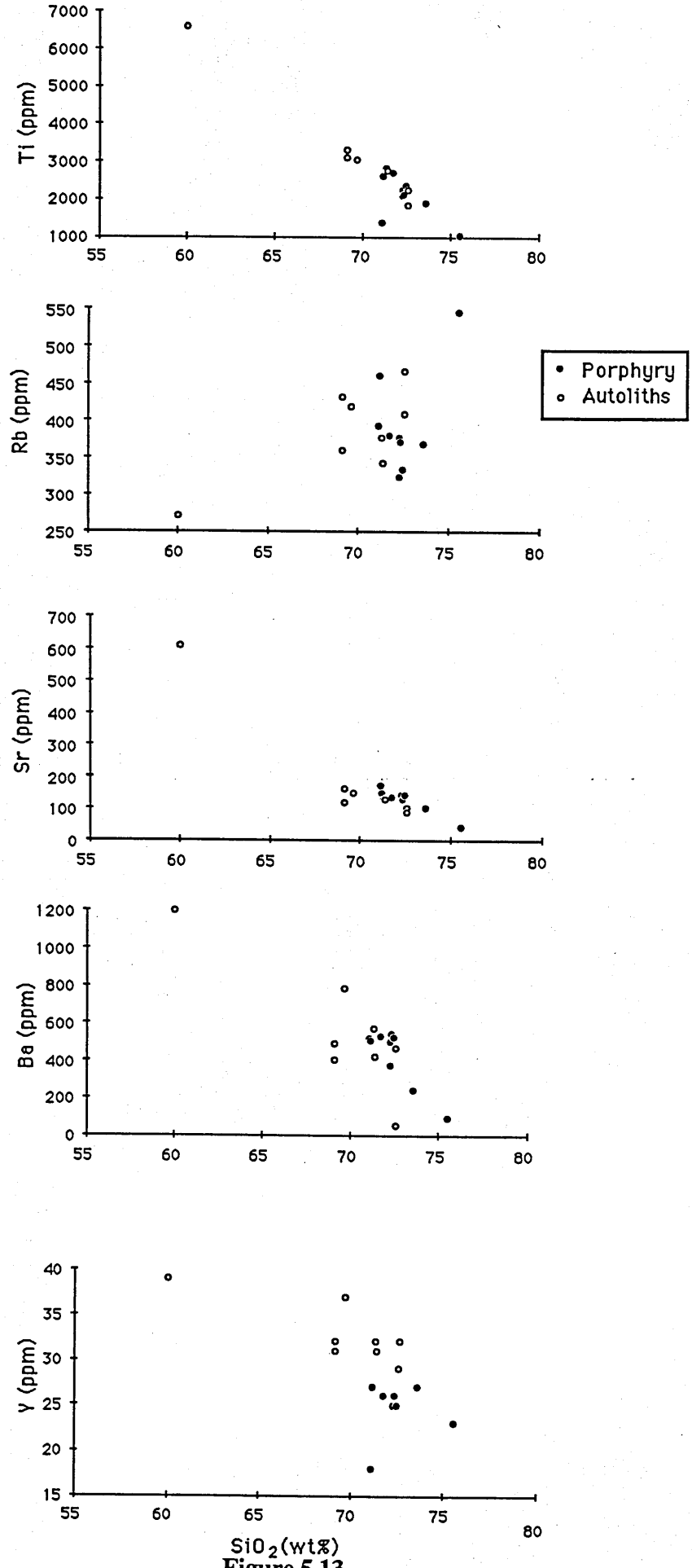

Figure 5.13

Variation diagrams for MVGP trace element data

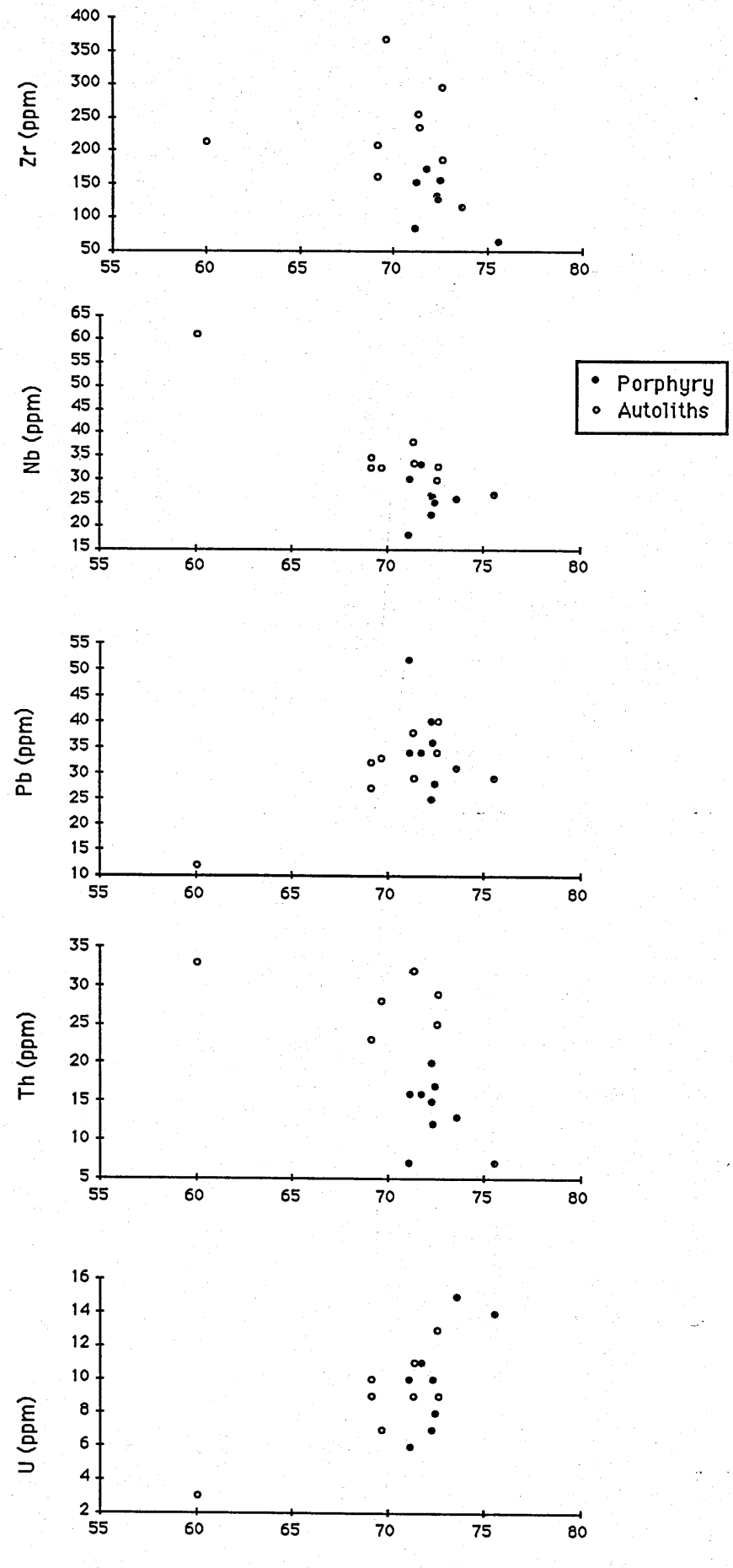

Figure 5.13 Cont.
Variation diagrams for MVGP trace element data

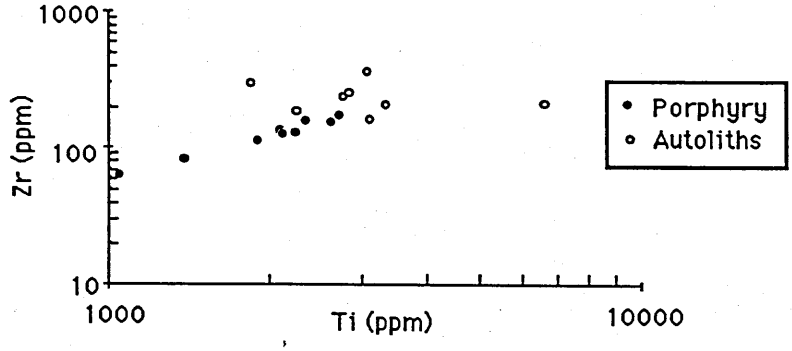

Figure 5.13 Cont.
Variation diagrams for MVGP trace element data

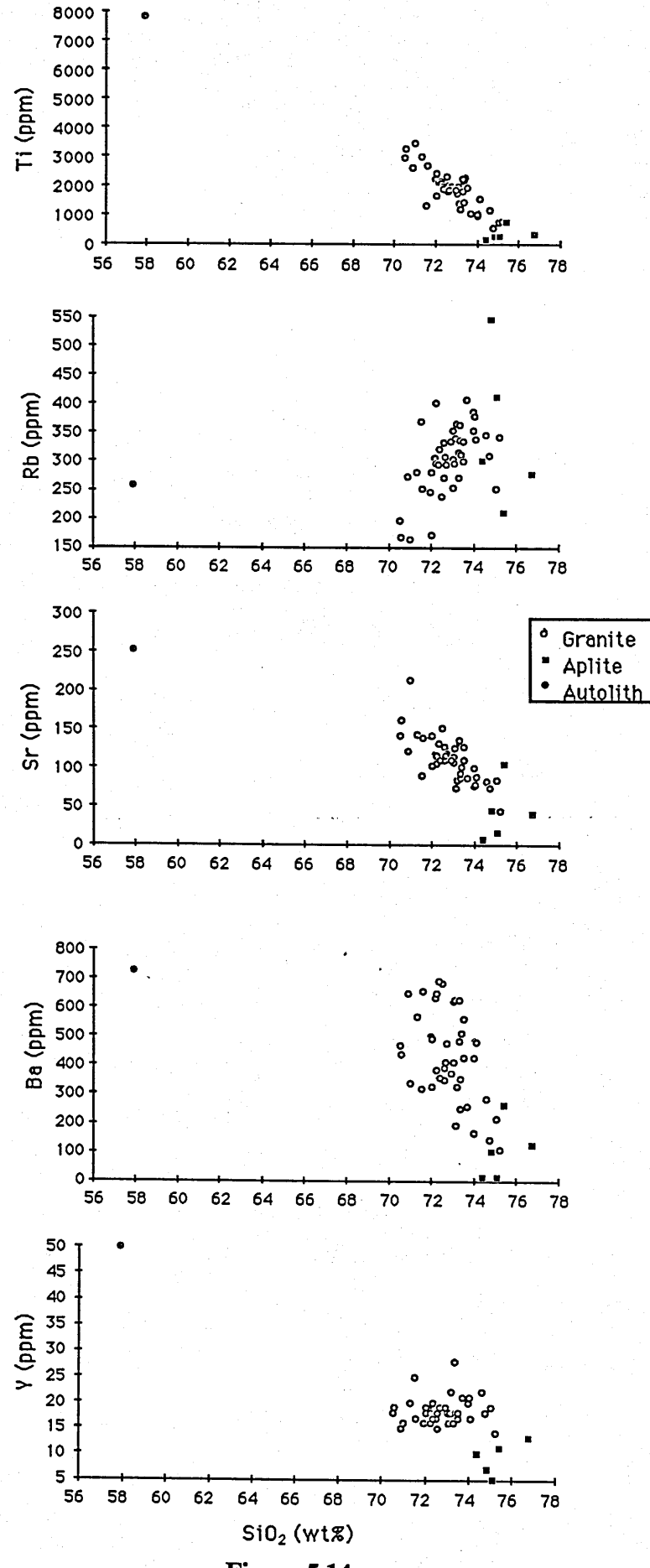

Figure 5.14

Harker diagram for CG trace element data

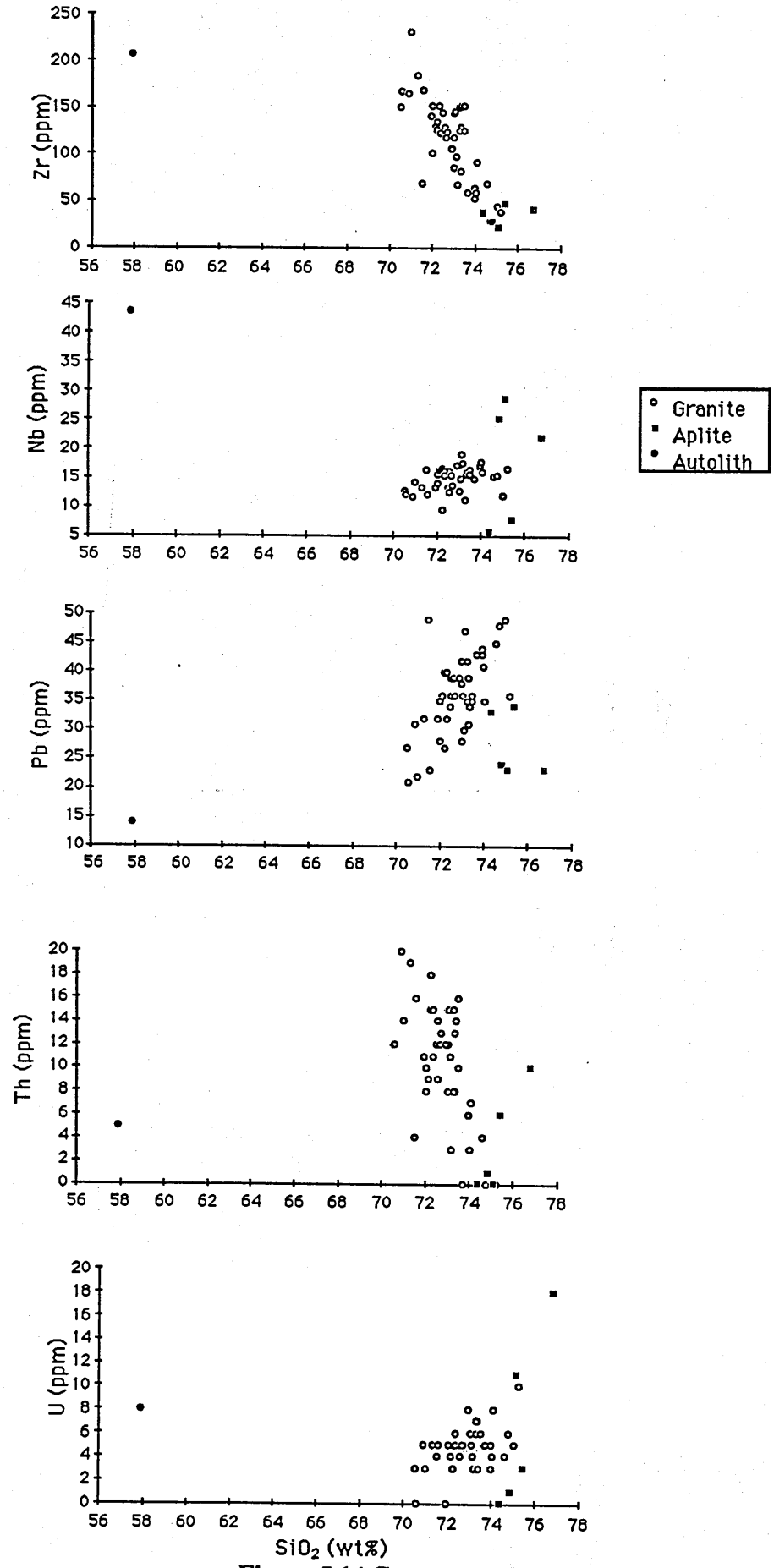

Figure 5.14 Cont.

Harker diagram for CG trace element data

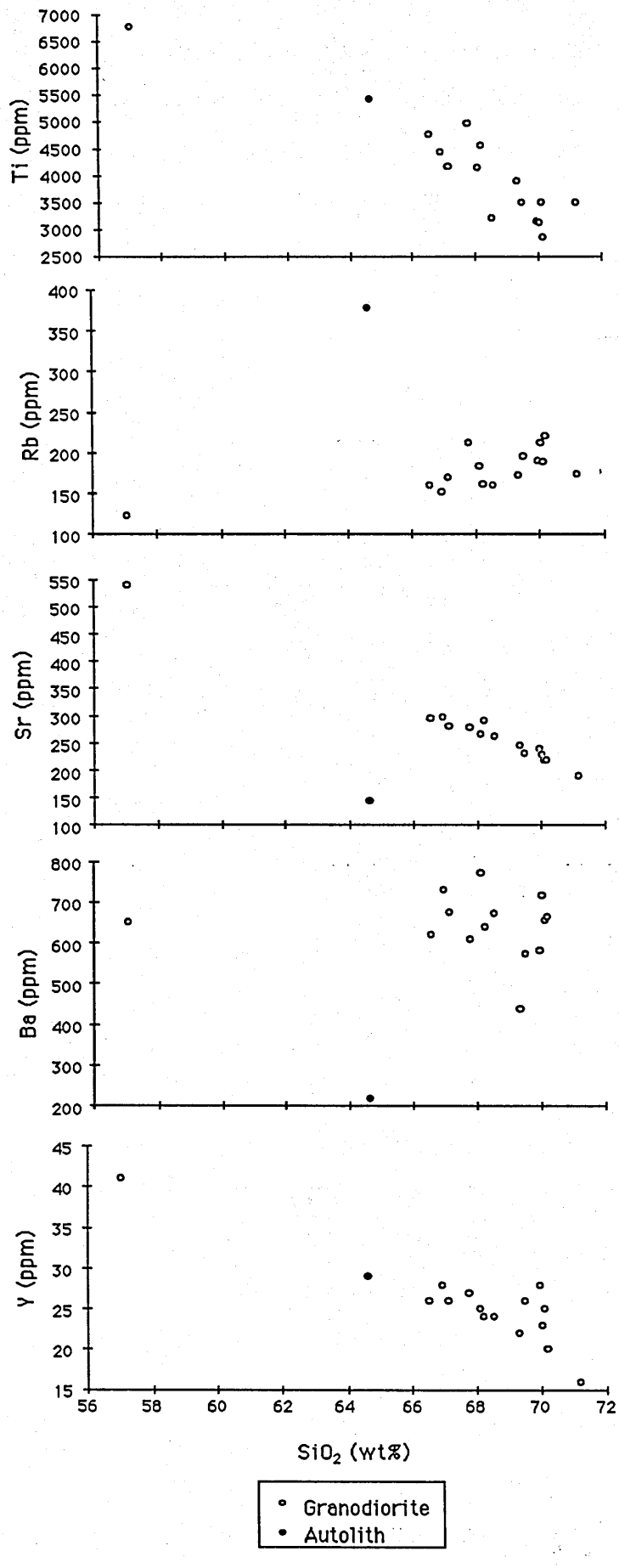

Figure 5.15

Harker diagram for AG trace element data

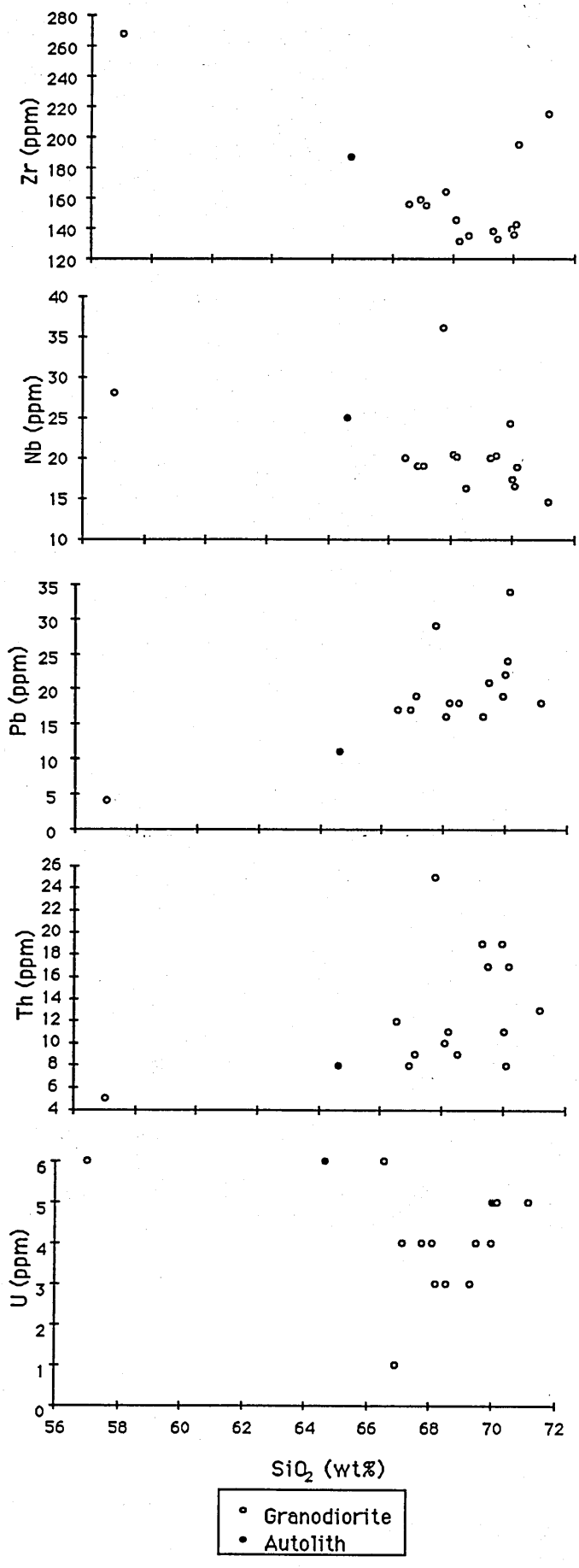

Figure 5.15 Cont.

Harker diagram for AG trace element data

from the autolith (see sections 3.6 and 5.5). This supports the idea that the autoliths are not simple cumulates of the granite but have interacted with the host magma; see section 5.5 for further discussion. The four heavily altered samples display deviations away from the trends of the fresh granite for all the elements except Zr, which, being hosted in zircon will be highly resistant to alteration (Webb *et al.*,1985).

The low mobility of Ti and Zr during alteration Webb *et al.* (1985) implies plots of log Zr vs. log Ti will preserve original magmatic trends in altered rocks. Such a plot for the MVGP (Figure 5.13) indicates that all the porphyry samples are cogenetic but that the autoliths are not related to the porphyry by simple fractional crystallization, see section 5.5 for further discussion. The MVGP data display high degrees of scatter for the majority of the elements on SiO_2 Harker diagrams, only Ti and Sr appear to display good fractionation trends. The autolith samples, except one have only slightly lower SiO_2 values than the host granite and in general have higher trace element concentrations. The sample B86/24 is significantly less felsic but has trace element concentrations compatible with the rest of the suite. The scattered trace element geochemistry is reminiscent of the scattered major element chemistry (section 5.2.1) and the petrographic evidence for element mobility in the MVGP (section 3.3.3 iii).

The CG data like the MAG data display good magmatic trends for the more immobile elements such as Ti and Zr. The LILE also show magmatic trends with a little more scatter due to their less immobile nature. Only Rb, Pb, and possibly U display incompatible behaviour. The single autolith lies off an extrapolation of the granite trend and cannot be a direct cumulate or primitive member of the fractionation suite, more likely it is the residue left after a melt has been extracted, see sections 3.6 and 5.5. The aplites display continuity with the granite samples for Ti, Sr, Ba and Zr, but lie off the fractionation trend for the other elements.

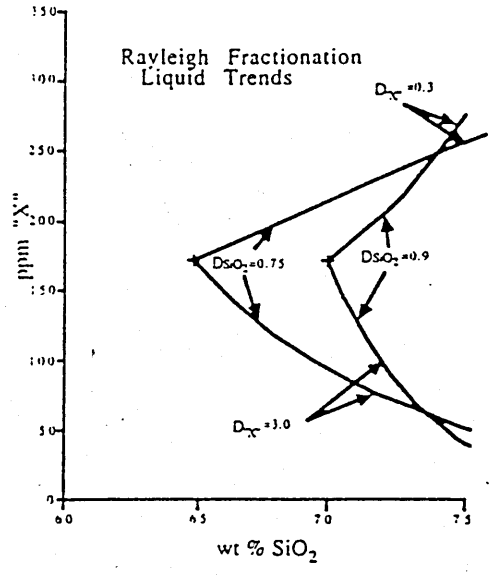

Figure 5.16

Calculated trends on a Harker diagram for the fractional crystallization of an incompatible element (D=0.3) and a compatible element (D=3) for two apparent distribution coefficients of silica (D=0.75 and 0.9) (after Wall *et al.*, 1987).

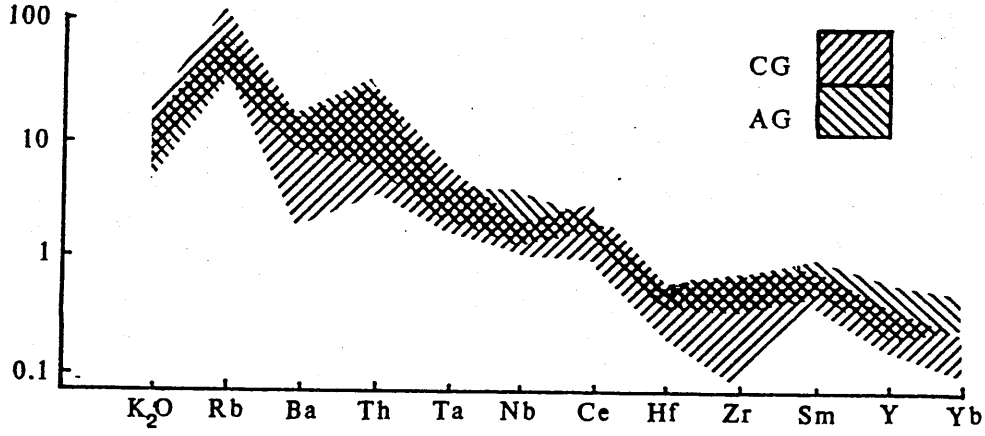

Figure 5.17

Multi-element ocean ridge granite normalized (ORG) plots for the CG and AG (after Pearce *et al.* ,1984).

The AG data like that of the MAG and CG display good fractionation trends for certain elements (Ti, Sr, Y, and Zr). A single sample (B86/85) has 10% less SiO_2 than the next most primitive sample but has a trace element character commensurate with it being part of the fractionation suite. The single autolith lies within the SiO_2 range of the host granite but lies off several of the fractionation trends indicating that like the other autoliths of the MAG, MVGP, and CG it is not simply related to the host granodiorite but rather may be the residue after melt extraction, see sections 3.6 and 5.5.

5.3.2 Comparative trace element plots

The main uses of trace elements in granitic studies (and any other igneous suite) are two fold; to model the observed evolution of the suite by coherent processes and to identify the source and method of melt production of the granitoid.

Figures 5.17 and 5.18 display the trace element characteristics of the four facies under study in terms of ocean ridge granite normalized diagrams (normalizing values from Pearce *et al.*, 1984).

The Sorata granitoids display a high degree of overlap in their geochemical characteristics. The CG displays a wider range of values due to it's more extensive evolutionary range. The AG is significantly more enriched in the HFSE and HREE (Ta, Nb, Y, Yb).

The Tres Cruses granites display more divergent diagrams, partially as a result of the MVGP being significantly more evolved than the MAG, the negative Ba and positive Rb anomalies reflecting feldspar fractionation; but also probably reflecting meaningful source differences.

The significance of these differences are investigated below but it should be noted that the patterns do show a high degree of similarity and the trace element variations being studied are fine scale features.

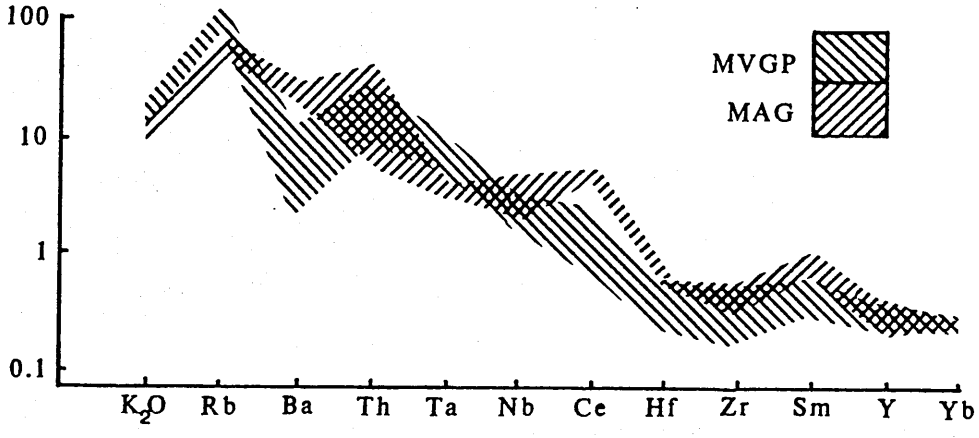

Figure 5.18

Multi-element ocean ridge granite normalized (ORG) plots for the MAG and MVGP (after Pearce *et al.*,1984).

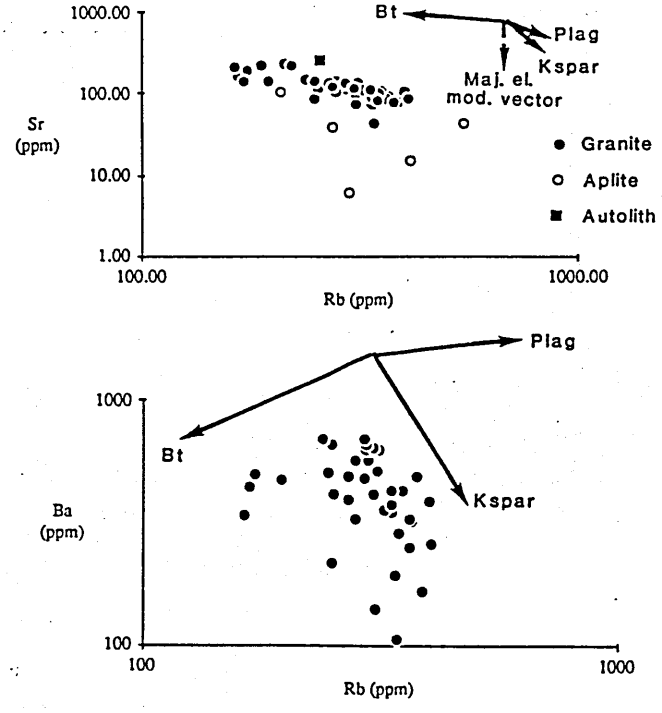

Figure 5.19

Log Rb vs. log Sr and log Rb vs. log Ba plots for the CG, calculated vectors for Rayleigh fractionation of the three LILE bearing phases present are indicated (vectors are for 20% fractionation), distribution coefficients tabulated in Table 5.3. A fractionation vector of the favoured major element model is also shown.

5.3.3 LILE modelling

The LILE elements: Sr, Rb, and Ba, are usually controlled in granitic systems by the crystallization of the major silicate phases; dominantly plagioclase, alkali feldspar, and biotite. These elements have therefore been used in the past to model the evolution of granitic melts (McCarthy and Hasty, 1976; McCarthy and Groves, 1979; Tindle and Pearce, 1981).

In the following section the LILE are used to model the evolution of the granitic melt in terms of assemblages of these phases. In the following modelling, it is assumed that the system evolved by perfect Rayleigh fractional crystallization, although the discussion in section 5.3 shows this can only be an approximation to the truth. The Rayleigh fractionation crystallization equation is as follows:

$$C = C_0 F^{(D-1)} \quad \text{.....Equation 5.1}$$

Where C is the concentration of the element in the final liquid

C_0 is the concentration of the element in the initial liquid

F is the weight fraction of liquid remaining

D is the bulk distribution coefficient of the element

Figures 5.19 to 5.21 show plots of Rb vs. Sr and Rb vs. Ba for the CG, AG, and MAG (the data for the MVGP are too scattered to allow modelling, see section 5.3.1). Superimposed on the diagrams are vectors for the Rayleigh fractionation of the three LILE bearing phases. The accuracy of the model relies on the accuracy of the distribution coefficients used (tabulated in Table 5.3). As noted in section 5.3 distribution coefficients in granitic melts can change considerably with melt composition; this, coupled with the assumption of simple Rayleigh fractionation, introduces large errors into the modelling and makes it suitable for assessing general trends only. The trends appear to be dominated by feldspar, Rb behaving incompatibly and Sr and Ba compatibly.

A vector for the assemblage calculated by major element modelling in section

5.2.3 is also shown in Figures 5.19 to 5.21. It is clear from the diagrams that the major element models do not fit the trace element data for any of the plutons. The cause of the discrepancy is thought to be the large quantity of biotite in the major element models (14 to 30%).

5.3.4 Calculation of trace element bulk distribution coefficients

It has been assumed above that Rayleigh fractionation is the most likely simple model to explain the observed trace element variations. Allegre *et al.*(1977) showed that the Rayleigh fractionation equation could be solved to give the bulk distribution coefficient of a compatible, or mildly incompatible element, if at least one element behaved highly incompatibly.

Assuming the basic Rayleigh equation, equation 5.1:

$$C = C_o F^{(D-1)}$$

For a highly incompatible element (hygromagmatophile element of Allegre *et al.*,1977) D « 1 therefore D-1 ≈ -1 and the Rayleigh equation simplifies to:

$$C^H = C^H_o F^{(D-1)} \approx C^H = C^H_o / F$$

$$\text{or } F = C^H_o / C^H$$

Where: C^H_o is the initial concentration of the hygromagmatophile element

C^H is the final concentration of the hygromagmatophile element

This can be substituted back for F into the Rayleigh equation, allowing it to be solved for a less incompatible element:

$$C = C_o (C^H_o / C^H)^{(D-1)}$$

$$\text{Log } C = \text{Log } C_o + (D-1) \text{ Log } (C^H_o / C^H)$$

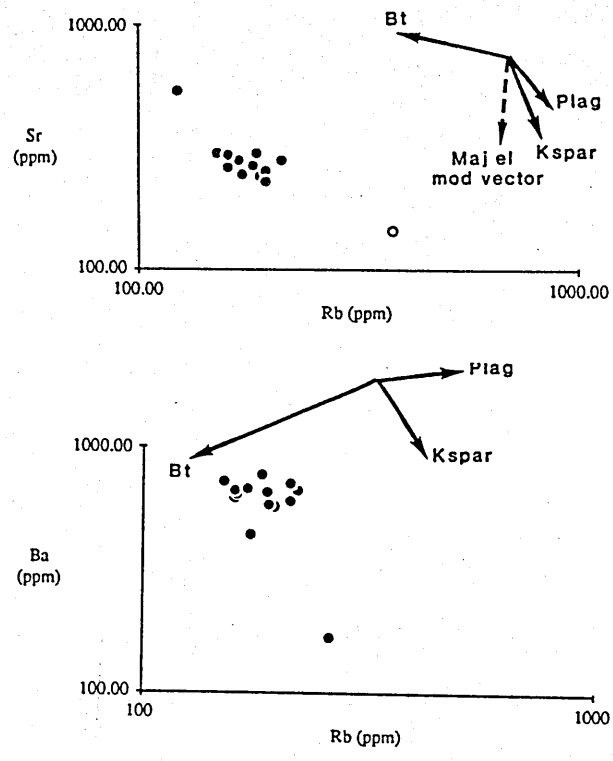

Figure 5.20

Log Rb vs. log Sr and log Rb vs. log Ba plots for the AG, calculated vectors for Rayleigh fractionation of the three LILE bearing phases present are indicated (vectors are for 20% fractionation), distribution coefficients tabulated in Table 5.3. A fractionation vector of the favoured major element model is also shown.

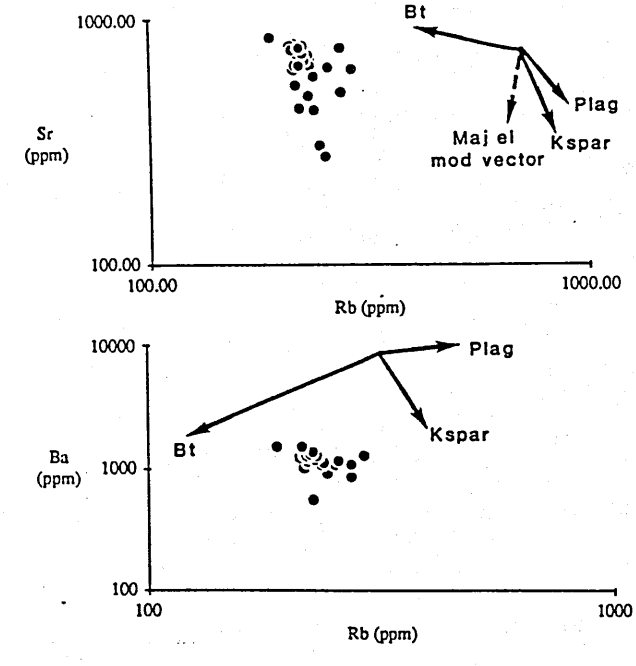

Figure 5.21

Log Rb vs. log Sr and log Rb vs. log Ba plots for the MAG, calculated vectors for Rayleigh fractionation of the three LILE bearing phases present are indicated (vectors are for 20% fractionation), distribution coefficients tabulated in Table 5.3. A fractionation vector of the favoured major element model is also shown.

	Plag	Kspar	Bt
Rb	0.09	0.38	3.5
Sr	6	9.4	0.36
Ba	0.5	6.6	6.5

Table 5.3
Distribution coefficients used in LILE modelling of the CG, AG, and MAG, Figures 19 to 21 (after Henderson, 1982).

$$\text{Log } C = \text{Log } C_o + (D-1) \text{ Log } C^H_o - (D-1) \text{ Log } C^H \text{.....Equation 5.2}$$

Equation 5.2 is in the form of a straight line, with gradient (1-D) and has been used to calculate the bulk distribution coefficient of a range of trace elements for the MAG, AG and CG. A regression line was fitted to a plot of a highly incompatible element (e.g. Ta, Pb, Th) vs. the element of unknown bulk distribution coefficient. The gradient and a correlation coefficient between 0 (no fit) and 1 (perfect fit) were calculated; the results are given in Table 5.4.

The major problem with this technique, is the lack of a trace element which is highly incompatible and a good fractionation index. The error introduced due to the assumption of total incompatibility of a highly incompatible element is quantified in Figure 5.22. The approximation always causes an under-estimation of the volume of residual liquid (F) and so an over-estimation of the calculated bulk distribution coefficient. However, the major source of error is usually the poor fit of the regression line.

Only Pb was sufficiently incompatible in the MAG to be used. The low correlation coefficients of many of the elements (values < 0.7) indicate that the results are only semi-quantitative.

Two sets of data are shown for the AG, based on Th and Ta as the highly incompatible elements. The negative bulk distribution coefficient for Ta in the Th model indicates that Ta is more incompatible than Th. The high correlation of Th with Ta, the middle and heavy REE suggests that they are controlled by the same minor phase, possibly zircon or xenotime, although this phase was not identified in the facies (section 3.4.2 iii). Ta is also strongly correlated to Ti, Y, Rb, and Sr suggesting control by sphene and the coincidental covariation of the feldspars with this minor phase. This is also reflected in the high correlation of Th and Ta for Eu.

The model for the CG is based on Ta as the highly incompatible element. None of the correlation coefficients are high indicating that the majority of the data are only

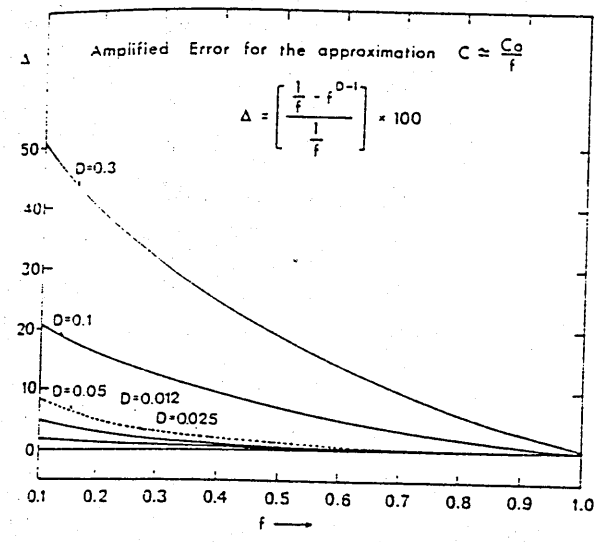

Figure 5.22

Error introduced by the approximation $C=C_o/F$ as a function of D and F (after Allegre *et al.*, 1977).

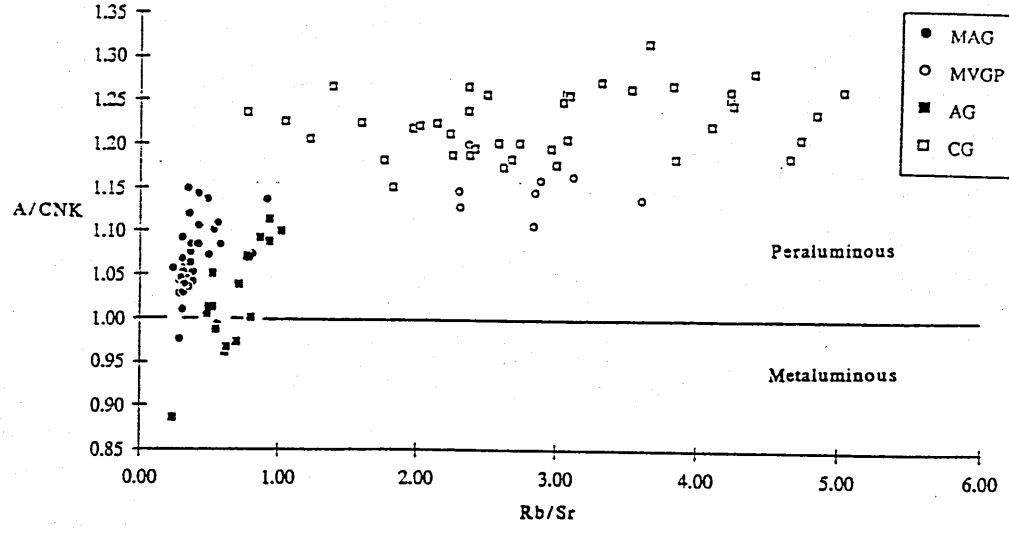

Figure 5.23

Shand index vs. Rb/Sr. The CG and MVGP display high Rb/Sr values and are strongly peraluminous, indicating a metasedimentary origin. The MAG and AG are weakly peraluminous to metaluminous and have low Rb/Sr suggesting a non upper crustal origin.

	CG				AG				MAG	
Trace el.	D on Ta	Fit Index	D on Pb	Fit Index	D on Ta	Fit Index	D on Th	Fit Index	D on Pb	Fit Index
Ti	2.89	0.25	3.35	0.91	1.61	1	1.61	0.5	1.19	0.61
Rb	0.34	0.58	0.18	0.38	0.55	0.94	0.55	0.8	0.83	0.3
Sr	2.11	0.29	2.38	0.83	1.54	1	1.55	0.53	1.41	0.67
Y	0.88	0.29	0.85	0.97	0.82	0.98	0.82	0.02	1.06	0.29
Hf	2.55	0.3	2.94	0.72	1.27	0.47	1.28	0.03	1.18	0.78
Zr	3.13	0.39	3.66	0.72	0.97	0.09	0.97	0.04	1.04	0.64
Nb	0.97	0.69	0.9	0.95	0.99	0.18	0.99	0.78	1.23	0.64
Ta	-	-	-0.25	0.79	-	-	-0.01	0.87	0.91	0.15
Pb	0.2	0.4	-	-	0.65	0.7	0.65	0.61	-	-
Th	-	-	-	-	0.1	0.87	-	-	1.14	0.02
U	0.29	0.2	0.11	0.96	0.34	0.76	0.34	0.38	0.74	0.22
La	3.08	0.77	3.59	0.37	0.98	0.03	0.98	0.52	1.18	0.83
Ce	2.95	0.74	3.43	0.05	0.93	0.76	0.93	0.34	1.16	0.81
Nd	2.8	0.69	3.24	0.6	0.63	0.89	0.62	1	1.05	0.74
Sm	2.31	0.59	2.64	0.83	0.66	0.98	0.65	0.96	1.04	0.72
Eu	2.02	0.69	2.27	0.6	1.26	0.99	1.27	1	1.13	0.8
Gd	2.64	0.22	3.05	0.86	1.21	0.02	1.21	0.48	1.26	0.99
Tb	1.88	0.08	2.1	1	0.72	0.98	0.72	0.94	1.05	0.77
Yb	0.86	0.33	0.83	1	0.65	1	0.88	0.88	0.99	0.78
Lu	0.96	0.75	0.95	1	0.82	0.87	1	1	0.99	0.75

Table 5.4

Results of distribution coefficient modelling based on method of Allegre *et al.* (1977). The accuracy of modelled value is estimated by the fit coefficient of the element data and the highly incompatible element on which the model is based; a high coefficient implies a good correlation and *vice versa.* Negative model distribution coefficients imply greater incompatibility than the highly incompatible element on

semi-quantitative.

Using the concentrations of the most incompatible element in the most and least evolved sample of each suite allows the degree of fractionation to be approximated. For the MAG the suite appears to span 60% crystallization, for the AG 35% based on Ta and 40% based on Th and for the CG 60%. The assumption of total incompatibility will make these values underestimates. The high values for the CG and the MAG suggest that the magmas were emplaced totally liquid as 40-60% is the upper limit placed on the volume of crystals a magma may contain and still behave as a fluid (Wickham, 1987); the lower degree of fractionation observed in the AG suggests that it may have been emplaced containing entrained crystals.

5.4 Petrogenesis

The use of geochemical and isotopic characteristics to classify granites is well established in the literature (Peacock, 1931; Shand, 1951; Chappell and White, 1974; Pearce *et al.*,1984; Harris *et al.*, 1986). This section attempts to identify some of the reasons for the success of these classifications, to identify the sources of the granitoids in the Cordillera Real, and to model the origins of the granitoids under investigation.

5.4.1 Probable source regions

The major distinction between granitoids containing a mantle component and those derived purely from sedimentary rocks can be made on a number of geochemical and isotopic criteria discussed below. The distinction between mature and immature sedimentary sources and the method of mantle component incorporation are less easily made.

One of the commonest sources of granitoids proposed is mature sedimentary material, which has been shown to display certain distinctive geochemical features (Chappell and White, 1974; Arth and Hanson, 1975; Miller, 1986). After the influential S-type and I-type classification of Chappell and White (*op cit.*), high degrees of peraluminosity have been commonly used as a distinctive feature of granitoids derived from sedimentary sources. The basis for this discrimination is that sedimentary processes quickly remove Ca and Na from a sediment to leave it preferentially enriched in Al (Chappell and White, *op cit.*). Miller (1985) has noted that strongly peraluminous melts can be produced by melting of sources other than pelite. Immature sediments of metaluminous to mildly peraluminous character can be melted to produce strongly peraluminous melts (Miller and Stoddard, 1980). Also, the experimental work of Kushiro and Yoder, (1972) has shown that anatexis of a peridotite at P_{H_2O} = 10 kbar and T = 1025 °C can produce peraluminous melts. The anatexis of mafic rocks can also produce peraluminous melts (Stern and Wyllie, 1978; Helz, 1976). Helz (1976) has shown that peraluminous quartz normative melts can be produced from basalts of tholeiitic, olivine tholeiitic and alkalic character at lower crustal pressures (P_{H_2O} = 5 kbar). Within the hornblende stability field the composition of the melts are quartzo-feldspathic and insensitive to the composition of the basalt; the TiO_2, FeO and MgO content of the melt increases abruptly on the breakdown of hornblende.

Zen (1986) pointed out that the fractional crystallization of a strongly metaluminous assemblage (e.g. hornblende dominated) from a metaluminous melt can also produce peraluminous granites.

It is clear therefore that high degrees of peraluminosity are not necessarily indicative of pelitic sources. However, large volumes of strongly peraluminous granites, not related to less evolved metaluminous rocks, are believed to be the product of melting pre-existing crustal rocks of weakly metaluminous to per-

aluminous character; including pelites, greywackes, and pre-existing metaluminous and peraluminous granites.

The trace elemental behaviour of Sr changes from incompatible to compatible at the mantle-crust boundary due to the stabilization of feldspar (Ellam and Hawkesworth, in prep.). Sedimentary processes also generally increase the Rb/Sr ratio due to high mobility of Sr in aqueous systems (Goldstein, 1987). The upper crust and upper crustal melts are therefore characterized by high Rb/Sr ratios, while granites derived from mantle melts can be expected to have significantly lower Rb/Sr ratios.

Figure 5.23 shows a plot of Shand index vs. Rb/Sr for the MAG, MVGP, CG, AG, and the IG. A clear division of the data fields into two groups can be made: a high Rb/Sr, high Shand index (strongly peraluminous) group: the CG and MVGP; and a low Rb/Sr, moderate to low Shand index (mildly peraluminous to metaluminous) group; the MAG, AG, and the IG. The low Rb/Sr ratio of the MAG is primarily the product of the high Sr contents of the samples (Figure 5.26) which suggests a feldspar free residue. This division can also be made on the basis of εSr data, Figure 5.24, (see section 6.3 for further discussion), indicating that the high Rb/Sr samples are derived from high time integrated Rb/Sr sources.

Miller (1986) noted that pelites have Rb/Ba ratios greater than average crust. Melting involving residual feldspar or biotite will enhance the Rb/Ba ratio of the melt; ratios of significantly greater than 0.25 can be expected from pelitic sources. Figure 5.25 shows a plot of Rb/Ba vs Rb/Sr. The high correlation of the data reflects both Rb being the numerator in both the abscissa and ordinate, and the increase in both the ratios with fractionation. The range of values for the MVGP and the CG indicate that they were derived from a high Rb/Ba source, arguably pelitic in character. The low Rb/Ba ratio of the MAG and AG reflects their high Ba contents which in the case of the MAG may in part be the product of a feldspar free residue as postulated above.

Based on the results of the better characterized plutons from the Cordillera Real,

the trace element characteristics for the other plutons sampled can be tentatively interpreted in terms of source regions. Figure 5.26 shows a plot of Rb vs. Sr for all of the plutons of the Cordillera Real sampled. The HPG and UG display a wide range of Rb/Sr ratios with values within the range of the MAG and AG plutons suggesting a similar character. The SG and CKG have uniformly low Rb/Sr ratios similar to the CG and MVGP, suggesting a similar crustal origin.

In summary the MVGP and CG are believed to have been derived from pre-existing high Rb/Sr, peraluminous crustal rocks, probably metapelites or pre-existing granites; the SG and CKG were probably derived from a similar source. The MAG and AG display major and trace element characteristics incompatible with a sedimentary source and are believed either to contain a significant component of juvenile mantle material or to have been derived from basic to intermediate igneous material. The distinction between these two origins is best made on the basis of Nd model ages and is addressed in Chapter 7. The IG and HPG are believed to have been derived from a similar source.

5.4.2 Discriminant diagrams

The discriminant diagrams of Pearce *et al.* (1984) and Harris *et al.* (1986) were an attempt to use the trace element geochemistry of granitoids from known tectonic setting to define discriminant geochemical diagrams, which can then be used to identify the tectonic setting of other granitoids. This approach is best applied to granitoids which contain a mantle component. It is not coincidental that many of the criteria for the tectonic settings of granites are the same as those used by Pearce and Norry (1979) to identify the mantle source of basalts. The inherent weakness of this style of discrimination when applied to granites derived from crustal sources, is that, the geochemistry of these granites is controlled by their source and liquid evolution, rather than their tectonic setting. The tectonic environment in which the granitoids

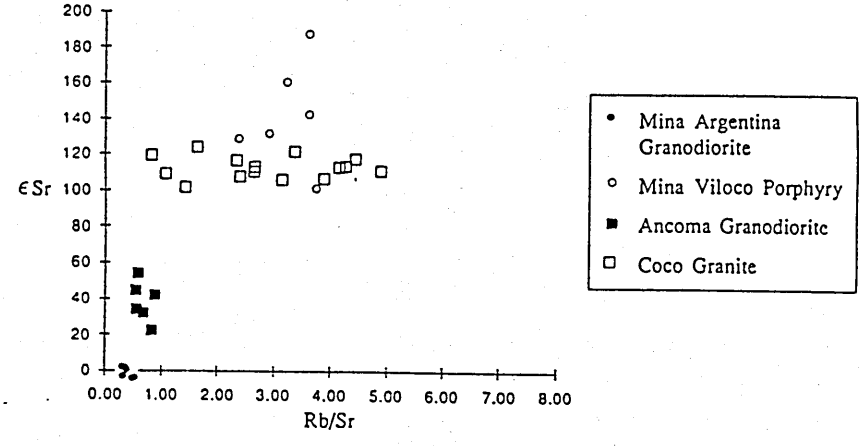

Figure 5.24

εSr vs. Rb/Sr. The CG and MVGP display high Rb/Sr and εSr values indicative of a metasedimentary source. The MAG and AG display low εSr and Rb/Sr values indicating a low time integrated Rb/Sr source.

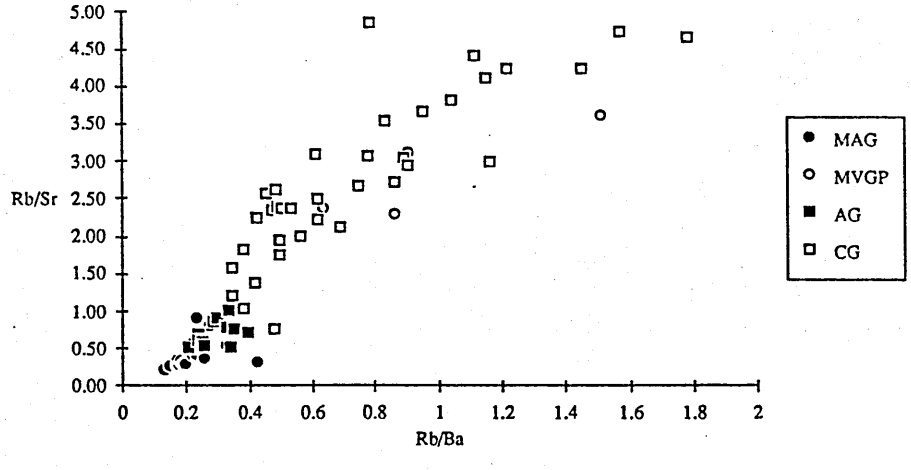

Figure 5.25

Rb/Ba vs. Rb/Sr. The high degree of correlation reflects the effects of fractionation of feldspars which control all three elements. Both the CG and MVGP display high values of Rb/Ba, a characteristic of pelites and their melts (Miller,1986).

form primarily controls the source of heat and water which cause melting to occur, rather than the actual source of the melt, although the two may be indirectly linked. Noting these limitations Figure 5.27 and 5.28 show discriminant diagrams for the granitoids of the Cordillera Real.

The four main plutons of this study are shown in Figure 5.27. The MVGP and the majority of CG data fall in the collisional granite field (redefined by Harris *et al.* (in press) as the upper crustal melt field) and the majority of the MAG and AG fall in the within plate and volcanic arc fields respectively. The split between crustally derived and mantle related granites noted above is corroborated by this classification. The division between the type of mantle component in the MAG and the AG is thought to be significant.

The other plutons of the Cordillera have been plotted in Figure 5.28. The correlation between the CKG, SG and the CG and MVGP is supported by the diagram in that the majority of the relevant data fall in the upper crustal melt granite field.. The majority of the IG, HPG, and UG data plot in the volcanic arc and within plate fields supporting their similarity to the MAG and AG in containing a mantle component.

The discriminant diagrams therefore support the conclusions of section 5.4.1 and further, indicate a difference in the mantle component of the AG and MAG.

5.4.3 Crustal melt modelling for the Coco Granite and Mina Viloco Granite Porphyry

It has been shown in section 5.4.1 and 5.4.2 that the CG and MVGP were probably derived from mature crustal sources. The high Rb/Ba values suggest a pelitic source. Assuming an individual sample, here the least evolved member of each group (B85/193 from the CG and B85/155A from the MVGP), represents the composition of a melt and ignoring the complications of entrained crystals already discussed in sections 5.2.2. The production of the melt from a pelitic source can be

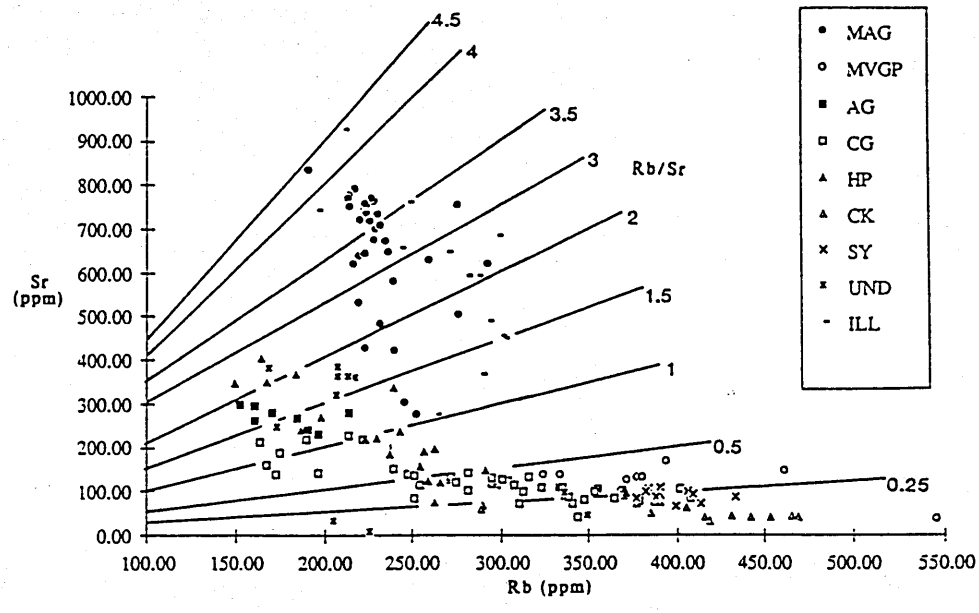

Figure 5.26

Rb vs. Sr plot, with Rb/Sr isopleths.

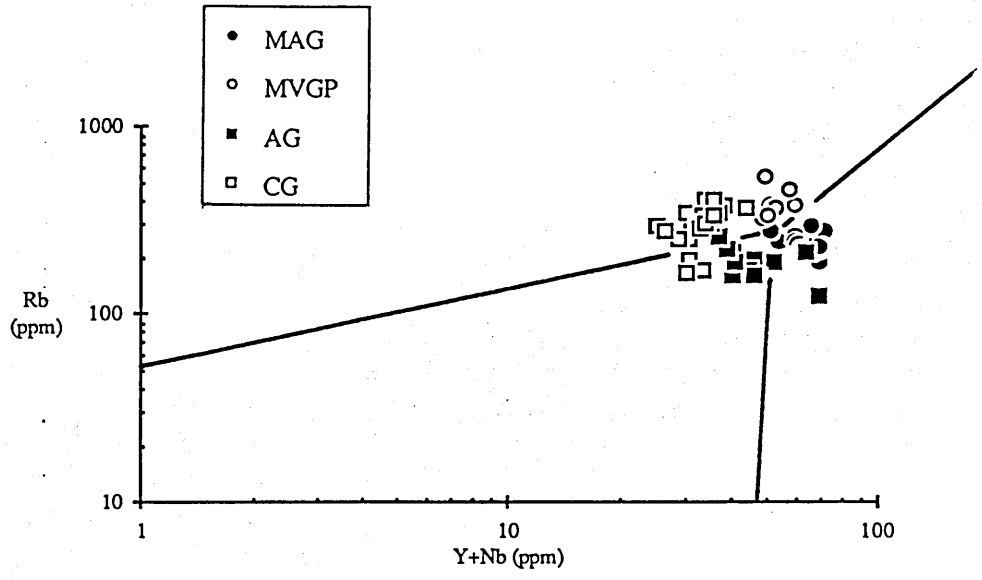

Figure 5.27

Discriminant diagram of Y+Nb vs. Rb for the four main plutons of this study (after Pearce *et al.*, 1984).

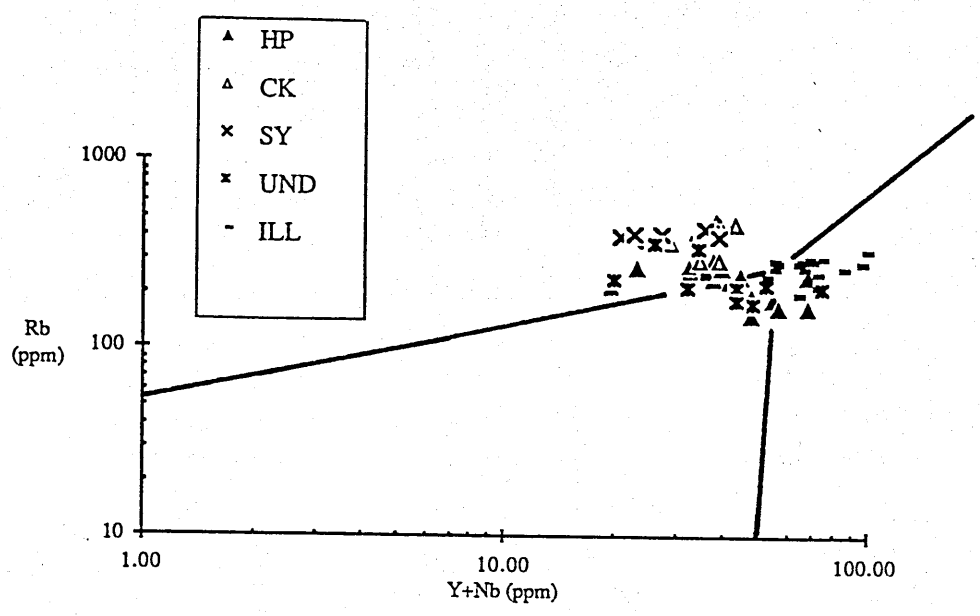

Figure 5.28

Discriminant diagram of Y+Nb vs. Rb for the five subsidiary plutons of this study (after Pearce *et al.*, 1984).

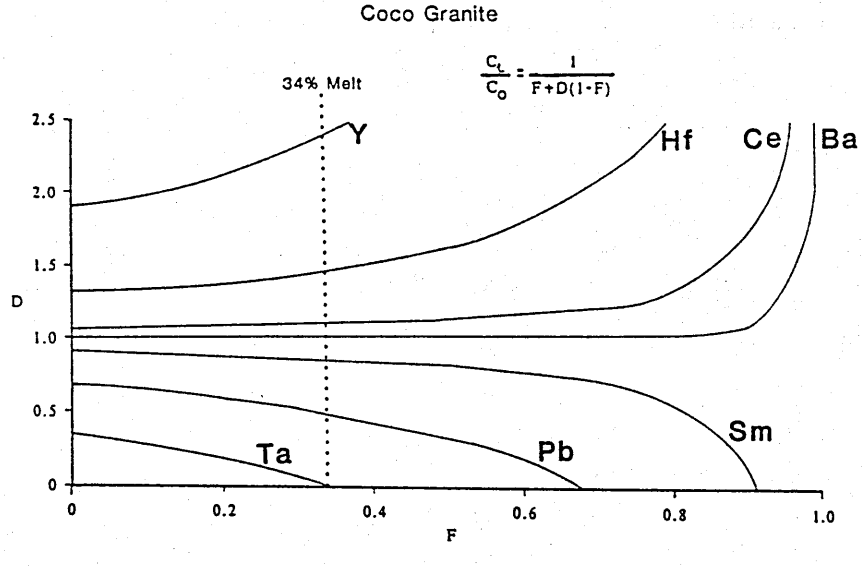

Figure 5.29

Bulk distribution coefficient (D) vs. Liquid weight fraction (F), for B85/193 of CG modelled as a melt of a pelite of presumed composition (after Taylor and McLennan, 1985). The maximum melt fraction is constrained by the necessity for D to be positive for all elements, this value is taken as the true melt fraction and the bulk distribution coefficients calculated accordingly and plotted in Figure 5.30. The equilibrium batch melting equation used is also shown.

modelled. The simple batch melting equation (Figure 5.29) can be solved for the bulk distribution coefficient (D) of an element for the entire range of melt fraction (F) if the composition of the melt and the source are assumed; this is show graphically in Figure 5.29. The source is assumed as a mature metasediment (Taylor and McLennan, 1985) and samples B85/193 and B85/155A, the least evolved samples analysed, are assumed as the melt compositions for the CG and MVGP respectively. A bulk distribution coefficient of less than zero is impossible, therefore the most incompatible element, defines an upper limit on the possible melt fraction. If this value is taken as the actual melt fraction then the bulk distribution coefficients of all the trace elements can be calculated as shown in Figure 5.29.

Figure 5.30 illustrates the calculated bulk distribution coefficients for B85/193 of the CG and B85/155A of the MVGP. The high bulk distribution coefficients for Ti, Sr, Y, Zr and Hf, Nb, Th, Yb and Lu for the CG indicate a possible residual mineralogy including ilmenite, plagioclase, zircon, and xenotime; the high ratio of the bulk distribution coefficients of Nb and Ta is unusual and probably indicates that the calculated Nb bulk distribution coefficient is in error. The low bulk distribution coefficient for Rb indicates that biotite was not a major residual phase. The high bulk distribution coefficients for Ti, Sr, Ce, Eu in the MVGP indicate possible residual rutile or ilmenite, plagioclase, and possibly monazite, but the low bulk distribution coefficients for the LREE suggest the model value of the bulk distribution coefficients are too high. The low bulk distribution coefficient of Rb indicates that biotite is not a major residual phase. The errors proposed in several of the calculated bulk distribution coefficients probably result from the assumed composition of the source.

The lack of biotite in the residue supports the model of fluid absent melting proposed in section 4.4.1, where melting is initiated by the breakdown of biotite releasing water to the system.

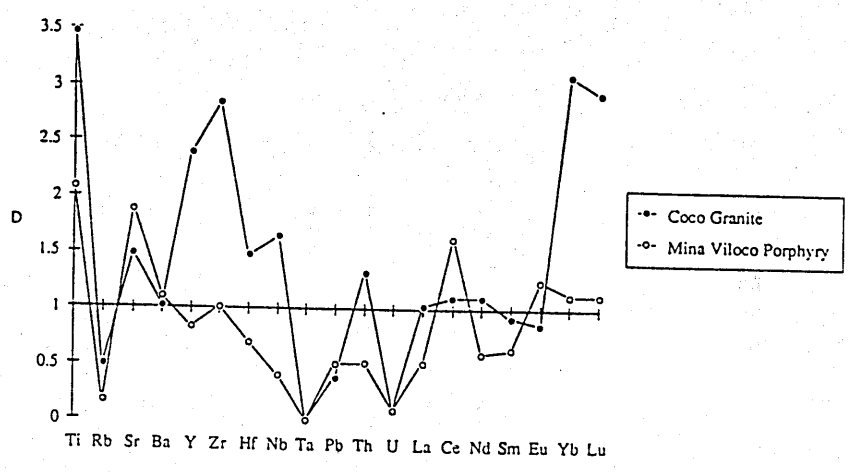

Figure 5.30

Multi-element plot for the calculated bulk distribution coefficients from Figure 5.29 for B85/93 of the CG and likewise for B85/155A of the MVGP.

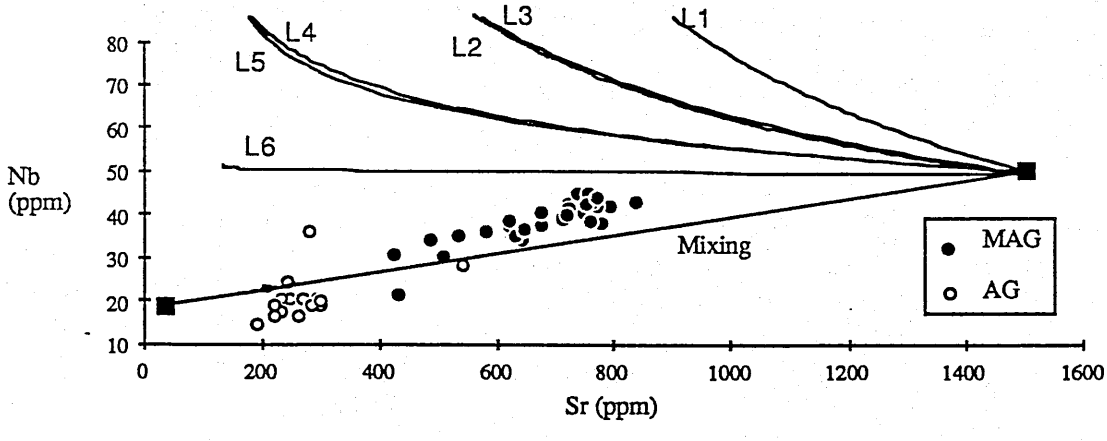

Figure 5.31

AFC and simple mixing trends for an alkali basalt and upper crust compared to the data for MAG and AG.

5.4.4. Mantle derived melts: components and mechanisms

The MAG and AG are believed to contain a significant component of mantle derived material, discriminant diagrams having identified the mantle component in the MAG to be of within plate character and that of the AG to be subduction related.

Assuming that the initial composition of the granitoids is the product of contamination of a basalt an attempt has been made to assess the method of contamination. Two styles of contamination are considered; simple mixing and assimilation and fractional crystallization (AFC). On thermal grounds AFC represents a more reasonable model since the heat energy lost by a magma assimilating hot crust will stimulate crystallization and the release of latent heat. The equation (listed below) from DePaolo (1981) has been used to model this style of evolution:

$$\frac{C_m}{C_m^o} = F^{-z} + \left[\frac{r}{r-1}\right]\frac{C_a}{zC_m^o}\left[1-F^{-z}\right]$$

Where C_m^o = initial element concentration

C_m = final element concentration

C_a = element concentration in assimilant

F = mass of magma remaining as a fraction of the mass of the original magma

r = the ratio of the rate of mass assimilation to the rate of mass crystal fractionation

z = (r+D-1)/(r-1), where D is the bulk distribution coefficient of the element

Figure 5.31 illustrates simple mixing and AFC trends for a typical within plate basalt mixing with or contaminated by typical local metapelite (values for B85/2 shown in Table 5.5). Also shown are the data sets for the MAG and AG. The lowest r value is constrained on the basis of thermal arguments. Taylor (1980) quotes specific heat

capacities of 0.25 cal $g^{-1}°C^{-1}$ for crustal rocks and average latent heat of crystallization of 100 cal g^{-1} for magma. The emplacement depth of the granitoids has been estimated at 12 to 20 km (section 4.3) implying ambient temperatures of 240 °C to 400 °C for a normal geothermal gradient. Assuming a melting temperature of 800 °C for crustal rocks (Miller, 1986; Clements and Vielzeuf, 1987), between 1.75 and 2.2 g of cumulate will provide the heat to melt 1 g of country rock; ignoring heat losses, values of between 2 and 2.5 g of cumulates are therefore considered reasonable (r values of 0.5 to 0.4). The results of the modelling (Figure 5.31) show that high values of r, around 1.5, are necessary to best model the MAG data, in contrast the AG data are best modelled by simple mixing. The high r values ($r \approx 1.5$) of the best model imply the country rock to have been significantly hotter than the 400 °C assumed; this is feasible if assimilation took place at greater depths than emplacement. The least evolved samples of the MAG are best modelled by very high r values and a magma at 50% of it's original volume (F=0.5 on Figure 5.31). The high values of r for this model imply large degrees of assimilation. For simple mixing, the extreme case where $r=\infty$, a 50% crustal component mix has 857 ppm Sr compared to the r=1.5 AFC model where for F=0.5 C_m^o=844. The primitive MAG samples are therefore approximately composed of 50% crustal component. The simple mixing model for AG indicates it to contain 90% crust, this value is based on a within plate basalt but would be insignificantly lower if a subduction related basalt were used.

In summary the trace element character of the MAG and to a lesser extent the AG can be modelled as containing a component of mantle material, probably of within plate affinities for the MAG and subduction related for the AG. The MAG data can be modelled as a basaltic mantle melt which assimilated approximately 50% upper crustal material by AFC, the high ambient temperature of the crust at the emplacement depth of the granitoids allowing high assimilation to fractionation ratios. The AG

	End Member	Sr (ppm)	Nb (ppm)
	Alkali Basalt	1500	50
	B85/2 (Crust)	71	16

Model Line	D_{Nb}	D_{Sr}	r
L1	0.2	1.5	5
L2	0.2	1.5	2
L3	0.5	1.5	5
L4	0.2	1.5	1.1
L5	0.5	1.5	1.1

Table 5.5
Compositions of end-members and variables used in AFC modelling Figure 5.31.

data is better modelled as a simple mix of mantle component and large quantities (90%) of upper crust, see section 6.4.1 for further quantification of the mantle component.

5.5 Autoliths

The origin of the autoliths and their relationship to the host granite based on petrographic studies has been discussed in section 3.5; this section investigates the geochemical relationship of the autoliths to their hosts.

The main petrographic characteristics of the autoliths are; their fine grain size, rounded outlines, and generally more mafic character than their hosts. The most likely origin for the autoliths on petrographic grounds is that they are fragments of either early formed cumulates, or of chilled margins, incorporated back into the granite and assimilated to a greater or lesser extent by the more evolved granite (section 3.5). The mafic character of the autoliths could therefore be the result of either melt extraction or mafic phase accumulation, or a combination of the two. Since the largest suite of autoliths was collected from the MAG, and this pluton has not apparently been affected by any post-magmatic processes, the following discussion therefore, is concerned primarily with the MAG autoliths.

Tindle and Pearce (1983) reported a similar group of autoliths from the Loch Doon pluton, from their work they concluded that the mafic nature of the autoliths was the result of the extraction of a minimum melt from the autolith to leave a refractory residue. Figure 5.32 shows a plot of Rb/Sr vs SiO_2 adapted from Tindle and Pearce (*op. cit.*). The trend defined by the MAG autoliths is similar to that of the Loch Doon autoliths, suggesting a similar cause for the mafic nature of the MAG autoliths. The majority of the autoliths define a linear trend of opposite slope to that of the host granite. This is believed to be the product of melt extraction since a

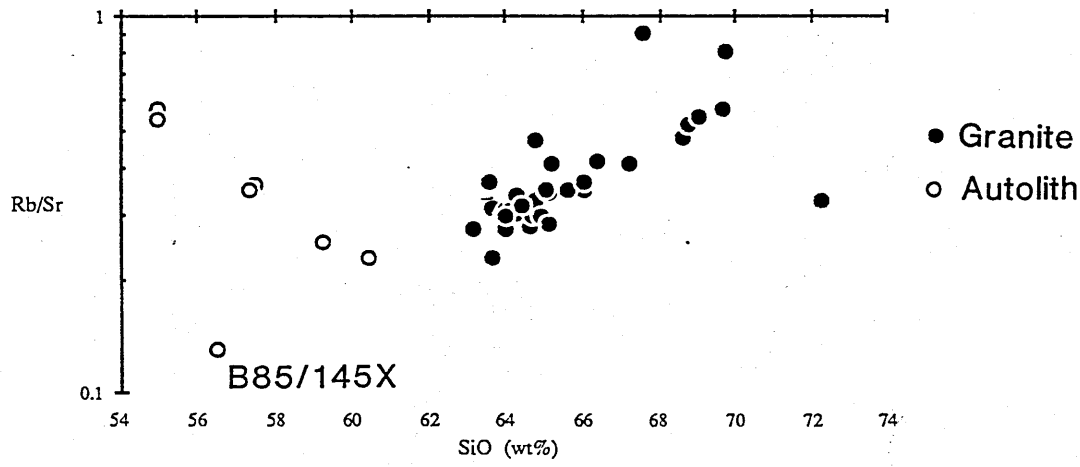

Figure 5.32

SiO_2 vs Rb/Sr for the autoliths of the MAG and the host granite.

minimum melt will remove quartz and feldspar, leaving a biotite rich residue, causing a fall in SiO_2 and rise in Rb/Sr as observed.

Tindle and Pearce (1983) suggested that autolith assimilation provided a useful analogy for intra-crustal melting of igneous protoliths. The role of biotite, however, is significantly different in these two systems. In the former, biotite is a stable residual phase, the bulk distribution coefficient of Rb is therefore greater than one and the melt has a low Rb/Sr ratio; in the latter, biotite is probably not a major residual phase and Rb therefore behaves incompatibly to produce a high Rb/Sr melt; Sr behaves compatibly in both cases due to residual plagioclase. The differing behaviour of biotite in the two systems is related to water; in the autolith melting system, the host granite melt buffers the water concentration at a value sufficient for water saturated melting to occur; in the intra crustal system, melting is probably often controlled by the availability of water (Miller, 1986) and biotite breakdown is often the primary source of water to allow melting to occur (section 4.4.1).

5.6 Rare earth element characteristics and modelling

The behaviour of rare earth elements (REE) in granitic systems has been shown to be controlled by volumetrically insignificant and largely refractory accessory phases (Fourcade and Allegre, 1981; Miller and Mittlefeldt, 1982; Gromet and Silver, 1983). Rapp and Watson (1986) and Watson and Harrison (1983) have pointed out that in peraluminous melts the saturation concentration of the melt in zircon and monazite are extremely low (≈25 ppm Zr and ≈23.4 ppm LREE), values in excess of these imply that the granitic melt contains a portion of xenocrystic zircon and monazite. Rapp and Watson (*op cit.*) also concluded that the dissolution rate of monazite is sufficiently sluggish that large grains (>50 μm) may require 10^7 years to

dissolve and may thus be residual during crustal fusion even under conditions for which it is soluble. These results indicate that a large portion of the REE in the granitoids under study are hosted in xenocrystic grains. The implications of this are that the REE evolution of the granitoids is not controlled by chemical processes such as Rayleigh fractionation but by the physical processes which separate cumulate crystals from the melt, a point noted in section 5.3 based only on the basis of difficulty of separating small crystals from a viscous melt; these factors are of prime importance in the interpretation of REE data from granitoids.

5.6.1 Rare earth element modelling

As noted above the role of accessory phases in the REE budget is of major importance (Fourcade and Allegre, 1981; Miller and Mittlefeldt, 1982; Gromet and Silver, 1983). This section attempts to model the REE content and evolution of the MAG, AG, and CG plutons in terms of both major phases (the proportions of which have already been described in chapter 3) and accessory phases (e.g. monazite, apatite, xenotime, sphene, zircon). The accessory phases were identified and where possible analysed for REE by energy dispersive microprobe techniques (see appendix A); where only partial REE data sets were obtained, due to concentrations below detection limits, values were estimated from extrapolation on chondrite normalized plots. For phases only qualitatively identified in a suite concentrations from other suites were used.

Table 5.6 summarises the REE concentrations used in the modelling. The data was obtained from the following sources; for biotite, plagioclase and alkali feldspar from Fourcade and Allegre (1981), for pyroxene from Tindle (1982), and for zircon from Nagasawa (1970) (see Appendix A for normalizing values). Figure 5.33 shows REE plots for the three least evolved samples and the accessory phases used in the modelling. The total REE budgets were calculated by the following steps:

1) The major phase contribution to the REE budget was calculated, using the

granite-norm major phase proportions and assumed REE contents, this contribution was subtracted from the total REE content of the sample (measured by INAA, see Appendix A)

2) The remaining REE content was modelled, using the measured or assumed REE contents of the identified accessory phases. The REE contents, of the accessory phases, were mixed in proportions which best replicate the desired REE content using the computer program Supermix (see section 5.2.3 for a further discussion of the method)

Figure 5.34 illustrates the calculated REE budgets; the fit of the modelling in all cases is poor, but does clearly show in the large majority of cases that the accessory phases contain between 85 and 92% of the total REE, this range is significantly higher (95 to 92%) if Eu is excluded, since an appreciable amount of Eu is accommodated in the feldspars. The model for B86/85 contains a quantity of sphene far larger than that observed or reasonably feasible, however sphene is an observed phase and therefore cannot be excluded from the model. Zr has been used as an independent check on the modelled abundance of zircon.

All the problems related to this style of modelling discussed in section 5.2.3 apply to this specific model, also several other major problems can occur, such as the low abundance of many of the important accessory phases leading to the possibility that they have not been correctly identified in the samples studied. The exclusion of LREE or HREE rich accessory phases from the model of a sample in which they occur would not be easily detected due to the nature of the modelling. In an attempt to identify this error Zr has been used as an independent check on the accuracy of the amount of zircon determined by the model. In all cases (except B86/77) the quantity of zircon, in the model, is significantly in excess of that necessary to account for the Zr content of the sample (Table 5.6). This suggests that a second, unidentified HREE phase may have been missed from the models.

The major problem in the specific models of this study, which is indicated by the

AG

	bt	plag	kspar	px	mon	sph	ap	zir
La	2.42	8.14	1.48	12.5	10603	870	535	23.6
Ce	4.77	11.65	2.13	36.6	22310	3010	1360	23.6
Nd	3.53	3.41	0.91	32.3	9162	2650	880	8.9
Sm	2.23	0.76	0.22	8	1506	685	187	5.7
Eu	0.09	1.28	0.98	0.64	127	118.1	34.2	0.21
Gd	2.9	0.55	0.22	7.2	1041	470	139	30.4
Tb	0.51	0.08	0.03	1.24	148	85.1	21.9	10.4
Yb	2.06	0.3	0.12	5.07	114.2	262	69.8	392
Lu	0.34	0.05	0.02	0.77	13.19	37.7	11.7	70
Zr	0	0	0	0	0	0	0	465000

B86/120

		bt	plag	kspar	px	mon	sph	ap	zir	% of tot.
Modal Abundance		4.6	34.8	24.3	1.8	0.28	0.1	0	0.43	
	B86/120									
	La	34.40	0.11	2.83	0.36	0.23	29.69	0.87	0.1	99.38
	Ce	70.31	0.22	4.05	0.52	0.66	62.47	3.01	0.1	101.02
	Nd	29.67	0.16	1.19	0.22	0.58	25.65	2.65	0.04	102.76
	Sm	6.01	0.1	0.26	0.05	0.14	4.22	0.69	0.02	91.24
Abundance	Eu	1.06	0	0.45	0.24	0.01	0.36	0.12	0	111.37
(ppm)	Gd	4.81	0.13	0.19	0.05	0.13	2.91	0.47	0.13	83.37
	Tb	0.82	0.02	0.03	0.01	0.02	0.41	0.09	0.04	75.87
	Yb	2.40	0.09	0.11	0.03	0.09	0.32	0.26	1.69	107.87
	Lu	0.40	0.02	0.02	0.01	0.01	0.04	0.04	0.3	110.64
	Zr	133.00	0	0	0	0	0	0	1999.5	1503.38

B86/85

		bt	plag	kspar	px	mon	sph	ap	zir	% of tot.
Modal Abundance		3.6	39.5	7.56	1.2	0.2	0.43	1.1	0.3	
	B85/85									
	La	35.10	0.09	3.22	0.11	0.15	21.21	3.74	5.89	0.1	98.30
	Ce	80.49	0.17	4.6	0.16	0.44	71.39	12.94	14.96	0.1	130.16
	Nd	42.43	0.13	1.35	0.07	0.39	18.32	11.4	9.68	0.04	97.51
	Sm	8.80	0.08	0.3	0.02	0.01	3.01	2.95	2.06	0.02	96.99
Abundance	Eu	2.06	0	0.51	0.07	0.01	0.25	0.51	0.38	0	83.82
(ppm)	Gd	8.50	0.1	0.22	0.02	0.09	2.08	2.02	1.53	0.13	72.81
	Tb	1.30	0.02	0.03	0	0.01	0.3	0.37	0.24	0.04	77.88
	Yb	3.56	0.07	0.12	0.01	0.06	0.23	1.13	0.77	1.69	114.30
	Lu	0.58	0.01	0.02	0	0.01	0.03	0.16	0.13	0.3	113.35
	Zr	268.00	0	0	0	0	0	0	0	1999.5	746.08

Table 5.6

Mineral REE compositions used in modelling and results of REE budget modelling, illustrated in Figure 5.34. HREE values for monazite and apatite and LREE values for xénotime and zircon are extrapolated

						CG			
			bt	plag	kspar	zir	mon	xen	ap
		La	2.42	8.14	1.48	23.6	10603	3.4	6868
		Ce	4.77	11.65	2.13	23.6	22310	19.8	13110
		Nd	3.53	3.41	0.91	8.9	9162	355.8	6001
	Concentrations	Sm	2.23	0.76	0.22	5.7	1506	832.3	862
	used	Eu	0.09	1.28	0.98	0.21	127	119.5	104
	in modelling	Gd	2.9	0.55	0.22	30.4	1041	2629.4	607
		Tb	0.51	0.08	0.03	10.4	148	726.6	87
		Yb	2.06	0.3	0.12	392	114.2	2824.7	53
		Lu	0.34	0.05	0.02	70	13.19	439.7	5
		Zr	0	0	0	465000	0	0	0

					B86/77					
			bt	plag	kspar	zir	mon	xen	ap	% of tot
		Modal abundance	3.70	39.70	12.60	0.02	0.24	0.04	0.26	
		B86/77								
	La	44.49	0.09	3.23	0.19	0.00	25.45	0.00	17.86	105.23
	Ce	92.30	0.18	4.63	0.27	0.00	53.54	0.01	34.09	100.45
	Nd	41.50	0.13	1.35	0.11	0.00	21.99	0.14	15.60	94.79
Abundance	Sm	7.35	0.08	0.30	0.03	0.00	3.62	0.33	2.24	89.85
(ppm)	Eu	1.46	0.00	0.51	0.12	0.00	0.30	0.05	0.27	86.06
	Gd	8.34	0.11	0.22	0.03	0.01	2.50	1.05	1.58	65.83
	Tb	0.80	0.02	0.03	0.00	0.00	0.35	0.29	0.23	115.75
	Yb	1.30	0.08	0.12	0.02	0.08	0.27	1.13	0.14	140.87
	Lu	0.24	0.01	0.02	0.00	0.01	0.03	0.18	0.01	113.24
	Zr	231.00	0.00	0.00	0.00	93.00	0.00	0.00	0.00	40.26

					B85/194					
			bt	plag	kspar	zir	mon	xen	ap	% of tot
		Modal abundance	1.20	23.00	29.40	0.08	0.19	0.01	0.11	
		B85/194								
	La	28.98	0.10	6.46	1.50	0.06	69.51	0.00	26.07	103.71
	Ce	61.17	0.09	4.38	1.02	0.03	69.30	0.00	23.58	98.40
	Nd	27.24	0.16	2.88	0.98	0.03	63.91	0.18	24.23	92.37
Abundance	Sm	5.40	0.50	3.24	1.20	0.08	53.01	2.16	17.57	77.75
(ppm)	Eu	0.91	0.12	32.35	31.66	0.02	26.50	1.84	12.51	104.99
	Gd	2.60	1.34	4.87	2.49	0.90	76.11	14.16	25.69	125.56
	Tb	0.66	0.93	2.61	1.51	1.21	42.52	15.41	14.48	78.68
	Yb	1.20	2.06	5.83	2.94	25.15	18.08	32.95	4.83	91.84
	Lu	0.19	2.15	6.42	3.56	28.37	13.19	32.40	3.05	89.14
	Zr	91.00	0.00	0.00	0.00	393.46	0.00	0.00	0.00	393.46

Table 5.6 Cont.

	MAG						
	mon	sph	ap	zir	bt	plag	alk
La	14302.87	870.00	6868.20	23.60	2.42	8.14	1.48
Ce	25075.92	3010.00	1311.00	23.60	4.77	11.65	2.13
Nd	7568.70	2650.00	6001.00	8.90	3.53	3.41	0.91
Sm	746.35	685.00	862.00	5.70	2.23	0.76	0.22
Eu	77.59	118.10	103.50	0.21	0.09	1.28	0.98
Gd	427.35	470.00	607.30	30.40	2.90	0.55	0.22
Tb	56.47	85.10	86.88	10.40	0.51	0.08	0.03
Yb	26.35	262.00	52.69	392.00	2.06	0.30	0.12
Lu	2.64	37.70	5.28	70.00	0.34	0.05	0.02
Zr				465000			

			B85/147							
			bt	plag	kspar	zir	mon	sph	ap	% of total
		Modal abundance	8.70	35.50	25.00	0.37	0.35	0.01	0.60	
		B85/147								
	La	92.47	0.21	2.89	0.37	0.09	50.06	0.09	41.21	102.64
	Ce	165.10	0.41	4.14	0.53	0.09	87.77	0.30	78.65	61.24
	Nd	60.04	0.31	1.21	0.23	0.03	26.49	0.27	36.01	107.49
	Sm	9.25	0.19	0.27	0.06	0.02	2.61	0.07	5.17	90.73
Abundance	Eu	2.11	0.01	0.45	0.25	0.00	0.27	0.01	0.62	76.41
(ppm)	Gd	8.88	0.25	0.20	0.06	0.11	1.50	0.05	3.64	65.33
	Tb	1.06	0.04	0.03	0.01	0.04	0.20	0.01	0.52	79.76
	Yb	2.08	0.18	0.11	0.03	1.45	0.09	0.03	0.32	105.87
	Lu	0.33	0.03	0.02	0.01	0.26	0.01	0.00	0.03	108.43
	Zr	183.00				1720.50	0.00	0.00	0.00	940.16

			B85/117							
			bt	plag	kspar	zir	mon	sph	ap	% of total
		Modal abundance	7.00	31.00	24.60	0.37	0.25	0.01	0.70	
		B85/117								
	La	81.42	0.17	2.52	0.36	0.09	35.76	0.09	48.08	106.93
	Ce	148.10	0.33	3.61	0.52	0.09	62.69	0.30	91.76	51.81
	Nd	57.80	0.25	1.06	0.22	0.03	18.92	0.27	42.01	108.57
	Sm	9.00	0.16	0.24	0.05	0.02	1.87	0.07	6.03	93.73
Abundance	Eu	1.93	0.01	0.40	0.24	0.00	0.19	0.01	0.72	81.61
(ppm)	Gd	7.44	0.20	0.17	0.05	0.11	1.07	0.05	4.25	79.39
	Tb	1.02	0.04	0.02	0.01	0.04	0.14	0.01	0.61	84.67
	Yb	2.10	0.14	0.09	0.03	1.45	0.07	0.03	0.37	103.77
	Lu	0.33	0.02	0.02	0.01	0.26	0.01	0.00	0.04	106.73
	Zr	161.00	0.00	0.00	0.00	1720.50	0.00	0.00	0.00	1068.63

Table 5.6 Cont.

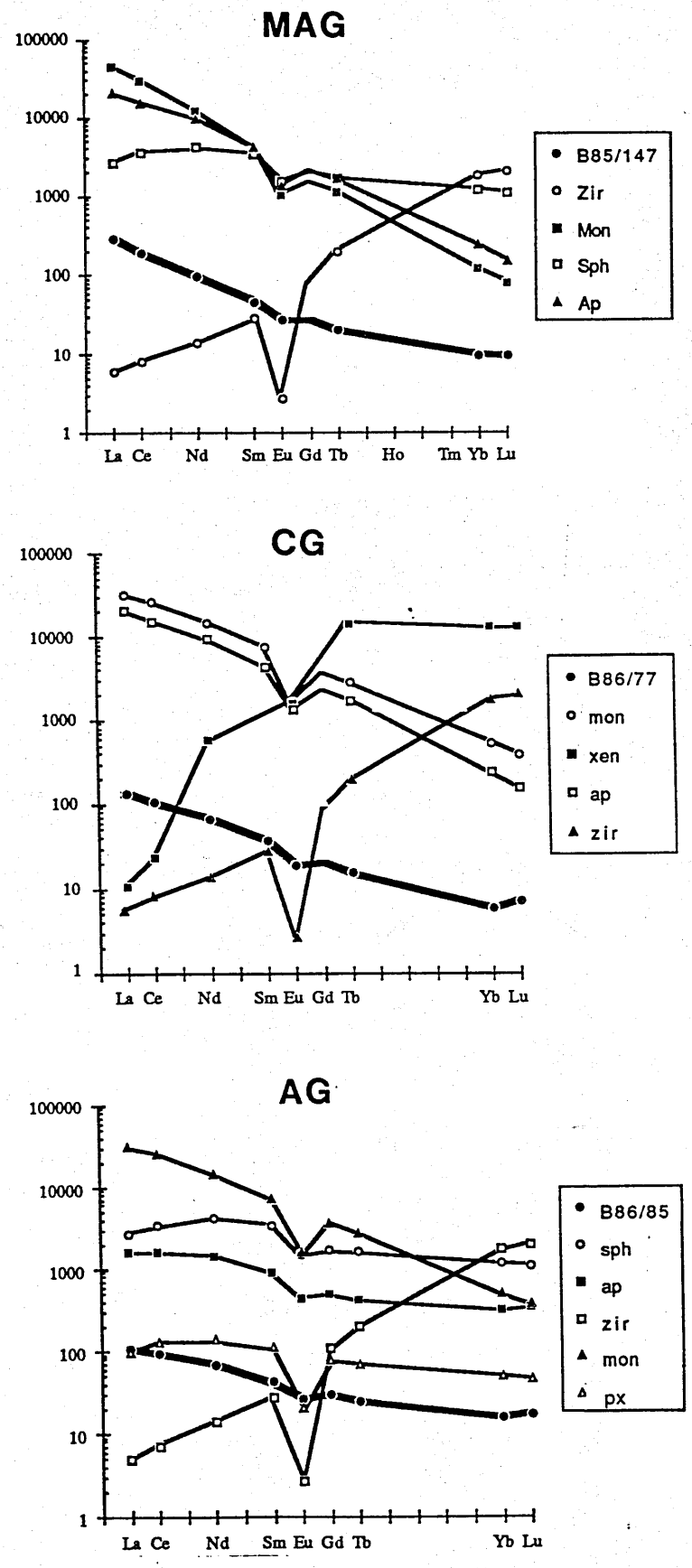

Figure 5.33

Chondrite normalized REE patterns for the three least evolved samples from the CG, AG, and MAG and the REE patterns of the phases used to model them.

results, is that of low totals for the MREE (Sm to Tb, excluding Eu); this probably reflects the reliance of the models on the low and therefore probably inaccurate MREE concentrations of the HREE and LREE rich phases. The high abundance of sphene in the model for B86/85 illustrates the problem identified in section 5.2.3, the amount of any phase cannot be constrained and is simply manipulated to minimize the overall error, this has led to assemblages with very small ΣR^2 values but which are geologically unreasonable.

The shortcomings notwithstanding, certain observation can be made on the accessory phase evolution of the facies. The MAG samples show little variation except for a slight fall in the amount of monazite and increase in apatite. The AG exhibits a marked reduction in the importance of sphene and apatite and increase in monazite and zircon with evolution. The CG exhibits a fall in the importance of xenotime and a rise in that of zircon and monazite with evolution. These trends possibly reflect the ease of extraction of apatite, which forms the largest grains of the accessory phases and xenotime relative to monazite and zircon which are often small grains included in biotites.

In summary 70 to 90% of the REE budgets of the granitoids modelled, are controlled by accessory phases. Since these phases compose <5% of the modal assemblage, their existence is easily overlooked, but is fundamental to the trace element evolution of the magma, as they control, not only the REE but also Zr, Hf, Nb, Ta, U, and Th concentrations. The low Sm/Nd ratio (0.09 to 0.15) of the two main host phases considered in the models (monazite and apatite) can potentially cause significant fractionation of the Sm/Nd ratio. This effect is generally considered not to occur in the crust (McCulloch and Wasserberg, 1978) but is observed in the granitoids under study , see section 6.6.1 for further discussion.

5.6.2 Rare earth element characteristics

Figures 5.35 to 5.38 illustrate the REE patterns and evolution of the granitoids of this study (normalization values from Nakamura, 1974). As noted above the REE budget is almost exclusively controlled by the accessory phases of the granitoid; the difficulty of fractionating these phases, due to their small size, and the inherited nature of the majority of the zircons and monazites implies that the REE pattern of a crustally derived granitoid will be highly similar to that of it's source. The patterns for the fresh Cordillera Real granitoids are all very similar; they are LREE enriched (Ce_N/Yb_N= 20 to 12) and have HREE concentrations of ≈10x chondrite, indicating a lack of garnet in the source residue. With evolution the MAG, CG, and MVGP become less LREE enriched probably reflecting the fractionation of monazite; the AG becomes more HREE depleted, probably reflecting zircon removal. All of the granitoids have negative europium anomalies believed to indicate, residual plagioclase in the source and in the case of the CG and MVGP a europium depleted source, a typical feature of mature metasediments. The MVGP and MAG display an decrease in Eu/Eu* with evolution (0.7 to 0.37 for the MVGP and 0.73 to 0.69 for the MAG) believed to reflect feldspar and/or apatite fractionation, the CG and AG display approximately constant Eu/Eu* values of between 0.55 and 0.71 with evolution. The aplite related to the MAG (B85/125) has an almost flat REE pattern (Ce_N/Yb_N= 3 to 1.1) reflecting extreme evolution; B85/192, the aplite related to the CG exhibits extreme LREE depletion probably related to fluid loss from the magma. The unusual pattern of B85/210 (Eu/Eu*=3.3, Ce_N/Yb_N=6.8) supports the textural interpretation of a feldspar dominated cumulate origin (see section 3.4.2 i). The high degrees of alteration noted in mineralized samples of the MAG (section 3.3.3 i) has not affected the REE concentrations as illustrated by sample B86/11.

The REE characteristics of the CG and MVGP (Figures 5.37 and 5.36) are similar to those of the local metasediments (Figure 5.39) supporting the model of their origin from upper crustal metasediments with large scale entrainment of accessory phases.

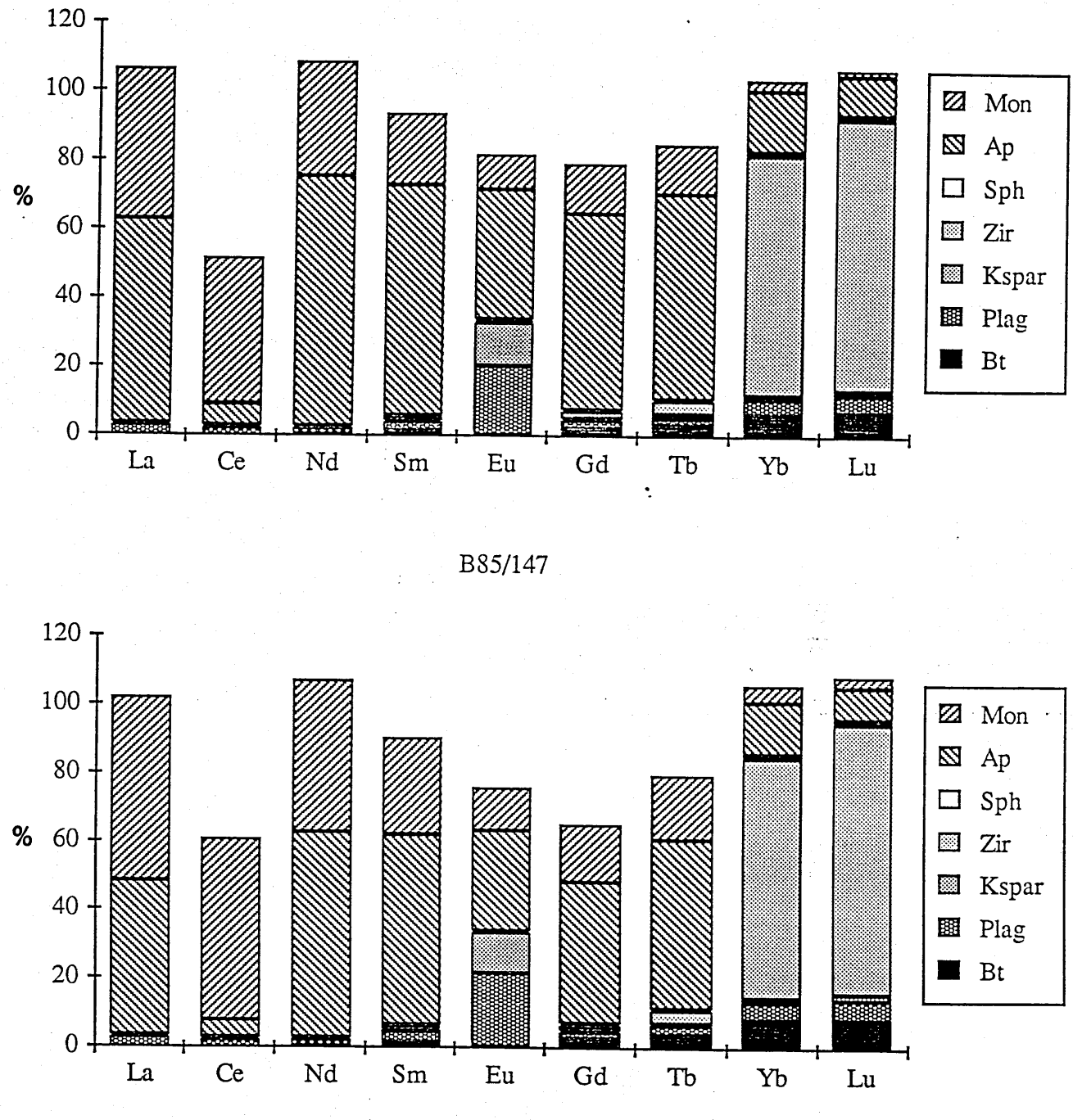

Figure 5.34

Histograms of the modelled accessory phase REE budgets for the unevolved and evolved samples of the MAG, AG and MAG.

CG

B86/77

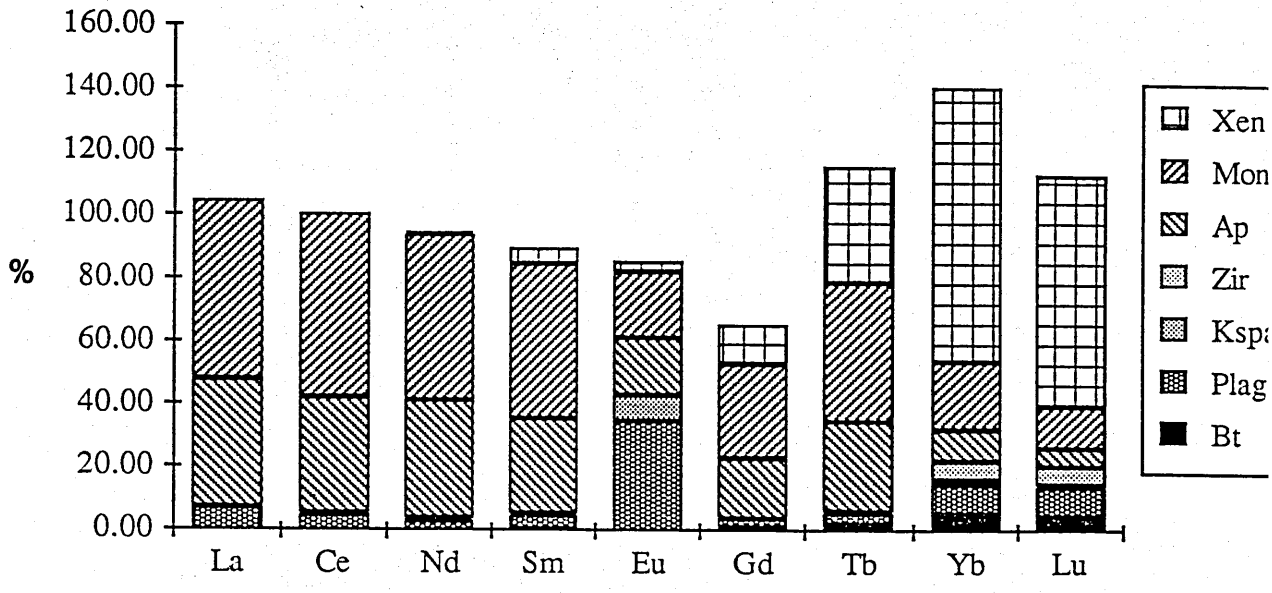

B85/194

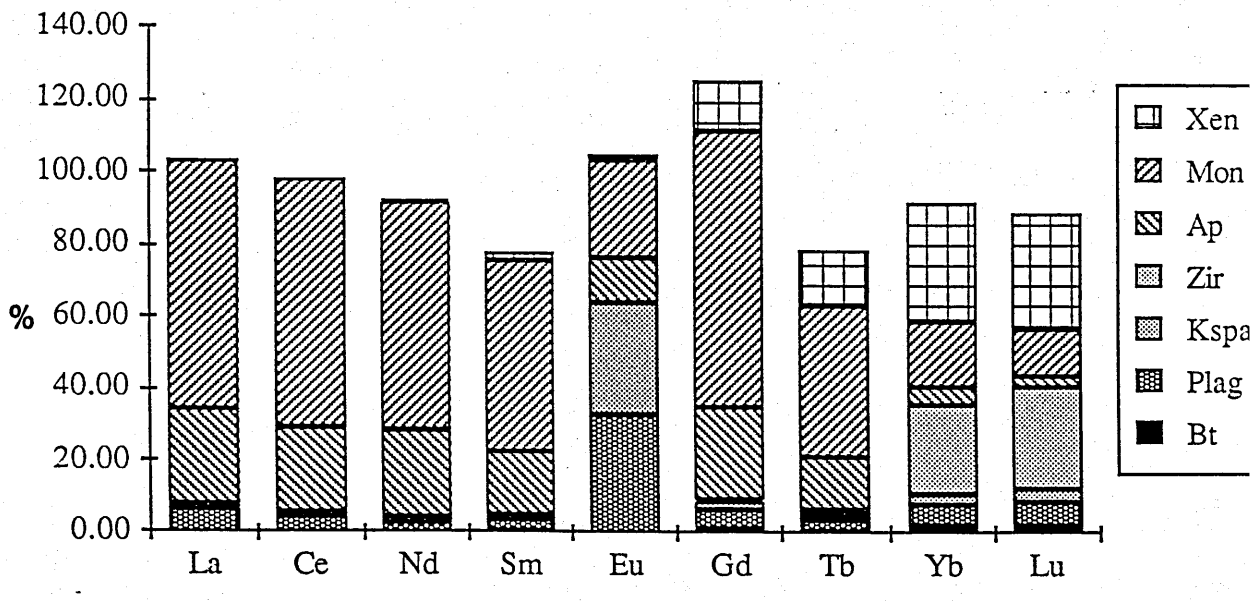

Figure 5.34 Continued

AG

B86/120

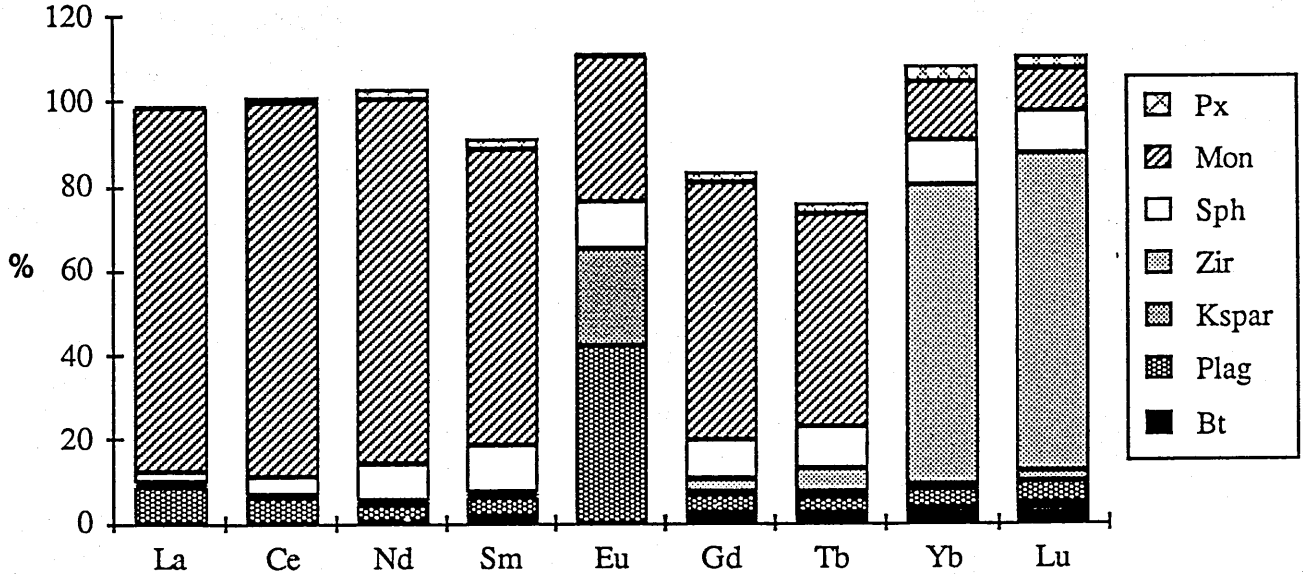

B86/85

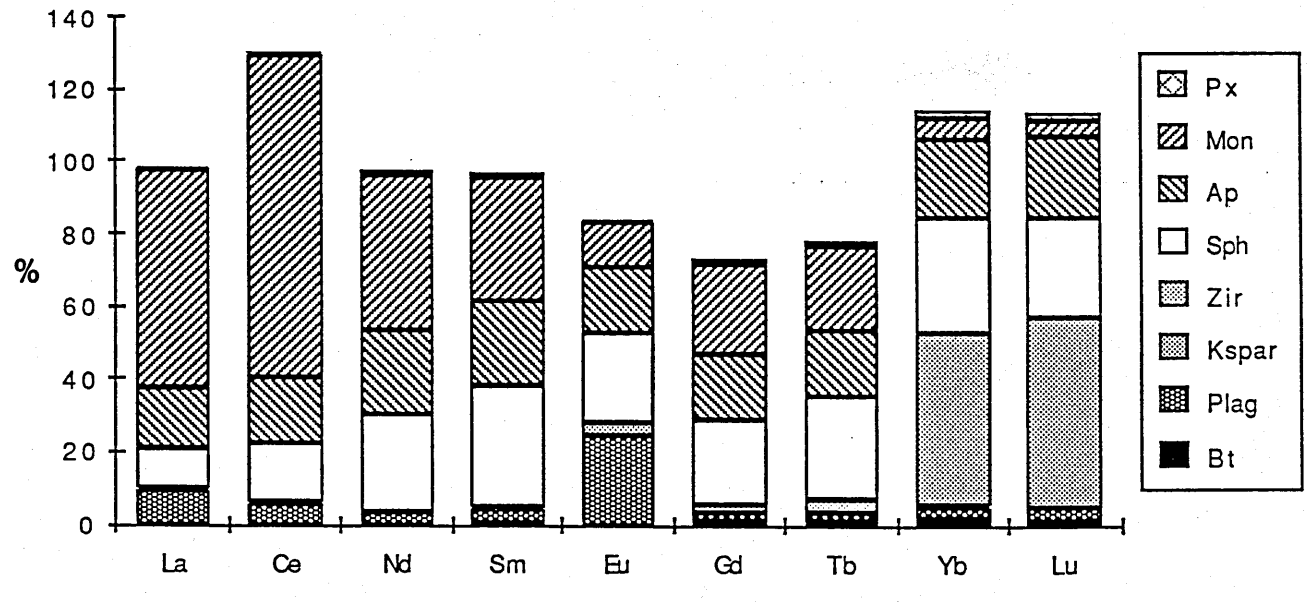

Figure 5.34 Continued

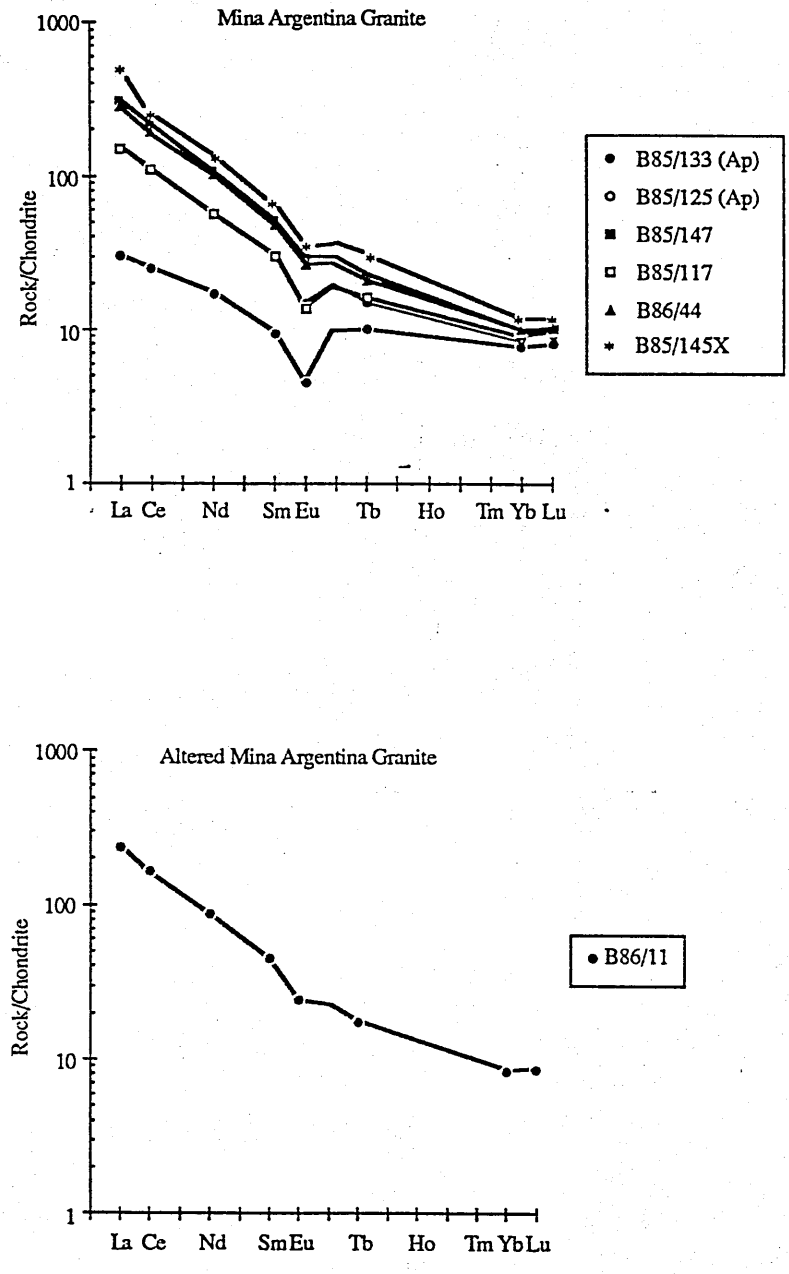

Figure 5.35

Chondrite normalized REE patterns of granite, aplite, and altered samples from the MAG.

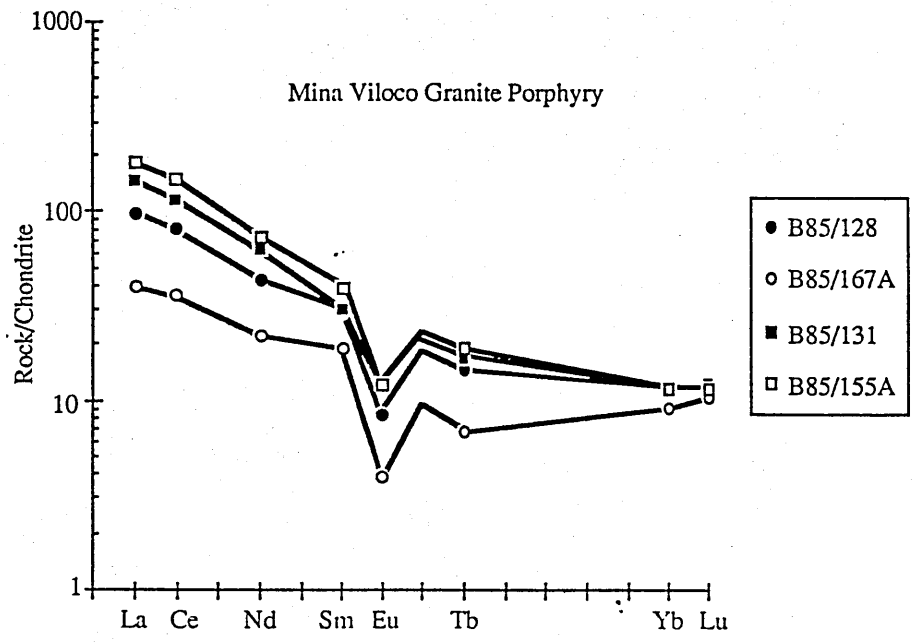

Figure 5.36

Chondrite normalized REE pattern for the MVGP.

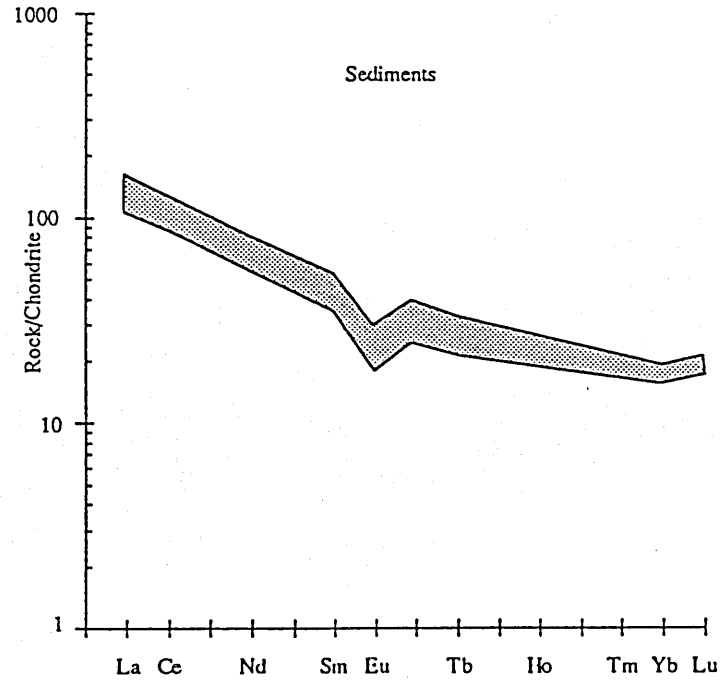

Figure 5.39

Chondrite normalized REE patterns of samples of pelitic metasediments taken as being representative of the local upper crust.

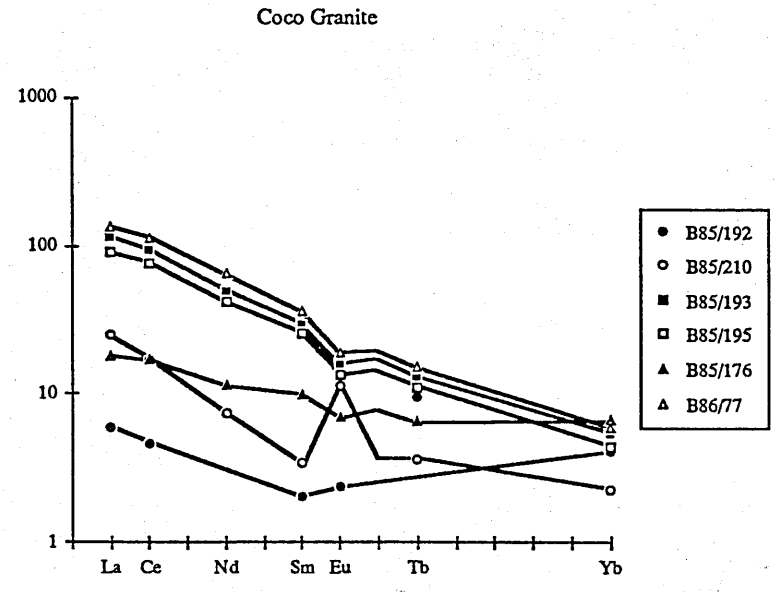

Figure 5.37

Typical chondrite normalized REE patterns for granite, aplite and cumulate (B85/210) samples of the CG. The granite evolution causes a fall in the concentration of REEs without an increase in the Eu anomaly, this is thought to reflect the fractionation of accessory phases at ther same rate feldspar. The aplite displays a heavily LREE depleted pattern reflecting the loss of a fluid from the magma

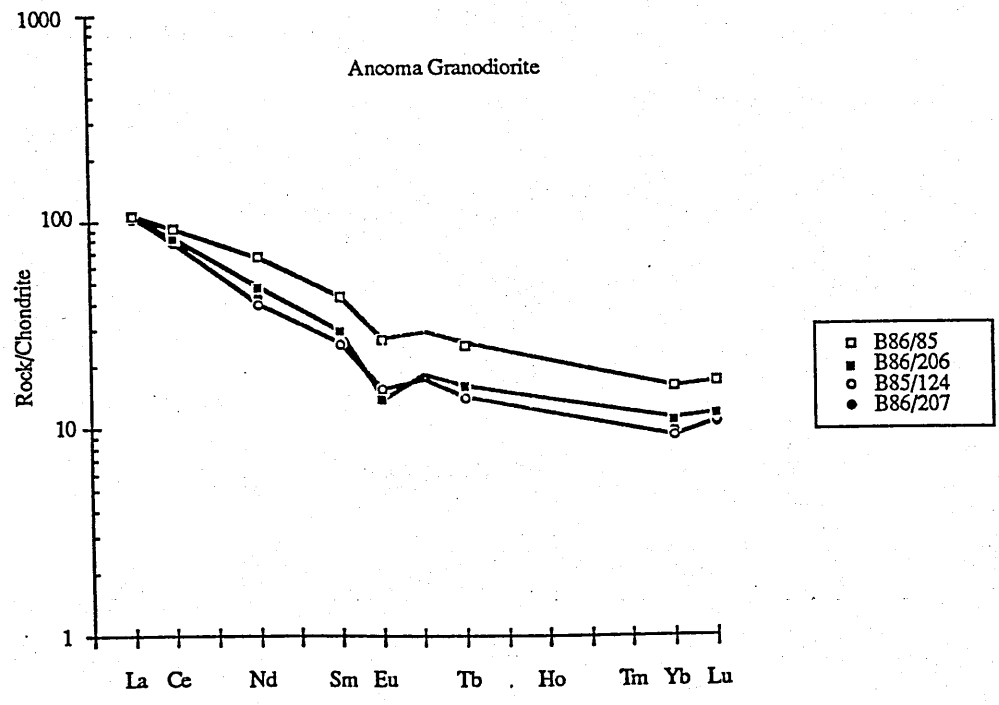

Figure 5.38

Typical Chondrite normalized REE patterns for samples of the AG.

The MAG autolith, B85/145X is considered not to have been affected by assimilation, see section 5.5. The Eu anomaly of B85/145X (Eu/Eu*=0.6) is negligible and it is thought that the initial MAG magma was not Eu depleted indicating a lack of large quantities of residual plagioclase and so supporting the model of a large mantle component. The AG patterns are more evolved than those of the MAG and are consistent with a plagioclase bearing source or early plagioclase fractionation.

5.7 Summary

Trace element studies of the granitoids of the Cordillera Real have identified two distinct groups. The CG and MVGP are characterized by high Rb/Sr, high Rb/Ba ratios and strongly peraluminous major element geochemistry; these features and the high εSr, discussed in chapter 6, are believed to be indicative of a mature meta-sedimentary source. The CKG and SG display similarly high Rb/Sr ratios and are thought to have been derived from a similar source. The MAG and AG in contrast are characterized by low Rb/Sr and Rb/Ba ratios and metaluminous to weakly peraluminous geochemistry; these features and their low εSr are thought to indicate derivation from a source containing a significant mantle component, this has been modelled and quantified to be approximately 50% of a within plate mantle component for the MAG and 10% of a probably subduction related mantle component for the AG. The HPG, UG and IG display similar Rb/Sr ratios and are thought to have been derived from a similar type of source.

If the characteristics of the source are assumed the petrogenesis of the granitoids can be modelled. The residual mineralogy of the CG and MVGP has been assessed and shown to contain phases such as a Ti phase (ilmenite, sphene or rutile), zircon, xenotime, plagioclase but not to contain significant quantities of biotite, or garnet,

based on HREE concentrations. The lack of residual biotite supports models of free water absent melting of metasediments (Miller, 1986; Clements and Vielzeuf, 1987) where the breakdown of biotite, is of primary importance in the process of release of water to allow melting to occur (see Section 4.4.1).

The MAG and AG have been modelled in terms of mantle components and upper crust. The mantle components are thought to have been significantly different for the two granitoids; the AG is subduction related and the MAG has within plate affinities. The method of incorporation of the crustal material into the mantle component can be modelled as an AFC process for the MAG; the AG is more accurately modelled as a simple mixture of crustal and mantle components.

The close association in time and space of granitoids derived both from metasediments and in part from subduction related mantle and within plate mantle indicates the overall complex tectonic setting of the Cordillera Real during the Palaeozoic, see chapter 7 for further discussion.

The intra-pluton major and trace element variations have been semi-quantitatively modelled in terms of fractional crystallization. The major element variations are best modelled by *in situ* fractional crystallization; the LILE variations were also modelled in terms of fractional crystallization of the same phases, however the two models do not predict the same fractionation assemblages. The cause of the discrepancy is thought to be the large quantities of biotite (14 to 30%) predicted by the major element model.

The role of accessory phases in the REE budget of the granitoids was indicated by best fit mixing models which predicted 85 to 92 % of the REE to be contained in accessory phases. The behaviour of these phases during melting, magma migration and crystallization will exercise the dominant control of the REE budget of a granitoid. The ability of phases such as monazite to fractionate the REE, specifically Sm and Nd may be of major importance in assessing the Nd isotopic evolution of

granitoids, see section 6.6.1 for further discussion.

The REE abundances of the CG and MVGP support the model of their origin from a mature metasedimentary protolith. The MAG REE concentrations indicate a lack of residual plagioclase, a conclusion supported by the high Sr concentrations. The REE concentrations of the AG are equivocal.

CHAPTER 6
Isotope Geochemistry

6.1 Introduction

This chapter presents new Sr isotope data for granitoids, sediments and mica separates and new Nd isotope data for granitoids and sediments. The three main aims of this chapter are:

1) To determine the age of the MAG, the MVGP, the CG, and the AG intrusions as accurately as possible using Rb-Sr whole rock geochronology and Rb-Sr mica-whole rock geochronology
2) To model quantitatively the isotopic characteristics of the granitoid source regions in terms of mantle and crustal components

Both Sr and Nd isotopes are reported using ε notation, which compares granitoid $^{87}Sr/^{86}Sr$ or ^{143}Nd / ^{144}Nd values at a given time, to those of a theoretical uniform bulk earth at the same time (DePaolo and Wasserberg, 1976), see appendix A for method and constants. The notation εSr_T is used to represent the εSr of a sample at a time T. I is used to signify emplacement age, likewise for εNd values.

All ages are quoted with two standard deviation errors.

6.2 Geochronology

6.2.1 Previous work

Early work on the Cordillera Real (Megard *et al.*, 1971; Martinez, 1980) reported the occurrence of foliated granitoids with wide metamorphic aureoles. Although no stratigraphic age could be assigned to the granitoids it was postulated that by analogy with similar plutons in the Peruvian Eastern Cordillera (section 2.3.1)

they are synkinematic Palaeozoic intrusions related to the Chanic orogeny (Late Devonian to Early Carboniferous). This inference is supported by a single, whole rock, ^{39}Ar-^{40}Ar age of 347 Ma of a lower Palaeozoic slate, from a portion of the Cordillera Real unaffected by plutonism. This indicates that the regional lower greenschist metamorphism and by implication the foliated syntectonic granitoids are due to a Chanic event (McBride *et al.*, 1987).

Previous isotope geochronological studies in the Cordillera Real have been limited to K-Ar and ^{39}Ar-^{40}Ar mineral separate work. Cordani (1967), Clark and Farrar (1973), Everden *et al.* (1977), Martinez (1980), and McBride *et al.* (1983 and 1987) all identified two apparent age groups in K-Ar mica dates obtained from the Cordillera Real. Upper Triassic to lower Jurassic (225-175 Ma), ages were obtained from plutons to the north (including the Sorata Complex) while intrusions to the south (including the Tres Cruses Complex) formed a younger, upper Oligocene to upper Miocene (30 -25 Ma), suite (Figure 6.1).

The large number of intermediate apparent ages reported by Cordani (1967), Everden *et al.* (1977) and McBride *et al.* (1987) (Figure 6.1) were all derived from samples of plutons from the 'older' group. These apparent ages were believed to be due to the partial degassing of the granitoids. The lack of any distinct igneous event during this period suggests the degassing was due to a thermo-tectonic event. The date of the degassing, determined from totally outgassed samples, is 39 Ma (McBride *et al.*, 1987).

^{39}Ar-^{40}Ar age spectra on mica separates from the suites of samples with older and younger K-Ar apparent mica ages, are uniform and in agreement with the K-Ar apparent ages. This led McBride *et al.* (1987) to conclude that the upper Triassic to lower Jurassic and upper Oligocene to lower Miocene ages are true emplacement ages and that one tectonic outgassing event occurred at 39 Ma. However, it will be shown below, that the upper Triassic to lower Jurassic ages are in fact all reset ages and that only the MVGP and not the whole of the Tres Cruses Complex is of Miocene age.

Tres Cruses Complex

Facies	Sample	Mica	Date (Ma)
M.A.G	B85/118	Biotite	25.9 ± 1
		Biotite	209 ± 6
		Biotite	23 ± 2
	B85/119	Biotite	24.4 ± 1.2
		Biotite	16.4 ± 0.1
		Biotite	37 ± 2
	B85/149	Biotite	25.6 ± 1.2
		Biotite	18.3 ± 0.6
		Biotite	24 ± 1
MVGP	B85/160	Biotite	23.9 ± 0.4

Sorata Complex

CG	B85/183	Muscovite	217 ± 5.6
		Biotite	15.3 ± 0.6
	B85/197	Muscovite	214 ± 7
		Biotite	178 ± 2.6
AG	B85/207	Biotite	213 ± 12
		Biotite	241 ± 8

Table 6.1

Summary of Rb-Sr mica dates for the Tres Cruses and Sorata Complexes.

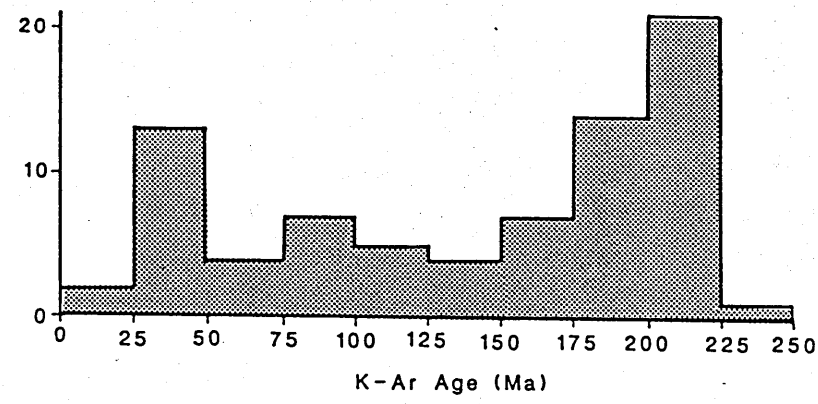

Figure 6.1

Histogram of the published K-Ar mica dates for the Cordillera Real from Cordani (1967), Clark and Farrar (1973), Everden *et al.* (1977), Grant *et al.* (1979) and McBride *et al.* (1983 and 1987).

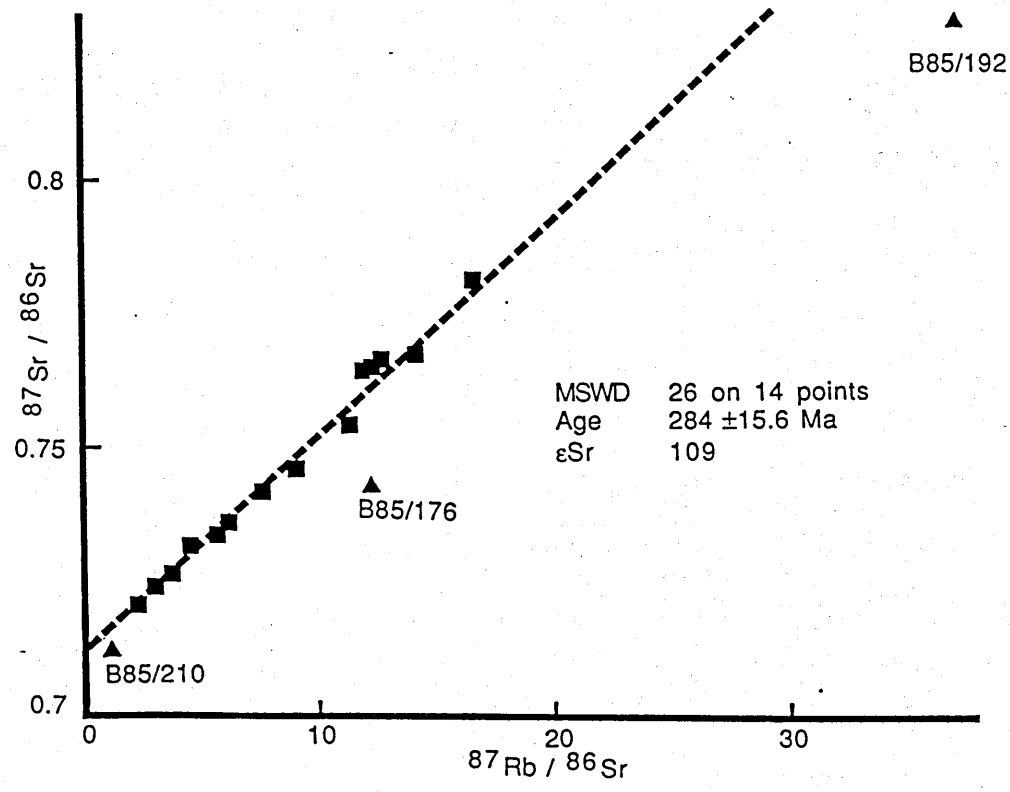

Figure 6.2

Isochron plot for the Coco Granite, errorchron shown based on 14 out of 17 points gives an age of 284 ± 16 Ma. Three data points shown as triangles were not used in the regression and are discussed in the text.

6.2.2 Rb-Sr whole rock geochronology

Figure 6.2 shows all the available data for the CG (17 points), of these 14 have been used to construct the 284 ± 16 Ma errorchron shown. Of the three points discarded from the errorchron, B85/176 and B85/192 are garnet bearing aplites (section 3.4.3 i) which are significantly more siliceous than other samples analysed from the CG. They also have trace element characteristics distinct from the CG, with lower Rb/Sr values than those inferred for members of the CG at similar degrees of fractionation (Figure 6.3). This may reflect the influence of external fluids. B85/210, is texturally and compositionally unique; it is a plagioclase cumulate and significantly less evolved than the rest of the suite (see section 3.4.2 i, for description and discussion), and is therefore not thought to be cogenetic with the CG.

The data collected from the AG do not define an isochron (Figure 6.4). In the field the AG occurs in the same area as the CG, although no contact between the two was observed (see section 3.4.1). Figure 6.4 shows the data and a 284 Ma reference line. On the basis of the data clustering along the line the AG is believed to have been emplaced at the same time as the CG. The reason for the data not defining an isochron is unclear. As the deviation of data points from the reference line appears to be random it seems unlikely that it is due to a coherent process. The scatter probably, reflects isotopic heterogeneities inherited from the source region and not homogenized in the melt, possibly due to it's high viscosity.

An errorchron has been calculated for eight of the twelve data points measured for the MAG (Figure 6.5). The age defined by the line, 300 ± 48 Ma, is within error of the AG errorchron, and consequently the CG, the AG and the MAG are believed to have been emplaced in the same episode. Four data points were not used in the construction of the errorchron. Of these, B85/125 is an aplite and has elevated Rb/Sr values (Figure 6.6), and like the aplites of CG, has probably been affected by external fluids. B85/122 exhibits textural evidence for alteration, which has mainly

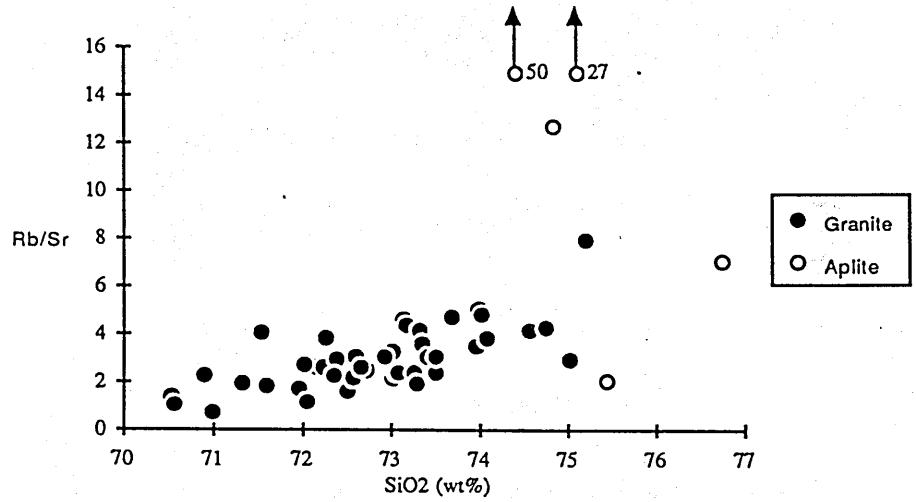

Figure 6.3

Rb/Sr vs. SiO_2 (wt%) for the CG. The aplite samples lie off the evolution line.

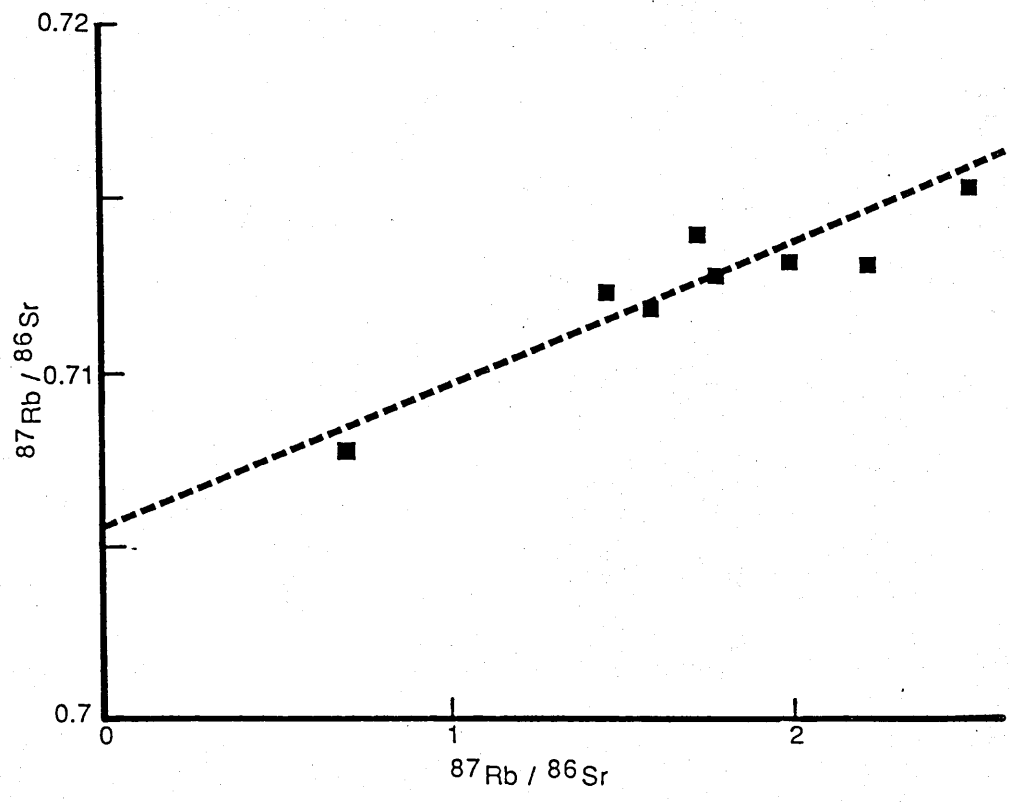

Figure 6.4

Isochron plot for the Ancoma Granodiorite. A 284 Ma reference line is shown.

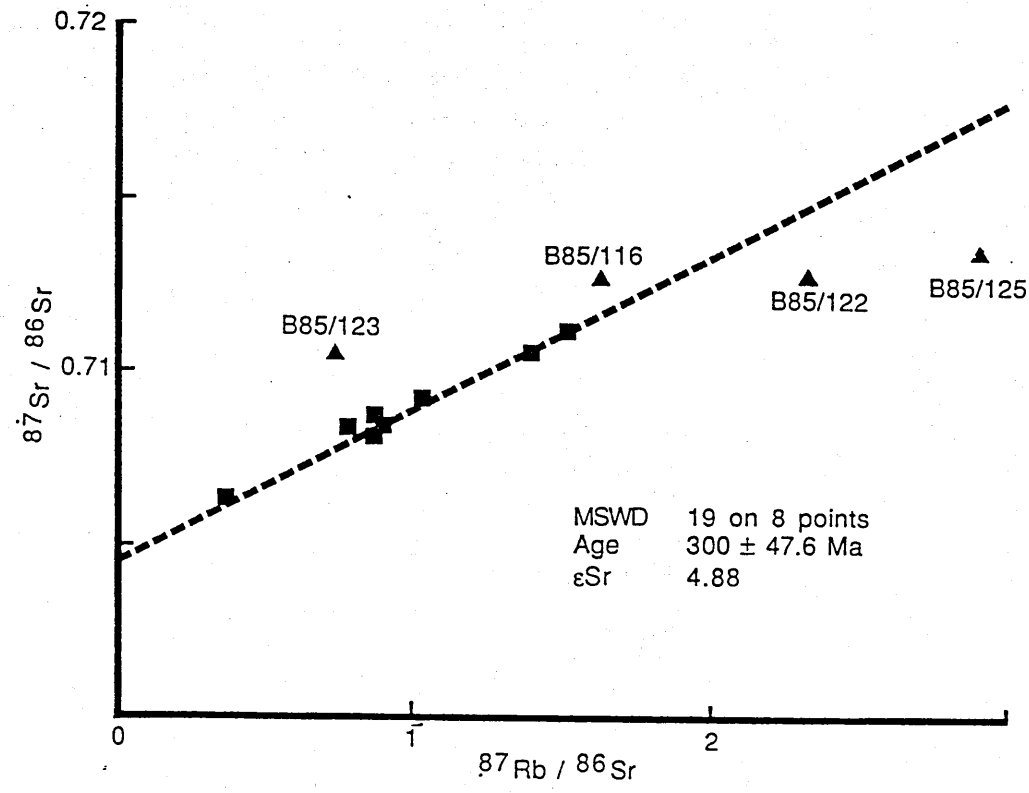

Figure 6.5

An isochron plot for the Mina Argentina Granite. The errorchron shown is based on 8 of the 12 data points and has an age significance of 300 ± 48 Ma. The four points shown as triangles were not used in the regression and are discussed in the text.

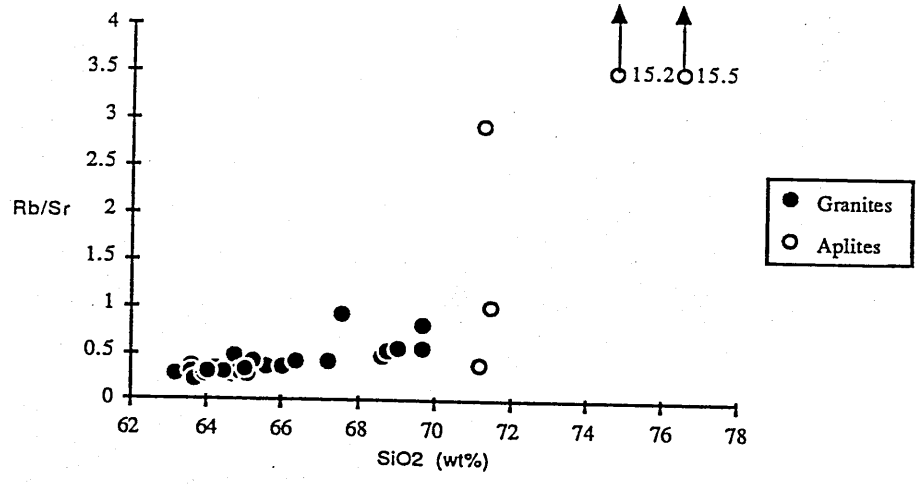

Figure 6.6

Rb/Sr vs. SiO_2 (wt%) for the MAG. The aplite samples lie off the evolution trend.

affected the feldspars (section 3.3.3 i).

B85/123 and B85/116 both lie above the errorchron. However, both are petrographically typical of the MAG and do not lie off the normal geochemical trends of the MAG. Their anomalous isotopic composition may be due to contamination by high $^{87}Sr/^{86}Sr$ material.

No clear age relationship exists in the MVGP Sr isotope data (Figure 6.7). Based on Rb-Sr mica separate work (section 6.2.3) this facies is thought to be mid-Tertiary in age. A 25 Ma reference line is shown in Figure 6.7 which passes through three of the data points. This may reflect either source region heterogeneities or more probably the affects of widespread fluid interaction, already postulated on petrographic grounds (section 3.3.3 iii).

6.2.3 Rb-Sr mica geochronology

In an attempt to refine the errorchrons determined for the AG, the CG, the MAG, and to date the MVGP, high purity ($\approx$ 99%) mica separates were extracted from selected samples and analysed for; Rb and Sr concentrations using standard isotope dilution techniques, and $^{87}Sr/^{86}Sr$ (see appendix A for methodology, Appendix D for values). These values were used with the isotopic compositions of the relevant whole rock to construct two point isochrons. Table 6.1 details the results of repeated runs and Figure 6.8 shows a histogram of the data. Repeated runs of individual samples show a degree of variability and the error for the $^{87}Sr/^{86}Sr$ determinations are high (Table 6.1). Nevertheless, two clear clusters of apparent ages can be seen: the northern, Sorata Complex with mid Triassic ages; and the southern, Tres Cruses Complex with mid Tertiary ages. These are in good agreement with the two groups of apparent ages previously identified by K-Ar and ^{39}Ar-^{40}Ar dating, see section 6.2.1, (McBride *et al.*,1987).

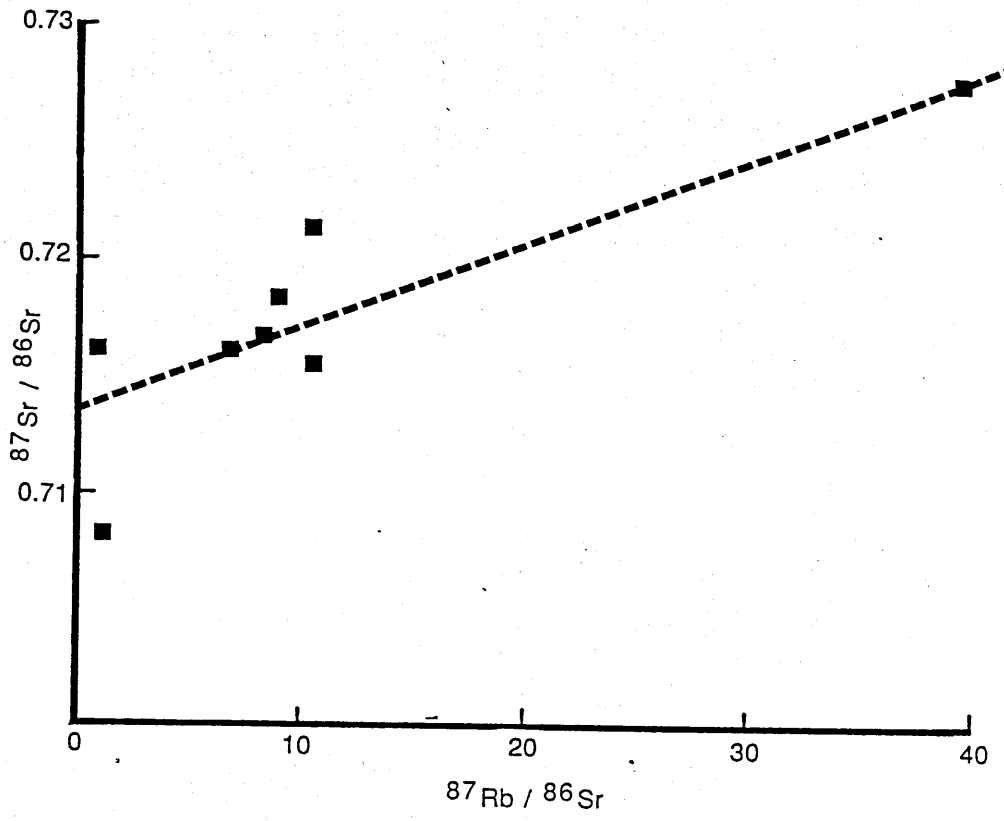

Figure 6.7

Isochron plot for the Mina Viloco Granite Porphyry. The reference line shown has an age significance of 25 Ma.

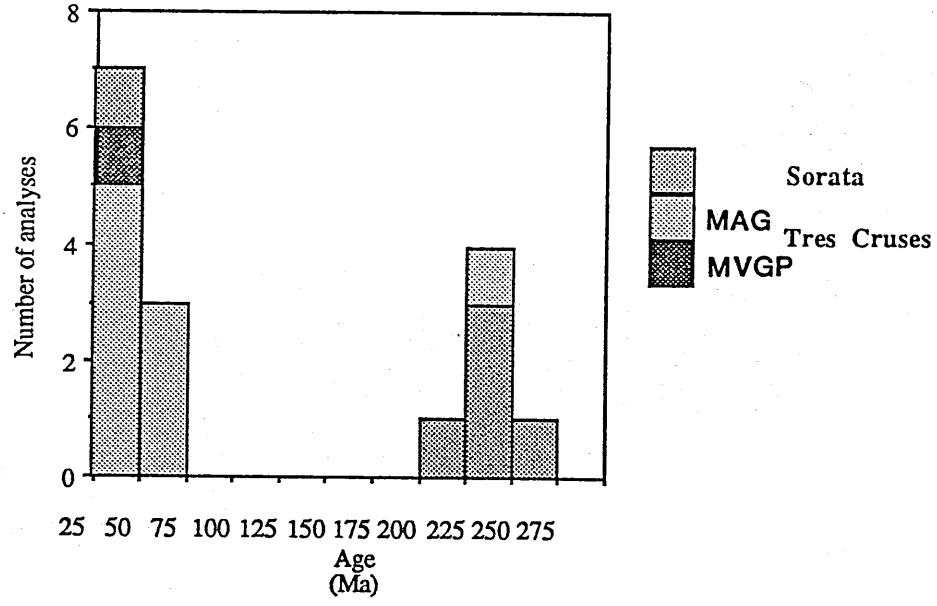

Figure 6.8

A histogram of the Rb-Sr mica ages for the Tres Cruses and Sorata Complexes.

6.2.4 Geochronological model for the Cordillera Real

The whole rock Rb-Sr errorchrons for the AG, the CG and the MAG are believed to define the true emplacement ages of these intrusives. The Rb-Sr mica separate and K-Ar, ^{39}Ar-^{40}Ar ages from the literature are thought to be reset ages and to reflect thermal or tectonic events in the mid Triassic and mid Tertiary.

Whole rock $^{87}Sr/^{86}Sr$ values from the MVGP do not define an isochron and the mica separate from this facies give mid Tertiary age like those of the MAG. These ages, however are believed to be true emplacement ages for the MVGP. Major and trace element modelling strongly suggests a mature sedimentary source for this facies (section 5.4.1). If a Palaeozoic age, similar to that of the other facies, is assumed for the MVGP then the calculated $(^{87}Sr/^{86}Sr)_{300}$ are impossibly low (0.67192 - 0.68453), however if the Rb-Sr mica age is taken as correct then reasonably high $(^{87}Sr/^{86}Sr)_{25}$ values are obtained (0.71762-0.71363), suggesting that the Rb-Sr mica age is the true emplacement age.

The overall geochronological evolution of the Sorata and Tres Cruses complexes and probably the whole Cordillera Real appears to be:

1) The emplacement of the AG, the CG, the MAG, and probably other plutons of the Cordillera, related to the Chanic orogeny (based on Rb-Sr whole rock errorchrons (284-300 Ma) and analogy with plutons in S.Peru, Megard *et al.* ,1971)
2) A Permo-Triassic (225-175 Ma) thermal event unrelated to magmatism in either the Sorata or Tres Cruses Complexes and possibly the whole Cordillera, but strong enough to totally reset the K-Ar and Rb-Sr isotope systematics of the micas (based on Rb-Sr , K-Ar, ^{39}Ar-^{40}Ar mica apparent ages, McBride *et al.*,1987)
3) An Upper Eocene (≈39 Ma) thermal event probably related to large scale thrusting of metasediments westwards over the granitoids along the fault to the east of the Cordillera (based on K-Ar and ^{39}Ar-^{40}Ar mica ages, McBride *et*

al.,1987)

4) The emplacement of the MVGP at 25 Ma (Rb-Sr and K-Ar mica ages, McBride *et al.*, 1987) related to crustal thickening at this time (section 2.5).

6.3 Strontium isotope variations

One of the characteristic features of mature sediments and granites derived from them is their high εSr values (Chappell and White, 1974). Granitoids containing a component recently derived from the mantle, whether in the form of basic volcanic sediments or directly as a melt, will have lower εSr values (Miller 1986)

These observations coupled with major and trace element considerations (section 5.4.1) allow the construction of isotope vs. element diagrams which discriminate between different source regions. Figures 5.24 and 6.9 show plots of εSr_I vs. Rb/Sr and εSr_I vs. Shand index. As discussed in section 5.4.1 high degrees of peraluminosity and high values of Rb/Sr in compositionally restricted granites are indicative of mature crustal, sedimentary sources. As shown in Figures 5.24 and 6.9 the MVGP and the CG display high values of εSr_I coupled with high Rb/Sr and Shand indices, supporting the model of their derivation from a mature sedimentary source. The MAG and the AG however, have low εSr_I values indicating derivation, at least in part, from sources more closely related to the mantle.

The time significance of the isochron plots noted in section 6.2.2 indicate that the MAG and CG evolved by closed system processes. The lack of coherent variations for the MVGP and AG on similar plots suggests that the granitoids did not evolve by open system but complex closed system behaviour.

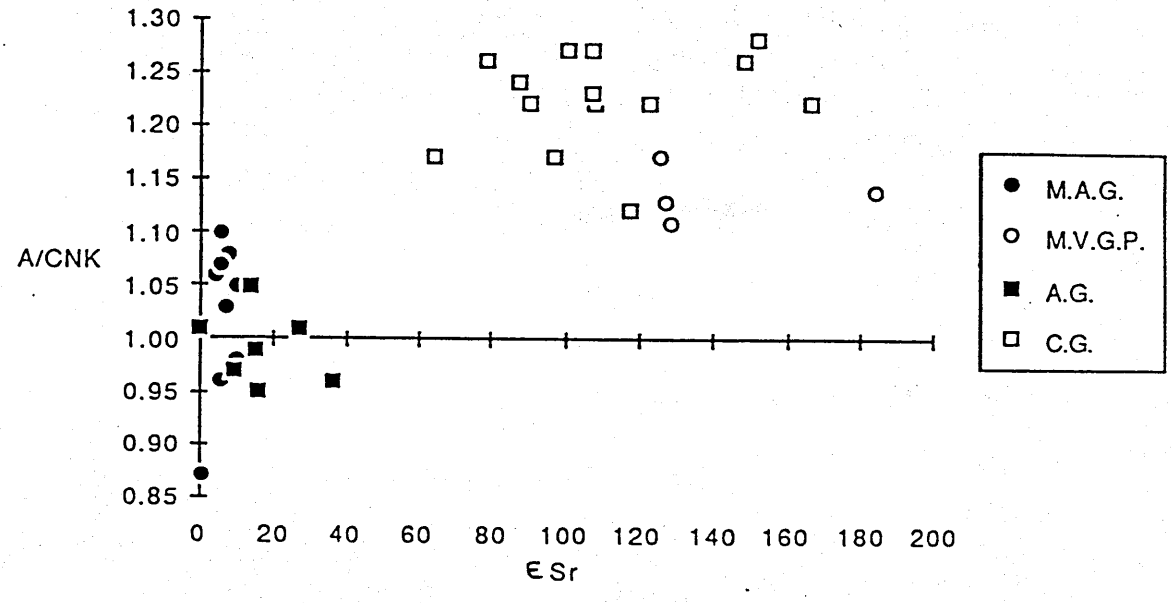

Figure 6.9

Discriminant diagram to show the highly peraluminous nature and high εSr of the MVGP and CG thought to be indicative of a mature crustal source, and the mildly peraluminous, low εSr character of the MAG and AG.

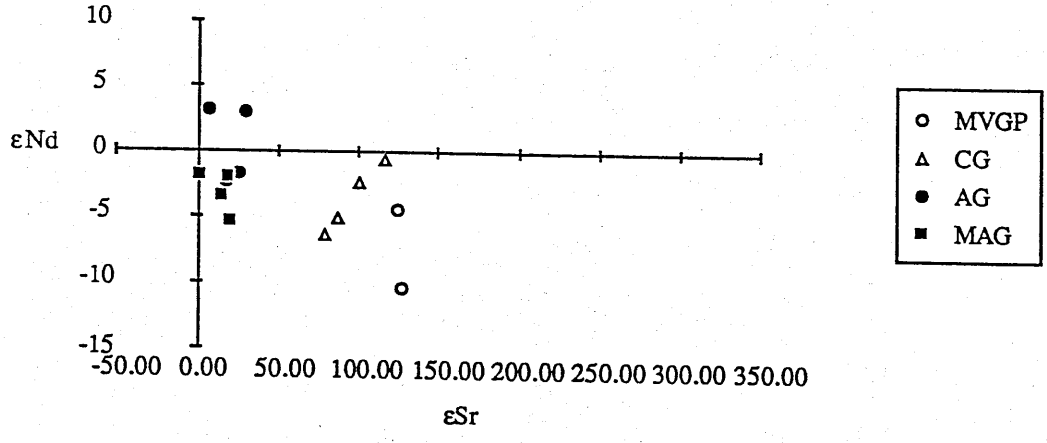

Figure 6.10

εSr vs.εNd plot for the Cordillera Granitoids. Note the overall concave upwards trend and the vertical trend for individual facies, except the CG, all CG values are however within two standard deviations of each other.

6.4 Neodymium isotope variations

A suite of granitoids and sediments analysed for Sr isotopes were also analysed for Nd isotopes; the results and methodology are given in Appendix A and B. The main aims in determining the Nd isotopes of these samples were; to constrain further the source of the granitoids, to model quantitatively possible processes involved in the formation of the granitoids, and to assess and model the evolution of the crust in the Central Andes.

6.5 Combined neodymium and strontium isotope geochemistry

Figure 6.10 shows a εSr vs. εNd diagram for all the granitoid data obtained calculated using the emplacement ages determined above. The overall curved trend of the data is typical of granitic rocks. The strongly peraluminous, two mica granites (MVGP and CG) form the lower part of the trend and the mildly peraluminous to metaluminous granitoids (MAG and AG) form the upper part, with two samples of the AG in the upper right hand quadrant. Although it has already been noted that the granitoids are the products of closed system evolution (MAG and CG) or incoherent processes (MVGP and AG) (see section 6.3), the inter-pluton variation is of interest, since the sources of the granitoids have been shown to be isotopically and trace elementally different (section 5.4.1). The variation can be interpreted in at least three ways; two (or more) component mixing, assimilation and fractional crystallization (AFC), and melting of previously remobilized crust. These models are discussed below.

6.5.1 Two component mixing

Within this geochemical model two physical methods of mixing, depending on the physical state of the mantle component, can be considered:

i) the mantle component may be a melt which is contaminated by crustal material; this mixing method will be termed 'contemporaneous mixing' since the extraction of the mantle component is effectively contemporaneous with emplacement of the granitoid

ii) the mantle component may be contained in a volcano-sedimentary sequence as recently erupted mantle derived volcanics, henceforth this method will be termed 'sedimentary mixing' due to the intermediary stage

The initial isotopic character of the mantle component in the second process will only be maintained for a short period of time after emplacement in the crust. For this reason the following modelling only relates to the contemporaneous mixing or sedimentary mixing soon after the extraction of the mantle component from the mantle.

In order to model the data the compositions of the mantle and crustal end-members must be constrained.

Mantle component

The presence of samples in the upper right-hand quadrant of Figure 6.9 confines the mantle component to lie in the upper left-hand (isotopically depleted) quadrant of the diagram. The trace element character of the mantle end-member is less easy to define. The Sr/Nd value of the mantle is generally greater than that of mature sediments, the presumed crustal end member; see below. The Sr/Nd value of the most primitive samples analysed of each facies are given in Table 6.2. On trace element grounds two types of mantle component were identified in the MAG and AG; a within plate component and a subduction related component respectively (section

	Sr (ppm)	Nd (ppm)	Sr/Nd	εSr_{300}	εNd_{300}
Calc-alkali basalt					
end-member	1144	32.4	35	-30	10
Within plate basalt					
end-member	1500	70	21	-30	10
B86/101	38	28	1.36	303.3	-2.19
B85/2	71	50	1.42	348.6	-8.07
Average Crust	350	26	9.72	320	-7
MAG	772	60	12	7	3.18
AG	267	28	9.5	15	-3.5
CG	78	9.6	8	87	-5
MVGP	40	9	4.4	125	-4

Table 6.2

Compositions of mantle and crustal components used in mixing model Figures 6.11 to 6.17 and most primitive samples of modelled facies.

5.4.2). Hawkesworth *et al.* (1987) noted a continuity of Sr/Nd ratios of MORB to within plate basalts of 10-20 and subduction related magmas have significantly higher values. Two end-members are considered; one a typical subduction related calc-alkali basalt end-member (Sr/Nd=21) (geochemistry and isotope values from Hawkesworth *et al.*, 1979) and an isotopically similar, within plate alkali basalt (Sr/Nd=35).

Crustal component

The trend of the data set on the εNd vs. εSr diagram (Figure 6.10) indicates that the crustal end-member has high εSr (< 150) and moderately negative εNd (≈ -10). Mature continental upper crust has high εSr and highly negative εNd (Allegre and Ben Othman, 1980). Lower crustal xenoliths have εSr and εNd close to zero and Lewisian granulites have negative εSr and highly negative εNd (Taylor and McLennan, 1985). None of these types of crust are likely to form a major component in the granitoids. Two samples of local upper crust (Palaeozoic metapelites), with high εSr_{300} and moderately negative εNd_{300}, are used as end-members in the calculations (Table 6.2).

Results

The Sr isotopic and SiO_2 values of the MAG can be modelled as simple mixtures of within plate alkali basalt and average crust, Figure 6.11.

The isotopic character of the granitoids can also be modelled by simple mixing (Figures 6.12 and .13). The two mixing models, for within plate basalt and calc-alkali basalt, produce similar results. The calc-alkali basalt end-member has a higher Sr/Nd ratio and therefore mixing models have more steeply curved trends. The within plate basalt end-member produces the best envelope around the data, but both models fail to include all the AG data. The proportion of mantle component in the MAG and the AG is modelled as 45 to 65% and that in the MVGP and CG as 25 to 35%.

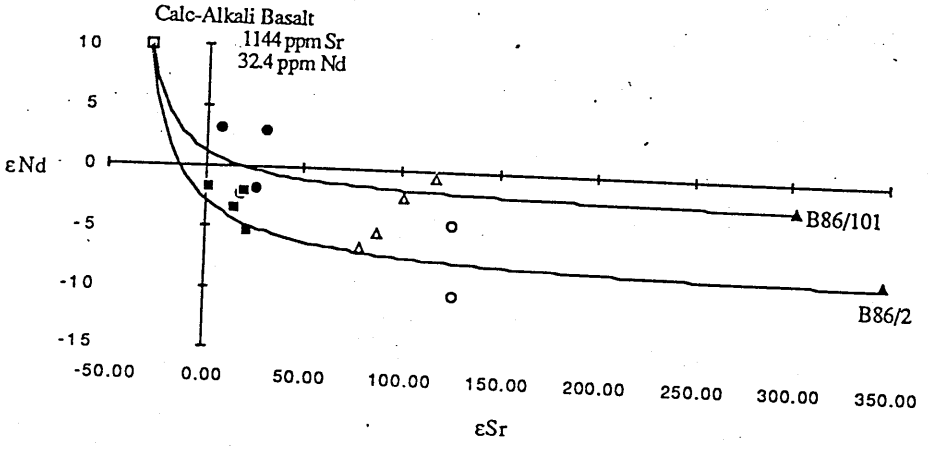

Figure 6.13

Mixing lines between calc-alkali basalt and upper crust. Symbols as in figure 6.10, values used in Table 6.2.

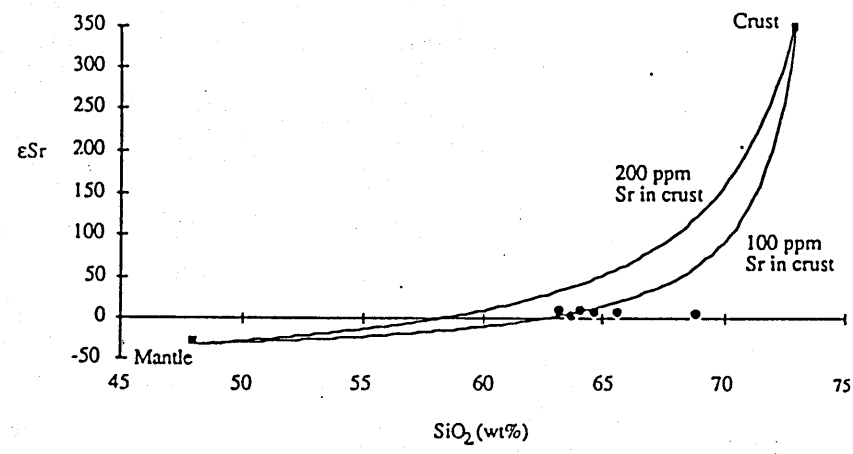

Figure 6.11

Simple mixing model for the MAG data of the alkali basalt mantle end member and two upper crustal compositions. See table 6.2 for basalt composition.

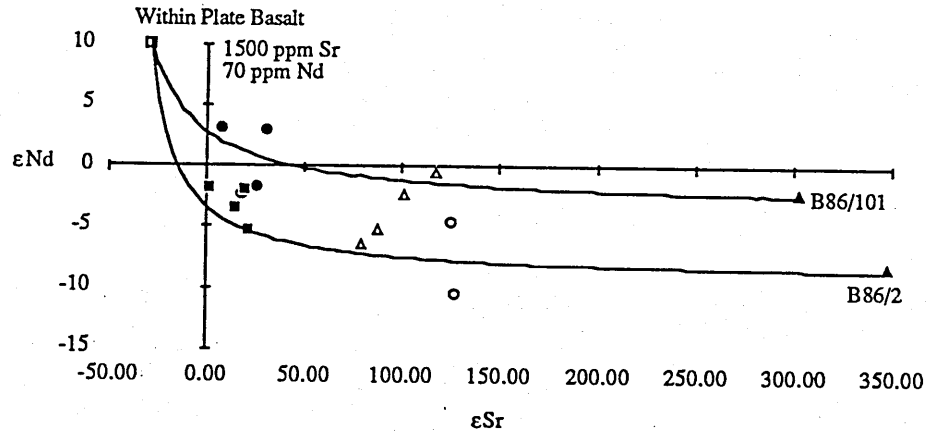

Figure 6.12

Mixing lines for within plate basalt and upper crust. Symbols as in figure 6.10, values used in Table 6.2.

Trace element modelling of the granitoids (section 5.4) failed to identify any mantle component in the CG and MVGP but indicated approximately a 50% mantle component in the MAG and 10% in the AG. The discrepancy for the CG and MVGP is probably due to the isotopic character of the crustal component chosen for the modelling having significantly higher εSr than the source of the CG and MVGP, implying the source to be younger than the lower Palaeozoic sediments used in the model. The discrepancy in the size of the mantle component for the AG is probably a result of the assumptions made in the modelling. The concordance of the results from trace element and isotopic modelling for the MAG suggests that the proportions of mantle and crustal components is approximately correct and that simple mixing is close to the method of their combination; this conclusion agrees with that of section 5.4.4 that the combination of crustal and mantle components in the MAG was by a AFC process with a high ratio of assimilation to fractionation, verging on simple mixing.

6.5.2 AFC modelling

Another level of complexity can be added to the contemporaneous mixing model considered above by allowing the magma to fractionate while it mixes with the crust. Thermal considerations of how a mantle melt can assimilate large quantities of cold crust require such a model, since the heat energy lost by the magma in melting crustal rocks will be replaced by the latent heat of crystallization of cumulates. The equation of DePaolo (1981), Equation 6.1, is used to model this type of evolution.

$$\varepsilon_m = \frac{\left[\frac{r}{r-1}\right]\left[\frac{C_a\varepsilon_a}{z}\right]\left[1-F^{-z}\right]+C_m^o F^{-z}\varepsilon_m^o}{\left[\frac{r}{r-1}\right]\left[\frac{C_a}{z}\right]\left[1-F^{-z}\right]+C_m^o F^{-z}}$$

Equation 6.1

ε_m = isotopic value of the final magma

ε_m = isotopic value of the initial magma

ε_a = isotopic value of the assimilated material

r = Ma/Mc, the ratio of the mass rate assimilation to the mass rate of crystal fractionation

C_a = concentration of element m in assimilant

C_m = concentration of element m in magma

C_m = concentration of element m in initial magma

F = the mass of magma remaining as a fraction of the mass of the original magma

z = (r+D-1)/(r-1), where D is the bulk distribution coefficient of element m

As discussed in section 5.4.4. Taylor (1980) considered the thermal controls on the assimilation, fractionation ratios of magma in the crust. Taylor (*op. cit.*) considered a value of r of 0.2 to be reasonable for the upper crust. However, the high ambient temperatures of the crust at the level of granitoid emplacement will allow higher values of r to occur and a standard r value of 0.4 has been assumed (see section 5.4.4.). The values of the bulk distribution coefficients are less easily constrained. Within a granitic system Sr will have a bulk distribution coefficient greater than one, due to the fractionation of plagioclase. REE studies of the facies under study (section 5.6.2) has shown that Nd concentrations fall with evolution. Given that the continental crust contains more Nd than the depleted mantle, the observed variation may only be explained by Nd having a distribution coefficient greater than 1. The compositions of the end-members are given in Table 6.2. Table 6.3 lists the parameters used to produce the model curves shown in Figures 6.14 to 6.17.

Curve		DSr	DNd	r
6.14	I	1.5	1	0.4
	II	1.5	2	0.4
	III	1.5	4	0.4
6.15	I	2.5	1	0.4
	II	2.5	2	0.4
	III	2.5	4	0.4
6.16	I	4.5	1	0.4
	II	4.5	2	0.4
	III	4.5	4	0.4
6.17	I	4.5	1	0.2
	II	4.5	1	0.4
	III	4.5	1	0.6

Table 6.3
Parameters used to construct the AFC models shown in Figures 6.14 to 6.17.

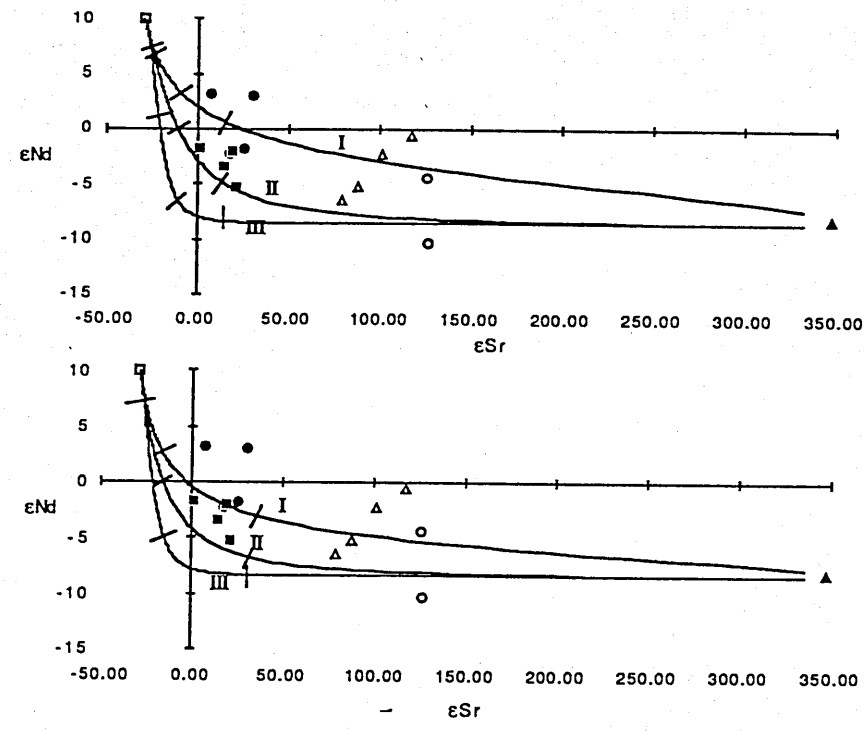

Figure 6.14

AFC model curves for within plate and calc-alkali basalts. D_{Nd} = 1, 2 and 4 (labelled I, II and III respectively) with constant D_{Sr} = 1.5 and r = 0.4 The curves are calibrated for F(ratio of magma volume to original magma volume) values of 0.25, .5 and 0.75. Symbols as in figure 6.10, values used in Table 6.3.

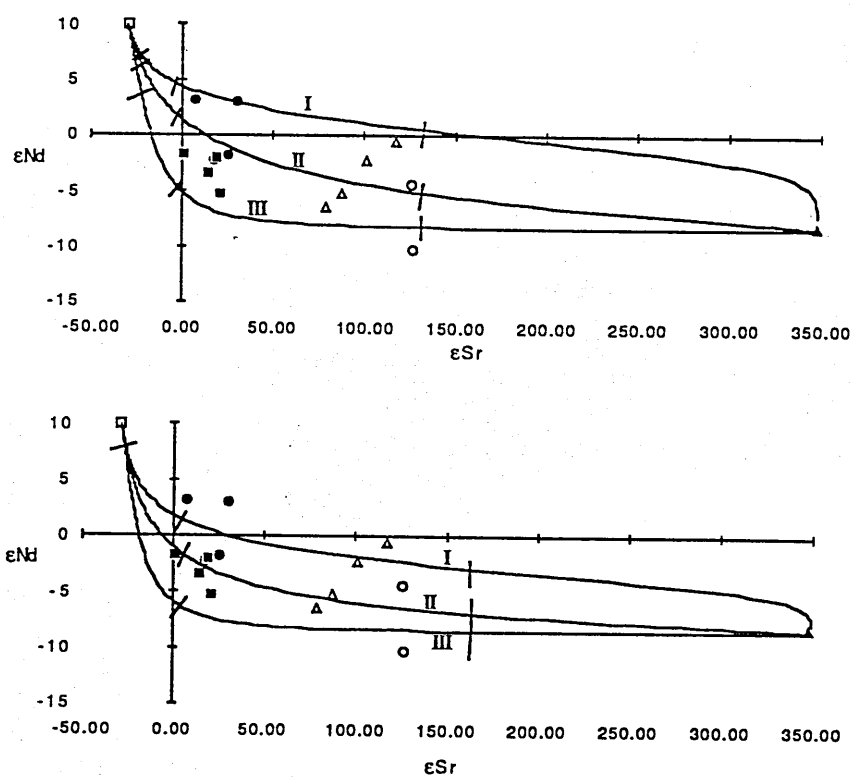

Figure 6.15

AFC model curves for within plate and calc-alkali basalts. D_{Nd} = 1, 2 and 4 (labeled I, II and III respectively) with constant D_{Sr} = 2.5 and r = 0.4. The curves are calibrated for F(ratio of magma volume to original magma volume) values of 0.25, 0.5 and 0.75. Symbols as in figure 6.10, values used in Table 6.3.

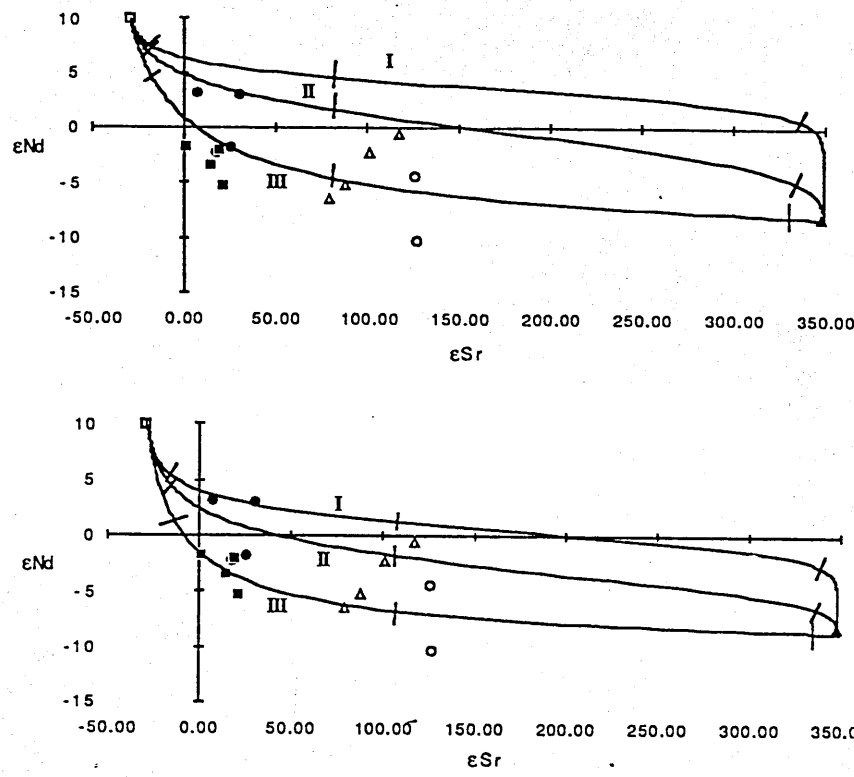

Figure 6.16

AFC model curves for within plate and calc-alkali basalts. D_{Nd} = 1, 2 and 4 (labeled I, II and III respectively) with D_{Sr} = 4.5, r = 0.4. The curves are calibrated for F (ratio of magma volume to original magma volume) values of 0.25, 0.5 and 0.75. Symbols as in figure 6.10, values used in Table 6.3.

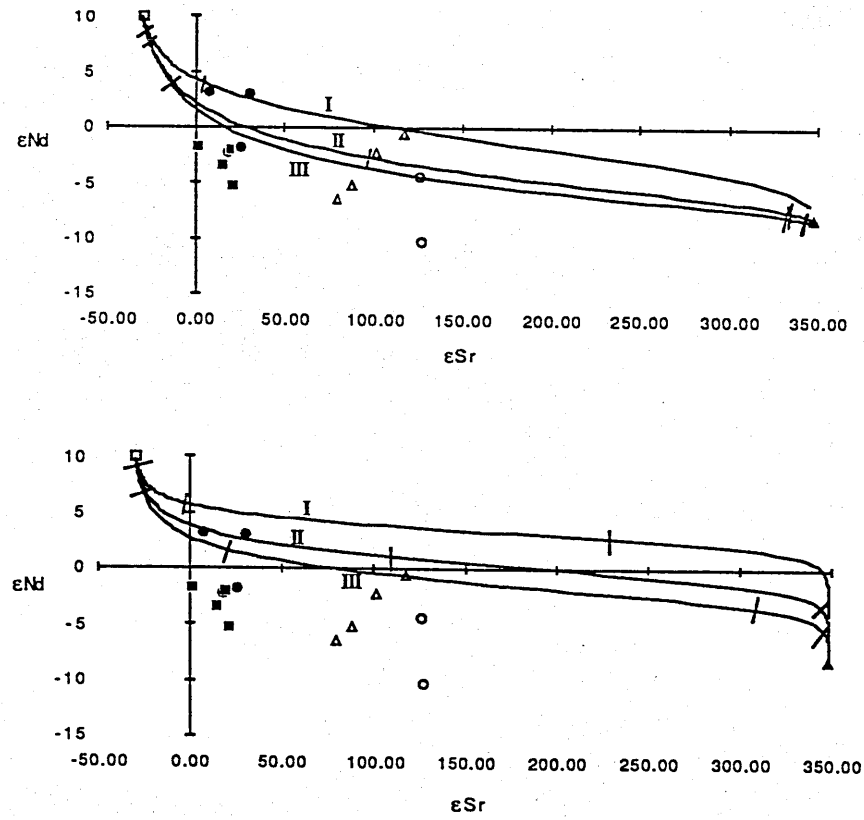

Figure 6.17

AFC model curves for within plate and calc-alkali basalts. r = 0.2, 0.4 and 0.6, (labeled I, II and III respectively) with constant D_{Sr} = 4.5 and D_{Nd} = 1. The curves are calibrated for F(ratio of magma volume to original magma volume) values of 0.25, .5 and 0.75. Symbols as in figure 6.10.

Results

Two sets of AFC lines are shown for each set of parameters; one for the within plate alkali basalt end-member and the second for the calc-alkali basalt end-member. Concave upward portions of the sigmoidal curves enclose the data set and can be produced by AFC models using geologically reasonable parameters. Relatively high values of D_{Sr} and low values of D_{Nd} are necessary for the model curves to enter the upper right-hand quadrant (Figures 6.14 to 6.17). Decreasing the value of r (i.e. decreasing the amount of material assimilated) increases the entry into the upper right-hand quadrant (Figure 6.17) but does not cause major changes in the shape of the curves. To enclose the low εNd data, low D_{Sr} and high D_{Nd} values are necessary (Figure 6.14 and 6.15 curves III). Too many parameters are involved in the modelling to allow the value of r to be constrained for comparison with the high value calculated for trace element models (section 5.4.4).

6.5.3 Crustal remobilization

McCulloch and Chappell (1982) suggested that the commonly observed curved granitic trend on εSr vs. εNd diagrams is purely intra-crustal in origin. Continental crust has higher Rb/Sr and lower Sm/Nd than the hypothetical bulk earth reservoir (see section 6.6.1 for discussion), therefore crust, newly formed from depleted mantle will evolve from the upper left quadrant into the lower right-hand quadrant of a εSr vs εNd diagram with time. Intra-crustal reworking will increase the Rb/Sr value of the crust and it is assumed in this model does not fractionate Sm/Nd (see section 6.6). Therefore with time the evolutionary trend of the reworked crust will flatten. To produce the spread of data observed, at any one time, pristine new crust must be formed continuously from the mantle with constant Rb/Sr and Sm/Nd.

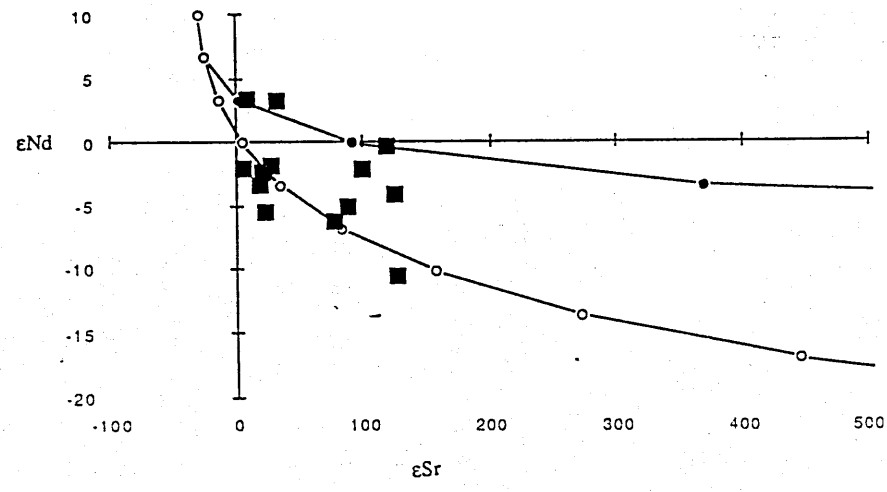

Figure 6.18

Evolutionary path of a piece of crust extracted from the depleted mantle 3000 Ma ago and remobilized every 300 Ma at which time it's Rb/Sr ratio was increased by 3x or 1.5x for the upper and lower curve respectively. Initial Rb/Sr = 0.06 and Sm/Nd = 0.19.

Results

Figure 6.18 shows the evolutionary path of a piece of crust extracted from the bulk earth reservoir 2.5 Ga ago and remobilized every 300 Ma. The upper line is for a 3x increase in Rb/Sr every 300 Ma and the lower line for an increase of 1.5x every 300 Ma. The data set for the Cordillera Real is enclosed by the two lines, indicating that the model can explain the inter-pluton variations. The large intra-pluton variations in εNd_I coupled to small variations in εSr_I are not so easily explained and are discussed below.

6.5.4 Discussion

All of the three models discussed can produce concave upward trends on εSr vs. εNd diagrams and therefore on purely isotopic grounds can explain the inter-pluton variations. Individual facies however have homogeneous εSr_I and heterogeneous εNd_I values, the exact opposite to the trend predicted by any of the above models.

Two explanations for this variation are proposed; either the ages used to determine the εSr and εNd values are wrong, or more complex multistage models are necessary.

The coincidence of the calculated Rb-Sr whole rock ages of the CG and the MAG indicate that the determined ages are true emplacement ages and therefore the plutons have evolved by simple closed system processes, modelled in section 5.2.3 and 5.3.3 as fractional crystallization.

Within the framework of multistage models, the last stage of development has been identified as fractional crystallization, a closed system process. Therefore, the intra-facies Nd isotope heterogeneity is a feature inherited from the source region. The presence of xenocrystic monazites and zircons (sections 5.3, 5.6, and 5.6.1) in all of the facies indicates that the large majority of the Nd budget of the magma was always contained in solid phases and not homogenized in the melt. The Nd isotope

characteristics of the granitoids are therefore an inherited feature of the source, while the Sr isotope characteristics are controlled by the evolution of the magma.

On isotopic arguments alone any of the three models discussed above could explain the εNd heterogeneity observed in the suites under study and could have been involved in the formation of the source of the granitoids. However, it has been argued in section 5.4.1 that the MVGP and the CG are derived from mature crustal sources, therefore the isotopic character of the granites is thought to be due to crustal remobilization, the εNd heterogeneity reflecting the varying age of the components which formed the source region.

The MAG and the AG are believed to be mixtures of mantle and upper crustal components (section 5.4.4). The isotopic character of the sources reflect the open system processes such as simple mixing and AFC involved in their formation (section 5.4.4).

6.6 Crustal evolution and Nd model ages

The major geological significance of Nd model ages, as proposed by McCulloch and Wasserberg (1978) is that the Nd model age of a crustal rock is the time since it was extracted from the mantle. This observation is based on two premises:

1) Crustal rocks have significantly lower Sm/Nd than the mantle, indicating that Sm/Nd fractionation occurred when the crust was extracted from the mantle.
2) The Sm/Nd ratio of a piece of crust cannot be significantly changed by crustal processes.

If these premises are correct then the model Nd age of a crustal rock is the time since it was extracted from the mantle. Such information can be used to construct growth curves for the crust, if samples representative of the crust can be obtained. Numerous workers (Allegre and Ben Othman, 1980; Harris *et al.*, 1984; Allegre and

Rousseau, 1984; Alberedè and Brouxel, 1987) have used both sediments and granites to this end. Before considering the geological significance of Nd model ages from Bolivia, these premises must be critically examined.

The first premise, that the main Sm/Nd fractionation event in the history of upper crustal material was its extraction from the mantle, can be tested by examining processes at continental destructive plate margins which are generally considered the most likely sites of continental crustal growth (Taylor, 1967).

In oceanic arcs Sm/Nd in basaltic andesites and basalts (SiO_2 <52 wt.%) ranges from 0.16 to 0.47 (Figure 6.19), the average value lies well above that of the upper crust. However, if the data are divided (on major element grounds) into tholeiitic and calc-alkali suites, the calc-alkali suite displays Sm/Nd values (average 0.23) very close to continental calc-alkali volcanics (0.21) and estimates of Sm/Nd for the total crust (0.22; Taylor and McLennan, 1985). This suggests that sub-continental lithospheric mantle may not be a necessity for the development of low Sm/Nd in the continental crust, as proposed by Rogers (1985). Instead low Sm/Nd ratios appear to be an intrinsic feature of the calc-alkali nature of continental subduction related magmatism.

The causes of the major and trace element differences between calc-alkali magmatism and tholeiitic magmatism are not clear but may result from either, differences in the residual and fractionation assemblages, and/or from source enrichment.

Grove and Kinzler (1986), have shown that in major element terms tholeiitic and calc-alkali andesites can be derived from the same olivine normative basalt via differing fractionation schemes. Tholeiites are believed to be the products of high level fractionation of plagioclase, rather than low level olivine fractionation, causing a characteristic iron enrichment in the magma. Calc-alkali basalts and andesites are believed to be the products of higher pressure fractionation dominated by olivine and augite with only minor plagioclase. Water saturation further decreases the stability of plagioclase and stabilizes amphibole which enhances the calc-alkali development of

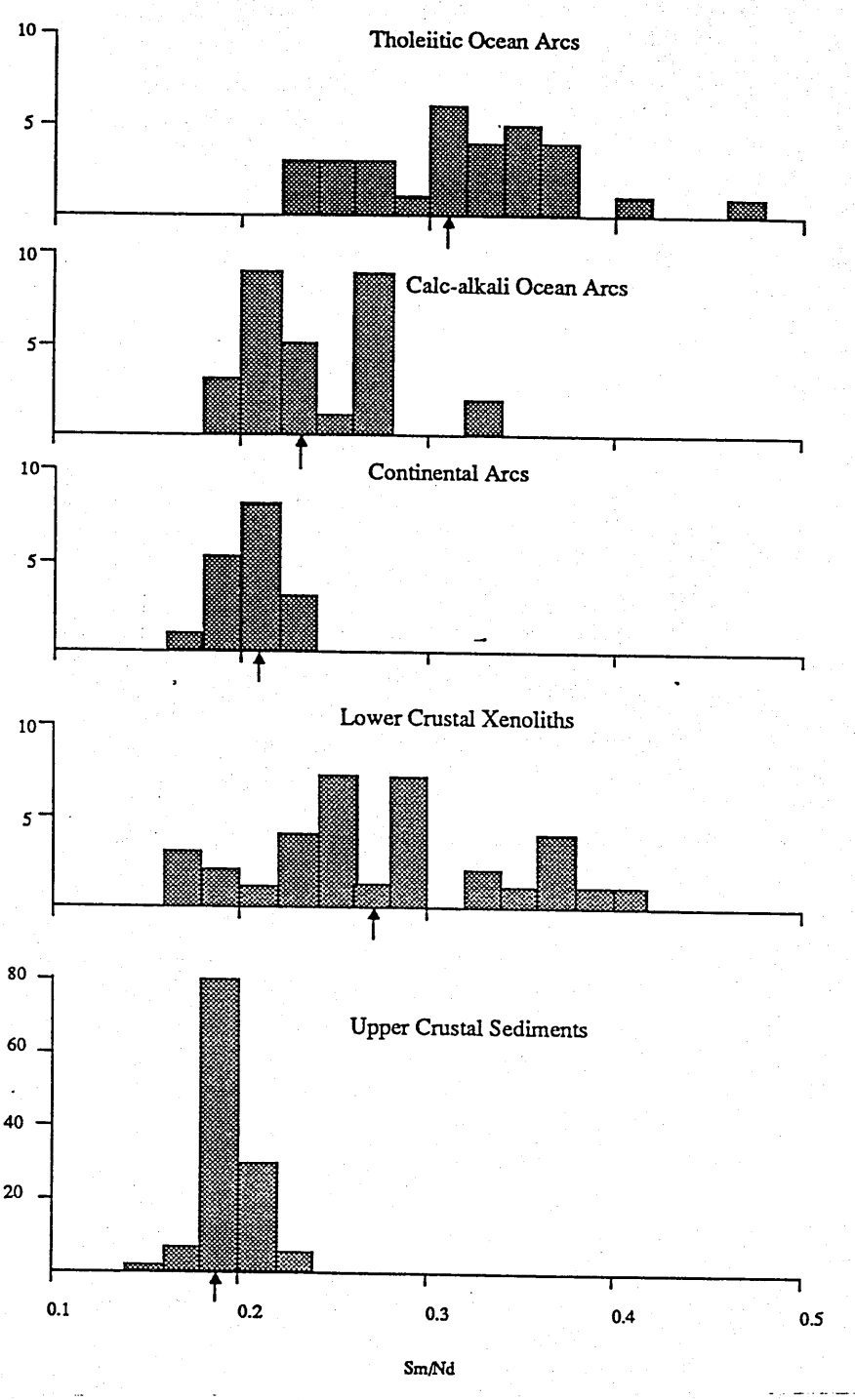

Figure 6.19

A histogram of Sm/Nd for basalts and basaltic andesites divided by crustal setting and major element chemistry, mean values indicated by arrows. (Hawkesworth and Powell, 1980; Gill, 1970; McCulloch and Perfit, 1982; Lopez-Escobar *et al.*, 1979; Hawkesworth *et al.*, 1979; Peccerillo and Taylor, 1976; Thorpe *et al.*, 1976) and lower crustal xenoliths (Rogers and Hawkesworth, 1982; Rudnick *et al.*, 1986, Rudnick and Taylor, 1987). The oceanic tholeiites display a wide range of Sm/Nd with an average of approximately 0.3. The oceanic and continental calc-alkali samples have lower Sm/Nd values and display a high degree of overlap, but have average values significantly above upper crust. Lower crustal xenoliths display a wide range of values, but have an average greater than that of the calc-alkali samples, accounted for by intra-crustal Sm/Nd fractionation and balanced by the low Sm/Nd upper crust.

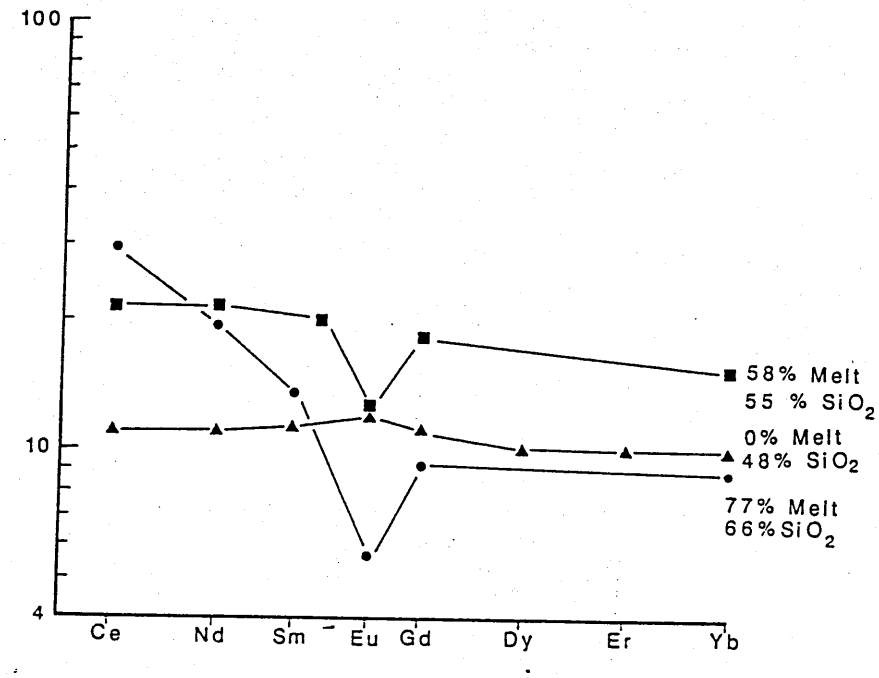

Figure 6.20

The modelled REE evolution of an olivine normative basalt from St. Kitts for the calc-alkali evolution scheme of Grove and Kinzler (1986). The modelled patterns are totally unlike observed REE evolution schemes for calc-alkali rocks.

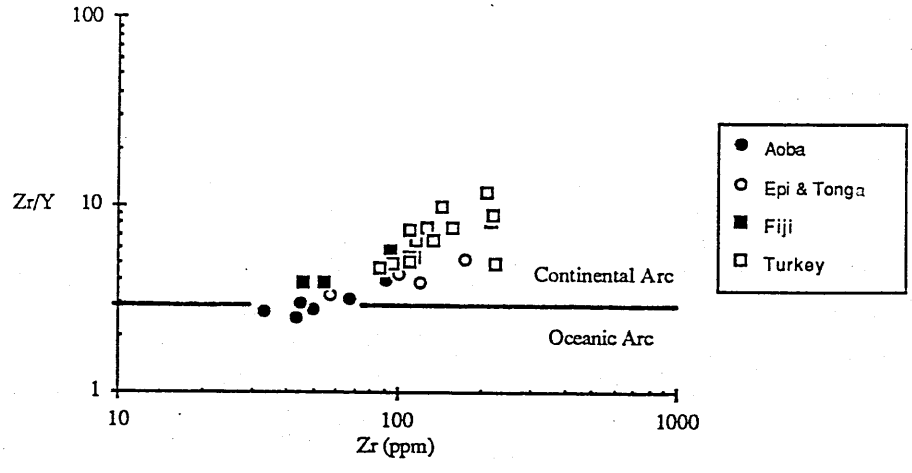

Figure 6.21

Zr/Y vs. Zr fields of continental and oceanic arcs from Pearce (1983). Open circles represent oceanic calc-alkali samples from data set of Figure 6.19 closed circles continental calc-alkali samples from same data set.

the magma. This model, based purely on major elements can be tested using trace elements. Figure 6.20 shows the modelled REE evolution of an olivine normative basalt from St. Kitts (Hawkesworth and Powell, 1980), of very similar composition to the initial magma of Grove and Kinzler (1986) from the same location, during the fractionation scheme proposed by Grove and Kinzler (1986). The evolved pattern is unlike that of any calc-alkali magma and therefore it seems unlikely that the tholeiites and calc-alkali magmas can be derived from the same source. Gorton (1977) working on calc-alkali and tholeiitic magmas from the New Hebrides came to a similar conclusion. It therefore seems more likely that the difference between calc-alkali and tholeiitic basalts lies in their source regions.

Pearce (1983) noted a fundamental difference between the enrichment of oceanic and continental calc-alkali rocks. Figure 6.21 shows a plot of Zr/Y vs. Zr with fields of continental and oceanic arcs defined by Pearce (*op. cit.*) on a wide data set. The available data from the subduction related rocks discussed above are also shown, all the oceanic arc data is calc-alkali. The Zr/Y ratios of arcs is interpreted as a measure of within plate enrichment, a feature of subcontinental lithosphere (Pearce and Norry, 1979). Almost all the oceanic calc-alkali data plots in the continental arc field suggesting the involvement of the subcontinental lithosphere in the oceanic arcs and its fundamental involvement in the LREE and alkali enrichment (calc-alkali nature) of the magmas.

In summary the flux of material from the mantle to the crust in continental subduction zones displays Sm/Nd ratios similar to those of bulk continental crust (continental calc-alkali volcanics Sm/Nd= 0.21, bulk continental crust Sm/Nd =0.22) due to the calc-alkali nature of the magmatism, which results from enriched continental lithospheric mantle in both continental and 'oceanic' arcs.

The upper crust has significantly lower Sm/Nd (0.19) than the mantle flux, indicating that extraction from the mantle is not the only cause of Sm/Nd fractionation.

The second assumption: that Sm/Nd cannot be fractionated by intra-crustal

processes, as noted above, is not borne out by differences between Sm/Nd in the upper crust (0.19; Figure 6.19) and that observed in continental arcs. Estimates of the composition of the lower crust suggest it to be significantly higher in Sm/Nd than the upper crust (estimate based on lower crustal xenoliths, Rudnick *et al.*,1986; Rudnick and Taylor, 1987; Rogers and Hawkesworth, 1982; 0.26-0.27; Figure 6.19), supporting arguments of intra-crustal Sm/Nd fractionation to be an important process. The bulk crustal Sm/Nd has been estimated by Taylor and McLennan (*op. cit.*) at 0.22 and matches well with an upper crust forming 25% of the total crust (top 10 -15 km; Griffin and O'Reilly, 1987) and the lower crust having an Sm/Nd of 0.26-0.27 Figure 6.19. Rogers and Hawkesworth (1982) have argued that the lower crust is dominated by mafic cumulate, formed by the ponding of upwelling magmas at the base of the crust due to the density change. This is a highly suitable mechanism for separation of a high Sm/Nd basic fraction from the low Sm/Nd intermediate fraction which continues upward to form the upper crust.

Within the upper crust, surface and metamorphic processes are unlikely to fractionate Sm/Nd in fine grained sediments (Chaudhuri and Cullers, 1979; Menzies *et al.*, 1979). Frost and Winston (1987) have pointed out that in coarse grained sediments REE can be fractionated by sedimentary processes. They have reported data from sediments in a single sedimentary supergroup; the fine grained sediments display a narrow range of Sm/Nd of 0.16 to 0.200 (average 0.19), while the coarse sediments display a wider range of Sm/Nd ratios 0.199 to 0.414 (average 0.262). The cause of the fractionation is that in coarse grained sediments the REE are dominantly controlled by heavy minerals of magmatic origin, rather than clays, which compose fine grained sediments. Concentrations and depletions of these heavy minerals due to their high density can cause significant changes in the Sm/Nd ratio of a sediment.

Magmatic processes can also cause significant changes in Sm/Nd. As noted in section 5.6.1 accessory phases control the REE budget of granitic systems and the

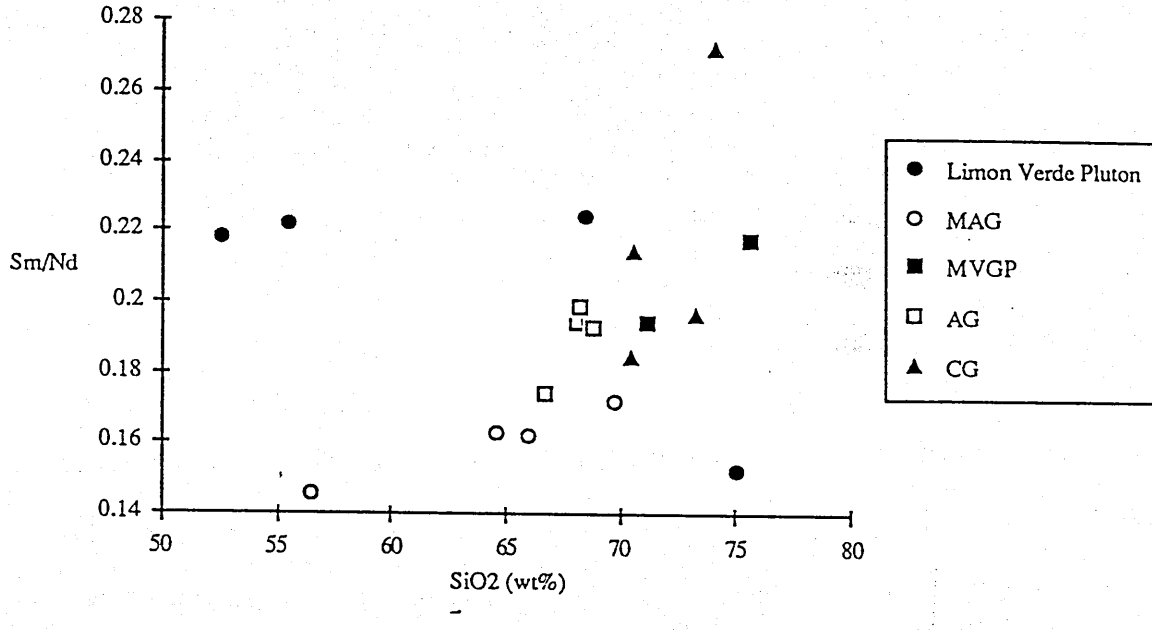

Figure 6.22

SiO_2 vs Sm/Nd for granitoids from the Cordillera Real, Bolivia and Coastal ranges, Chile (Limon Verde Pluton; Rogers, 1985). The majority of the suites show steep positive trends reflecting the control of accessory phases on REE of the acidic rocks.

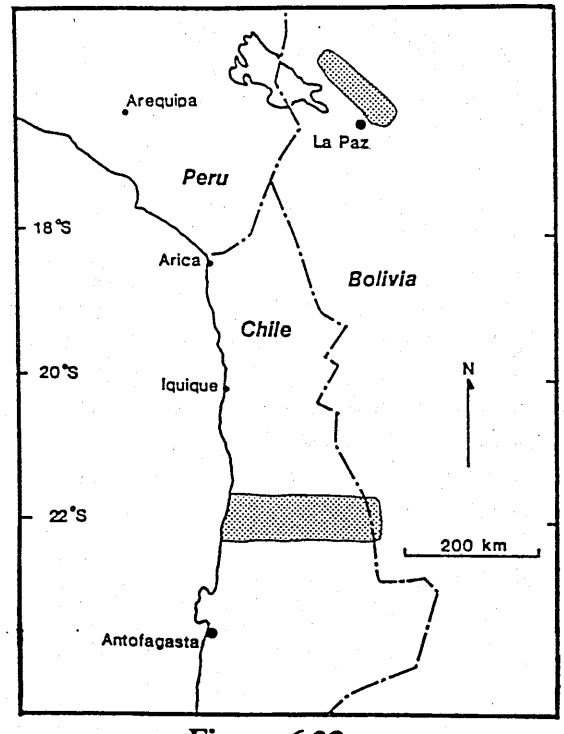

Figure 6.23

Location map for the samples used in model age studies.Chilean Data from Rogers (1985).

majority of the Hercynian granitoids studied show an increase in Sm/Nd with evolution (Figure 6.22), reflecting the control of minor phases. This variation, however is restricted to high silica melts dominantly derived from upper crustal sources, and as such is not an important effect in bulk crustal Sm/Nd fractionation. This problem of acidic magma derived from upper crust, fractionating Sm/Nd can be overcome by calculating the model age of a sample based on it's initial $^{143}Nd/^{144}Nd$ and an average bulk crustal Sm/Nd of 0.19 (based on compilation of sedimentary values, see Figure 6.19 for references). This procedure has been used throughout the following work.

It therefore seems likely that upper crustal, non-magmatic, processes do not fractionate Sm/Nd in fine grained sediments; while lower to upper crustal fluxes, being dominantly magmatic, do cause changes in Sm/Nd. Intermediate magmas (up to 65% SiO_2), emplaced into the upper crust, are mainly the result of lower crustal fractional crystallization and have lower Sm/Nd ratios than the cogenetic lower crustal cumulates. Less volumetrically important, acidic (greater than 65% SiO_2) magmas, emplaced into the upper crust, are often the results of anatexis of mature sedimentary sources and usually have higher Sm/Nd ratios than average upper crust due to the commonly residual nature of accessory phases.

In summary, the moderately low Sm/Nd (0.21) ratios of mantle to crust additions at destructive continental margins appear to be related to enriched subcontinental lithosphere. The low Sm/Nd (0.19) values of the upper crust are however the product of intra-crustal fractionation, the lower crust forming a reservoir with average Sm/Nd ratios (0.26-0.27) higher than that of bulk crust (0.22). Therefore, Nd model ages are dependent, both on the time of extraction from the mantle and from the lower crust.

6.6.1 Model ages

The foregoing discussion has placed some limitation on the interpretation of Nd

model ages. The effects of these and other limitations may be of importance and must be considered in the interpretation of Nd model ages. All Nd model ages will underestimate the time of extraction from the mantle due to the high Sm/Nd (0.22-0.25) lower crustal stage being ignored in the calculations. However, this error may be small due to the comparatively short lower crust residence time of a fractionating magma. Granitoids with high silica values (> 65 wt % SiO_2) will commonly have been affected by Sm/Nd fractionation due to accessory phase fractionation; in granites believed to have been derived from mature sediments this may be corrected for by using a bulk mature sedimentary Sm/Nd value (taken here as 0.19) in the Nd model age calculation rather than the measured Sm/Nd. The role of inherited accessory phases in controlling the REE budget of granitoids was highlighted in sections 5.3 and 5.6.1. The importance of inherited accessory phases in preserving source region Nd isotope characteristics was discussed in section 5.6.1 and will be reflected as a range of Nd model ages dependent on the heterogeneity of the source.

All of the sediments of this study are fine grained and therefore are not prone to sedimentary Sm/Nd fractionation (section 6.6) and are taken to represent the Nd isotopic character of a large area of the Central Andes. The granitoid samples while representing much smaller sample volumes do provide information on the subsurface character of the crust. See appendix A for calculations and constants used.

The major result of the model age determinations for the granitoids of the Cordillera Real is that the Nd model ages are all significantly older than the emplacement ages; this was expected for the CG and MVGP which are thought to have been derived from metasediments. However, the Nd model ages of the MAG and AG are also significantly older than the emplacement age (approximately 3-4x), this implies that either the source of the granitoids had existed in the crust for a significant time before the granitoid was emplaced, or, more likely, the granitoids are combinations of crust and juvenile mantle. Assuming the Nd contents of the crust and mantle component to be as shown in Table 5.5 and the model age of the mantle component to be 0 Ga and the upper crust to be 1.8 Ga (Nd model age of B85/2), a

crustal component of 35 to 45% would be necessary to produce the observed range of model ages; this value is similar to those calculated in section 5.4.4. for the amount of crust involved in the formation of the MAG, but significantly smaller than that calculated for the AG. The implications of the lack of agreement for the two models, if they are both correct, is that the source of the AG matured in the upper crust for 600 Ma, or longer in the lower crust. This could explain the differing type of mantle component identified in the MAG and AG. Unfortunately it is more probable that the models used are over simplistic.

6.6.2 Nd model ages in the Central Andes

The data base for this section is based on work by the author in the Cordillera Real, Bolivia and work by Rogers (1985) on rocks from a traverse along 22 °S from the Chilean coast to the Bolivian border (Figure 6.23).

Figure 6.24 shows a simple plot of T^{Nd}_{DM} vs stratigraphic age for intrusive and extrusive igneous samples and sediments from the Central Andes. The division between the Hercynian and the Andean data at about 200-250 Ma is clearly defined in the Nd model ages. The Hercynian samples have old model ages (0.55-1.4 Ga) indicative of old crustal sources, supported by their Sr isotopic and trace elemental character (sections 6.3 and 5.3); the San Ignacio (1300 Ma), the Sunsas and Aguapei (1000 Ma) mobile belts to the east of the Cordillera Real provide a likely source for crust of this age and do contain metapelitic units. The Andean rocks of emplacement age 200 to 50 Ma have model ages of 300-1000 Ma. This indicates either a 300-1000 Ma (pre-Hercynian) intra-crustal source or, more likely, a mixed source with a wide range of model ages; the older Nd model ages probably result from mixing of crust with Nd model ages greater than 1 Ga with a juvenile mantle component. The youngest age of a suite, may however, date a mantle extraction event. For intrusions younger than 50 Ma the Nd model ages become significantly older with values similar to the Hercynian granitoids. This indicates an increase in the role of old

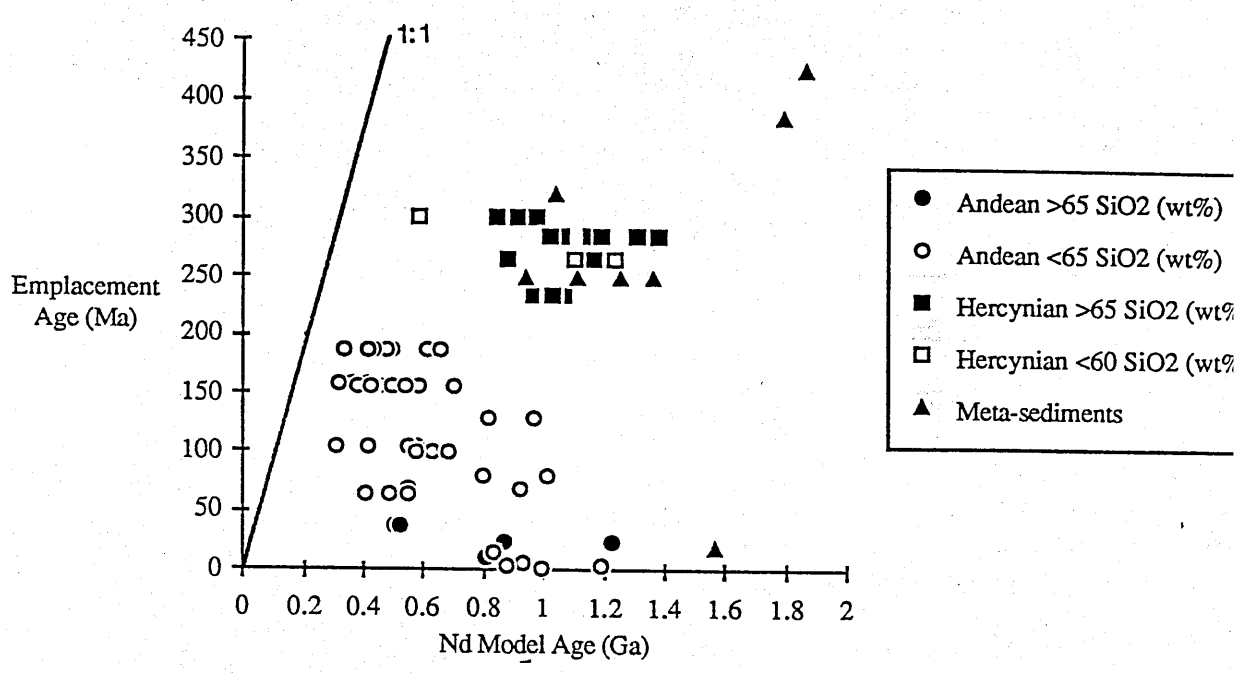

Figure 6.24

Nd model age vs emplacement age for Andean and Hercynian volcanics, plutonics and sediments. Nd Model ages of granitoids > 65% SiO_2 have been calculated using a constant Sm/Nd ratio of 0.19; see section 6.6.1 for details.

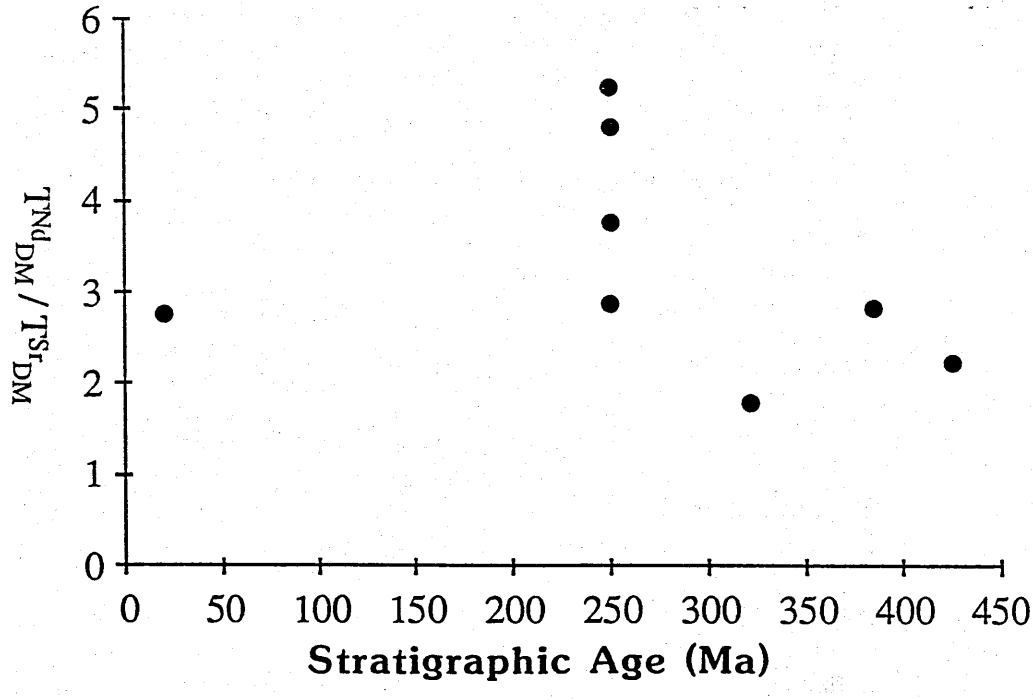

Figure 6.25

T^{Nd}_{DM}/T^{Sr}_{DM} vs stratigraphic age for Central Andean sediments (including data, Rogers, 1985). The Hercynian data show a systematic increase in T^{Nd}_{DM}/T^{Sr}_{DM} with stratigraphic age reflecting an increase in the rate of crustal recycling during the orogen.

continental crust during the Tertiary, identified as the time of crustal thickening in the Andes (section 2.5). The cause of the uplift is thought to be intra-crustal thrusting, which would provide conditions of rising geotherms in wet upper crust leading to intra-crustal melting (Harris *et al.*, in press). The single Tertiary sediment has a Nd model age indistinguishable from the Palaeozoic sediments. This suggests that the crust formed during the Andean did not form part of the provenance for the Altiplano sediments during the Tertiary. This may reflect Andean uplift only occurring during the Tertiary leaving insufficient time for erosion and incorporation into Tertiary sediments.

6.6.3 Sr model ages and intra-crustal recycling

Sr model ages can be calculated in the same way as Nd model ages, but do not carry the same age significance. Intra-crustal processes almost invariably cause Rb/Sr to increase so that Sr model ages are usually younger than Nd model ages and the ratio of $T^{Nd}_{DM} / T^{Sr}_{DM}$ supplies information about the extent and rate of intra-crustal reworking. Figure 6.25 shows a diagram of $T^{Nd}_{DM} / T^{Sr}_{DM}$ vs stratigraphic age for sediments. The trend reflects variation, both in Sr model ages, due to intra-crustal processes and Nd model ages, due to differing age source regions. Davies *et al.* (1985) pointed out that to a first approximation:

$$T^{Nd}_{DM} / T^{Sr}_{DM} = (Rb/Sr)T^{Strat} / (Rb/Sr)T^{Nd}_{DM}$$

This equation can be used to calculate the minimum change in Rb/Sr with time of the source of the sediment. The oldest sedimentary sample with a Nd model age of 1.86 Ga represents crust that has undergone an increase in Rb/Sr of at least 2.2x in 1.43 Ga (≈1.2x per 500 Ma); while the youngest Palaeozoic sediments have an average Nd model age of 1.2 Ga and represent crust that has undergone an Rb/Sr increase of at least 4x in 0.95 Ga (≈2 per 500 Ma). The single Tertiary sediment has a model age of 1.6 Ga and a source with a minimum Rb/Sr growth rate of 1.3 per 500 Ma.

Martin and Meybeck (1979) estimated that Rb/Sr increased by 68% every

sedimentary cycle; if this is taken as the only cause of Rb/Sr increase then sedimentary reworking occurred at least every 1 Ga for the source of the early Palaeozoic and Tertiary and every 400 Ma for the source of the late Palaeozoic sediment. The increase in recycling during the Palaeozoic reflects the development of the Hercynian Orogeny, an intra-crustal event in the area of study. During the Hercynian, the recycling must have been more rapid than calculated since the calculated recycling rate for the late Hercynian sediments represents a minimum average over the previous 1.2 Ga. The recycling rate for the source of the Tertiary sediment is an over estimate due to the young age of the sample rather than the true rate.

Using the initial $^{87}Sr/^{86}Sr$ ratio of a granitoid sample and it's Nd model age the time integrated Rb/Sr ratio of the protolith can be calculated. Figure 6.26 shows a plot of protolith Rb/Sr vs Nd model age. The majority of the Andean data display low protolith Rb/Sr values ($\approx$ 0.1) over a range of Nd Model ages from 0.5 to 1 Ga. This reflects the immature nature of the protolith which has not undergone extensive intra-crustal reworking. The Hercynian data and some of the Andean data display higher protolith Rb/Sr values indicating derivation from sources which have undergone extensive intra-crustal recycling, an inference supported by their old model ages. Calculated Rb/Sr evolution lines for varying rates of Rb/Sr increase are shown in Figure 6.26. The majority of the Hercynian data are enclosed by evolution lines for increases in Rb/Sr of 1.2x per 500 Ma to 1.75x per 500 Ma. Some of the Hercynian data and the stratigraphically older, high protolith Rb/Sr Andean data require higher rates of Rb/Sr fractionation of up to 3x per 500 Ma. Recycling rates of 1.5x to 2x per 500 Ma for Damara (SW Africa) granitoid protoliths from McDermott (1986) are shown for comparison.

In summary, there are distinct model age differences between the Andean and Hercynian data. The Andean granitoid samples are characterized by comparatively low Nd model ages, reflecting mantle inputs during the orogenic event. The Nd

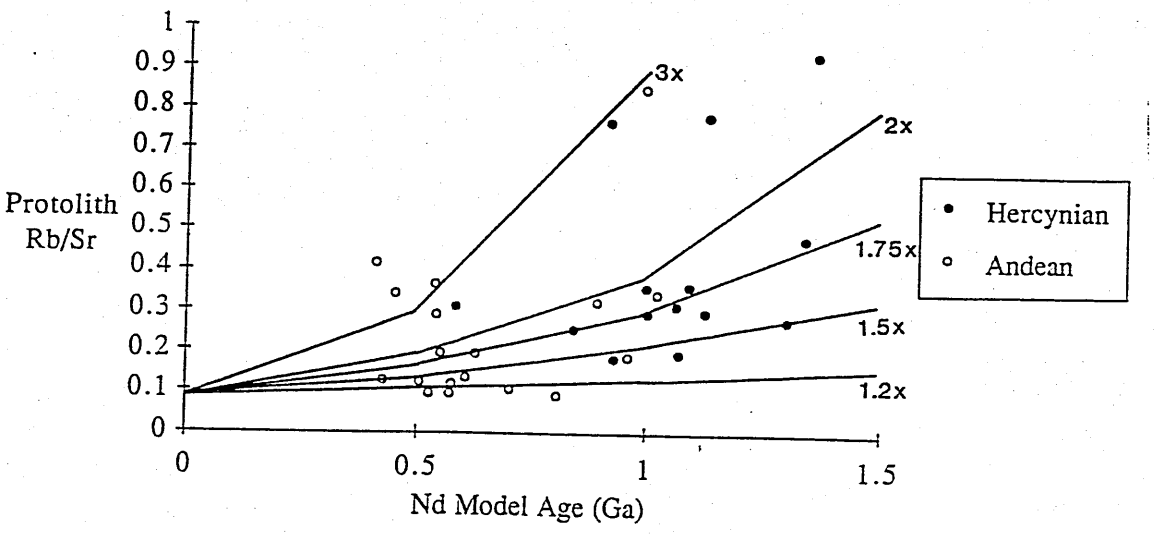

Figure 6.26

Nd model ages vs calculated protolith Rb/Sr for Hercynian and Andean granitoids. The Andean data display predominantly low protolith Rb/Sr values reflecting immature crustal sources while the Hercynian data have higher protolith Rb/Sr values reflecting mature crustal sources. The majority of the Hercynian data are enclosed by models of Rb/Sr increasing by 1.2x and 1.75x per 500 Ma, but some data requires recycling rates of as high as 3x per 500 Ma. Recycling rates of 1.5x to 2x per 500 Ma calculated by Mc Dermott (1986) for the Damara granitoids (SW Africa) are shown for comparison.

model ages increase with decreasing emplacement age consistent with crustal thickening by intra-crustal thrusting. The source regions are dominantly characterized by low Rb/Sr ratios reflecting their non-sedimentary nature.

The Hercynian granitoid samples all have Nd model ages of around 1 Ga reflecting the intra-crustal nature of the Hercynian Orogeny. The protolith Rb/Sr ratios are higher than those of the majority of the Andean granitoids and crustal recycling rates for the protoliths are estimated at between 1.2x and 1.75x per 500 Ma although values as high as 3x per 500 Ma may have occurred. In section 6.5.3, on the basis of εSr and εNd variations, similar ranges for the rate of change in Rb/Sr in the granitoid protoliths were estimated at 1.95x and 6x per 500 Ma (1.5x and 3x per 300 Ma), these values are comparable to those of McDermott (1986) for granitoids in SW Africa, 1.5x and 2x per 500 Ma and Southern Britain (Davies *et al.*, 1985) 1.5x per 500 Ma (2x per 900 Ma).

Palaeozoic sediments also reflect varying rates of Rb/Sr increase during the Hercynian. The change appears to be systematic and rates of Rb/Sr change increase from 1.2x to rates over 2x per 500 Ma for the period early to late Hercynian; this reflects the intra-crustal nature of the Hercynian and the high recycling rates during the Palaeozoic. A single Tertiary sediment has a Nd model age identical to that of the Palaeozoic sediments indicating a lack of Andean material in the source region, probably due to the short period of time after Tertiary uplift that the sediment was deposited.

CHAPTER 7
Summary

7.1 Introduction

In this chapter the geochemical and isotopic constraints on the petrogenesis of the granitoids of the Cordillera Real are summarized. The generation of pure crustal melts and melts containing mantle components; and the controls on magma ascent and emplacement are discussed. The results of the Nd and Sr model age study of Hercynian and Andean granitoids and metasediments are summarized and the implications discussed. Finally an overall model for the formation of the Cordillera Real is presented, synthesizing the geochemical and geochronological results of this work and the structural and sedimentological results of other studies in the Central Andes.

7.2 Crustal melt petrogenetic modelling

Mature metasedimentary melts, in the Cordillera Real, are characterized geochemically by being strongly peraluminous and by having high Rb/Sr and Rb/Ba ratios (section 5.4.1). Isotopically mature metasedimentary melts have high εSr and Nd model ages significantly older (>1 Ga) than their emplacement age (chapter 6). The CG and MVGP display all of these characteristics and are believed to be derived from a metasedimentary source. The CKG and SG are thought to have been derived from the same type of source, although they have not been shown to exhibit all the features listed above.

The least evolved samples of the CG and MVGP, can be modelled, on trace

element grounds, as between 24 to 34 wt% partial melts of a typical metapelite. Such melt fractions exceed the critical melt volume necessary for a melt to segregate from it's source (section 4.4.1). Fluid absent, biotite breakdown appears to be a feasible method to produce such melts. The emplacement conditions of approximately 500 to 700 °C and 2 to 5 kbar (chapter 4) place a lower limit on the conditions for melting.

7.3 Modelling of melts containing mantle components

Granitoids, in the Cordillera Real, containing a mantle component (in the broadest sense) are characterized geochemically by being metaluminous to weakly peraluminous, trace elementally they have low Rb/Sr ratios (section 5.4.1). Isotopically such granitoids are more distinctly characterized by low εSr and εNd (chapter 6). The MAG and AG fulfil these criteria. The mantle component can be classified as either, within plate or, subduction related, based on the abundance of HFS elements (section 5.4.2). The mantle components in the MAG and AG have been identified as being of within plate and subduction related affinities respectively. The HPG, IG, and UG are believed to belong to this group, although it has not been demonstrated that they display all the criteria listed above. The IG shows trace elemental similarities to the MAG and is thought to contain a similar within plate mantle component, whereas the mantle component in the HPG and UG is believed to be of subduction related affinities.

The identification of a whole rock Rb-Sr age for the MAG indicates that the observed evolution was a closed system process and did not involve crustal contamination. Mixing and AFC modelling demonstrates that the least evolved samples of the MAG contain 50% of a within plate mantle component which has assimilated upper crust by AFC with large ratios of assimilation to fractionation (>10:1). The AG is better modelled as a simple mixture of approximately 90% upper

crust and 10% subduction related mantle component.

The Nd model ages of samples of the MAG (1 Ga) and AG (1.1 Ga), which must be mixed ages, are significantly older than their emplacement age (300 Ma), this suggests that the crustal component in the source of the granitoids was old (> 1 Ga) upper crust, presuming the mantle component to be juvenile. A mixture of approximately 55% local metasediments (13.5 ppm Nd, Nd model age ≈1.8 Ga) and a juvenile within plate mantle component (50 ppm Nd, Nd model age 0 Ga) produces model ages of 1 Ga. This quantity of crustal component agrees with the estimate based on AFC modelling of the MAG and is believed to be good evidence for a two stage model for the MAG.

The first stage involved the open system incorporation of 50% crust into a within plate basalt by AFC with a high ratio of assimilation to fractionation, a feasible process some depth (≈20 km) due to the high ambient temperatures. The second stage involved the closed system evolution of the magma by fractional crystallization at the depth of emplacement (approximately 8 to 20 km). The division between the first and second stage was primarily controlled by the crystal content of the magma. The upward motion of the magma through increasingly cooler crust would cause the ratio of assimilation to fractionation to fall with decreasing depth, resulting in a rapid increase in the crystal content of the magma. Once the magma contained less melt fraction than the critical melt fraction (30 to 50 %; section 4.4) upwelling would cease. The evolution of the magma after this event would be by *in situ* fractional crystallization. Minor assimilation might occur at the margins of the cooling pluton but the contamination would not spread through the body of the pluton due to the lack of internal convection.

The evolution of the AG is less clear. Simple mixing modelling of the AG indicates it contains only 10% mantle component. The Nd model ages of the AG (1.1 Ga) are considerably younger than those of a 90% old upper crust, 10%

subduction related basalt mixture (1.6 to 1.7 Ga); this implies either a larger mantle component, or more likely, assimilation of considerably younger crust.

7.4 In situ evolution

The age significance of the isochron plots for the MAG and CG indicate that, the observed variations in the plutons are the product of isotopically closed systems, so that geochemical variations can be modelled in terms of fractional crystallization. Calculated assemblages are dominated by quartz and feldspar in both major and trace element models (Table 7.1). The major and trace element models (sections 5.2.3 and 5.3.3) differ significantly in that the predicted amount of biotite in the major element fractionating assemblage is much larger than that in the LILE model. The cause of this discrepancy is not clear. The nature of the major element mixing modelling, which minimizes the discrepancy between the target and the model, can produce inaccurate models which nevertheless have low ΣR^2 values and therefore may appear to be good approximations to the truth. The uncertainty in the distribution coefficients used in the trace element calculations may be a major cause of inaccuracy.

The REE and many of the trace elements are dominated by accessory phases (e.g. monazite, zircon, xenotime), it is the physical behaviour of these phases in melts will therefore be of great importance in the chemical evolution of the magma.

7.5 Crustal evolution summary

Nd model age studies of Hercynian and Andean granitoids and metasediments have shown a marked increase in the amount of mantle input to the Central Andean crust at the start of the Andean orogeny (section 6.6.2). The Hercynian granitoids all

Phase	CG	AG	MAG	MVGP
Qtz	33	21	21	X
Plag	45	50	35	X
K spar	0	0	17	
Bt	18	22	28	X
Cpx		7.5		
Musc	5			
Opq	0.5	1	0.02	
Ap			1.5	
Zir	X	X	X	X
Mon	X	X		
Xen	X			X
Sph		X	X	

Table 7.1

Summary table of the best fit model fractionating assemblages (expressed as percentages of assemblage) calculated by major and REE modelling in chapter 5.

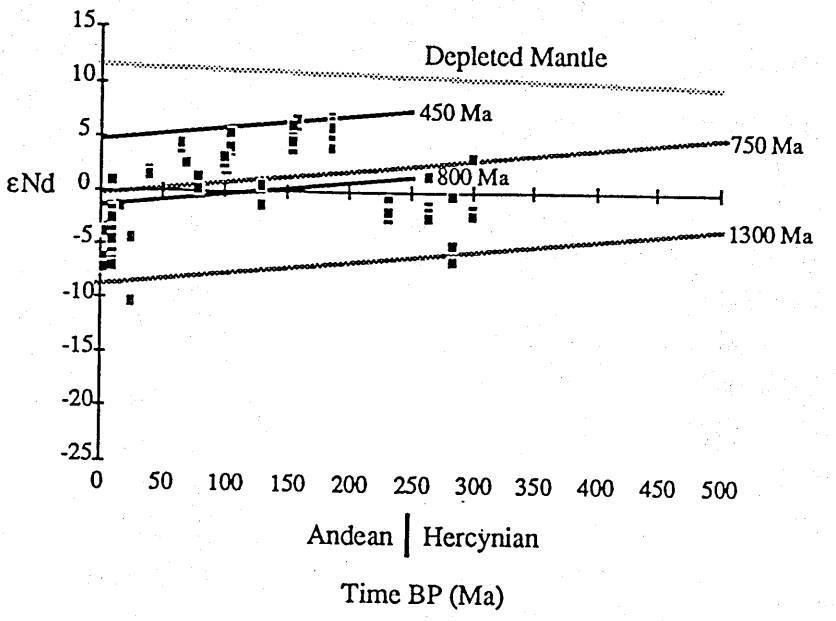

Figure 7.1

Evolution diagram for εNd vs. time. Vectors for mantle depleted 3500 Ma BP and crust extracted from the depleted mantle at times indicated are shown, the times were selected to envelope the Hercynian and Andean data. Also the data from magmatic samples of this study and Rogers (1985).

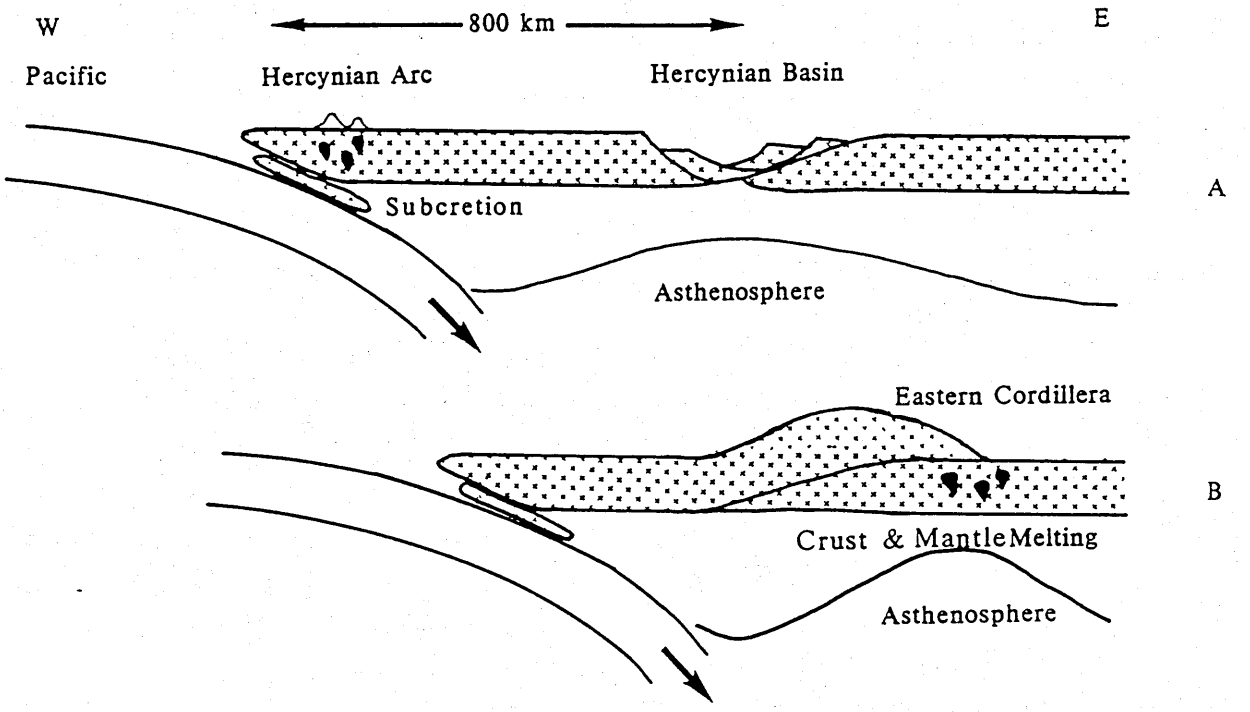

Figure 7.2

Diagrammatic model for the evolution of the Eastern Cordillera before and during the Chanic tectonic event. The removal of the South Pacific Continent by subduction erosion causes the migration of the back arc extension zone from beneath the Hercynian trough eastwards and initiates mantle and crustal melting in the Eastern Cordillera.

have Nd model ages of about 1 Ga and high, calculated protolith Rb/Sr (0.2 to 1), reflecting the dominance of upper crustal recycling during the orogeny. The general rate of upper crustal recycling (measured as the rate of Rb/Sr increase) is estimated to have been 1.2 to 1.75x per 500 Ma although values as high as 3x per 500 Ma have also been estimated (section 6.6.3); these values are comparable with those for the intra-crustal Damara (SW Africa) orogeny 1.5x to 2x per 500 Ma (McDermott, 1986).

The Andean granitoids, relative to the Hercynian, have lower Nd model ages of between 0.5 and 1 Ga and lower protolith Rb/Sr values (0.1 to 0.4) indicating the increase in mantle flux into the crust during the Andean orogeny. Andean upper crustal recycling rates are estimated to have been lower, between 0.75x per Ga and 1.5x per 500 Ma (section 6.6.3). The low calculated upper crustal recycling rates may be an artifact of the young ages of the samples, however they probably do reflect the larger mantle input to the Andean orogeny relative to that of the Hercynian.

Two models for the thickening of the Andean crust have been considered; magmatic underplating, and intra-crustal thrusting. Nd isotope studies allow these two models to be differentiated. Figure 7.1 illustrates the Nd isotope data for the Central Andes and bounding evolution lines for crust extracted from a depleted mantle reservoir at specified times (450 to 800 Ma for the Andean data and 750 to 1300 Ma for the Hercynian data). Crustal thickening by magmatic underplating should cause a shift to higher εNd values directly after the event; intra-crustal reworking should not affect the εNd values.

The end of the Hercynian was marked by major uplift, and crustal thickening, during the Saalian Tectonic Event (section 2.2.2 vi). The boundary between the Hercynian and Andean orogenies is defined by a significant increase in the εNd values. This sharp increase in the εNd values of samples directly after this event possibly indicates that the thickening was related to magmatic underplating. The 25 Ma crustal thickening event in the Eastern Cordillera coincides with a fall in the εNd

values from Andean values back to those of the crust involved in the Hercynian orogeny, indicating crustal thickening during this event was an intra-crustal process, involving crust of the same age as the Hercynian, and not involving any mantle input as suggested by James *et al.*, (1976) and Clark and McNutt, (1982).

7.6 Mineralization

The Sn/W mineralization associated with the granitoids in the Cordillera Real occurs in granitoids derived both from metasedimentary sources and those containing both metasedimentary and mantle components; this implies that the source of the metals must be the crustal component. The Rhondonia anorogenic granites, emplaced at 980 Ma (Preim *et al.*, 1971) into crust stabilized at 1 Ba during the Sunsas and Aguapei orogeny occur to the east (section 2..2.1) and provide a suitable crustal Sn/W anomaly, in crust of the same age as the Nd model ages of the CG and MVGP. It seems probable that the Bolivian tin belt is a reworking of an earlier mineralization event, probably with intermediate sedimentary cycles, related to Palaeozoic, anorogenic granites of marked structural and geochemical affinity to the Nigerian Younger Granites (Kloosterman, 1967).

7.7 Geotectonic model for the Cordillera Real

Prior to this work, based on K-Ar and ^{39}Ar-^{40}Ar dating (Cordani, 1967; Clark and Farrar, 1973; Everden *et al.*, 1977; Martinez, 1980; and McBride *et al.*, 1983 and 1987) the Sorata complex was believed to be of late Triassic age and the Tres Cruses complex of mid Tertiary age (section 6.2.1). Rb-Sr whole rock

geochronology has shown that the Sorata Complex and the MAG, which forms the majority of the Tres Cruses Complex, were emplaced between the late Carboniferous and early Permian. The MVGP is thought to be a mid Tertiary granite emplaced into the Cordillera Real as the northern most part of the magmatic event responsible for the heavily mineralized sub-volcanic stocks of the Central Bolivian tin belt (Turneaure, 1960 a and b). The thermal event related to the emplacement of the MVGP is believed to have been responsible for the resetting of the K-Ar and Rb-Sr systematics of the micas in the MAG, the large majority of which give mid Tertiary ages. K-Ar and Ar^{39}-Ar^{40} ages from micas of the Sorata and Zongo complexes show a range of ages (225-39 Ma) believed to have been caused by degassing, due to a thrusting. One major thrusting event has been dated at 39 Ma from totally out-gassed mica samples, (McBride *et al.*, 1987). Therefore two periods of evolution of the Eastern Cordillera are related to the petrogenesis of the granitoids; the late Palaeozoic and the mid Tertiary.

During the Palaeozoic the Eastern Cordillera lay at the margin of the intra-crustal Hercynian Trough which was bounded to the west by a continental mass (the South Pacific Continent) of which the Arequipa Massif is a remnant (Figure 7.2). The fate of this continental block is not well understood. It has been proposed (Rogers, 1985) that subduction-erosion, or decretion, (Dewey and Windley, 1981) removed the block during the late Palaeozoic and early Mesozoic. Along the western side of the South Pacific continent subduction of the Pacific is thought to have occurred during the Palaeozoic and a Hercynian arc may have developed (Figure 7.2 a).

The magmatic activity in the Cordillera Real during the late Hercynian was dominated by crustal anatexis (forming the CG, CKG, SG) but also tapped both subduction related (forming the AG) and within plate mantle (forming the MAG) reservoirs. Magmatism occurred directly after the closure of the Hercynian Trough, which before this time formed a back arc basin related to the subduction of the Pacific beneath the South Pacific Continent. Figure 7.2 b illustrates the most likely scenario.

Analogies with the Damara Orogeny of Southern Africa can be drawn for the late Palaeozoic events of the Eastern Cordillera. McDermott (1986) proposed a two stage model for the intra-crustal Damara Orogeny. An early stage involved the rifting of an intra-cratonic sedimentary basin and a late stage which involved compression, the closure of the basin and crustal thickening (Figure 7.3). The Damaran rifting was believed to be asymmetric in nature due to the structural and metamorphic asymmetry of the belt. Granitoid emplacement was therefore concentrated not above the thinned crust but above the thinned lithosphere, the location of higher heat flow. The same asymmetry of crustal extension and granitoid emplacement exists in the Chanic evolution of the Eastern Cordillera (Figure 7.2 a); the exact role of the subduction zone in the development of this asymmetry is not clear, but the erosion of the South Pacific Continent may have caused the migration of the lithospheric extension zone eastward to maintain the distance from the subduction zone leading to granitoid formation to the east of the back arc basin Figure 7.2 b.

The MVGP, the sole pluton related to the mid Tertiary thermal event, is thought to have been derived from mature metasediments and was emplaced at the same time as the uplift in the Eastern Cordillera. Large scale, crustal thrusting of the Brazilian shield beneath the Eastern Cordillera from east to west has been proposed as a likely cause of the uplift (Lyon-Caen *et al.*, 1987). Such large scale crustal thrusting provides a highly suitable method for the rapid heating of metasediments to produce granitic melts such as the MVGP (Figure 7.4).

The plutons of the Cordillera Real therefore appear to be related to two distinct thermotectonic events in the evolution of the Central Andes. The late Palaeozoic orogeny resulted from the closure of a major back arc basin and involved crustal melting and mantle inputs. In contrast the mid Tertiary orogeny was essentially a crustal melting event, related to intra-crustal thrusting which resulted in the uplift of the Eastern Cordillera with no detectable mantle input.

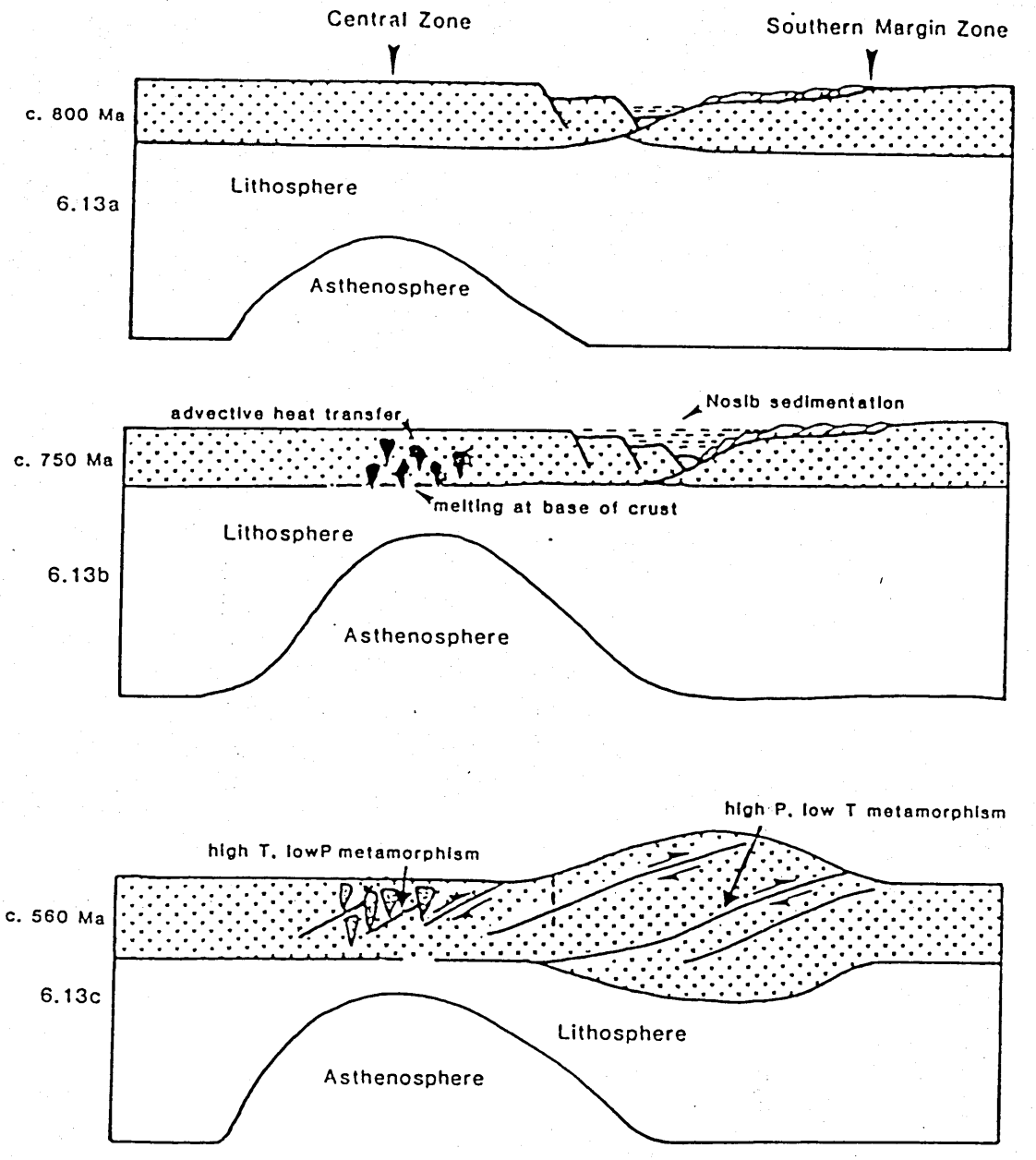

Figure 7.3

Asymmetric rift model for the evolution of the Damara orogeny (after Mc Dermott, 1986). The upwelling asthenosphere caused melting at the base of the crust and the generation of early granitoids. These magmas transported heat up into the upper crust causing melting. Collision and thrusting caused crustal thickening but no granitoid development.

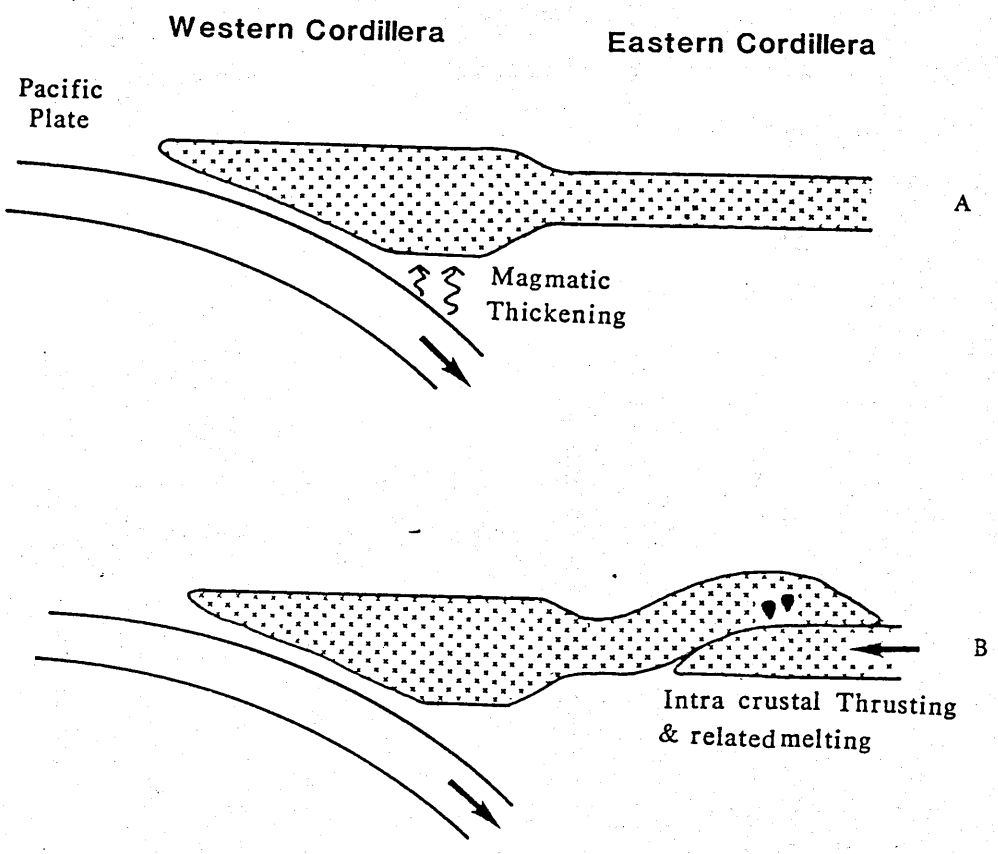

Figure 7.4

Diagrammatic model for the development of the Eastern Cordillera during the mid Tertiary crustal thickening event. Crustal melting is initiated by the intra-crustal thrusting of the Brazilian shield eastwards beneath the Eastern Cordillera.

7.8 Future work

To the north of the Cordillera Real, near the Peruvian border, a single unvisited pluton has been identified by GEOBOL and may provide a link between the Palaeozoic granitoids of Bolivia and Peru.

The Pre-Cambrian crustal evolution of the Central Andes is not well constrained. Nd model age studies of metasedimentary samples from the mobile belts to the east of the Eastern Cordillera would allow a better assessment of crustal growth in an area of semi-continuous subduction since approximately 1.5 Ba (the age of the San Ignacio mobile belt, section 2.2.1) and crust since 2 Ba (the Brazilian protolith, Figure 2.1).

As discussed in section 6.6 the cause of the LREE enrichment of calc-alkali magmatism, probably the major method of crustal growth, is not well understood. A combined isotopic, trace elemental and REE study of both continental and oceanic arc magmatism is needed to identify the cause of the Sm/Nd enrichment of the new crust be it an enriched source (subcontinental lithosphere), fractionation assemblage, or depth and/or degree of melting.

The Sm/Nd values of the lower crust appear to be significantly higher than those of the upper crust (section 6.6). A detailed mineralogical, trace elemental and REE study of lower crustal xenoliths is needed to try to identify the cause of Sm/Nd fractionation between the lower and upper crust and to constrain it's importance.

Appendix A
Analytical techniques and sample preparation

A 1 Sample powder preparation

Granitoid samples of 4-7 kg and smaller samples of uncommon or fine grained material, such as inclusions and meta-sediments were collected. Only fresh material, often from recent cuttings was taken. All samples were split into ≈ 2 cm cubes using a hydraulic splitter and any weathered material removed . At least 2 kg of these pieces were crushed in a hardened steel jaw crusher to <5 mm pieces. A representative 150 g portion of this crushate was taken using cone and quartering techniques. This sample was powdered in a agate lined tema mill for approximately 15 minutes to produce a powder of less than 200 mesh grain size.

A 2 XRF sample preparation

Two separate preparation techniques were followed to obtain elemental concentrations; pressed powder pellets were prepared for trace element analysis and glass discs, for major element analysis.

To form pellets ≈8 g of rock powder and a Moviol binder were mixed and pressed into 3 cm diameter pellets using a hydraulic press. The pellets were dried in an oven at 110 °C overnight before analysis

Glass discs were formed from a flux of 4:1 mixture of lithium metaborate:tetraborate mixture (Spectraflux 100B) in a 6:1 ratio with pre-dried rock powder. The mixture was fused in a platinum-gold alloy crucible in a muffle furnace at 1100 °C for fifteen minutes. The resulting glass was poured into a 3 cm mould and cast to form glass disc. A correction for flux volatilization was applied to each batch of beads. Loss on ignition data was calculated for each sample by heating 2.5 g of pre-dried sample to 1000 °C in a silica crucible for twenty minutes and measuring the mass loss.

A 3 XRF Analysis

All XRF analysis was carried out at the Open University on a Link Systems Meca 10-44 energy dispersive XRF spectrometer (EDXRF). This incorporates a low power (49 kW) silver anode side window X-ray tube operated in pulsed mode with

maximum settings of 49 kV or 1 mA and a Si(Li) detector with resolution of 125 eV at 5.9 KeV. The EDXRF has been calibrated using international standards and representative analyses of standards used over the period of this study are given in **Table A 3.1.**

For major element analyses, glass discs were counted in duplicate for 500 seconds at 10 kV, 0.2 mA with no primary beam filter. Powder pellets for trace element analyses were counted twice for 800 seconds at 45 kV, 0.3 mA with a 127 μm silver primary beam filter. Instrumental drift within single batches (16 samples and 4 standards per batch) was monitored by analyzing USGS AGV-1 for major elements and USGS GSP-1 for trace elements in each batch. An internal monitor sample (KND 1.1) was run several times over the period of this study to assess the differences between calibrations.

Ba analyses were carried out using a Co anode, side window, X-ray tube operated in pulsed mode with maximum settings of 20 kV or 0.1 mA and a Fe foil primary bean filter. Count times of 1200 sec were used.

All EDXRF results are tabulated in Appendix B. Detection limits for the major elements are generally 0.05 wt% except for the light elements Na, Mg, Al, and Si for which the detection limits are between 0.2 wt% (Si) and 0.96 wt% (Na). Precision is better than 1% relative (at a 2 sigma certainty level) except Al (2%), Mg (3%), and Na (10%). Trace element detection limits are 6 ppm for Rb, Sr, Y, Nb and Ni, 15 ppm for Zr, and 31 ppm for Ba. Precision for all trace elements is about 2% at 100 ppm level. Full details of the EDXRF system are given in Potts *et al.* (1984) and Potts *et al.* (1986).

A 4 Instrumental Neutron activation analysis (INAA)

INAA was carried out on 36 samples to determine the concentrations of rare earth elements (REE) as well as Ta and Hf.

0.3 g of pre-dried rock powder was accurately weighed into a polythene capsule and sealed. The capsules were stacked into a cylinder with a pre-weighed lacquered iron foil between each capsule to monitor the neutron flux along the length of the cylinder. Each cylinder contained 9 samples and 2 standards. The two standards used were the irradiation standard AC (OURS) and a sample of Whin Sill, which was used as an internal standard.

Element	Abbey (1983)	8/4/86	1/3/87	1/4/87	10/8/87
SiO_2	59.61	59.95	59.35	59.13	59.29
TiO_2	1.06	1.08	1.07	1.06	1.07
Al_2O_3	17.19	17.29	17.11	17.05	17.11
Fe_2O_3	6.78	7.03	6.82	6.75	6.81
MnO	0.1	0.09	0.1	0.09	0.09
MgO	1.52	1.53	1.45	1.5	1.54
CaO	4.94	4.94	4.96	4.93	4.96
Na_2O	4.32	4.14	4.12	4.38	4.04
K_2O	2.92	2.92	2.91	2.88	2.9
P_2O_5	0.51	0.56	0.53	0.47	0.52
	Abbey (1983)	**11/2/85**	**21/10/85**	**11/3/86**	**11/2/87**
Sr	240	235	235	235	230
Rb	250	253	254	252	253
Y	29	29	28	28	28
Nb	23	25.2	23.3	24.1	24.3
Zr	500	502	504	503	506

Table A 3.1

Tabulation of published values of Major element standard AGV-1 (andesite) and trace element standard GSP-1 (granodiorite) and representative analyses of the standards at the Open University over period of this study.

Samples were irradiated in a core tube at the Imperial College reactor centre, Silwood Park, Ascot, in a thermal flux of 5 x 10^{12} n cm^2 sec^{-1} for 24-30 hours. Following irradiation the samples were allowed to 'cool' for about a week to allow the short lived radioisotopes to decay. The samples were 'counted' at the Open University using two detectors on either side of the sample capsule; a planar low energy photon spectrometer (LEPS) and a coaxial Ge(Li) detector. Each sample was 'counted' for 800 sec on the LEPS detector for Sm, and on the coaxial detector for La, Co, and Sc. The other elements were determined by counting each sample for 2.5 x 10^4 to 5 x 10^4 sec using the LEPS detector. The iron foils were 'counted' using the coaxial detector for 300 sec each, to assess the variations in the neutron flux. Data were processed using spectroscopy amplifiers and a multichannel analyser. Photopeak data were corrected for neutron flux variations calculated using the iron foil data. Details of counting conditions, peak fitting, calibration, and corrections are given in Potts *et al.* (1981) and Potts *et al.* (1985). The data was normalized to Chonditic values using the values of Nakamura (1974), see Table A4.1.

Element	Normalizing value
La	0.328
Ce	0.805
Nd	0.630
Sm	0.203
Eu	0.077
Gd	0.276
Tb	0.052
Ho	0.780
Tm	0.034
Yb	0.220
Lu	0.0339

Table A 4.1

Chondrite normalizing values from Nakamura (1974).

A 5 Radiogenic isotope analysis: chemistry

All isotopic analyses and preparation were carried out in a clean-air laboratory in which a positive air pressure was maintained. All solutions were made up with either twice quartz distilled or Milli-Q reverse osmosis purified, water. Sample dissolutions were carried out in teflon beakers for Sr and teflon bombs for Nd, both were normally opened only in laminar air flow cupboards.

Bombs and beakers were cleaned between batches by washing in QD or Milli-Q water and soaking in 15 M HNO_3 (aq) at 80 °C overnight, washed in pure water overnight and allowed to dry inverted on tissue paper.

Total procedural blanks for Sm and Nd are <1 nd and 8 ng for Sr.

A 5.1 Sr chemistry

Approximately 150 mg of rock powder was weighed into a teflon beaker to which approximately 2 ml of 15 M HNO_3 (aq) were added then 5 ml of 40% HF (aq). The solution was covered and allowed to stand cold for several hours, then it was evaporated to near dryness under evaporating lamps in a laminar flow cupboard. A further 2 ml of 15 M HNO_3 (aq) was added and evaporated to near dryness. Approximately 6 ml of 6 M HCl (aq) was added and warmed under the evaporating lamps, at this stage total dissolution should have occurred and a clear yellow-orange solution should result. If total dissolution was not achieved the solution was evaporated to near dryness and the last two acid stages repeated till total dissolution was achieved. Accessory phases were occasionally observed in the solutions and proved insoluble by this method, this was not considered an important problem fro Sr isotope studies. The final solution was evaporated to near dryness and re-dissolved in 1 ml of 2.5 M HCl (aq), any residue was centrifuged off.

Sr separation was carried out using columns of 10 ml of pre-conditioned Bio-rad AG50W x8, 200-400 mesh resin. The sample was loaded on to the resin with the minimum disturbance. The sample was slowly washed on to the resin with two 1 ml aliquots of 2.5 M HCl (aq), each aliquot was allowed to soak in to the resin before the second was added. If the Rb fraction was needed 26 ml of 2.5 M HCl (aq) was eluted and the Rb fraction was collected in 10 ml of 2.5 M HCl (aq) and 12 ml of 2.5 M HCl (aq) eluted. If the Rb fraction was not needed 48 ml of 2.5 M HCl (aq) was then eluted through the resin. The Sr fraction was collected in 10 ml of 2.5 M HCl

(aq). The Rb and Sr solutions were evaporated to dryness and stored for analysis.

A 5.2 Sr mica work

Micas were separated from washed 2 - 4 mm fractions of crushate using a sloped, gently vibrating, sheet of filter paper to which the mica plates adhere and the more equant, felsic grains roll off. The mica concentrate was then hand picked under a binocular microscope to produce an approximately 98% pure, mica separate. Approximately 40 mg of mica was accurately weighed into a teflon beaker and dissolution was carried out as detailed above for Sr whole rock work. The samples were passed through the Sr columns as detailed above The Sr fractions were passed through the columns a second time to overcome problems with Rb contamination of the Sr fraction.

A 5.3 Nd and Sm chemistry

Dissolutions were carried out in teflon bombs to ensure total dissolution of REE rich accessory phases. Approximately 150 mg of rock powder was weighed into a teflon bomb and 2 ml of 15 M HNO_3 (aq) followed by 5 ml of 40% HF (aq) added. The mixture was allowed to stand cold for several hours in sealed bombs. Each bomb was then placed in a tight polythene sleeve to hold the top in place; the assembly was then placed in a monel jacket and placed in an oven at 180 °C overnight. After cooling the bomb was removed from the casing and the solution evaporated under lamps to near dryness. 2 ml of 15 M HNO_3 (aq) was added and evaporated to near dryness and 6 ml of 6 M HCl (aq) added. If total dissolution was not achieved at this stage then the bomb was reassembled and returned to the oven for a further 24 hours. When total dissolution was achieved the MREE were separated on the Sr columns by following the procedure for Sr, as described above, but after the Sr fraction had been collected 22 ml of 3 M HNO_3 (aq) was eluted through the columns and the MREE fraction was collected in a further 24 ml of 3 M HNO_3 (aq). This fraction was evaporated to dryness and re-dissolved in 1 ml of 0.25 M HCl (aq). The MREE fraction was loaded on to pre-conditioned reverse chromatography columns, composed of 1 g of teflon powder (Voltalef 300LD PL micro) with 100 mg DEP ((Di(2-ethylhexyl) phosphate). The sample as washed-in with 2 x 1 ml of 0.25 M HCl (aq), a further 8 ml of 0.25 M HCl (aq) eluted through the columns and the Nd collected in 4 ml of 0.25 M HCl (aq) which was evaporated to dryness and stored for analysis. If the Sm was needed 6 ml of 0.5 M HCl (aq)was eluted and the Sm

fraction collected in 4 ml of 0.5 M HCl (aq) which was evaporated to dryness and stored for analysis.

A 5.4 Spikes

The following spikes were used to determine the concentrations of Rb and Sr in mica separates; and Nd and Sm concentrations in whole rock samples:

RBSRHI	SMND
Sr = 0.00705 μmol g^{-1} of ^{84}Sr	Nd = 0.0533 μmol g^{-1} of ^{150}Nd
Rb = 0.34 μmol g^{-1} of ^{87}Rb	Sm = 0.0163 μmol g^{-1} of ^{147}Sm
^{84}Sr = 99.783%	^{150}Nd = 97.71%
^{87}Rb = 98%	^{147}Sm = 98.08%

Mica samples were weighed out on a 0.0001 mg balance using teflon weighing boats and one or two drops of RBSRHI spike added. Whole rock samples were weighed on a 0.01 mg balance in teflon bombs and one or two drops of SMND added. Chemical dissolution was performed in the described manner.

A 6 Radiogenic isotope analysis: Mass spectrometry

A 6.1 Sample loading

Nd samples were run on an Finnigan M80 261, solid source, multi-collector mass spectrometer interfaced with a HP 9836 computer and Finnigan software (Finnigan MS) All other samples were run on a Vacuum Generators Isomass 54E solid source, mass spectrometer interfaced with a HP 9845T computer and in-house designed software (VG MS). All analyses took place at $<10^{-7}$ torr and an accelerating potential of 8 kV.

Filaments for both machines were out-gassed before use. Single filaments were out-gassed for 5 minutes at 4.5 A in a vacuum better than 10^{-6} torr. Triple filaments were out-gassed at 4.5 A at 10^{-5} torr for 5 minutes allowed to cool and further outgassed at 4.5 A for 5 minutes at 10^{-6} torr.

All Sr, spiked Nd and Sm samples were loaded onto out-gassed single Ta, triple Ta/Re (Re centre filament), and single Ta VG MS filaments respectively. Triple filaments were used to allow the ionization of the Nd on the centre filament at a higher temperature that the release temperature of the side filaments. All loading took place in a filtered air loading bay. Sr was dissolved in a drop of pure water and

added to a dried drop of H_3PO_4 on a Ta filament. A small current was passed through the filament to dry the solution and gradually increased to burn off the excess H_3PO_4. spiked Nd samples were dissolved in pure water and loaded on to the side filaments of a Ta/Re triple filament, which were gently heated to dry the sample. Sm samples were dissolved in pure water and loaded on to single Ta filaments without H_3PO_4 and heated till the sample was dry. Unspiked Nd samples were loaded as aqueous solutions onto outgassed Ta filaments of the Finnigan MS filament assembly which were gently heated to dry the sample. The loaded samples were placed in a 6 sample turret for the VG MS or a 13 sample magazine for the Finnigan MS. The VG MS turret was allowed to stand overnight in a vacuum oven at 80 °C over night before use.

A 6.2 Running conditions

A 6.2.1 Sr

Sr isotope abundances were measured with a beam intensity of 15 pA at a filament current of 2.5 A. Peaks were counted for four periods of 1.28 sec after which the magnet stepped to the next peak. The measurement cycle was 88, 87, 86, 85.5, 85, and 84. The 84 peak was eliminated after the first set of results and the 85 peak after the Rb contribution to the 87 peak was less than 0.01%. Peak intensities were measured using a double interpolation algorithm (Dobson, 1978) and were corrected for zero, dynamic memory, and Rb interferences where necessary. Mass fractionation was corrected for, by assuming that $^{86}Sr/^{88}Sr=0.1194$ and that there is a linear dependence of mass fractionation on mass difference. The isotope ratios were stored as sets of 10 and mean and standard deviation of each set calculated. Sets which did not satisfy Chauvenet's criterion were rejected. Sets with total errors (1σ) of 100 ppm or more were rejected, those with error (1σ) in excess of 500 ppm were ignored. Chauvenet's criterion was then applied to all the accepted and rejected sets and the running mean calculated. The analysis continued till at least 100 ratios had been excepted and the error (1σ) was 20 ppm or less. Repeat analyses of NBS 987 standard were carried out and all runs were normalized to a NBS 987 value of $^{87}Sr/^{86}Sr=0.71018$.

A 6.2.2 Nd

Nd measurements were made on both the VG MS and the Finnigan MS. On the

VG MS Nd measurements and data reduction was similar to that for Sr. Measurements were made with a 144 beam intensity of 7 pA with a centre filament current of 3.9 A and a side filament current of 2 A. The measuring cycle was 146, 144, 143, 142.5, 142, and 147. The 142 peak was eliminated after the first set and the 147 peak was eliminated when Sm contribution to the 144 peak was less than 0.01%. Mass fractionation was corrected by assuming linear dependence on mass difference and that $^{146}Nd/^{144}Nd=0.7219$. Sets were rejected when the error (1σ) was 100 ppm or worse and ignored when it was greater than 500 ppm. Analysis was continued until at least 200 ratios were accepted and the error (1σ) was 10 ppm or less.

On the Finnigan MS simultaneous measurements of the intensities of the 143, 144, 146, and 147 peaks were made. Data collection was initiated once the 144 beam intensity reached 5 pA. Data was collected in sets of 10 isotope ratios to which the Dixon rejection test was applied up to 1 group of ratios was dropped from the set if the test was failed. Ten sets were collected. A running value and associated error was calculated on the accumulated sets. Final values and associated errors are the product of between 90 and 100 measurements of the isotope ratios.

The standard BCR-1 was used as to correct instrumental drift on both machines and all data was corrected to a BCR-1 value of 0.51262.

A 6.3 Isochron plots

A revised algorithm after York (1969) was used. Quoted errors are at the two sigma level; the errors are multiplied by the square root of the MSWD when the MSWD > 1.

A 6.4 Data representation

For the principals of isotope systematics, the reader is referred to Faure (1977) and Hawkesworth and van Calsteren (1984).

Several diagrams in chapters 5 and 6 display Sr and Nd data using the ε form of DePaolo and Wasserberg (1976), defined as:

$$\varepsilon Nd = \left[\frac{\left[{}^{143}Nd / {}^{144}Nd \right] \text{ Sample at time t}}{\left[{}^{143}Nd / {}^{144}Nd \right] \text{ CHUR at time t}} - 1 \right] \times 10^4$$

$$\varepsilon Sr = \left[\frac{\left[{}^{87}Sr / {}^{86}Sr \right] \text{ Sample at time t}}{\left[{}^{87}Sr / {}^{86}Sr \right] \text{ Bulk earth at time t}} - 1 \right] \times 10^4$$

Model ages are reported relative to depleted mantle:

$$T_{DM}^{Nd} = \left[\frac{1}{\lambda} \right] Ln \left[\frac{({}^{143}Nd / {}^{144}Nd)_{Sample} - ({}^{143}Nd / {}^{144}Nd)_{DM}}{({}^{147}Sm / {}^{144}Nd)_{Sample} - ({}^{147}Sm / {}^{144}Nd)_{DM}} + 1 \right]$$

$$T_{DM}^{Sr} = \left[\frac{1}{\lambda} \right] Ln \left[\frac{({}^{87}Sr / {}^{86}Sr)_{Sample} - ({}^{87}Sr / {}^{86}Sr)_{DM}}{({}^{87}Rb / {}^{86}Sr)_{Sample} - ({}^{87}Rb / {}^{86}Sr)_{DM}} + 1 \right]$$

Where:

$\lambda\ {}^{147}Sm = 6.54 \times 10^{-12}\ y^{-1}$

$({}^{147}Sm / {}^{144}Nd)_{CHUR} = 0.1967$

$({}^{143}Nd / {}^{144}Nd)_{DM} = 0.51310$

$({}^{147}Sm / {}^{144}Nd)_{DM} = 0.2238$

$\lambda\ {}^{87}Rb = 1.42 \times 10^{-11}\ a^{-1}$

$({}^{87}Sr / {}^{86}Sr)_{Bulk\ earth} = 0.7047$

$({}^{87}Rb / {}^{86}Sr)_{Bulk\ earth} = 0.0847$

$({}^{87}Sr / {}^{86}Sr)_{DM} = 0.70306$

$({}^{87}Rb / {}^{86}Sr)_{DM} = 0.0487$

A 7 Electron microprobe analysis

Microprobe mineral analyses were carried out on polished, carbon coated, thin sections.

Two separate microprobe systems were used to collect data for this work; major element analyses were carried out using a Cambridge Instruments Microscan 9 wave length dispersive microprobe, incorporating a fully computerized system for multi element analysis and accessory phases (zircon, apatite, monazite, xenotime, sphene) were analysed using a Geoscan microprobe, energy dispersive Si(Li) detector and multichannel analyser controlled by a Link Systems AN 10000 soft ware

A 7.1 Wavelength dispersive microprobe analysis

An accelerating voltage of 20 kV and a probe current of 30 nA were used for all analyses. To eliminate the possibility of sample decomposition, the electron beam was defocussed to a diameter of approximately 15 μm.

The machine was calibrated using mineral standards every 24 hours. A in-house, multi-element, secondary standard ABG (a basaltic glass) was analysed regularly to assess shifts in calibration.

A 7.2 Energy dispersive microprobe analysis

An accelerating voltage of 20 kV and probe current of 4.05 nA were used for all energy dispersive (ED) analyses. The low probe current was used to minimize pulse pile up and counter dead time. A count time of 200 sec avoided channel overflow but allowed peak resolution. The low probe current and short count time allowed a 2 μm diameter beam to be used without sample decomposition; this was of use in the analysis of accessory phases, which often occur as grains in the 1-20 μm range.

Calibration was based on a suite of natural and synthetic standards (Tindle, 1982). A Co standard was analysed every three analyses to correct for drift in the energy scale relative to the absolute energy level of Co K_{σ} line. Full peak fitting and ZAF (atomic number, mass absorption, and fluorescence) corrections were made on line by Link Systems soft ware. Due to the nature of the peak fitting procedure used to obtain quantitative analyses some elements although potentially detectable in certain minerals could not be analysed for, due to peak interference.

Appendix B
Whole rock geochemical and isotopic data

Major elements are expressed as wt % oxides and trace elements as ppm, see section A3 for techniques and precisions. Aplites, autoliths and altered samples are indicated: all other samples are fresh granitoids.

Sr 87/86 is used to denote $^{87}Sr/^{86}Sr$. Nd 143/144 to denote $^{143}Nd/^{144}Nd$. Iso Dil indicates concentrations determined by isotope dilution techniques (see section A5.4)

CG	B85/201 APL	B85/192 APL	B85/172 APL	B86/117 APL	B86/126 APL	B86/81B Autolith
SiO2	74.41	74.85	75.11	75.44	76.77	64.64
TiO2	0.01	0.04	0.03	0.14	0.05	0.79
Al2O3	15.03	16.01	15.47	14.76	13.50	15.91
Fe2O3	1.17	0.65	0.71	0.43	0.13	5.65
MnO	0.28	0.16	0.12	0.02	0.01	0.13
MgO	0.13	0.13	0.13	0.29	0.12	1.75
CaO	0.29	0.33	0.31	0.81	0.43	2.45
Na2O	3.85	2.71	4.62	5.04	3.63	3.78
K2O	5.22	5.26	3.35	4.11	5.94	2.54
P2O5	0.26	0.33	0.32	0.21	0.07	0.22
S	0.02	0.02	0.01	0.00	0.01	0.01
LOI	0.49	1.01	0.76	0.51	0.46	0.90
Total	101.16	101.50	100.94	101.76	101.12	98.77
Ti	134	244	215	719	298	5432
Rb	300	546	411	210	276	378
Sr	6	43	15	104	39	144
Ba	10	100	10	261	125	218
Y	10	7	5	11	13	29
Hf		2				
Zr	37	28	22	47	41	187
Nb	5	25	29	8	22	25
Ta		10				
Pb	33	24	23	34	23	11
Th	0	1	0	6	10	8
U	0	1	11	<3	18	6
La		1.95				
Ce		3.77				
Nd		0.18				
Sm		0.42				
Eu		0.18				
Gd						
Tb		0.50				
Ho						
Tm						
Yb		0.90				
Lu						
Sr 87/86		0.82809 ± 3				
Sm (Iso Dill)						
Nd (Iso Dill)						
Nd 144/143						

	B86/64	B86/65	B85/183	B85/210	B86/98	B86/60
SiO2	70.53	70.58	71.33	71.54	71.96	72.04
TiO2	0.43	0.47	0.43	0.18	0.33	0.37
Al2O3	15.70	15.84	15.74	14.87	15.33	15.54
Fe2O3	3.16	3.45	2.60	1.44	2.21	2.77
MnO	0.06	0.05	0.04	0.03	0.04	0.04
MgO	0.85	0.95	0.77	0.22	0.51	0.73
CaO	1.91	2.26	1.57	0.70	1.68	2.05
Na2O	3.42	3.62	3.13	3.00	3.35	3.57
K2O	3.06	2.64	4.54	5.51	4.08	3.04
P2O5	0.16	0.16	0.25	0.29	0.24	0.20
S	0.01	0.01	0.01	0.01	0.01	0.01
LOI	1.11	1.00	0.88	0.84	0.74	0.94
Total	100.40	101.03	101.29	98.63	100.48	101.30
Ti	2945	3255	2986	1310	2224	2420
Rb	196	167	281	369	247	172
Sr	142	161	143	90	141	141
Ba	469	438	569	321	501	493
Y	18	19	20	25	16	18
Hf				2		
Zr	150	167	184	69	140	151
Nb	13	12	13	16	13	15
Ta				2		
Pb	27	21	32	49	32	28
Th	12	12	19	4	11	10
U	<3	0	5	4		<5
La				8.19		
Ce				13.40		
Nd				4.68		
Sm				0.71		
Eu				0.88		
Gd						
Tb				0.19		
Ho						
Tm						
Yb				0.50		
Lu				0.09		

Sr 87/86 0.72751 ± 5 0.72411 ± 5 0.73381 ± 2 0.71237 ± 3
Sm (Iso Dill) 5.39 ± 3
Nd (Iso Dill) 25.15 ± 2
Nd 144/143 0.512181 ± 4

CG	B86/74	B86/70	B86/66	B85/179	B85/178	B86/116
SiO2	72.72	73.01	73.03	73.04	73.07	73.13
TiO2	0.28	0.24	0.29	0.27	0.27	0.21
Al2O3	15.48	15.61	15.28	15.00	15.08	14.72
Fe2O3	1.96	1.70	2.07	1.85	1.86	1.78
MnO	0.03	0.03	0.03	0.03	0.02	0.04
MgO	0.46	0.33	0.46	0.29	0.50	0.30
CaO	1.27	1.36	1.03	1.07	1.05	1.05
Na2O	2.97	3.12	2.98	2.99	2.90	3.65
K2O	4.74	4.88	4.84	5.25	5.08	4.15
P2O5	0.22	0.19	0.28	0.29	0.23	0.16
S	0.01	0.01	0.01	0.01	0.02	0.01
LOI	1.03	0.52	0.96	0.86	0.77	0.72
Total	101.17	101.00	101.26	100.95	100.85	99.92
Ti	1970	1742	1931	1909	1969	1381
Rb	294	254	354	303	297	340
Sr	118	114	107	126	126	73
Ba	478	413		622	626	191
Y	19	18	18	16	16	18
Hf						
Zr	124	85	118	144	145	97
Nb	14	13	17	15	15	19
Ta						
Pb	36	42	28	38	36	30
Th	13	8	12	15	15	11
U	<5	6	6	6	5	4
La						
Ce						
Nd						
Sm						
Eu						
Gd						
Tb						
Ho						
Tm						
Yb						
Lu						
Sr 87/86						
Sm (Iso Dill)						
Nd (Iso Dill)						
Nd 144/143						

CG	B85/197	B86/95	B86/88	B85/193	B85/195	B86/91
SIO2	72.16	72.23	72.25	72.52	72.58	72.59
TIO2	0.30	0.32	0.30	0.34	0.30	0.28
AI2O3	15.27	15.16	15.06	15.75	14.99	14.95
Fe2O3	2.05	1.83	2.09	2.41	1.98	1.96
MnO	0.03	0.03	0.04	0.04	0.04	0.03
MgO	0.61	0.46	0.50	0.62	0.40	0.45
CaO	1.27	1.33	0.87	1.72	1.11	0.97
Na2O	3.27	2.95	2.89	3.42	3.24	2.92
K2O	4.92	4.94	5.12	3.80	4.53	4.92
P2O5	0.27	0.22	0.23	0.19	0.22	0.27
S	0.01	0.01	0.01	0.01	0.01	0.01
LOI	0.64	1.00	1.00	0.71	0.72	0.96
Total	100.80	100.48	100.36	101.53	100.12	100.31
Ti	2123	2169	2063	2292	1812	1989
Rb	306	296	401	239	271	333
Sr	117	115	105	151	127	109
Ba	636	651	384	686	393	
Y	19	16	18	17	15	18
Hf				4	3	
Zr	130	135	126	144	122	128
Nb	16	9	16	13	12	16
Ta				2	2	
Pb	36	40	27	34	39	36
Th	9	18	15	12	9	14
U	4	5	<3	4	4	<5
La				37.18	29.80	
Ce				74.52	61.63	
Nd				30.64	26.50	
Sm				5.88	5.23	
Eu				1.21	1.04	
Gd				2.76	2.98	
Tb				0.67	0.58	
Ho						
Tm				0.21	0.16	
Yb				1.18	0.97	
Lu				0.19	0.15	
Sr 87/86	0.74191 ± 9		0.75056 ± 2	0.7315 ± 5	0.73692 ± 7	
Sm (Iso Dill)						
Nd (Iso Dill)						
Nd 144/143						

CG	B86/61A	B86/87	B85/190	B85/194	B85/206	B85/176
SiO2	73.97	73.99	74.02	74.09	74.58	74.74
TiO2	0.13	0.13	0.14	0.22	0.16	0.07
Al2O3	15.15	14.79	15.08	14.94	14.98	15.35
Fe2O3	1.31	1.19	1.29	1.61	1.30	0.77
MnO	0.04	0.03	0.04	0.04	0.03	0.04
MgO	0.24	0.13	0.17	0.32	0.18	0.19
CaO	0.88	0.68	0.79	1.06	0.75	0.73
Na2O	2.91	3.11	3.30	3.36	2.90	3.63
K2O	5.17	4.95	4.91	4.77	5.30	4.63
P2O5	0.29	0.26	0.28	0.27	0.35	0.25
S	0.01	0.01	0.01	0.02	0.01	0.02
LOI	0.94	0.89	0.83	0.71	0.48	1.08
Total	101.04	100.16	100.86	101.41	101.02	101.50
Ti	975	1029	983	1543	1148	555
Rb	353	387	378	338	347	310
Sr	100	77	78	88	82	73
Ba	425	166	484		285	141
Y	21	20	21	17	22	18
Hf			3	3		1
Zr	64	53	59	91	68	29
Nb	17	17	18	16	15	15
Ta			2	3		3
Pb	44	43	41	35	45	48
Th	6	6	3	7	4	0
U	5	<3	4	8	4	6
La			29.80	28.98		5.88
Ce			61.63	61.17		13.90
Nd			26.49	27.24		7.23
Sm			5.23	5.40		2.05
Eu			1.04	0.91		0.54
Gd				2.60		1.69
Tb			0.58	0.66		0.34
Ho						
Tm			0.16			
Yb			0.97	1.20		1.49
Lu			0.15	0.19		0.25
Sr 87/86			0.76754 ± 3	0.75395 ± 3	0.76454 ± 4	0.74221 ± 3
Sm (Iso Dill)			2.605 ± 3			
Nd (Iso Dill)			9.569 ± 2			
Nd 144/143			0.512317 ± 4			

CG	B85/205	B85/181	B86/86	B86/99	B85/186	B85/175
SiO2	73.17	73.28	73.34	73.36	73.42	73.51
TiO2	0.16	0.28	0.19	0.29	0.17	0.28
Al2O3	14.99	15.14	14.95	15.14	14.99	15.07
Fe2O3	1.28	1.89	1.53	1.99	1.31	1.97
MnO	0.03	0.03	0.04	0.05	0.03	0.02
MgO	0.13	0.43	0.14	0.49	0.26	0.37
CaO	0.76	1.15	0.86	0.87	0.74	0.98
Na2O	2.69	3.17	2.99	3.09	2.77	2.74
K2O	5.42	5.03	5.03	4.47	5.58	5.19
P2O5	0.23	0.23	0.27	0.28	0.28	0.31
S	0.01	0.01	0.01	0.02	0.01	0.01
LOI	0.96	0.62	0.93	1.09	0.89	0.54
Total	99.83	101.26	100.28	101.14	100.45	100.99
Ti	1196	1798	1412	2140	2272	1929
Rb	365	315	364	336	312	300
Sr	83	133	86	92	101	127
Ba	327	628	251	352	510	561
Y	22	16	28	18	18	17
Hf	3					
Zr	67	150	82	129	152	152
Nb	17	15	16	15	16	16
Ta	3					
Pb	47	42	39	31	34	35
Th	3	15	8	13	14	16
U	3	6	7	<3	3	5
La	28.98					
Ce	61.17					
Nd	27.24					
Sm	5.40					
Eu	0.91					
Gd						
Tb	0.66					
Ho						
Tm						
Yb	1.19					
Lu	0.19					
Sr 87/86	0.76678 ± 5				0.74617 ± 4	0.73957 ± 7
Sm (Iso Dill)					8.058 ± 2	
Nd (Iso Dill)					40.96 ± 4	
Nd 144/143					0.512167 ± 3	

CG	B85/196	B86/94	B86/90	B86/93	B86/89	B86/77
SiO2	73.50	71.60	72.02	72.65	72.94	71.00
TiO2	0.32	0.39	0.27	0.28	0.28	0.58
Al2O3	15.10	15.48	15.48	15.04	15.26	15.94
Fe2O3	1.89	2.49	1.90	1.81	1.74	3.50
MnO	0.03	0.04	0.03	0.03	0.04	0.05
MgO	0.40	0.73	0.42	0.33	0.43	1.00
CaO	1.20	1.70	1.30	1.22	1.01	2.50
Na2O	2.80	3.52	3.17	3.18	2.91	3.50
K2O	5.30	4.22	4.90	4.87	5.18	2.40
P2O5	0.25	0.23	0.26	0.32	0.32	0.15
S	0.01	0.01	0.01	0.00	0.01	0.01
LOI	0.54	0.47	0.74	0.77	0.86	0.54
Total	101.34	100.88	100.50	100.50	100.98	101.17
Ti	1919	2680	1641	1865	1863	3475
Rb	334	251	281	307	334	163
Sr	109	138	103	115	110	214
Ba	428	659	327	411	374	339
Y	18	17	19	19	19	16
Hf						6
Zr	125	168	101	118	106	231
Nb	16	12	14	15	17	14
Ta						1
Pb	36	23	35	39	39	22
Th	10	16	8	12	12	14
U	6	<5	5	5	8	<3
La						44.49
Ce						92.30
Nd						41.50
Sm						7.35
Eu						1.46
Gd						8.34
Tb						0.80
Ho						1.83
Tm						
Yb						1.30
Lu						0.24
Sr 87/86						0.72164 ± 5
Sm (Iso Dill)						
Nd (Iso Dill)						
Nd 144/143						0.512456 ± 3

CG	B85/185	B85/182	B86/67	B85/191	B85/189	B85/177
SiO2	75.03	75.20	72.38	73.30	73.69	72.35
TiO2	0.10	0.10	0.31	0.16	0.15	0.31
Al2O3	14.89	14.52	15.36	15.02	14.91	14.88
Fe2O3	0.93	1.08	1.99	1.40	1.22	1.88
MnO	0.04	0.05	0.04	0.02	0.04	0.02
MgO	0.19	0.25	0.45	0.17	0.17	0.47
CaO	0.95	0.61	1.33	0.73	0.74	1.12
Na2O	3.79	3.91	3.41	3.40	3.52	2.97
K2O	4.34	4.15	4.46	4.98	4.81	5.18
P2O5	0.16	0.24	0.30	0.25	0.33	0.24
S	0.02	0.01	0.01	0.01	0.01	0.01
LOI	0.75	0.46	0.80	0.88	0.80	0.51
Total	101.19	100.58	100.84	100.32	100.39	99.94
Ti	721	755	1972	2226	1051	1872
Rb	251	343	322	271	407	294
Sr	84	43	109	135	86	131
Ba	216	106	357	483	259	691
Y	19	14	20	16	21	17
Hf						
Zr	45	38	123	125	59	152
Nb	12	17	16	11	15	15
Ta						
Pb	49	36	32	35	43	40
Th	0	0	11	8	0	15
U	5	10	<5	7	5	6
La						
Ce						
Nd						
Sm						
Eu						
Gd						
Tb						
Ho						
Tm						
Yb						
Lu						
Sr 87/86						
Sm (Iso Dill)						
Nd (Iso Dill)						
Nd 144/143						

CG	B86/71
SiO2	70.90
TiO2	0.43
Al2O3	15.60
Fe2O3	3.20
MnO	0.07
MgO	0.90
CaO	2.00
Na2O	3.35
K2O	3.90
P2O5	0.14
S	0.01
LOI	0.82
Total	101.32
Tl	2604
Rb	274
Sr	121
Ba	650
Y	15
Hf	
Zr	165
Nb	12
Ta	
Pb	31
Th	20
U	<5
La	
Ce	
Nd	
Sm	
Eu	
Gd	
Tb	
Ho	
Tm	
Yb	
Lu	
Sr 87/86	
Sm (Iso Dill)	
Nd (Iso Dill)	
Nd 144/143	

AG	B85/213B AUTO	B86/120	B86/115	B86/123	B85/207	B86/121
SiO2	57.91	69.49	69.95	67.78	68.10	69.31
TiO2	1.14	0.51	0.48	0.61	0.57	0.52
Al2O3	17.17	15.18	14.88	15.25	14.97	15.00
Fe2O3	7.88	3.27	2.86	4.00	3.67	3.39
MnO	0.13	0.06	0.06	0.06	0.06	0.06
MgO	3.39	1.20	1.10	1.56	1.55	1.26
CaO	4.46	2.68	2.63	3.13	3.05	3.05
Na2O	4.48	3.32	3.25	3.22	3.59	3.70
K2O	2.95	3.80	4.37	3.00	3.63	2.59
P2O5	0.42	0.18	0.20	0.27	0.24	0.19
S	0.01	0.01	0.01	0.01	0.01	0.01
LOI	0.59	1.01	0.51	0.56	0.62	0.49
TOTAL	100.53	100.71	100.30	99.45	100.06	99.57
Ti	7829	3499	3159	4961	4145	3908
Rb	258	196	190	213	184	173
Sr	252	231	241	280	267	246
Ba	727	574	580	609	773	440
Y	50	26	28	27	25	22
Hf	6	4			4	
Zr	207	133	139	164	145	138
Nb	44	20	24	36	21	20
Ta	5	2			2	
Pb	14	21	19	29	16	16
Th	5	17	19	25	10	19
U	8	4		4	4	3
La	25.29	34.44			36.07	
Ce	61.41	70.31			70.16	
Nd	38.69	29.67			27.54	
Sm	9.10	6.01			5.26	
Eu	1.30	1.06			1.13	
Gd		4.81			3.42	
Tb	1.37	0.82			0.74	
Ho						
Tm	0.70				0.39	
Yb	4.34	2.40			2.15	
Lu	0.73	0.40			0.36	
Sr 87/86		0.71527 ± 4			0.71308 ± 2	
Sm (Iso Dill)					5.475 ± 5	
Nd (Iso Dill)					28.15 ± 9	
Nd 143/144					0.512319 ± 12	

AG	B86/76	B86/69	B86/84	B86/125	B86/130	B86/83
SiO2	70.00	70.08	70.15	66.70	68.81	71.16
TiO2	0.46	0.48	0.45	0.63	0.49	0.50
Al2O3	15.53	15.58	15.63	15.60	15.21	15.81
Fe2O3	3.20	3.21	2.83	4.23	3.16	3.49
MnO	0.05	0.06	0.05	0.06	0.05	0.05
MgO	1.03	1.09	0.79	1.91	1.22	0.78
CaO	2.36	2.33	1.98	3.39	2.89	2.90
Na2O	3.84	3.69	3.68	3.90	3.54	4.32
K2O	3.38	3.66	4.21	3.48	3.63	1.68
P2O5	0.22	0.20	0.30	0.21	0.20	0.23
S	0.01	0.01	0.01	0.01	0.01	0.01
LOI	0.84	0.70	0.89	0.50	0.74	0.53
TOTAL	100.92	101.09	100.97	100.62	99.95	101.46
Ti	3119	3510	2856	5092	3125	3494
Rb	213	189	221	187	196	174
Sr	230	220	219	302	253	189
Ba	718	657	665			
Y	23	25	20	28	24	16
Hf						
Zr	136	142	195	143	140	215
Nb	17	16	19	23	21	15
Ta						
Pb	22	24	34	15	18	18
Th	11	8	17	14	14	13
U	<5	<5	<5			<5
La						
Ce						
Nd						
Sm						
Eu						
Gd						
Tb						
Ho						
Tm						
Yb						
Lu						
Sr 87/86				0.71274 ± 4	.71310 ± 4	
Sm (Iso Dill)					5.132 ± 6	
Nd (Iso Dill)					26.65 ± 1	
Nd 143/144					0.512403 ± 27	

AG	B86/124	B85/208	B85/213A	B86/118	B86/131	B86/85
SIO2	68.21	66.93	67.14	68.52	66.55	57.02
TIO2	0.61	0.64	0.58	0.51	0.62	1.23
AI2O3	15.77	16.27	15.36	15.24	15.10	18.06
Fe2O3	3.89	4.28	3.90	3.33	4.03	7.53
MnO	0.06	0.07	0.07	0.05	0.07	0.12
MgO	1.75	1.76	1.65	1.21	1.51	3.13
CaO	3.42	3.48	3.34	3.08	3.40	6.49
Na2O	3.64	3.76	3.75	3.67	3.38	3.87
K2O	3.40	3.28	3.45	3.80	3.29	2.04
P2O5	0.25	0.26	0.21	0.17	0.23	0.47
S	0.01	0.02	0.01	0.01	0.02	0.02
LOI	0.41	0.74	0.51	0.71	0.44	0.76
TOTAL	101.42	101.49	99.97	100.30	98.64	100.74
Ti	4570	4446	4175	3215	4760	6786
Rb	161	152	170	160	160	123
Sr	293	299	281	262	296	541
Ba	641	731	677	672	621	
Y	24	28	26	24	26	41
Hf	5					6
Zr	131	159	155	135	156	268
Nb	20	19	19	16	20	28
Ta	2					2
Pb	18	17	19	18	17	<4
Th	11	8	9	9	12	5
U	3	1	4	3	6	6
La	34.18					35.10
Ce	68.10					80.49
Nd	27.83					42.43
Sm	5.17					8.80
Eu	1.19					2.06
Gd	5.28					8.50
Tb	0.73					1.30
Ho	2.54					1.68
Tm						0.70
Yb	2.06					3.56
Lu	0.37					0.58
Sr 87/86	0.71184 ± 4	0.71222 ± 2	0.71392 ± 4			0.70736 ± 3
Sm (Iso Dill)	4.813 ± 4					
Nd (Iso Dill)	24.17 ± 8					
Nd 143/144	0.512401 ± 22					

MAG	B86/14 ALTERED	B86/11 ALTERED	B86/13 ALTERED	B85/148 APL	B85/169 APL	B85/162A APL
SiO2	55.99	60.78	59.87	71.23	76.50	71.30
TiO2	00.67	00.67	00.81	00.30	00.11	00.33
Al2O3	14.10	14.59	16.13	14.44	14.32	15.41
Fe2O3	18.20	12.82	11.17	01.41	00.93	02.86
MnO	00.03	00.25	00.28	00.02	00.04	00.05
MgO	01.00	02.00	01.92	00.58	00.00	00.25
CaO	00.56	00.51	01.16	01.26	00.39	01.12
Na2O	00.32	00.31	00.35	03.81	03.11	04.19
K2O	01.47	02.65	03.57	05.21	05.41	04.68
P2O5	00.38	00.38	00.41	00.17	00.24	00.12
S	0.32	0.05	0.06	0.02	0.01	0.02
LOI	6.68	4.90	3.90	0.74	0.40	0.73
TOTAL	99.72	99.91	99.63	99.19	101.46	101.06
Ti	4482	4379	5125	1875	642	2290
Rb	94	237	259	214	410	373
Sr	18	17	68	534	27	128
Ba					20	
Y	18	24	28	26	19	40
Zr	197	203	213	171	43	394
Hf		4				
Nb	43	38	47	35	13	38
Ta		2				
Pb	14	<5	43	23	29	29
Th	68	23	31	24	0	27
U		<6	<7	6	9	11
La		77.67				
Ce		144.60				
Nd		54.63				
Sm		9.22				
Eu		1.88				
Gd		7.88				
Tb		0.92				
Ho						
Tm						
Yb		1.87				
Lu		0.29				
Sr 87/86						
Sm (Iso Dill)						
Nd (Iso Dill)						
Nd 143/144						

MAG	B85/133 APL	B85/125 APL	B86/22	B85/122	B85/134	B85/123
SIO2	74.75	71.47	65.17	69.72	67.58	66.01
TIO2	00.15	00.40	00.75	00.58	00.64	00.66
AI2O3	14.53	14.76	16.20	14.89	16.21	16.25
Fe2O3	01.32	02.10	04.16	03.13	03.64	03.72
MnO	00.02	00.04	00.04	00.03	00.04	00.04
MgO	00.34	00.99	02.29	01.58	01.73	02.05
CaO	00.38	01.29	03.24	01.53	02.33	02.90
Na2O	03.33	03.11	02.76	03.19	02.99	02.91
K2O	04.75	05.34	04.39	05.39	04.72	04.66
P2O5	00.18	00.22	00.37	00.30	00.40	00.35
S	0.02	0.02	0.03	0.02	0.02	0.02
LOI	0.45	0.86	0.83	0.67	0.40	1.34
TOTAL	100.22	100.60	100.23	101.03	100.70	100.91
Ti	858	2650	5883	4538	4548	4848
Rb	309	265	230	245	252	215
Sr	20	266	108	305	278	622
Ba	110			1086		
Y	17	24	26	21	23	25
Zr	55	114	195	153	173	168
Hf	2	4				
Nb	20	25	40	32	34	38
Ta	8	2				
Pb	39	46	18	36	24	28
Th	4	12	29	22	22	24
U	12	8		8	8	6
La	9.24	45.45				
Ce	20.14	87.68				
Nd	9.94	33.03				
Sm	1.83	5.58				
Eu	0.34	1.06				
Gd		6.06				
Tb	0.50	0.75				
Ho						
Tm	0.28	0.33				
Yb	1.65	1.85				
Lu	0.26	0.31				
Sr 87/86		0.71337 ± 2		0.71277 ± 4		0.71038 ±4
Sm (Iso Dill)						57.49 ± 3
Nd (Iso Dill)						9.32 ± 2
Nd 143/144						0.512358 ± 5

MAG	B85/142B	B86/10	B86/23	B86/50	B86/44	B86/43
SIO2	65.12	64.27	64.45	65.05	64.02	
TIO2	00.75	00.78	00.77	00.74	00.81	
AI2O3	16.30	16.28	16.51	16.08	16.56	
Fe2O3	04.13	04.32	04.37	04.18	04.56	
MnO	00.05	00.03	00.04	00.05	00.06	
MgO	02.17	02.21	02.35	02.24	02.30	
CaO	03.29	03.15	03.29	02.82	03.35	
Na2O	02.99	02.97	03.11	03.08	02.87	
K2O	04.31	04.71	04.42	04.56	04.34	
P2O5	00.40	00.39	00.38	00.36	00.36	
S	0.03	0.09	0.03	0.02	0.02	
LOI	0.92	0.91	0.24	1.05	1.01	
TOTAL	100.46	100.06	99.96	100.23	100.26	
Ti	5184	5433	5855	5972	6800	6247
Rb	213	227	225	222	226	222
Sr	753	677	721	647	772	762
Ba						
Y	24	24	27	25	25	24
Zr	181	191	163	174	193	155
Hf					6	
Nb	42	40	40	37	44	38
Ta					2	
Pb	19	23	17	25	27	17
Th	23	27	24	32	28	24
U	6	<6	<7	<6	<7	<7
La					87.94	
Ce					163.80	
Nd					60.52	
Sm					9.63	
Eu					2.09	
Gd					7.49	
Tb					1.08	
Ho						
Tm						
Yb					2.03	
Lu					0.32	
Sr 87/86						
Sm (Iso Dill)						
Nd (Iso Dill)						
Nd 143/144						

MAG	B85/117	B85/137	B85/118	B85/120	B86/18	B85/152
SiO2	66.37	67.23	68.64	68.80	69.06	64.89
TiO2	00.65	00.64	00.52	00.44	00.50	00.80
Al2O3	16.26	15.91	15.49	15.77	16.01	16.36
Fe2O3	03.66	03.34	03.11	02.70	02.88	04.19
MnO	00.07	00.03	00.05	00.03	00.05	00.03
MgO	01.83	01.80	01.57	01.17	01.27	02.31
CaO	02.68	02.29	02.22	02.07	02.40	03.30
Na2O	02.99	02.90	03.12	03.43	03.22	03.12
K2O	04.54	04.60	04.87	04.53	04.40	04.68
P2O5	00.35	00.34	00.33	00.24	00.31	00.42
S	0.02	0.03	0.03	0.03	0.01	0.03
LOI	1.00	1.19	0.98	0.94	0.74	0.73
TOTAL	100.42	100.30	100.93	100.15	100.85	100.86
Ti	5025	4289	3943	3321	3739	5711
Rb	238	218	231	222	275	223
Sr	582	534	486	430	507	759
Ba						
Y	24	26	27	17	21	24
Zr	161	171	134	145	145	192
Hf	5					
Nb	36	35	34	22	30	45
Ta	3					
Pb	28	23	36	28	29	17
Th	20	24	17	18	28	5
U	6	6	5	4	<6	5
La	81.42					
Ce	148.10					
Nd	57.80					
Sm	9.00					
Eu	1.93					
Gd	7.44					
Tb	1.02					
Ho						
Tm	0.35					
Yb	2.10					
Lu	0.33					
Sr 87/86			0.71055 ± 5	0.71111 ± 4		
Sm (Iso Dill)						
Nd (Iso Dill)						
Nd 143/144						

MAG	B85/153	B86/19	B86/52	B86/53	B86/34	B86/26
SiO2	64.72	64.75	64.77	65.11	65.22	66.05
TiO2	00.78	00.71	00.76	00.75	00.69	00.69
Al2O3	16.47	15.80	16.33	16.44	16.05	16.03
Fe2O3	04.46	04.08	04.08	04.13	03.87	03.80
MnO	00.04	00.05	00.05	00.05	00.05	00.04
MgO	02.54	02.04	02.11	02.01	02.08	01.92
CaO	03.46	03.01	02.75	02.78	02.92	02.95
Na2O	03.16	02.81	02.25	02.83	02.87	03.00
K2O	04.15	04.63	05.24	04.59	04.40	04.70
P2O5	00.40	00.34	00.36	00.30	00.39	00.35
S	0.02	0.03	0.03	0.03	0.02	0.03
LOI	0.75	0.70	1.54	1.08	0.83	0.68
TOTAL	100.95	98.95	100.27	100.10	99.39	100.24
Tl	5618	5883	5703	5789	5250	5590
Rb	227	231	291	218	258	235
Sr	766	713	622	642	631	650
Ba						
Y	26	26	28	26	24	26
Zr	189	171	196	197	177	174
Hf						
Nb	43	39	38	34	35	37
Ta						
Pb	16	23	29	28	20	18
Th	27	24	28	25	24	23
U	6	<7		<7		
La						
Ce						
Nd						
Sm						
Eu						
Gd						
Tb						
Ho						
Tm						
Yb						
Lu						
Sr 87/86						
Sm (Iso Dill)						
Nd (Iso Dill)						
Nd 143/144						

MAG	B86/21	B86/51	B86/27	B86/45	B86/46	B85/147
SiO2	63.94	64.00	64.02	64.16	64.32	64.65
TiO2	00.77	00.75	00.79	00.78	00.77	00.77
Al2O3	16.38	16.50	16.41	16.22	16.13	16.34
Fe2O3	04.33	04.06	04.44	04.49	04.21	04.24
MnO	00.04	00.05	00.06	00.06	00.05	00.04
MgO	02.24	02.28	02.38	02.26	02.08	02.30
CaO	03.36	03.30	03.34	03.18	03.25	03.48
Na2O	02.59	03.14	03.00	03.17	03.07	03.00
K2O	04.27	04.29	04.24	04.20	04.26	04.28
P2O5	00.41	00.35	00.36	00.42	00.41	00.37
S	0.03	0.02	0.02	0.02	0.03	0.03
LOI	0.78	0.56	0.75	0.91	0.94	0.71
TOTAL	99.14	99.30	99.81	99.87	99.52	100.21
Ti	6091	5973	6148	6234	5998	5716
Rb	222	213	219	219	223	212
Sr	751	779	723	724	740	772
Ba						
Y	26	25	28	26	26	25
Zr	193	181	195	182	202	183
Hf						6
Nb	41	38	42	42	45	42
Ta						2
Pb	19	24	20	30	22	14
Th	25	26	28	29	27	22
U				<7		5
La						92.47
Ce						165.10
Nd						60.04
Sm						9.25
Eu						2.11
Gd						8.88
Tb						1.06
Ho						
Tm						0.32
Yb						2.08
Lu						0.33
Sr 87/86			0.70870 ± 4			0.70818 ± 4
Sm (Iso Dill)						57.04 ± 3
Nd (Iso Dill)						9.29 ± 4
Nd 143/144						0.512417 ± 3

MAG	B85/116	B85/119	B85/149	B85/156	B86/9	B86/49
SiO2	69.69	65.59	63.18	63.58	63.63	63.69
TiO2	00.55	00.69	00.78	00.83	00.80	00.80
Al2O3	15.18	16.11	15.98	16.46	16.35	16.42
Fe2O3	02.92	03.89	04.32	04.37	04.75	04.72
MnO	00.03	00.04	00.04	00.04	00.04	00.06
MgO	01.60	02.02	02.39	02.65	02.21	02.60
CaO	01.85	02.94	03.54	03.39	03.33	03.65
Na2O	03.23	02.91	03.31	03.93	02.77	02.81
K2O	04.92	04.36	04.15	03.66	04.43	03.94
P2O5	00.27	00.29	00.35	00.45	00.38	00.42
S	0.02	0.02	0.03	0.01	0.05	0.01
LOI	0.72	0.69	0.82	0.89	0.81	1.10
TOTAL	100.98	99.55	98.89	100.26	99.55	100.22
Ti	4175	5563	5843	6214	6302	5926
Rb	239	234	216	274	229	190
Sr	424	676	794	758	737	838
Ba	1089	1256	1482			
Y	23	25	24	28	27	27
Zr	117	180	185	197	182	192
Hf						
Nb	31	37	42	44	43	43
Ta						
Pb	33	26	15	18	19	25
Th	14	20	23	6	29	33
U	6	6	7	0		<7
La						
Ce						
Nd						
Sm						
Eu						
Gd						
Tb						
Ho						
Tm						
Yb						
Lu						
Sr 87/86	0.71254 ± 3	0.70917 ± 3	0.70832 ± 4		0.70841 ± 4	
Sm (Iso Dill)	38.52 ± 2					
Nd (Iso Dill)	6.62 ± 2					
Nd 143/144	0.512342 ± 3					

MAG Enclaves	B85/141	B85/144	B85/145XA	B85/145X	B85/145D	B85/146A
SiO2	57.48	60.48	55.02	56.50	59.23	57.36
P2O5	0.90	0.14	0.76	0.65	0.73	0.93
TiO2	1.32	1.05	1.29	1.58	1.33	1.30
Al2O3	15.53	19.10	16.30	16.77	16.02	15.52
Fe2O3	7.33	7.01	7.23	7.74	7.20	7.48
MnO	0.08	0.19	0.10	0.06	0.05	0.09
MgO	4.55	2.01	4.96	4.40	3.63	4.54
CaO	4.80	0.16	6.46	4.76	3.96	4.78
Na2O	2.44	1.56	2.62	3.10	3.15	2.35
K2O	3.22	5.36	2.51	3.49	3.10	3.18
P2O5	0.90	0.14	0.76	0.65	0.73	0.93
S	0.05	0.04	0.03	0.02	0.02	0.06
LOI	0.98	0.90	0.87	1.00	0.86	1.10
TOTAL	99.58	98.14	98.91	100.72	100.01	99.62
Ti	9160	5478	10861	8777	9664	8852
Rb	256	232	257	160	264	249
Sr	714	708	853	1232	656	716
Ba						
Y	39	47	36	32	48	40
Zr	251	248	292	250	246	255
Hf	7	0	7	6	0	0
Nb	82	33	58	78	66	80
Ta	5	0	4	4	0	0
Pb	7	15	7	7	10	8
Th	33	18	23	30	24	31
U	9	4	10	6	7	10
La	163.80		107.70	144.60		
Ce	299.10		199.20	257.50		
Nd	114.00		81.54	97.30		
Sm	15.87		12.34	13.90		
Eu	2.68		2.23	2.92		
Gd	14.58		10.85	15.36		
Tb	1.63		1.41	1.57		
Ho				2.83		
Tm	0.51		0.55			
Yb	3.22		3.02	3.02		
Lu	0.51		0.48	0.47		
Sr 87/86				0.70628 ± 7		
Sm (Iso Dill)				13.51 ± 3		
Nd (Iso Dill)				92.93 ± 7		
Nd 143/144				0.512578 ± 21		

MAG Enclaves	B86/28	B85/145
SiO2	59.46	61.11
P2O5	0.57	0.56
TiO2	1.13	1.14
Al2O3	16.09	16.98
Fe2O3	6.61	6.27
MnO	0.08	0.05
MgO	4.25	3.65
CaO	4.09	4.71
Na2O	2.74	2.91
K2O	3.16	2.74
P2O5	0.57	0.56
S	0.02	0.02
LOI	0.70	0.76
TOTAL	99.47	101.46
Ti	85	7960
Rb	279	213
Sr	607	823
Ba		
Y	35	35
Zr	231	246
Hf		0
Nb	51	56
Ta		0
Pb	15	13
Th	28	31
U	<7	0
La		
Ce		
Nd		
Sm		
Eu		
Gd		
Tb		
Ho		
Tm		
Yb		
Lu		
Sr 87/86		
Sm (Iso Dill)		
Nd (Iso Dill)		
Nd 143/144		

MVGP	B85/158	B85/160	B86/38	B85/154	B85/128	B85/167A
SIO2	71.13	72.29	72.29	72.37	73.61	75.54
P2O5	00.23	00.25	00.19	00.20	00.17	00.22
TIO2	00.23	00.31	00.33	00.31	00.27	00.13
AI2O3	16.20	14.71	14.07	14.68	14.12	14.12
Fe2O3	01.61	02.37	02.62	02.38	00.20	01.55
MnO	00.05	00.06	00.04	00.05	00.06	00.04
MgO	00.26	00.46	00.24	00.44	00.39	00.25
CaO	00.69	01.14	01.33	01.12	01.09	00.60
Na2O	03.65	03.65	03.21	03.32	03.64	03.67
K2O	06.57	04.82	04.23	04.78	04.12	04.58
P2O5	00.23	00.25	00.19	00.20	00.17	00.22
	0.01	0.01	0.01	0.01	0.01	0.02
	0.69	1.00	0.95	0.69	0.78	0.69
TOTAL	101.55	101.32	99.70	100.55	98.63	101.63
Ti	1386	2093	2249	2124	1904	1045
Rb	393	377	323	371	368	545
Sr	171	133	141	129	102	40
Ba					244	94
Y	18	25	26	26	27	23
Zr	83	134	132	127	115	63
Hf					4	2
Nb	18	27	22	26	26	27
Ta					5	7
Pb	52	40	25	36	31	29
Th	7	15	20	12	13	7
U	10	7	10	10	15	14
La					31.41	12.85
Ce					64.96	28.87
Nd					26.85	14.12
Sm					6.05	3.88
Eu					0.65	0.3
Tb					6.62 0.7534	0.35
Tm						
Yb					2.54	1.98
Lu					0.42	0.35
Sr 87/86	0.71599 ± 7	0.71663 ± 3	0.71603 ± 7	0.71655 ± 2	0.72133 ±3	0.72754 ± 4
Sm (Iso Dill)	2.908 ± 2					1.977 ± 2
Nd (Iso Dill)	14.96 ± 5					9.071 ± 9
Nd 143/144	0.512095 ± 20					0.512399 ± 24

MVGP	B85/131	B85/167	B85/157
SiO2	71.73	71.19	72.47
P2O5	00.29	00.21	00.25
TiO2	00.37	00.34	00.37
Al2O3	14.59	15.10	14.37
Fe2O3	02.84	02.59	02.58
MnO	00.05	00.05	00.05
MgO	00.61	00.42	00.54
CaO	01.32	01.15	01.19
Na2O	03.24	03.26	03.13
K2O	04.63	05.11	04.31
P2O5	00.29	00.21	00.25
	0.01	0.01	0.00
	0.67	0.70	0.78
TOTAL	100.36	100.34	100.04
Ti	2703	2612	2344
Rb	380	461	333
Sr	134	148	141
Ba		510	524
Y	26	27	25
Zr	172	153	156
Hf	5		
Nb	33	30	25
Ta	4		
Pb	34	34	28
Th	16	16	17
U	11	6	8
La	46.69		
Ce	90.95		
Nd	38.88		
Sm	6.08		
Eu	0.94		
	6.07		
Tb	0.86		
Tm	0.45		
Yb	2.62		
Lu	0.41		
Sr 87/86			
Sm (Iso Dill)			
Nd (Iso Dill)			
Nd 143/144			

MVGP Autoliths	B86/33	B86/32	B85/155A	B86/39	B86/24	B86/40
SiO2	71.33	72.58	69.15	71.41	60.02	69.16
P2O5	00.20	0.20	0.27	0.14	0.62	0.24
TiO2	00.43	0.35	0.49	0.40	1.14	0.45
Al2O3	14.63	14.54	14.97	14.10	16.36	15.33
Fe2O3	03.03	2.50	3.89	2.99	6.67	3.46
MnO	00.05	0.06	0.07	0.05	0.08	0.06
MgO	00.42	0.39	0.69	0.45	4.24	0.62
CaO	01.23	0.93	1.48	1.19	4.18	1.50
Na2O	03.47	3.64	4.05	3.61	3.19	3.97
K2O	04.70	4.99	3.87	4.56	3.14	4.61
P2O5	00.20	0.20	0.27	0.14	0.62	0.24
	0.01	0.01	0.01	0.01	0.03	0.01
	0.57	0.75	0.47	0.75	0.85	0.88
TOTAL	100.27	101.14	99.68	99.80	100.52	100.53
Tl	2821	2253	3319	2752	6602	3095
Rb	377	466	431	342	270	360
Sr	132	100	119	127	609	162
Ba			489			
Y	32	29	31	31	39	32
Zr	255	186	208	235	214	161
Hf			6			
Nb	38	30	35	33	61	33
Ta			4			
Pb	38	34	32	29	12	27
Th	32	25	23	32	33	23
U	9	13	10	11		
La			59.79			
Ce			118.40			
Nd			45.55			
Sm			7.72			
Eu			0.92			
			7.99			
Tb			0.99			
Tm			0.42			
Yb			2.55			
Lu			0.39			
Sr 87/86			0.71528 ± 3		0.70812 ± 2	

MVGP Autoliths	B86/31	B85/155B	B86/36	B86/37	B86/35	B86/42
SiO2	69.66	72.63	74.76	73.86	73.62	72.56
P2O5	0.13	0.00	0.17	0.20	0.22	0.18
TiO2	0.43	0.27	0.13	0.19	0.25	0.33
Al2O3	15.37	14.66	13.81	13.79	14.16	14.51
Fe2O3	3.43	2.31	1.54	2.20	2.17	2.41
MnO	0.05	0.04	0.04	0.05	0.06	0.04
MgO	0.46	0.31	0.16	0.23	0.37	0.49
CaO	1.51	0.96	0.46	0.70	0.61	1.27
Na2O	4.02	3.79	3.51	3.28	3.21	3.46
K2O	4.58	4.74	4.69	4.83	5.08	4.43
P2O5	0.13	0.00	0.17	0.20	0.22	0.18
	0.01		0.01	0.02	0.01	0.01
	0.39		0.69	1.01	0.74	0.86
TOTAL	100.17	99.71	100.14	100.56	100.72	100.73
Ti	3053	1843	860	1276	1766	2166
Rb	419	409	500	524	406	345
Sr	148	87	31	55	54	155
Ba						
Y	37	32	21	24	29	25
Zr	368	296	57	84	98	143
Hf						
Nb	33	33	23	26	25	23
Ta						
Pb	33	40	27	21	38	26
Th	28	29	9	11	14	16
U	7	9	24	21	18	8
La						
Ce						
Nd						
Sm						
Eu						
Tb						
Tm						
Yb						
Lu						
Sr 87/86						

	B85/51	B85/72	B85/45	B85/43	HP B85/55	B85/84	B85/83	B85/52	B85/76
Ti	1820	2788	1837	5482	1909	3097	2701	4547	1586
Rb	390	243	262	239	237	197	229	183	371
Sr	90	239	77	340	186	271	223	370	96
Ba	342	556		797	472	669		899	326
Y	16	25	20	41	21	26	22	33	17
Zr	112	120	108	182	108	139	28	81	88
Nb	13	19	12	27	17	19	20	22	17
Pb	35	32	17	6	36	29	66	28	39
Th	18	6	10	9	8	10	10	10	7
U		7			9	4	4		

	B85/46	B85/47	B85/48	B85/70	B85/71	B85/74	B85/82	B85/54	B85/44
Ti	1973	1885	2180	2147	2334	2229	4684	4400	2102
Rb	290	370	254	223	256	262	149	164	258
Sr	148	106	158	220	191	198	347	406	124
Ba			413				782	840	
Y	23	16	21	23	23	23	29	34	20
Zr	110	115	123	17	115	105	182	197	115
Nb	14	12	15	19	18	17	19	23	19
Pb	35	32	32	29	36	33	23	23	25
Th	13	7	12	9	7	7	10	12	13
U		4				6		6	5

	B85/75	B85/82A	B85/73
Ti	700	7212	3390
Rb	265	167	186
Sr	121	352	240
Ba			277
Y	17	42	22
Zr	46	240	170
Nb	6	27	26
Pb	44	728	21
Th		17	8
U			

				UND					
	B85/94	B85/108	B85/107	B85/101	B85/100	B85/109	B85/99	B85/98	B85/104
Ti	3801	2707	464	3992	3807	1597	3830	2599	387
Rb	168	206	349	217	213	336	207	173	205
Sr	382	320	46	360	362	97	362	247	32
Ba	764		81	795	835			656	53
Y	26	26	10	29	29	18	29	27	7
Zr	163	126	36	163	170	97	154		28
Nb	22	18	16	4	24	17	3	17	13
Pb	30	50	19	24	26	36	24	39	28
Th	10	8			12	7		9	
U					5	4		4	4

	B85/106	B85/102
Ti	593	7607
Rb	226	207
Sr	8	386
Ba	258	865
Y	8	40
Zr	27	264
Nb	12	37
Pb	9	16
Th	4	10
U		4

CK

	B85/42	B85/29	B85/26	B85/27	B85/28	B85/41	B85/40	B85/33	B85/34
Tl	617	1262	1478	1272	1217	772	799	690	708
Rb	418	289	377	288	405	442	431	415	469
Sr	34	69	73	61	65	41	46	42	43
Ba	40		214			34			
Y	17	16	18	19	19	19	20	21	18
Zr	49	66	76	75	71	50	48	49	45
Nb	17	19	18	20	19	20	18	19	20
Pb	28	41	42	39	40	29	32	31	31
Th			5	6	4				
U	3	4	5	7	4	5	14	4	4

	B85/37	B85/38	B85/30	B85/31
Tl	882	848	931	1039
Rb	465	453	390	385
Sr	45	42	76	50
Ba		70	193	
Y	18	22	14	20
Zr	46	55	43	63
Nb	21	21	14	17
Pb	31	30	48	35
Th				
U	3	19	5	12

SY

	B85/18 PEG	B85/64 GNT. PEG	B85/25A	B85/25	B85/24	B85/22	B85/21	B85/11	B85/13
Tl	371	115	1267	804	1692	1398	1501	2160	2141
Rb	218	282	413	399	383	377	433	406	382
Sr	66	13	73	68	107	85	88	101	99
Y	7	4	19	14	19	19	17	14	13
Zr	28	14	69	40	87	71	72	120	118
Nb	13	20	18	13	16	17	19	8	10
Pb	16	19	42	46	51	44	48	48	45
Th			4		6			17	19
U		6	7	5	5	7		10	10

	B85/10	B85/20	B85/17
Tl	1957	1812	2280
Rb	390	388	409
Sr	110	88	93
Y	15	20	16
Zr	128	84	140
Nb	6	19	7
Pb	52	45	42
Th	17	4	2
U	10	6	6

ILL	B85/245	B85/248	B85/243	B85/240	B85/225	B85/234A APL	B85/234B	B85/239	B85/238A
SiO2	68.15	65.96	67.45	69.60	69.13	75.10	71.32	70.41	68.14
TiO2	0.54	0.64	0.55	0.51	0.41	0.21	0.28	0.39	0.56
Al2O3	15.27	16.05	15.15	14.59	15.04	13.42	15.43	15.38	15.33
Fe2O3	2.69	3.87	3.14	2.77	2.03	0.83	1.59	2.03	2.99
MnO	0.03	0.03	0.03	0.03	1.11	0.01	0.04	0.03	0.04
MgO	1.51	1.99	1.49	1.40	1.83	0.39	0.60	0.91	1.59
CaO	2.58	3.03	2.54	2.29	3.82	0.98	1.53	1.78	2.49
Na2O	3.48	3.43	3.40	3.12	4.71	3.15	3.93	3.76	3.60
K2O	4.68	4.73	4.70	4.81	0.28	5.64	4.75	4.88	4.65
P2O5	0.27	0.45	0.25	0.25	0.01	0.07	0.23	0.28	0.26
S	0.02	0.01	0.03	0.02	0.58	0.01	0.02	0.01	0.01
LOI	0.54	0.40	0.53	0.41	0.58	0.48	0.55	0.50	0.67
TOTAL	99.76	100.59	99.26	99.80	99.53	100.29	100.27	100.36	100.33
Ti	3804	4257	3927	3611	2936	1383	1840	2634	3903
Rb	247	210	297	280	292	263	288	299	269
Sr	765	929	687	595	491	277	369	458	650
Ba	1241	1774	1203		865	594			
Y	19	23	18	19	25	30	20	21	20
Hf			5		4			4	
Zr	175	216	179	157	151	97	137	144	174
Nb	52	48	46	44	44	55	34	46	45
Ta			3		4			5	
Pb	17	28	16	18	38	14	56	40	19
Th	31	39	24	22	22	28	19	19	22
U	16	10	13	11	11	30	11	13	14
La			80.87		66.14			60.87	
Ce			152.90		124.00			117.20	
Nd			54.36		45.06			42.41	
Sm			8.75		8.07			7.76	
Eu			1.54		1.39			1.33	
Gd			7.69						
Tb			0.85		1.00			0.89	
Ho									
Tm									
Yb			1.53		1.95			1.69	
Lu			0.27		0.29			0.27	

ILL	B85/233	B85/230	B85/228	85/B237	85/B246	B85/227 AUTO	B85/224	B85/240A	B85/235 APL
SiO2	68.21	68.67	68.38	70.19		61.75	62.73	62.54	75.92
TiO2	0.50	0.46	0.54	0.41		0.87	0.99	0.88	0.24
Al2O3	15.63	15.53	15.22	15.29		14.70	15.75	15.57	15.58
Fe2O3	2.68	2.61	2.53	2.24		7.28	6.14	5.48	0.13
MnO	0.02	0.02	0.03	0.04		0.05	0.07	0.07	0.01
MgO	1.34	1.27	1.50	0.98		2.99	3.10	3.33	0.13
CaO	2.02	2.47	2.56	1.73		3.38	3.58	3.46	2.71
Na2O	3.41	3.87	3.98	3.76		3.17	3.22	3.54	6.23
K2O	5.67	4.54	3.80	4.85		3.57	3.76	3.37	0.18
P2O5	0.26	0.22	0.26	0.27		0.55	0.54	0.41	0.03
S	0.01	0.02	0.01	0.01		0.02	0.02	0.02	0.01
LOI	1.08	0.54	1.70	0.59		0.61	0.45	0.86	0.37
TOTAL	100.83	100.22	100.51	100.36		98.94	100.35	99.53	101.54
Ti	3457	3295	3295	2860	3162	5972	6625	5986	1158
Rb	286	243	195	301	292	265	283	337	7
Sr	596	659	745	451	522	678	775	757	457
Ba					1564	1264	1386		120
Y	18	18	22	20	20	1	26	37	0
Hf									
Zr	159	166	175	158	181	201	236	254	94
Nb	37	34	41	54	34	53	69	62	35
Ta									
Pb	18	17	15	38	28	12	14	9	33
Th	25	18	27	20	29	20	36	28	9
U	11	7	9	8	10	7	11	8	2
La									
Ce									
Nd									
Sm									
Eu									
Gd									
Tb									
Ho									
Tm									
Yb									
Lu									

Sediments	B85/2	B85/200	B86/100	B86/110	B86/1	B86/102
Strat. Age	u Ord.	1 Sil.	Sil.	Sil	Dev.	Dev.
Assumed Age (Ma)	440	420	425	420	390	370
SiO2			69.31	53.45	60.49	80.55
TiO2			0.8	0.44	1.05	0.7
Al2O3			15.3	15.74	23.17	12.79
Fe2O3			5.78	7.49	2.73	1.08
MnO			0.07	0.13	0.03	0.01
MgO			1.46	6.81	1.46	0.41
CaO			0.52	11.45	0.06	0.11
Na2O			0.96	1.52	0.29	0.3
K2O			2.85	0.18	6	2.27
P2O5			0.23	0.05	0.1	0.1
S			0.06	0.02	0.02	0.01
LOI			3.12	2.38	5.54	3.03
TOTAL			100.46	99.66	100.94	101.36
Ti	3708	5651	5749	2374	7266	5299
Rb	109	165	126	4	424	118
Sr	71	120	65	87	211	93
Ba	484	1294	550		386	
Y	27	35	35	13	49	33
Hf		8.14	7.73			14.5
Zr	308	265	258	26	256	454
Nb	13.3	17.5	15.3	3.7	22.7	14.5
Ta		1.6	1.26			1.24
Pb	20	22	20	<4	17	24
Th	11	12	12	<3	26	18
U	<3	<3	3.5	<3	10	5
La		48.39	45.44			36.93
Ce		99.06	100.12			84.43
Nd		42.03	46.45			39.94
Sm		7.95	9.2			8.38
Eu		1.7	1.79			1.51
Gd		5.86	9.4			6.95
Tb		1.14	1.42			1.26
Ho			3.59			2.42
Tm		0.606	0.61			0.53
Yb		3.75	3.68			4.04
Lu		0.62	0.63			0.73
Sr 87/86	0.74377 ± 4	0.73443 ± 3		0.74626 ± 4	0.7501 ± 3	0.73577 ± 5
Sm (Iso Dill)	11.29 ± 1					8.03 ± 1
Nd (Iso Dill)	49.91 ± 3					37.26 ± 2
Nd 143/144	0.51211 ± 20					0.51207 ± 20

Sediments	B86/101	B85/202	B86/2	B86/111	B86/TER	River Sed B86/3ii
Strat. Age	Carb.			Quat	Ter	Mod
Assumed Age (Ma)	300			1.5		
SiO2	63.73	69.21	73.22	73.38	60.87	
TiO2	0.54	0.93	0.65	0.84	0.96	
Al2O3	14.07	15.51	12.76	16.67	20.54	
Fe2O3	5.62	6.4	5.14	1.17	6.64	
MnO	0.04	0.05	0.11	0.01	0.03	
MgO	2.61	1.4	1.57	0.66	1.4	
CaO	1.05	0.17	0.29	0.12	0.11	
Na2O	0.73	1.26	1.96	1.13	0.99	
K2O	8.98	3.93	1.94	3.42	4.23	
P2O5	0.12	0.15	0.17	0.14	0.18	
S	0.01	0.01	0.01	0.02	0.02	
LOI	2.89	1.88	2.37	3.93	5.36	
TOTAL	100.39	100.9	100.19	101.49	101.33	
Ti	3568	5787	4128	5544	6453	4274
Rb	78	161	122	159	205	143
Sr	38	104	34	121	167	213
Ba	194		146	345	614	442
Y	21	37	50	36	38	27
Hf			8.35	7.11	4.96	
Zr	257	379	291	252	185	140
Nb	12.1	18.4	13.5	17.6	19.2	12.3
Ta			1.27	1.45	1.58	
Pb	8	25	7	53	19	20
Th	11	14	14	16	21	15
U	<5	<3	<4	6	<6	<5
La			53.59	35.8	49.53	
Ce			64.43	77.75	105.1	
Nd			54.49	35.52	48.22	
Sm			11.03	7.17	9.015	
Eu			2.25	1.4	1.73	
Gd			9.5	6.2	7.93	
Tb			1.722	1.14	1.26	
Ho			2.54	2.91	1.7	
Tm			0.6	0.61	0.57	
Yb			4.18	3.5	3.6	
Lu			0.73	0.64	0.59	
Sr 87/86	0.75051 ± 4			0.73327 ± 5		
Sm (Iso Dill)	5.39 ± 1			6.94 ± 1		
Nd (Iso Dill)	28.88 ± 2			33.35 ± 2		
Nd 143/144	0.51236 ± 3			0.512144 ± 24		

Appendix C Microprobe analyses

B85/6

SiO2	37.51	37.30	37.96	37.35	34.35	35.15	34.33	34.76	34.44	46.76	46.50	47.21	46.73	46.62
TiO2	0.00	0.00	0.04	0.04	1.90	1.58	1.56	1.77	1.83	0.32	0.39	0.30	0.34	0.24
Al2O3	62.89	62.55	61.95	62.68	20.54	20.33	20.35	20.39	20.55	37.23	37.17	36.49	36.61	36.97
FeO	0.21	0.35	0.25	0.21	24.37	23.77	24.23	24.45	24.39	0.73	0.76	0.67	0.57	0.02
MnO	0.00	0.02	0.02	0.02	0.29	0.23	0.23	0.27	0.23	0.03	0.00	0.06	0.03	0.27
MgO	0.01	0.01	0.01	0.01	6.13	6.14	6.37	6.50	6.34	0.30	0.28	0.25	0.25	0.65
CaO	0.01	0.01	0.01	0.01	0.03	0.04	0.07	0.01	0.01	0.01	0.04	0.12	0.04	0.03
Na2O	0.00	0.03	0.00	0.01	0.26	0.21	0.23	0.24	0.24	1.29	1.31	1.45	1.34	1.25
K2O					7.94	7.80	7.55	8.08	8.01	9.67	9.79	9.36	9.35	9.20
BaO					0.11	0.10	0.10	0.11	0.11					
Cl					0.01	0.01	0.01	0.01	0.01					
Total	100.63	100.27	100.24	100.33	95.93	95.36	95.03	96.59	96.16	96.34	96.24	95.91	95.26	95.25
	Formula units dased on 20 oxygens				Formula units based on 22 oxygens					Formula units based on 22 oxygens				
Si	4.0243	4.0199	4.0869	4.0204	5.2839	5.4040	5.3151	5.3085	5.2839	6.1108	6.0920	6.1867	6.1598	6.1403
Ti	0.0000	0.0000	0.0030	0.0030	0.2193	0.1826	0.1815	0.2035	0.2106	0.0312	0.0387	0.0295	0.0334	0.0241
Al	7.9528	7.9472	7.8618	7.9519	3.7236	3.6836	3.7132	3.6710	3.7157	5.7350	5.7401	5.6362	5.6889	5.7393
Fe	0.0188	0.0315	0.0227	0.0189	3.1351	3.0561	3.1377	3.1227	3.1288	0.0796	0.0829	0.0737	0.0633	0.0017
Mn	0.0000	0.0014	0.0014	0.0014	0.0377	0.0298	0.0300	0.0355	0.0297	0.0034	0.0000	0.0069	0.0035	0.0525
Mg	0.0022	0.0022	0.0022	0.0022	1.4055	1.4065	1.4711	1.4790	1.4494	0.0578	0.0551	0.0494	0.0496	0.0710
Ca	0.0016	0.0016	0.0016	0.0016	0.0046	0.0070	0.0117	0.0023	0.0023	0.0020	0.0062	0.0165	0.0062	0.0041
Na	0.0000	0.0057	0.0000	0.0028	0.0785	0.0613	0.0677	0.0722	0.0726	0.3279	0.3326	0.3693	0.3422	0.3198
K					1.5570	1.5300	1.4920	1.5730	1.5670	1.6132	1.6361	1.5642	1.5731	1.5460
Ba					0.0067	0.0059	0.0060	0.0066	0.0067					
Cl					0.0031	0.0031	0.0032	0.0031	0.0031					
Total	11.9997	12.0095	11.9796	12.0022	15.4550	15.3699	15.4292	15.4774	15.4698	13.9609	13.9837	13.9324	13.9200	13.8988
	Andalusite				Biotites					Muscovites				

	B85/202						
SiO2	37.44	36.39	36.30	36.35	36.43	45.95	45.71	50.52	46.41	48.05	46.40	46.18
TiO2	2.70	3.03	2.80	2.64	3.23	0.62	0.56	0.39	0.45	0.43	0.56	0.79
Al2O3	20.79	20.45	20.43	20.94	20.91	36.19	36.39	33.40	36.22	34.32	36.52	36.55
FeO	21.54	22.32	21.67	21.65	21.95	0.95	0.94	0.02	0.03	0.02	0.02	0.02
MnO	0.12	0.14	0.15	0.12	0.15	0.00	0.02	0.62	0.43	0.92	0.46	0.39
MgO	5.87	5.80	5.80	5.88	5.42	0.43	0.52	0.91	0.88	1.07	0.80	1.25
CaO	0.00	0.00	0.00	0.00	0.00	0.01	0.01	0.03	0.01	0.01	0.01	0.03
Na2O	0.11	0.13	0.11	0.11	0.13	0.68	0.60	0.36	0.48	0.38	0.46	0.48
K2O	9.66	9.90	9.77	9.81	9.91	11.42	11.38	9.93	10.36	10.37	10.57	10.48
BaO	0.13	0.15	0.14	0.16	0.15	0.08	0.11	0.00	0.00	0.00	0.00	0.00
Total	98.36	98.31	97.17	97.66	98.28	96.33	96.24	96.18	95.27	95.57	95.80	96.17
	Formula units based on 22 oxygens					**Formula units based on 22 oxygens**						
Si	5.5329	5.4305	5.4617	5.4356	5.4235	6.0806	6.0553	6.5720	6.1499	6.3416	6.1201	6.0842
Ti	0.2999	0.3403	0.3172	0.2973	0.3617	0.0615	0.0559	0.0384	0.0447	0.0427	0.0557	0.0778
Al	3.6208	3.5965	3.6221	3.6924	3.6687	5.6454	5.6821	5.1227	5.6570	5.3383	5.6785	5.6765
Fe	2.6617	2.7851	2.7261	2.7080	2.7350	0.1054	0.1040	0.0017	0.0035	0.0017	0.0017	0.0017
Mn	0.0153	0.0174	0.0195	0.0155	0.0192	0.0000	0.0017	0.1206	0.0849	0.1810	0.0902	0.0759
Mg	1.2924	1.2910	1.3013	1.3108	1.2034	0.0850	0.1027	0.0991	0.0978	0.1176	0.0881	0.1374
Ca	0.0000	0.0000	0.0000	0.0000	0.0000	0.0021	0.0021	0.0041	0.0021	0.0020	0.0020	0.0041
Na	0.0314	0.0373	0.0321	0.0318	0.0371	0.1750	0.1529	0.0914	0.1230	0.0968	0.1185	0.1227
K	1.8207	1.8845	1.8749	1.8712	1.8823	1.9274	1.9238	1.6470	1.7500	1.7460	1.7780	1.7610
Ba	0.0072	0.0087	0.0081	0.0095	0.0087	0.0041	0.0054	0.0000	0.0000	0.0000	0.0000	0.0000
Total	15.2823	15.3913	15.3630	15.3721	15.3396	14.0865	14.0859	13.6970	13.9129	13.8677	13.9328	13.9413
	Biotites					**Muscovites**						

B85/202

SiO2	41.67	48.11	47.72	47.07	47.99	47.93	48.14	48.20	48.08
TiO2	0.02	0.04	0.02	0.02	0.02	0.04	0.02	0.04	0.04
Al2O3	59.53	32.81	32.53	32.00	32.49	32.75	32.68	32.89	32.66
FeO	0.38	10.96	10.25	9.81	10.51	10.41	10.47	10.40	10.29
MnO	0.02	0.50	0.48	0.45	0.47	0.42	0.43	0.43	0.43
MgO	0.01	5.56	5.49	5.29	5.63	5.50	5.40	5.65	5.38
CaO	0.04	0.04	0.03	0.04	0.06	0.04	0.00	0.01	0.04
Na2O	0.01	0.51	0.96	1.09	0.59	0.89	0.93	0.87	1.06
K2O	0.08	0.00	0.01	0.01	0.00	0.00	0.00	0.00	0.00
BaO									
Total	101.76	98.53	97.49	95.78	97.76	97.98	98.07	98.49	97.98
	Formula units based on 20 oxygens								
Si	4.4076	5.5715	5.5773	5.5925	5.5913	5.5737	5.0331	5.0163	5.0311
Ti	0.0014	0.0031	0.0016	0.0016	0.0015	0.0031	0.0014	0.0028	0.0028
Al	7.4221	4.4793	4.4818	4.4818	4.4624	4.4889	4.0278	4.0346	4.0280
Fe	0.0334	0.0486	0.0476	0.0453	0.0459	0.0412	0.9152	0.9052	0.9004
Mn	0.0014	0.9590	0.9566	0.9371	0.9772	0.9538	0.0384	0.0382	0.0385
Mg	0.0022	1.0616	1.0016	0.9746	1.0241	1.0126	0.8409	0.8771	0.8390
Ca	0.0049	0.0053	0.0035	0.0054	0.0071	0.0053	0.0000	0.0016	0.0048
Na	0.0028	0.1143	0.2185	0.2512	0.1325	0.1996	0.1891	0.1751	0.2145
K	0.0110	0.0000	0.0010	0.0010	0.0000	0.0000	0.0000	0.0000	0.0000
Ba									
Total	11.8868	12.2427	12.2895	12.2905	12.2420	12.2782	11.0459	11.0509	11.0591

Cordierites

SiO2	47.61	47.53	47.55	48.18	48.01	24.12	22.91	22.58	23.28	21.74
TiO2	0.02	0.02	0.02	0.02	0.00	0.00	0.07	0.10	0.09	0.05
Al2O3	32.06	32.16	32.17	32.56	32.74	24.35	23.62	23.66	23.59	23.02
FeO	9.76	9.83	9.57	0.61	0.61	0.23	0.24	0.24	0.26	0.24
MnO	0.65	0.61	0.64	4.99	5.08	9.04	9.19	8.97	9.13	8.49
MgO	5.06	4.91	4.99	9.86	9.94	28.05	29.37	29.33	28.99	28.79
CaO	0.03	0.04	0.04	0.04	0.04	0.04	0.07	0.76	0.08	0.22
Na2O	1.25	1.44	1.45	1.28	1.26	0.02	0.02	0.02	0.00	0.02
K2O	0.00	0.01	0.01	0.01	0.01	0.08	0.01	0.01	0.00	0.01
BaO										
Cl										
Total	96.44	96.55	96.44	97.55	97.69	85.93	85.50	85.67	85.42	82.58
	Formula units based on 20 oxygens					Formula units based on 28 oxygens				
Si	5.620	5.6098	5.6124	5.5163	5.4929	5.2549	5.0810	5.0135	5.1498	5.0116
Ti	0.002	0.0018	0.0018	0.0017	0.0000	0.0000	0.0115	0.0173	0.0143	0.0089
Al	4.461	4.4740	4.4756	4.3941	4.4152	6.2520	6.1742	6.1932	6.1525	6.2551
Fe	0.964	0.9703	0.9447	0.0584	0.0584	0.0420	0.0455	0.0456	0.0482	0.0473
Mn	0.065	0.0610	0.0640	0.4839	0.4923	2.9356	3.0382	2.9699	3.0112	2.9165
Mg	0.890	0.8639	0.8780	1.6828	1.6953	5.1094	5.4473	5.4465	5.3634	5.5515
Ca	0.004	0.0051	0.0051	0.0049	0.0049	0.0096	0.0163	0.1803	0.0196	0.0544
Na	0.286	0.3296	0.3319	0.2842	0.2795	0.0082	0.0085	0.0085	0.0000	0.0089
K		0.0015	0.0015	0.0015	0.0015	0.0220	0.0030	0.0030	0.0000	0.0030
Ba										
Cl										
Total	12.2911	12.3169	12.3148	12.4278	12.4400	19.6337	19.8255	19.8778	19.7590	19.8572
	Cordierites					Chlorites				

B85/9

SiO2	34.68	34.46	33.68	34.10	45.19	45.46	45.75	45.28
TiO2	2.24	1.44	1.87	2.93	0.86	0.67	0.82	0.80
Al2O3	20.06	20.65	20.93	21.94	36.06	36.35	35.76	35.70
FeO	23.11	23.12	22.24	21.87	1.11	1.05	0.98	1.37
MnO	0.15	0.15	0.17	0.17	0.03	0.03	0.02	0.02
MgO	6.62	6.66	6.30	6.65	0.39	0.36	0.42	0.48
CaO	0.00	0.00	0.00	0.00	0.00	0.00	0.00	0.00
Na2O	0.24	0.22	0.26	0.29	1.10	1.15	1.05	1.13
K2O	8.14	8.06	8.09	7.07	9.02	9.40	9.36	9.24
BaO	0.00	0.00	0.00	0.00	0.30	0.32	0.24	0.28
Cl	0.01	0.01	0.00	0.00				
Total	95.42	94.92	93.54	95.02	94.06	94.79	94.40	94.30
	Formula units based on 22 oxygens				Formula units based on 22 oxygens			
Si	5.3347	5.3237	5.2649	5.1901	6.066	6.0660	6.1184	6.0793
Ti	0.2590	0.1672	0.2197	0.3358	0.087	0.0672	0.0825	0.0808
Al	3.6374	3.7605	3.8573	3.9358	5.705	5.7172	5.6370	5.6496
Fe	2.9734	2.9868	2.9078	2.7845	0.125	0.1172	0.1096	0.1538
Mn	0.0199	0.0199	0.0222	0.0216	0.003	0.0034	0.0023	0.0023
Mg	1.5178	1.5338	1.4687	1.5080	0.078	0.0716	0.0837	0.0961
Ca	0.0000	0.0000	0.0000	0.0000	0.000	0.0000	0.0000	0.0000
Na	0.0722	0.0668	0.0785	0.0869	0.286	0.2975	0.2723	0.2942
K	1.5970	1.5870	1.6130	1.3730	1.545	1.6002	1.5970	1.5827
Ba	0.0105	0.0090	0.0000	0.0000	0.016	0.0167	0.0126	0.0147
Cl	0.0031	0.0032	0.0000	0.0000				
Total	15.4250	15.4579	15.4321	15.2357	13.9104	12.6884	13.9153	13.9535
	Biotites				Muscovites			

B85/W1

SiO2	34.46	38.46	23.74	23.51	23.95	47.26	37.26	37.20	36.86	36.58	34.86	37.22
TiO2	2.70	3.81	0.05	0.05	0.07	0.07	0.14	0.05	0.54	0.07	0.07	0.05
Al2O3	18.97	16.41	21.91	21.67	21.87	35.20	21.39	21.47	21.45	20.87	21.22	21.53
FeO	28.06	26.88	36.41	36.51	36.48	2.25	34.01	34.99	33.75	34.98	34.83	35.20
MnO	0.59	0.56	1.04	1.38	1.10	0.05	6.47	5.64	7.10	5.24	5.73	5.37
MgO	3.93	3.76	5.40	5.20	5.35	0.64	1.39	1.42	1.30	1.46	1.40	1.47
CaO	0.03	0.02	0.01	0.01		0.01	1.27	1.04	1.09	1.05	1.04	1.08
Na2O	0.06	0.02	0.02	0.00		0.53						
K2O	6.07	3.83	0.01	0.01		10.05						
BaO												
Cl												
Total	94.81	93.88	88.59	88.34	88.82	96.06	101.93	101.82	102.10	100.29	101.66	101.29
	Formula units based on 22 oxygens		**Formula units based on 28 oxygens**			**Formula units based on 22 oxygens**	**Formula units based on 24 oxygens**					
Si	5.403	5.9266	5.2872	5.271	5.318	6.8047	5.9647	5.9639	5.9047	5.9644	5.9971	5.9571
Ti	0.318	0.4418	0.0084	0.008	0.012	0.0080	0.0163	0.0061	0.0651	0.0083	0.0081	0.0061
Al	3.506	2.9812	5.7516	5.726	5.724	5.9736	4.0369	4.0560	4.0502	4.0110	4.0152	4.0625
Fe	3.680	3.4637	6.7817	6.846	6.775	0.2714	4.5539	4.6907	4.5212	4.7702	4.6752	4.7123
Mn	0.078	0.0734	0.1962	0.262	0.207	0.0057	0.8780	0.7654	0.3103	0.7231	0.7786	0.7277
Mg	0.919	0.8626	1.7928	1.738	1.771	0.1382	0.3327	0.3383	0.3103	0.3540	0.3596	0.3516
Ca	0.005	0.0460	0.0024	0.002		0.0022	0.2179	0.1783	0.1873	0.1838	0.1786	0.1851
Na	0.018	0.0058	0.0086	0.000		0.1477						
K	1.214	0.7524	0.0028	0.003		1.8457						
Ba												
Cl												
Total	15.1417	14.5194	19.8316	19.8563	19.8063	15.1972	16.0004	16.0005	16.0037	16.0281	15.9868	16.0042
	Biotites		**Chlorite**			**Muscovite**	**Garnets**					

B85/N60

SiO2	32.62	35.35	35.01	34.25	33.20	32.95	32.74	32.44	32.26	37.22	39.51	36.98	29.76
TiO2	2.12	1.62	1.57	1.63	1.64	1.48	1.64	1.34	1.57	0.02	0.04	0.02	0.12
Al2O3	21.09	22.07	21.49	21.12	20.85	21.35	21.29	20.40	20.72	62.68	61.19	61.88	24.10
FeO	23.47	21.32	21.84	23.13	23.58	24.73	22.86	0.11	0.11	0.24	0.22	0.36	26.15
MnO	0.09	0.14	0.14	0.14	0.12	0.14	0.17	5.38	5.63	0.02	0.00	0.02	0.21
MgO	4.30	5.52	6.11	5.86	6.45	6.38	5.68	25.99	25.74	0.00	0.01	0.01	7.49
CaO	0.15	0.06	0.04	0.07	0.03	0.03	0.07	0.08	0.07	0.01	0.01	0.03	0.03
Na2O	0.09	0.20	0.15	0.09	0.08	0.08	0.09	0.12	0.13				0.17
K2O	4.16	6.21	6.64	6.02	5.45	5.03	4.70	5.48	5.31				0.92
Bao					0.09	0.07	0.09			0.01	0.00	0.01	0.01
Cl					0.05	0.04	0.05						0.01
Total	88.09	92.49	92.99	92.31	91.54	92.28	89.38	91.34	91.54	100.20	100.98	99.31	88.97
	Formula units based on 22 oxygens									**Formula units based on 20 oxygens**			**Formula units based on 22 oxygens**
Si	5.3263	5.4556	5.4136	5.3635	5.2619	5.1958	5.2757	5.2279	5.1767	4.0126	4.2148	4.0242	6.1127
Ti	0.2597	0.1879	0.1820	0.1919	0.1959	0.1755	0.1992	0.1620	0.1889	0.0015	0.0029	0.0015	0.0185
Al	4.0584	4.0154	3.9160	3.8986	3.8961	3.9672	4.0444	3.8756	3.9192	7.9648	7.6940	7.9388	5.8347
Fe	3.2049	2.7511	2.8235	3.0286	3.1254	3.2611	3.0808	0.0145	0.0144	0.0214	0.0200	0.0331	4.4921
Mn	0.0126	0.0180	0.0180	0.0182	0.0164	0.0183	0.0229	1.2929	1.3455	0.0014	0.0000	0.0014	0.0365
Mg	1.0470	1.2697	1.4092	1.3669	1.5249	1.5002	1.3647	3.5028	3.4533	0.0000	0.0022	0.0022	2.2934
Ca	0.0269	0.0093	0.0070	0.0118	0.0047	0.0047	0.0121	0.0145	0.0120	0.0016	0.0016	0.0033	0.0066
Na	0.0300	0.0604	0.0441	0.0283	0.0231	0.0231	0.0293	0.0360	0.0417				0.0677
K	0.8660	1.2220	1.3090	1.2020	1.1020	1.0110	0.9650	1.1270	1.0870				0.2411
Ba					0.0053	0.0045	0.0054			0.0005	0.0000	0.0005	0.0008
Cl					0.0131	0.0098	0.0134						0.0033
Total	14.8318	14.9894	15.1224	15.1098	15.1688	15.1712	15.0129	15.2532	15.2387	12.0038	11.9355	12.0050	19.1074
	Biotites									**Andalusites**			**Chlorite**

B85/N60

SiO2	44.96	44.12	44.30	46.10	46.23	46.54
TiO2	0.28	0.48	0.33	0.37	0.34	0.28
Al2O3	36.33	35.54	34.40	36.07	36.50	37.12
FeO	1.53	2.94	3.81	0.76	1.18	1.16
MnO	0.00	0.02	0.03	0.05	0.00	0.00
MgO	0.35	0.38	0.32	0.30	0.39	0.34
CaO	0.01	0.04	0.10	0.01	0.03	0.03
Na2O	1.11	1.07	1.42	1.12	1.10	1.10
K2O	9.18	8.82	8.47	8.99	9.28	9.28
Bao						
Cl						
Total	93.75	93.41	93.18	93.77	95.05	95.85

Formula units based on 22 oxygens

Si	6.0569	6.0077	6.0719	6.1659	6.1241	6.1076
Ti	0.0283	0.0495	0.0344	0.0376	0.0335	0.0276
Al	5.7681	5.7054	5.5580	5.6865	5.6990	5.7427
Fe	0.1720	0.3344	0.4372	0.0846	0.1304	0.1276
Mn	0.0000	0.0018	0.0036	0.0053	0.0000	0.0000
Mg	0.0693	0.0771	0.0659	0.0594	0.0766	0.0669
Ca	0.0021	0.0064	0.0150	0.0021	0.0041	0.0041
Na	0.2903	0.2834	0.3762	0.2895	0.2833	0.2797
K	1.5778	1.5321	1.4810	1.5341	1.5675	1.5540
Ba						
Cl						
Total	13.9648	13.9978	14.0432	13.8650	13.9185	13.9102

Muscovites

B85/203

SiO2	34.79	35.50	35.42	35.17	45.78	46.43	46.14	46.44	46.59	46.51
TiO2	3.24	3.05	3.30	3.37	0.80	0.49	0.04	0.81	0.43	0.99
Al2O3	20.53	20.72	20.58	20.61	36.85	36.86	33.65	36.69	36.80	36.57
MnO	0.28	0.24	0.28	0.24	0.87	0.00	0.05	0.02	0.02	0.00
MgO	6.87	6.94	6.76	6.81	0.03	0.40	2.02	0.43	0.43	0.52
FeO	21.31	21.17	20.88	21.26	0.45	0.60	3.91	0.69	1.08	0.74
CaO	0.01	0.01	0.01	0.01	0.01	0.01	0.03	0.01	0.01	0.01
Na2O	0.06	0.07	0.07	0.07	0.42	0.38	0.37	0.39	0.36	0.36
K2O	8.45	8.97	9.04	8.86	10.61	10.87	10.16	10.70	10.63	10.73
BaO	0.12	0.14	0.14	0.15	0.12					
Cl	0.01	0.01								
Total	95.67	96.82	96.48	96.55	95.94	96.04	96.37	96.18	96.35	96.43

	Formula units based on 22 oxygens				20.0000 Formula units based on 22 oxygens					
Si	5.2940	5.3368	5.3417	5.3069	6.046	6.1103	6.1515	6.1033	6.1162	6.0985
Ti	0.3713	0.3451	0.3746	0.3826	0.079	0.0482	0.0037	0.0795	0.0425	0.0978
Al	3.6827	3.6709	3.6589	3.6653	5.737	5.7176	5.2874	5.6831	5.6935	5.6529
Mn	0.0355	0.0311	0.0352	0.0313	0.096	0.0000	0.0053	0.0017	0.0017	0.0000
Mg	1.5595	1.5550	1.5199	1.5327	0.003	0.0781	0.4007	0.0839	0.0840	0.1011
Fe	2.7117	2.6619	2.6330	2.6836	0.089	0.0663	0.4362	0.0755	0.1184	0.0814
Ca	0.0023	0.0022	0.0023	0.0023	0.001	0.0020	0.0042	0.0020	0.0020	0.0020
Na	0.0162	0.0213	0.0213	0.0214	0.108	0.0958	0.0968	0.0995	0.0923	0.0920
K	1.6400	1.7200	1.7380	1.7060	1.788	1.8240	1.7270	1.7930	1.7800	1.7940
Ba	0.0074	0.0081	0.0081	0.0088						
Cl	0.0031	0.0031	0.0000	0.0000						
Total	15.3237	15.3555	15.3330	15.3409	13.9473	13.9423	14.1128	13.9215	13.9306	13.9197

Biotites

Muscovites

B85/203

SiO2	37.44	37.61	37.29	37.31	37.31
TiO2	0.02	0.04	0.02	0.04	0.04
Al2O3	63.59	63.07	62.77	62.61	62.37
MnO	0.02	0.02	0.03	0.02	0.00
MgO	0.03	0.04	0.01	0.07	0.01
FeO	0.22	0.46	0.21	0.43	0.21
CaO	0.01	0.01	0.01	0.01	0.04
Na2O	0.01	0.01		0.01	
K2O	0.04	0.01		0.10	
BaO	0.00	0.00			
Cl					
Total	101.38	101.27	100.35	100.60	99.98

Formula units based on 20 oxygens

Si	3.9907	4.0161	4.0131	4.0129	4.0298
Ti	0.0014	0.0029	0.0015	0.0030	0.0030
Al	7.9899	7.9393	7.9633	7.9382	7.9390
Mn	0.0014	0.0014	0.0028	0.0014	0.0000
Mg	0.0044	0.0067	0.0022	0.0112	0.0022
Fe	0.0199	0.0412	0.0189	0.0390	0.0189
Ca	0.0016	0.0016	0.0016	0.0016	0.0050
Na	0.0028	0.0028		0.0028	
K	0.0040	0.0010		0.0130	
Ba					
Cl					
Total	12.0161	12.0130	12.0034	12.0231	11.9979

Andalusites

Appendix D
Rb-Sr mica separate data

		Rb	± 2σ	Sr	± 2σ	Rb/Sr	87/86	± 2σ	AGE	± 2σ
						TRES CRUSES				
B85/118	Biotite									
	1152	3.1	21.62	0.05	53.284	0.765	0.001	25,9	1
	759	1	4.163	0.004	182.3204	2.56	0.003	209	6
	758	2	16.27	0.05	46.58881	0.754	0.002	23	2
B85/119	Biotite									
	724	1	5.92	0.02	122.2973	0.833	0.03	24.4	1.2
	734	1	6.74	0.03	108.9021	0.7827	2E-04	16.4	0.6
	772	3	9.1	0.06	84.83516	0.839	0.002	37	2
B85/149	Biotite									
	588	1	7.01	0.01	83.88017	0.797	0.02	25.6	1.2
	707	3	11.16	0.02	63.35125	0.756	0.002	18.3	0.6
	677	1.5	13.14	0.04	51.52207	0.759	0.002	24	1
B85/160	Biotite									
	1421	3	11.21	0.01	126.7618	0.84	0.001	23.9	0.4
						SORATA				
B85/183	Muscovite									
	605	1	14.24		42.48596	1.105	0.002	217	8
B85/183	Biotite									
	1141	3	11.56	0.02	98.70242	0.795	0.001	15.3	0.6
B85/197	Muscovite									
	770	2	10.05	0.01	76.61692	3.852	0.007		
	787	1.6	9.58	0.02	82.15031	1.5	0.005	214	7
B85/197	Biotite									
	1374	2	4.2	0.1	327.1429	3.852	0.007	177.9	2.6
B85/207	Biotite									
	567	1	5.05	0.07	112.2772	1.8	0.03	213	12
	708	0.9	6.46	0.06	109.5975	1.915	0.011	241	8

Abbey S. (1980). Studies in "standard samples" for use in the general analysis of silicate rocks and minerals. Geostand. Newslett., **4**, 163-190.

Ahlfeld F. (1935). The Bolivian tin belt. Neues Jahrb. f. Min., **65**, 286-456.

Alberede F. and M. Brouxel (1987). The Sm/Nd secular evolution of the continental crust and the depleted mantle. Earth Planet. Sci. Lett., **82**, 25-35.

Allegre C.J. and D. Ben Othman (1980). Nd-Sr isotopic relationship in granitoid rocks and continental crust development: a chemical approach to orogenesis. Nature, **286**, 335-342.

Allègre C.J. and D. Rousseau (1984). The growth of the continental crust through geological time studied by Nd isotope analysis of shales. Earth Planet. Sci. Lett., **67**, 19-34.

Allegre C.J., M. Treuil, J.F. Minster, B. Minster and F. Alberede (1977). Systematic use of trace elements in igneous processes. Part 1: fractional crystallization processes in volcanic suites. Contrib. Mineral. Petrol., **60**, 57-75.

Allmendinger R.W. (1986). Tectonic development, southeastern border of the Puna Plateau, Northwestern Argentine Andes. Bull. Geol. Soc. Am. , **97**, 1070-1082.

Anderson R.N. and J.G. Sclater (1972). Topography and evolution of the East Pacific Rise between 5° and 20° S. Earth Planet. Sci. Lett., **14**, 431-442.

Arndt N.T. and S.L. Goldstein (1987). Use and abuse of crustal-formation ages. Geology, **15**, 893-895.

Arth J.G. and G.N. Hanson (1975). Geochemistry and origin of the early Pre-Cambrian crust of north-eastern Minnesota. Geochim. Cosmochim. Acta., **39**, 325-362.

Arzi A.A. (1976). Critical phenomena in the rheology of partially melted rocks. Tectonophysics, **44**, 173-184.

Atherton M.P. (1984). The Coastal Batholith of Peru. In: Andean Magmatism; chemical and isotopic constraints. Eds. R.S. Harmon and B.A. Barreiro. Pub. Shiva, England, 168-179.

Atherton M.P., W.J. McCourt, L.M. Sanderson and W.P. Taylor (1979). The geochemical character of the segmented Peruvian Coastal Batholith and associated volcanics. In: Origin of granite batholiths geochemical evidence. Eds. M.P. Atherton and J. Tarney. Pub. Shiva, England.

Atherton M.P. and L.M. Sanderson (1985). The chemical variation and evolution of the super-units of the segmented Coastal Batholith. In: Magmatism at a Plate Edge. Eds. W.S. Pitcher, M.P. Atherton, E.J. Cobbing and R.D. Beckinsale. Pub. Blackie, Glasgow.

Atherton M.P. and L.M. Sanderson (1987). The Cordillera Blanca Batholith: a study of granite intrusion and the relation of crustal thickening to peraluminosity. Geol. Rund., **76**, 213-232.

Atherton M.P. ,V. Warden and L.M. Sanderson (1985). The Mesozoic marginal basin of Central Peru: a geochemical study of within-plate-edge volcanism . In: Magmatism at a Plate Edge. Eds. W.S. Pitcher, M.P. Atherton, E.J. Cobbing and R.D. Beckinsale. Pub. Blackie, Glasgow.

Bailey (1977). Fluorine in magmatic rocks and melts: a review. Chem. Geol., **19**, 1-42.

Bard J.P., R. Botello, C. Martinez and T. Subieta (1974). Relations entre tectonique, metamorphisme et mise en place d'un granite Eohercynian a deux micas dans la Cordillere Real de Bolivie (massif de Zongo-Yani). Cah. ORSTOM,ser. Geol., **6**, 3-18.

Beckinsale R.D., A.W. Sanchez-Fernandez, M. Brook, E.J. Cobbing, W.P. Taylor and N.D. Moore (1985). Rb-Sr whole-rock isochron and K-Ar age determinations for the Coastal Batholith of Peru. In: Magmatism at a Plate Edge. Eds. W.S. Pitcher, M.P. Atherton, E.J. Cobbing and R.D. Beckinsale. Pub. Blackie, Glasgow, 177-202.

Bellido E. and C. Guevara (1963). Geolgica de los Cuadrangulos de Punta de Bombon y Clemesi. Bol. Com. Carta. Geol. Nac. Lima, **5**.

Ben Othman D., S.Fourcade and C.J. Allegre (1984). Recycling processes in granite-granodiorite complex genesis: the Querigut case studied by Nd-Sr isotope systematics. Earth Planet. Sci. Lett., **69**, 290-300.

Benjamin M.T., N.M. Johnson and C.W. Naeser (1987). Recent rapid uplift in the Bolivian Andes: evidence from fission-track dating. Geology, **15**, 680-683.

Berg K. and A. Baumann (1985). Plutonic and metasedimentary rocks from the Coastal Range of Northern Chile: Rb-Sr and U-Pb isotopic systematics. Earth Planet. Sci. Lett., **75**, 101-115.

Booth B. (1968). Petrogenetic significance of alkali feldspar megacrysts and their inclusions in cornubian granites. Nature, **217**, 1036-1038.

Braun E.V. (1967). Geologie und lagerstatten im Gebiet von Vilcabamba (S. Peru). Geol. Jahrb., **84**, 215-260.

Breitkruz C. (1985). Plutonism in the Central Andes. Zbl. Geol. Paläont., **9/10**, 1283-1293.

Brown G.C. and W.S. Fyfe (1970). The production of granitic melts during ultrametamorphism. Contrib. Mineral. Petrol., **28**, 310-318.

Caminos R., C.A. Cingolani, F. Herve and E. Linares (1982). Geochronology of the pre-Andean metamorphism and magmatism in the Andean Cordillera between latitudes 30° and 36°S. Earth Sci. Rev., **18**, 333-353.

Carlier G., G. Grandin, G. Laubacher, R. Marocco and F. Mégard (1982). Present knowledge of the magmatic evolution of the Eastern Cordillera of Peru. Earth. Sci. Rev., **18**, 253-283.

Chappell B. W. and A.J.R. White (1974). Two contrasting granite types. Pacific Geology, **8**, 173-174.

Chaudhuri S. and R.L. Cullers (1979). The distribution of rare-earth elements in the deeply buried Gulf coast sediments. Chem. Geol., **24**, 327.

Clark A.H. and E. Farrar (1973). The Bolivian tin province: notes on the available geochronological data. Econ. Geol., **68**, 102-106.

Clark A.H. and R.H. McNutt (1982). Interrelated arc-broadening, topographic uplift and crustal contamination of magmas in two transects of the Mesozoic-Cenozoic central Andes. Proc. 5th Int. Conf. Geochron. Cosmochron. Isotope Geol., 55-56.

Clemens J.D. and D. Vielzeuf (1987). Constraints on melting and magma production in the crust. Earth Planet. Sci. Lett., **86**, 287-306.

Clemens J.D. and V.J. Wall (1981). Origin and crystallization of some peraluminous (S-type) granitic magmas. Can. Mineral., **19**, 111-131.

Clemens J.D. and V.J. Wall (1988). Controls on the mineralogy of S-type volcanic and plutonic rocks. Lithos, **21**, 53-66.

Cobbing E.J. (1985). The tectonic setting of the Peruvian Andes . In: Magmatism at a Plate Edge. Eds. W.S. Pitcher, M.P. Atherton, E.J. Cobbing and R.D. Beckinsale. Pub. Blackie, Glasgow, 3-12.

Cobbing E.J., W.S. Pitcher, J.J. Wilson, J.W. Baldock, W.P. Taylor, W.J. McCourt and N.J. Snelling (1981). The geology of the western Cordillera of Northern Peru . Overseas Mem. Inst. geol. Sci. London, **5**, 143 pp.

Cocherie A. (1986). Systematic use of trace element distribution patterns in log-log diagrams for plutonic suites. Geochim. Cosmochim. Acta., **50**, 2517-2522.

Coira B., J. Davidson, C.Mpodozis and V. Ramos (1982). Tectonic and magmatic evolution of the Andes of Northern Argentina and Chile. Earth. Sci. Rev., **18**, 303-332.

Cordani U.G. (1967). Unpublished letter in the library of the Servicio Geológico de Bolivia, La Paz, Bolivia.

Crough S.T. (1983). Apatite fission-track dating in the eastern Andes. Bolivia. Earth Planet. Sci. Lett., **64**, 396-397.

Dalmayrac B., G. Laubaucher, R. Marocco, C. Martinez and P. Tomasi (1980). La Chaine Hercynienne D'amerique du Sud, structure et evolution d'un orogene intracratonique. Geol. Rund. , **69**, 1-21.

Damm K.W. and S. Pichowiak (1981). Petrology, chronology and chemistry of magmatic rocks from the Coast Range between Taltal and Chanaral (North Chile). Zentralbl. Geol. Palaont., **1**, 319-332.

Damm K.W., S. Pichowiak and W. Zeil (1981). The plutonism in the North Chilean Coastal Range and its geodynamic significance. Geol. Rund., **70**, 1054-1076.

Davies G., A.Gledhill and C. Hawkesworth (1985). Upper crustal recycling in southern Britain: evidence from Nd and Sr isotopes. Earth Planet. Sci. Lett., **75**, 1-12.

DePaolo D.J. (1981). Trace element and isotopic effects of combined wall-rock assimilation and fractional crystallization. Earth Planet. Sci. Lett., **53**, 189-202.

De PaoloD.J. and G.J. Wasserburg (1976). Nd isotopic variations and petrogenetic models. Geophys. Res. Lett. , **3**, 249-252.

Dewey J.F. and B.F. Windley (1981). Growth and differentiation of the continental crust. Phil. Trans. R. Lond., **A 301**, 189-206.

Didier J. (1973). Granites and thier enclaves: Developments in petrology 3. Pub. Elsevier, Amsterdam.

Dobson M.H. (1978). A linear method for second-degree interpolation in cyclical data collection. J. Phys. E. Sci. Instrum. , **11**, 296.

Egeler C.G. and T. De Booy (1956). Geology and petrology of part of the Southern Cordillera Blanca, Peru. Verh. K. Ned. geol. Mijndouwkd. Genoot Geol. Ser., **97**, 71-131.

Everden J.F., S.J. Kritz and C. Cherroni (1977). Potassium-argon ages of some Bolivian rocks. Econ. Geol. , **72**, 1042-1061.

Ewart A. and C.J. Hawkesworth (1987). The Pleistocene-Recent Tonga-Kermadec arc lavas: interpretation of new isotopic and rare earth data in terms of a depleted mantle source model. J. Petrol., **28**, 495-530.

Exley C.S. and M.Stone (1982). Petrology of the granites and minor intrusions. In: Igneous rocks of the British Isles. Ed. D.S. Sutherland. Pub. Wiley & Sons. London.

Exley R.A. (1980). Microprobe studies of REE-rich accessory minerals: implications for skye granite petrogenesis and REE mobility in hydrothermal systems. Earth Planet. Sci. Lett., **48**, 97-110.

Farrar E., A.H. Clark, S.J. Haynes, G.S. Quirt, H. Conn and M. Zentilli (1970). K-Ar evidence for the post-Palaeozoic migration of granitic intrusion foci in the Andes of Northern Chile. Earth Planet. Sci. Lett., **10**, 60-66.

Faure G. (1977). Principals of isotope geology. Pub. Wiley, New York; , 464 pp.

Fershlater G.B. and N.S. Borodina (1977). Petrology of autoliths in granitic rocks. Internat. Geology Rev., **19**, 458-468.

Fourcade S. and C.J. Allegre (1981). Trace element behaviour in granite genesis: a case study the calc-alkaline plutonic association from the Querigut complex (Pyrénées, France). Contrib. Mineral. Petrol., **76**, 177-195.

Francis G.A. (1956). La geologia de la zona enter Macusani y Ollachea, Departamento de Puno.. Instityto Nacional de Investigaciones y Fomento Minero., Boletin, **21**, 5-10.

Frost C.D. and D. Winston (1987). Nd isotope systematics of coarse- and fine-grained sediments: examples from the middle Proterozoic Belt Percell Supergroup. J. Geology, **95**, 309-327.

Futa K. (1981). Sm-Nd systematics of a tonalitic augen gneiss and its constituent minerals from northern Mitchigan. Geochim. Cosmochim. Acta., **45**, 1245-1249.

Gill J.B. (1970). Geochemistry of Viti Levu, Fiji, and its evolution as an island arc. Contrib. Mineral. Petrol., **27**, 179-203.

Goldstein S.L. (1987). Decoupled Rb-Sr and Sm-Nd isotopic evolution of the continental crust. L.P.I. workshop on: The Growth of the Continental Crust. Oxford.

Gorton M.P. (1977). The geochemistry and origin of Quaternary volcanism in the New Hebridies. Geochim. Cosmochim. Acta., **41**, 1257-1270.

Grant J.N., C. Halls, W. A. Salinas and N. Snelling (1979). K-Ar ages of igneous rocks and mineralization in part of the Bolivian tin belt. Econ. Geol., **74**, 838-851.

Griffith W.L. and O'Reilly S.Y. (1987). Is the Moho the crust-mantle boundary? Geology, **15**, 241-244.

Gromet L.P. and L.T. Silver (1983). Rare earth element distribution among minerals in a granodiorite and their petrogenetic implications. Geochim. Cosmochim. Acta., **47**, 925-939.

Gromet L.P. and L. T. Silver (1987). REE variations across the Peninsular Ranges Batholith: implications for the batholithic petrogenesis and crustal growth in magmatic arcs. J. Petrol., **28**, 75-125.

Grove T.L. and R.J. Kinzler (1986). Petrogenesis of andesites. Ann. Rev. Earth Planet. Sci., **14**, 417-454.

Halpern M. (1978). Geological significance of Rb-Sr isotopic data of Northern Chile crystalline rocks of the Andean orogen between 23° and 27°S. Bull. Geol. Soc. Am. , **89**, 522-532.

Halpern M. and C.O. Latorre (1973). Estudio geochronologico initial de rocas del noreste Argentino. Assoc. Geol. Argent. Rev., **28**, 195-205.

Hanson G.N. (1978). The application of trace elements to the petrogenesis of igneous rocks of granitic composition. Earth Planet. Sci. Lett., **38**, 26-43.

Harris N.B.W., C.J. Hawkesworth and A.C. Ries (1984). Crustal evolution in north-east and east Africa from Nd ages. Nature , **309**, 773-776.

Harris N.B.W., J.A. Pearce and A.G. Tindle (1986). Geochemical characteristics of collision-zone magmatism. In: Collision Tectonics. Eds. Coward M.P. & A.C. Reis. Geological Society Special Publication No.19, 67-81.

Harris N.B.W., X. Ronghua, C.L. Lewis and J. Chengwei (in press). Plutonic rocks of the 1985 Tibet geotraverse; Lhasa to Golmud. Phil. Trans. R. London.

Hawkesworth C.J., M. Hammill, A.R. Gledhill, P. van Calsteren and G. Rogers (1982). Isotopic and trace element evidence for the late-stage intra-crustal melting in the High Andes. Earth Planet. Sci. Lett., **58**, 240-254.

Hawkesworth C.J., J.D. Kramers and R. McG. Miller (1981). Old Nd ages in the Namibian Pan-African rocks. Nature, **289**, 278-282.

Hawkesworth C.J. and M.J. Norry (1983). Continental basalts and mantle xenoliths. Pub. Shiva, England, 272 pp.

Hawkesworth C.J., M.J. Norry, J.C. Roddick, P.E. Baker, P.W. Francis and R.S. Thorpe (1979). $^{143}Nd/^{144}Nd$ and $^{87}Sr/^{86}Sr$, and incompatible element variations in calc-alkali andesites and plateau lavas from South America. Earth Planet. Sci. Lett., **42**, 45-57.

Hawkesworth C.J. and M. Powell (1980). Magma genesis in the Lesser Antillies island arc. Earth Planet. Sci. Lett., **51**, 297-308.

Hawkesworth C.J. and P. van Calsteren (1984). Radiogenic isotopes - some geological applications. In: Rare Earth Element Geochemistry. Ed. P. Henderson, Pub. Elsevier, Oxford., 375-421.

Hawkesworth C.J., P. van Calsteren, N.W. Rogers and M.A. Menzies (1987). Isotope variations in recent volcanics: a trace element perspective. In: Mantle Metasomatism. Eds. M.A. Menzies and C.J. Hawkesworth. Pub. Academic Press. London, 365-385.

Helz R.T. (1976). Phase relations of basalts in their melting ranges at PH_2O = 5 kbar. Part II: melt compositions. J. Petrol., **17**, 139-193.

Helwig J. (1972). Stratigraphy, sedimentation, palaeogeography and palaeoclimates of Carboniferous ("Gondwana") and Permian of Bolivia. Am. Assoc. Pet. Geol., **56**, 1008-1033.

Henderson P. (1982). Inorganic Geochemistry. 353pp. Pub. Pergamon Press, Exeter.

Hine R., I.S. Williams, B.W. Chappell and A.J.R. White (1978). Geochemical contrasts between I- and S-type granitoids of the Kosciusko Batholith. Jour. Geol. Soc. Australia, **25**, 219-234.

Holland T.J.B. and R. Powell (1985). An internally consistent thermodymanic data set with uncertainties and correlations: 2: data and results. J. Metam. Geol., **3**, 343-370.

Huete C., V. Maksaev, R. Moscoso, C. Ulricsen and H. Vergara (1977). Antescedentes geochronologicos de rocas intrusivas y volcanicas en la Cordillera de los Andes comprendida entre la Sierra Moreno y el rio Loa a los 21° y 22° lat. S. II Region, Chile. Rev. Geol. Chile, **4**, 35-41.

Hyndman D.W. (1981). Controls on the source and depth of emplacement ofgranitic magma. Geology, **9**, 244-249.

Issacson P.E. (1975). Evidence for a western extracontinental land source during the Devonian period in the Central Andes. Bull. Geol. Soc. Am., **86**, 39-46.

James D.E. (1971). Plate tectonic model for the evolution of the Central Andes. Bull. Geol. Soc. Am., **82**, 3325-3346.

James D.E. (1982). A combined O, Sr Nd, and Pb isotopic and trace element study of crustal contamination in central Andean lavas. I. Local geochemical variations. Earth Planet. Sci. Lett., **57**, 47-62.

James D.E., C. Brooks and A. Cuyuamba (1976). Andean Cenozoic volcanism: magma genesis in the light of strontium isotopic composition and trace element geochemistry. Bull. Geol. Soc. Am., **87**, 592-600.

Kelly W.M.C. and F.S. Turneaure (1970). Mineralogy, paragenesis and geothermometry of the tin and tungsten depsits of the eastern Andes, Bolivia. Econ. Geol., **65**, 609-680.

Kontac D.J., A.M Clark and E. Farrar (1984). The magmatic evolution of the Cordillera Oriental, Southeastern Peru. In: Andean Magmatism; chemical and isotopic constraints. Eds. R.S. Harmon and B.A. Barreiro. Pub. Shiva, England, 203-219.

Kontac D.J., A.H. Clark, E. Farrar and D.F. Strong (1985). The rift-associated Permo-Triassic magmatism of the Eastern Cordillera: a precursor to the Andean Orogeny. In: Magmatism at a Plate Edge. Eds. W.S. Pitcher, M.P. Atherton, E.J. Cobbing and R.D. Beckinsale. Pub. Blackie, Glasgow, 30-36.

Koosterman J.B. (1967). A tin province of the Nigerian type in the southern Amazonia. A technical conference on tin. Ed. Fox. London.

Kushiro I.S. and H.S. Yoder (1972). Origin of the calc-alkaline peraluminous andesites and dacites. Carnigie Inst. Washington Year Book, **71**, 411-413.

Larson R.L. and W.C. Pitman (1972). World-wide correlation of Mesozoic magnetic anomalies and its implications. Bull. Geol. Soc. Am., **83**, 3645-3662.

Laubacher G. and F. Megard (1985). The Hercynian basement: a review. In: Magmatism at a Plate Edge. Eds. W.S. Pitcher, M.P. Atherton, E.J. Cobbing and R.D. Beckinsale. Pub. Blackie, Glasgow, 29-35.

Le Bel L., A. Cocherie, J.C. Baubron, A.M. Fouillac and C.J. Hawksworth (1985). A high-K, mantle derived plutonic suite from 'Linga', near Arequipa (Peru). J. Petrol., **26**, 124-148.

Leake B.E. (1978). Nomenclature of amphiboles. Mineral. Mag., **42**, 533-563.

Lehmann B. (1978). A Precambrian core sample from the Altiplano, Bolivia. Geol. Rundschau., **67**, 270-278.

Leyreloup J. (1982). Petrology and geochemistry of granulite xenoliths from Central Hoggar (Algeria) - Implications for the lower crust. Contrib. Mineral. Petrol., **79**, 68.

Linares E. (1977). Catálogo de edades radiométricas determinadas para la República Argentina. Asoc. Geol. Argent. Publ. Espec. Ser., **B4**.

Litherland M., B.A. Klinck,E.A. O'Connor and P.E.J. Pitfield (1985). Andean-trending mobile belts in the Brazilian Shield. Nature, **314**, 345-348.

Lohmann H.H. (1970). Outline of the tectonic history of the Bolivian Andes. Am. Assoc. Pet. Geol. Bull., **54**, 735-757.

Lopez-Escobar L., F.A. Frey and M. Veragara (1977). Andesites and high-alumina basalts from the Central-South Chile High Andes: geochemical evidence on their petrogenesis. Contrib. Mineral. Petrol., **63**, 199-228.

Losert J. (1973). Genesis of copper mineralization in the Jurassic volcanic rocks of the Buena Esperanza mining area (Antifogasta Province), Northern Chile. Dep. Geol. Univ. Chile, **30**.

Lyon-Caen H., P. Molnar and G. Suarez (1985). Gravity anomalies and flexure of the Brazilian Shield beneath the Bolivian Andes. Earth Planet. Sci. Lett., **75**, 81-92.

Maaloe S. and P.J. Wyllie (1975). Water Content of a Granite Magma deduced from the sequence of crystallization determined experimentally with water-undersaturated conditions. Contrib. Mineral. Petrol., **52**, 175-191.

Mahood G. and W. Hildreth (1983). Large partition coefficients for trace elements in high-silica rhyolites. Geochim. Cosmochim. Acta., **47**, 11-30.

Mammerickx J., E. Herron and L. Dorman (1980). Evidence for two fossil spreading ridges in the Southeast Pacific . Bull. Geol. Soc. Am. , **91**, 263-271.

Manning D.A.C. (1980). The effect of fluorine on liquidus phase relationships in the system Qz-Ab-Or with excess water at 1 kb. Contrib. Mineral. Petrol., **76**, 206-215.

Martin H. and M. Meybeck (1979). Elemental mass-balance of material carried by major world rivers. Marine Chem., **7**, 173-206.

Martinez C. (1980). Structure et évolution de la chaîne Hercyniénne et de la chaîne Andine dans le nord de la Cordillére des Andes de Bolivie. Trav. Doc. Orstom., **119**, 352 pp.

McBride S.L. (1977). A K-Ar study of the Cordillera Real, Bolivia and its regional setting. Unpub. PhD Thesis, Queens Univ. Kingston, Ontario.

McBride S.L., A.H. Clark, E. Farrar and D.A. Archibald (1987). Delimitation of a cryptic Eocene tectono-thermal domain in the Eastern Cordillera of the Bolivian Andes through K-Ar dating and 40Ar-39Ar step heating. J. Geol. Soc. London, **144**, 243-255.

McBride S.L., R.C.R. Robertson, A.H. Clark and E. Farrar (1983). Magmatic and metallogenic episodes in the northern tin belt, Cordillera Real, Bolivia. Geologische Rundschau, **73**, 685-713.

McCarthy T.S. and R.A. Hasty (1976). Trace element distribution patterns and their relationship to the crystallization of granitic melts. Geochim. Cosmochim. Acta., **40**, 1351-1358.

McCarthy T.S. and D.I. Groves (1979). The Blue Tier Batholith, Northeastern Tasmania. A cumulate-like product of fractional crystallization. Contrib. Mineral. Petrol., **71**, 193-209.

McCulloch M.T. and B.W. Chappell (1982). Nd isotopic characteristics of S- and I-type granites. Earth Planet. Sci. Lett., **58**, 51-64.

McCulloch M.J. and G.L. Wasserberg (1978). Sm-Nd and Rb-Sr geochronology of continental crust formation. Times of addition to continents of chemically-fractionated mantle derived materials are determined. Science, **200**, 1003-1011.

McCulloch M.T. and M.R. Perfit (1981). 143Nd/144Nd and 87Sr/86Sr, and trace element constraints on the petrogenesis of Aleutian island arc magmas. Earth Planet. Sci. Lett., **56**, 167-179.

McDermott P. F. (1986). Granite petrogenesis and crustal evolution studies in the Damara Pan-African orogenic belt. Unpub. PhD Thesis, Open University.

McNutt R., J.H. Crocket, A.H. Clark, J.F. Caelles, E. Farrar, S. Haynes and M. Zentilli (1975). Inital 87Sr/86Sr ratios of plutonic and volcanic rocks of the Central Andes between latitudes 26° and 29°S. Earth Planet. Sci. Lett., **27**, 305-333.

Mégard F., B. Dalmayrac, G. Laubacher, R. Marrocco, C. Martinez, J. Paredes and P. Tomasi (1971). La chaîne hercyniénne au Pérou et an Bolivie, premiers résultats. Cah. Orstom. Sér. Geól., **III**, 5-44.

Menzies M., W.Seyfried Jr. and D. Blanchard (1979). Experimental evidence of rare earth element immobility in greenstones. Nature, **282**, 398.

Miller C.F. (1986). Are all strongly peraluminous magmas derived from pelitic sedimentary sources? J. Geology, **93**, 673-689.

Miller C.F. and D.W. Mittlefeld (1982). Crystal fractionation:controlling factor of differentiation in highly felsic magma chambers? Geol. Soc. Am. Abstr. Prog., **14**, 656.

Miller C.F. and E.F. Stoddard (1980). Origin of strongly peraluminous granitic magmas: a non- pelitic source? Geol. Soc. Am. Abstr. Prog., **12**, 483-484.

Mukasa S.B. and G.R. Tilton (1984). Lead isotope systematics in batholithic rocks of the Western and Coastal Cordilleras, Peru.. In: Andean Magmatism; chemical and isotopic constraints. Eds. R.S. Harmon and B.A. Barreiro. Pub. Shiva, England, 180-189.

Nagasawa H. (1970). Rare earth concentrations in zircons and apatites and their host dacites and granites. Earth Planet. Sci. Lett., **9**, 359-364.

Nakamura N. (1974). Determination of REE, Ba, Fe, Mg, Na and K in carbonaceous and ordinary meteorites. Geochim. Cosmochim. Acta., **38**, 757-775.

Nobel D.C., L.S. Miles, F. Megard and H. Bowman (1978). Comendite (peralkaline rhyolite) and basalt in the Mitu Group, Peru: evidence for Permian-Triassic lithospheric extension in the Central Andes. J. Res. U.S. Geol. Serv., **6**, 453-457.

Pacci D., F. Munizaga, F. Herve, K. Kawashita and U.G. Cordani (1980). Acerca de la edad Rb-Sr Precambrica de rocas de la Formacion Esquistos de Belem. Dept. de Parinacota, Chile . Rev. Geol. Chile, **10**.

Paul A. (1976). Cerium-titanium yellow colour in glass. Phys. Chem. Glasses, **17**, 7-9.

Peacock M.A. (1931). Classification of igneous rock series. J. Geol., **39**, 65-67.

Pearce J.A. (1983). Role of sub-continental lithosphere in magma genesis at active continental margins. Continental basalts and mantle xenoliths. Eds. C.J. Hawkesworth and M.J. Norry, 230-249.

Pearce J.A., N.B.W. Harris and A.G. Tindle (1984). Trace element discrimination diagrams for the tectonic interpretation of granitic rocks. J. Petro, **25**, 956-983.

Pearce J.A. and M.J. Norry (1979). Petrogenetic implications of Ti, Zr, Y and Nb variations in volcanic rocks. Contrib. Mineral. Petrol., **69**, 33-47.

Peccerillo A. and S.R. Taylor (1976). Geochemistry of Eocene calc-alkali volcanic rocks from Kastamonu area, Northern Turkey. Contrib. Mineral. Petrol., **58**, 63-81.

Pitcher W.S. (1974). The Mesozoic and Cenozoic batholiths of Peru. Pacif. Geology, **8**, 51-62.

Pitcher W.S. (1979). The nature, ascent and emplacement of granitic magmas. J. Geol. Soc. London, **136**, 627-662.

Pitcher W.S. (1984). Phanerozoic plutonism in the Peruvian Andes. In: Andean Magmatism; chemical and isotopic constraints. Eds. R.S. Harmon and B.A. Barreiro. Pub. Shiva, England, 152-167.

Potts P.J., O.W. Thorpe, M.C. Issacs and D.W. Wright (1985). High-precision instrumental neutron-activation analysis of geological samples employing simultaneous counting with both planar and coaxial detectors. Chem. Geol., **48**, 145-155.

Potts P.J., O.W. Thorpe and J.S. Watson (1981). Determination of the rare-earth element abundances in twenty-nine international rock standards by instrumental neutron activation analysis: a critical appraisal of calibration errors. Chem. Geol., **34**, 331-352.

Potts P.J., P.C. Webb and J.S. Watson (1984). Energy dispersive X-ray Fluorescence analysis of silicate rocks for major and trace elements. J.S. X-ray Spectrom., **13**, 2.

Potts P.J., P.C. Webb and J.S. Watson (1986). Silicate rock analysis by energy-dispersive X-ray Fluorescence using a cobalt Anode X-ray tube. Part 1. Optimization of excitation conditions for chromium, vanadium, barium and the major elements.. J. Anal. Atom. Spec., **1**, 467-471.

Powell R. and T.J.B. Holland (1985). An internally consistent thermodynamic data set with uncertainties and correlations. 1. Methods and a worked example.. J. Metam. Geol., **3**, 327-370.

Preim H.N.A., N.A.I.M. Boelriijk, E.H. Hebeda, E.A.Th. Verdurmen and E.H. Bon (1971). Granitic complexes and associated tin mineralizations of 'Grenville' age in Rondônia, western Brazil. Bull. Geol. Soc. Am., **82**, 1095-1102.

Preim H.N.A., P.A.M. Andriessen, N.A.I.M. Boelrijk, H. De Boorder, E.H. Hiebedd, A. Huguett, E.A. TH. Verdurmen, R.H. Versdure (1971). Geochronology of the Precambrian in the Amazon region of south east Colombia (Western Guiana Shield). Geologie Mijnb., **61**, 229-242.

Puchelt H. and R. Emmermann (1976). Bearing of rare earth patterns of apatites from igneous and metamorphic rocks. Earth Planet. Sci. Lett., **31**, 279-286.

Rapp R.P. and E.B. Watson (1986). Monazite solubility and dissolution kinetics: implications for the thorium and light rare earth chemistry of felsic magmas. Contrib. Mineral. Petrol., **94**, 304-316.

Redwood S.D. (In Prep.). The Miocene arc broadening of the Central Andes; a combined Sr, Nd, and O isotope study of the petrogenesis of the magmatism of the Northern Altiplano of Bolivia.

Regan P.F. (1985). The early basic intrusions. In: Magmatism at a Plate Edge. Eds. W.S. Pitcher, M.P. Atherton, E.J. Cobbing and R.D. Beckinsale. Pub. Blackie, Glasgow, , 72-91.

Rogers G. (1985). A geochemical traverse across the north Chilean Andes. Unpub. PhD Thesis, Open University.

Rogers N.W. (1977). Granulite xenoliths from Lesotho kimberlites and the lower continental crust. Nature, **270**, 681.

Rogers N.W. and C.J. Hawkesworth (1982). Proterozoic age and cumulate origin for granulite xenoliths, Lesotho. Nature, **299**, 409-413.

Rudnick R.L., W.F. McDonough, M.T. McCulloch and S.R. Taylor (1986). Lower crustal xenoliths from Queensland, Australia: evidence for deep crustal assimilation and fractionation of continental basalts. Geochim. Cosmochim. Acta., **50**, 1099-1115.

Rudnick R.L. and S.R. Taylor (in press). The composition and petrogenesis of the lower crust: a xenolith study. J. Geophys. Res.

Schreiber H.D., H.V. Lauer, T. Thanyasiri (1980). The redox state of cerium in basaltic magmas: an experimental study of iron-cerium interactions in silicate melts.. Geochim. Cosmochim. Acta., **44**, 1599-1612.

Shackleton R.M., A.C. Reis, M.P. Coward and P.R. Cobbold (1979). Structure, metamorphism and geochronology of the Arequipa Massif of Coastal Peru. J. geol. Soc. London, **136**, 195-214.

Shand S.J. (1951). Eruptive rocks. Pub. J. Wiley, N. York.

Stern C.R. and P.J. Wyllie (1978). Phase compositions through crystallization intervals in andesite-basalt-H2O at 30 kbar with implications for subduction zone magmas. Am. Mineral., **63**, 641-663.

Stewart J.W., J.F. Evernden and N.J. Snelling (1974). Age determinations from Andean Peru: a reconnaissance survey. Bull. Geol. Soc. Am., **85**, 1107-1116.

Stone M. and G.C. Austin (1961). The metasomatic origin of the potash feldspar megacrysts in the granites of southwest England. J. Geology, **69**, 464-472.

Streckeisen A. (1976). To each plutonic rock its proper name. Earth Sci. Rev., **12**, 1-33.

Swanson S.E. (1977). Relation of nucleation and crystal growth rate to the development of granitic textures. Am. Miner, **62**, 966-978.

Taylor H.P. Jr. (1980). The effects of assimilation of country rocks by magma on $^{18}O/^{16}O$ and $^{87}Sr/^{86}Sr$ systematics in igneous rocks. Earth Planet. Sci. Lett., **47**, 243-254.

Taylor S.R. (1967). The origin and growth of the continents. Tectonophysics, **4**, 17.

Taylor S.R. and S.M. McLennan (1985). The continental crust: its compositon and evolution . Blackwell scientific publications; Geosciences Texts, , 312 pp.

Thompson A.B. (1982). Dehydration melting of pelitic rocks and the generation of H_2O-undersaturated granitic liquids. Am. J. Sci., **282**, 1567-1595.

Thorpe R.S., P.J. Potts and P.W. Francis (1976). Rare earth data and petrogenesis of andesite from the North Chilean Andes. Contrib. Mineral. Petrol., **54**, 65-78.

Tindle A.G. (1982). Petrogenesis of the Loch Doon granitic intrusion, Southern Uplands of Scotland. Unpub. PhD Thesis, Open University.

Tindle A.G. and J.A. Pearce (1981). Petrogenetic modelling of the in situ fractional crystallization in the zoned Loch Doon pluton, Scotland. Contrib. Mineral. Petrol., **78**, 196-207.

Tindle A.G. and J.A. Pearce (1983). Assimilation and partial melting of the continental crust: evidence from the mineralogy and geochemistry of autoliths and xenoliths . Lithos, **83**, 185-202.

Tosdal R.M., A.H. Clark and E. Farrar (1984). Cenozoic polyphase landscape and tectonic evolution of the Cordillera Occidental, southernmost Peru. Bull. Geol. Soc. Am. , **95**, 1318-1332.

Turneaure F.S. (1960a). A comparative study of major ore deposits of Central Bolivia. Part I. Econ. Geol., **55**, 217-254.

Turneaure F.S. (1960b). A comparative study of major ore deposits of Central Bolivia. Part II. Econ. Geol., **55**, 574-606.

Turner J.C.M. and V. Mendez (1979). Puna. II Simp. Geol. Reg. Argent., **1**, 13-56.

Tuttle O.F. and N.L. Bowen (1958). Origin of granite in the light of experimental studies in the system $NaAlSi_3O_8$-$KAlSi_3O_8$-SiO_2-H_2O. Geol. Soc Am., Memoir 74.

Uyeda S. and H. Kanamori (1979). Back-arc opening and mode of subduction. J. Geophys. Res., **84**, 1049-1061.

Vernon R.H. (1983). Resistite, xenoliths and microgranitoid enclaves in granites. Journal and proc. Roy. Soc. New S. Wales, **116**, 77-103.

Vernon R.H. (1986). K-feldspar megacrysts in granites phenocrysts, not porphyroblasts. Earth Sci. Rev., **23**, 1-63.

Von Hilebrant A. (1973). Neue ergebrisse uber der Jura in Chile und Argentina. Munster. Forsch. Geol. Palaontol., **31/32**, 167-199.

Von Platen H. (1965). Experimental anatexis and genesis of migmatites. In: Controls of metamorphism. Eds. W.S. Pitcher & G. W. Flinn. Pub. Oliver and Boyd, Ebinburgh, 202-218.

Wall V.J., J.D. Clements and D.B. Clark (1987). Models for granitoid evolution and source compositions. J. Geology, **95**, 731-749.

Watson E.B. (1979). Zircon saturation in felsic liquids: experimental data and applications to trace element geochemistry. Contrib. Mineral. Petrol., **70**, 407-419.

Watson E.B. (1987). The role of accessory minerals in granitoid geochemistry (Abs.). The origin of granites, a conference. The Royal Society and the Royal Society of Edinburgh. Edinburgh., 19-21.

Watson E.B. and T. M. Harrison (1983). Zircon saturation revisited: temperature and composition effects in a variety of crustal magma types. Earth Planet. Sci. Lett., **64**, 295-304.

Webb P.C., A.G. Tindle, S.D. Barritt, G.C. Brown and J.F. Miller (1985). Radiothermal granites of the United Kingdom: comparison of fractionation patterns and variation of heat production for selected granites. In: High heat production (HHP) granites, hydrothermal circulation and ore genesis. The Inst. of Mining and Metalogy, London., 408-424.

Whitford D.J., I.A. Nicholls and S.R. Taylor (1979). Spatial variations in the geochemistry of Quaternary lavas across the Sunda Arc in Java and Bali. Contrib. Mineral. Petrol., **70**, 341-356.

Wickham S.M. (1987). The segregation and emplacement of granitic magmas. J. Geol. Soc. London, **144**, 281-297.

Wilson D.V. (1985). The deeper structure of the Central Andes and some geophysical constraints. In: Magmatism at a Plate Edge. Eds. W.S. Pitcher, M.P. Atherton, E.J. Cobbing and R.D. Beckinsale. Pub. Blackie, Glasgow, 13-18.

Winkler H.G.F. (1976). Petrogenesis of metamorphic rocks (2nd ed.). Pub. Springer-Verlag, N. York.

Wright T.L. and P.C. Doherty (1970). A linear programming and least squares computer method for solving petrologic mixing problems. Bull. Geol. Soc. Am., **81**, 1995-2008.

Wyllie P.J., K.G. Cox and G.M. Biggar (1962). The habit of apatite in synthetic systems and igneous rocks. J. Petrol., **3**, 238-243.

York D. (1969). Least squares fitting of a straight line with correlated errors. Earth. Planet. Sci. Lett., **5**, 320-324.

Zen E-An (1986). Aluminum enrichment in silicate melts by fractional crystallization: Some mineralogic and petrographic constraints. J. Petrol., **27**, 1095-1117.